

Free surface effects in TEM imaging of dislocation lines and loops in Fe

THÈSE N° 6262 (2014)

PRÉSENTÉE LE 24 JUIN 2014

À LA FACULTÉ DES SCIENCES DE BASE
LABORATOIRE DE SPECTROMÉTRIE ET MICROSCOPIE ÉLECTRONIQUE
PROGRAMME DOCTORAL EN SCIENCE ET GÉNIE DES MATÉRIAUX

ÉCOLE POLYTECHNIQUE FÉDÉRALE DE LAUSANNE

POUR L'OBTENTION DU GRADE DE DOCTEUR ÈS SCIENCES

PAR

Wenwang WU

acceptée sur proposition du jury:

Prof. H. Hofmann, président du jury
Prof. C. Hébert, directrice de thèse
Prof. W. Curtin, rapporteur
Prof. B. Devincré, rapporteur
Dr R. Schäublin, rapporteur



ÉCOLE POLYTECHNIQUE
FÉDÉRALE DE LAUSANNE

Suisse
2014



Abstract

Understanding of the physical and geometrical characteristics of the radiation induced defects in ferritic steels based on Fe-Cr is essential to optimize their properties as structural materials for nuclear power plants. Their observation in a thin foil by transmission electron microscopy (TEM) in diffraction contrast mode is one of the most used techniques. However, the comparison between the experimental TEM images and those that can be obtained by simulation is needed to give a reliable assessment of the characteristics of these defects, especially for the small radiation induced dislocation loop. Indeed, its black-white contrast is not directly related to its actual characteristics, and even more so when the loop size comes down to nanometres. In addition, it has been already noticed that the relaxation at the free surfaces of the needed thin foil for TEM should be taken into account in the analysis, but it remained a challenge till today.

The dislocation loops formed in the Fe-Cr base alloys have a Burgers vector of the type $\frac{1}{2} a_0 \langle 111 \rangle$ or $a_0 \langle 100 \rangle$. Experimentally, irradiation by accelerated ions is often used to study the dislocation loop, and the dynamic study of its formation and evolution can be done in situ in a TEM with ions. Ion irradiation presents several advantages over post-irradiation studies conducted on samples irradiated in a nuclear reactor. However, the ratio of $\frac{1}{2} a_0 \langle 111 \rangle$ to $a_0 \langle 100 \rangle$ loops is modified during in-situ TEM experiments irradiation of ferritic material as the very mobile loops $\frac{1}{2} a_0 \langle 111 \rangle$ can be lost at the free surfaces of the thin foil.

This work is part of a project to validate the simulations with experiments to better understand the mechanism of formation of the dislocation loop in Fe-Cr, particularly in relation to temperature and its characteristics, that is its vector Burgers, habit plane, size and shape. The aim of this work is to implement different models of continuum elasticity to address the problem of surface relaxation of the TEM thin foil, which induces a so-called 'image' force on a dislocation loop or line. Models are implemented in the TEM image simulation code 'CUFOUR', based on Schaeublin-Stadelmann equations, in order to understand the impact on the TEM images. Strengths that characterize this work are:

- A robust method for calculating anisotropic image forces has been successfully developed in Fourier space. This new method works for a straight dislocation or a dislocation loop in a semi-infinite space, or a thin foil.
- The method of has been successfully implemented in CUFOUR code.
- A screw dislocation, $\frac{1}{2} a_0 \langle 111 \rangle$, straight and inclined in a thin foil of ultra high purity Fe, was used to validate the simulation of TEM images with experimental TEM. A good agreement between experiment and simulation is found.
- Different types of dislocation loop were implemented in CUFOUR. The effect of the diffraction condition, the loop characteristics and properties of the thin foil is systematically studied. The effect of the image forces on the TEM image was particularly studied. It appears that close to the surface they can completely invert its black-white contrast.
- The anisotropy of Fe has a strong influence on the images forces, relative to the isotropic case. The anisotropy thus cannot be ignored. In iron, temperature increases this effect. The elastic energy induced by the free surface becomes remarkable when the depth of the dislocation loop beneath the surface is comparable to the characteristic length thereof. Moreover, there is large difference between the $\frac{1}{2} a_0 [111]$ loop in a (111) foil and the $a_0 [100]$ loop in a (100) foil.

Keywords: transmission electron microscopy, diffraction contrast image, image stress effect, anisotropy, dislocation loop, column approximation, CUFOUR, Schaeublin-Stadelmann equations.

Résumé

Comprendre les caractéristiques physiques et géométriques des défauts induits par irradiation dans les aciers ferritiques à base de Fe-Cr est fondamental pour optimiser leurs propriétés comme matériaux de structure pour les centrales nucléaires. Leur observation par microscopie électronique à transmission (MET) en mode de contraste de diffraction est l'une des techniques les plus utilisées. Cependant, la comparaison entre les images MET expérimentales et celles que l'on peut obtenir par simulation est nécessaire pour porter un jugement fiable sur les caractéristiques de ces défauts, en particulier pour les petites boucles de dislocations. En effet, le contraste noir - blanc observé pour la boucle de dislocation n'est pas directement lié à ses caractéristiques réelles, et ce d'autant plus lorsque la taille de la boucle est nanométrique. De plus, il a été déjà remarqué que la relaxation aux surfaces libres de la lame mince nécessaire pour la MET devrait être tenu en compte dans l'analyse, mais cela est resté un défi.

Les boucles de dislocation formées dans les alliages à base de Fe-Cr sont de type $\frac{1}{2} a_0 \langle 111 \rangle$ et $a_0 \langle 100 \rangle \{100\}$. Expérimentalement, on utilise souvent des irradiations par ions accélérés pour étudier le mécanisme de formation de la boucle de dislocation, ainsi que les processus de son développement dynamique avec des irradiations aux ions conduites in situ dans un MET, ce qui présente plusieurs avantages par rapport aux études post-irradiation conduites sur des échantillons irradiés en réacteur nucléaire. Cependant, le rapport $\frac{1}{2} a_0 \langle 111 \rangle / a_0 \langle 100 \rangle$ des boucles est modifié au cours des expériences MET in-situ d'irradiation de matériau ferritique, car les boucles $\frac{1}{2} a_0 \langle 111 \rangle$ très mobiles peuvent être perdues aux surfaces libres de la lame mince.

Ce travail fait partie d'un projet visant à valider les simulations par des expériences pour mieux comprendre le mécanisme de formation de la boucle de dislocation dans les alliages Fe-Cr, en particulier en relation avec la température et ses caractéristiques, soit son vecteur Burgers, plan d'habitat, taille et forme. Le but de ce travail a été de mettre en œuvre différents modèles d'élasticité du continuum afin de traiter du problème de la relaxation de surface de la lame mince, qui induisent une force dite 'image', pour une ligne et une boucle de dislocation. Les modèles développés ont été implémentés dans le code de simulation 'CUFOUR' de simulation d'images MET, basé sur les équations Schaeublin – Stadelmann, afin d'en comprendre l'impact sur les images MET. Les points forts qui caractérisent ce travail sont les suivants :

- Une méthode robuste de calcul de la force image anisotrope a été développée avec succès dans l'espace de Fourier. Cette nouvelle méthode fonctionne pour une dislocation droite et une boucle de dislocation dans un semi-espace infini ou un film mince.
- La méthode de calcul des forces images a été implémentée avec succès dans le code 'CUFOUR'.
- Une dislocation vis, $\frac{1}{2} a_0 \langle 111 \rangle$, droite et inclinée dans une lame mince de Fe ultra pur, a été utilisée pour valider les simulations avec de la MET expérimentale.
- Différents boucles de dislocation ont été mises en œuvre dans CUFOUR. L'effet de la condition de diffraction, des caractéristiques de la boucle et des propriétés de la lame mince est étudié systématiquement. L'effet des forces images sur l'image MET a été particulièrement étudié. Il apparaît que ces forces images peuvent complètement inverser son contraste noir-blanc.
- L'anisotropie du Fe a une forte influence sur les forces images, relativement au cas isotrope. L'anisotropie ne peut donc être ignorée. Dans le fer cet effet augmente avec la température. En outre, l'énergie élastique induite par la surface libre devient remarquable lorsque la profondeur de la boucle de dislocation sous la surface est comparable à la longueur caractéristique de celle-ci. L'effet entre une boucle de type $\frac{1}{2} a_0 [111]$ dans une lame (111) par rapport à une boucle de même taille de type $a_0 [100]$ dans une lame (100) est très différent.

Mots-clés: microscopie électronique à transmission , contraste de diffraction , surfaces libres, effet des forces images, approximation de la colonne, fer pur, énergie élastique, dislocation, CUFOUR , équations Schaeublin – Stadelmann.

Content

ABSTRACT.....	I
RÉSUMÉ	III
CONTENT.....	V
ABBREVIATION AND ACRONYMS	1
LIST OF SYMBOLS	3
INTRODUCTION.....	5
CHAPTER. 1: BACKGROUND AND LITERATURE REVIEW	7
1.1. Fe-Cr based alloy application in future nuclear reactors.....	8
1.1.1. Displacement cascade and defects evolution	9
1.1.2. Fe-Cr based alloy as structural material	10
1.2. Dislocation loops in irradiated Fe-Cr alloy.....	11
1.2.1. Dislocation loops formed in Fe-Cr alloy under irradiation	11
1.2.2. Formation mechanism of $a_0\langle 001 \rangle$ dislocation loop	13
1.3. TEM imaging of defects.....	14
1.3.1. TEM application for studying irradiation induced dislocation loop	14
1.3.1.1. Black-white contrast of four types of dislocation loops.....	15
1.3.1.2. L-vector analysis of dislocation loops black-white contrast and its limit	16
1.3.2. The necessity for TEM image simulation	17
1.3.2.1 Dynamic diffraction principle in TEM imaging of defects.....	17
1.3.2.2 Multislice approach.....	17
1.3.2.3 Differential equations approach	18
1.4 Free surface effect of defects	20
1.4.1. Continuum micromechanics of defects	20
1.4.2. Anisotropic elasticity of defects in solid	22
1.4.3. Half infinite space, thin foil	23
1.4.4. Surface relaxation effects on TEM contrast	26
CHAPTER 2: EXPERIMENT.....	29
2.1. Preparation of TEM sample.....	30
2.1.1. Initial material.....	30
2.1.2. Mechanical and electrochemical polishing	30
2.2. Many beam dynamical theory	31
2.3. TEM diffraction imaging of defects	34
2.3.1. BF, DF, WBDF	34
2.3.2. TEM observation technique of crystal defects.....	35
2.3.3. The deviation vector	36

2.4. Quantitative characterization of dislocation	36
2.4.1. Basic $g \cdot b$ analysis principle	36
2.4.2. Determination of sample thickness via EELS.....	37
CHAPTER. 3: ELASTIC IMAGE FIELD CALCULATION METHOD.....	39
3.1. General methodology.....	40
3.2. Fourier space solution for anisotropic half space problem	42
3.2.1. The image stress of a cubic crystal with [001] orientation	43
3.2.2. The image stress of a HCP crystal with [0001] orientation	45
3.3. Fourier space solution for anisotropic thin foil problem.....	46
3.3.1. The image stress of a cubic crystal thin foil with [001] orientation.....	47
3.3.2. The image stress of a cubic crystal thin foil with [111] orientation.....	48
3.4. Image energy calculation.....	50
3.4.1. Image energy for the half space	50
3.4.2. Image energy for the thin foil	50
3.5. Displacement field of dislocation loop within bulk material.....	51
3.6. Self-energy of a dislocation loop within bulk material	52
3.6.1. Interaction energy between two dislocation loops	52
3.6.2. Self-energy of a dislocation loop with isotropic elasticity.....	52
3.6.3. Self-energy of a dislocation loop with anisotropic elasticity	53
CHAPTER. 4: TEM IMAGE SIMULATION METHOD	55
4.1. General methodology.....	56
4.1.1. Simulation scheme for inclined dislocation	57
4.1.2. Simulation scheme for dislocation loops	58
4.2. Inclined dislocation	59
4.2.1. Image solution of inclined dislocation	59
4.2.1.1. Isotropic Devincere-Weinberger model.....	59
4.2.1.2. Isotropic Mura-Weinberger model.....	60
4.2.1.3. Anisotropic Willis-Steeds-Lothe (WSL) and Wu model	61
4.2.2. Bulk solution via finite dislocation segment.....	62
4.2.2.1. Isotropic Mura model.....	62
4.2.2.2. Anisotropic Willis-steeds-Lothe model	62
4.2.3. Total solution, as image + bulk solutions	62
4.2.3.1. Isotropic Devincere-Weinberger-Mura model.....	62
4.2.3.2. Isotropic Mura-Weinberger-Mura model.....	63
4.2.3.3. Anisotropic WSL-Wu-WSL model.....	63
4.2.4. Bulk solution via infinite dislocation	63
4.2.4.1. Isotropic Hirth-Lothe model	63

4.2.4.2. Anisotropic Stroh model	63
4.3. Dislocation loop	64
4.3.1. Image solution.....	64
4.3.1.1. Isotropic Devincre-Weinberger model.....	64
4.3.1.2. Isotropic Mura-Weinberger model.....	64
4.3.1.3. Anisotropic WSL-Wu model	64
4.3.1.4. Anisotropic Mura-Wu model	65
4.3.2. Bulk solution.....	66
4.3.2.1. Isotropic Mura model.....	66
4.3.2.2. Anisotropic WSL model	66
4.3.3. Total solution, as image + bulk solutions	66
4.3.3.1. Isotropic Devincre-Weinberger-Mura model.....	66
4.3.3.2. Isotropic Mura-Weinberger-Mura model.....	66
4.3.3.3. Anisotropic WSL-Wu-WSL model.....	67
4.3.3.4. Anisotropic Mura-Wu-WSL model	67
4.4. General considerations on the different models.....	67
CHAPTER.5: RESULTS	69
5.1. Elastic field calculation.....	70
5.1.1. Energy of dislocation loop	70
5.1.2. The relative error of image stress calculation for half space and thin foil	71
5.1.3. Image force for half space.....	73
5.1.3.1. Inclined dislocation	73
5.1.3.2. Dislocation loop	75
5.1.3.3. Factors influencing the effect of dislocation loop image stress	76
5.1.4. Image force for thin foil	79
5.1.4.1. Inclined dislocation	79
5.1.4.2. Dislocation loop	81
5.1.4.3. Comparison between bulk, image and total displacement field.....	84
5.1.4.4. Factors influencing thin foil effect.....	87
5.2. TEM image simulation results for inclined dislocation	91
5.2.1. Comparison between elasticity models.....	92
5.2.2. Verification by TEM experiments with intensity profile information	94
5.2.2.1. Inclined dislocation within [001] bcc Fe thin foil	94
5.2.2.2. Verification of inclined dislocation within [011] bcc Fe thin foil.....	95
5.2.3. Image force effect induced end-on contrast	97
5.2.4. Image force effect relation to TEM foil thickness	98
5.2.5. Effect of anisotropy.....	99

5.2.6. Effect of zone axis	100
5.2.6.1. Simulated $\frac{1}{2} a_0[111]$ dislocation line under [001] zone axis.....	100
5.2.6.2. Simulated $\frac{1}{2} a_0[111]$ dislocation line under [011] zone axis.....	101
5.3. TEM image simulation results for dislocation loop	102
5.3.1. Comparison between elasticity models.....	102
5.3.2. Comparison between CA and non-CA TEM image simulation schemes	103
5.3.3. The convergence of anisotropy towards isotropy	105
5.3.4. Comparison between two beam and many beam simulation schemes.....	105
5.3.5. Experimental verification with Frank edge-on loop within irradiated copper	106
5.3.6. The L, g and b vectors relation analysis.....	108
5.3.7. Image force dependencies.....	110
5.3.7.1. Zone axis effect.....	110
5.3.7.2. Loop depth within thin TEM foil effect.....	113
5.3.7.3. Loop radius effect	115
5.3.7.4. Anisotropy ratio effect	116
5.3.7.5. Image stress effect at upper and lower surfaces.....	117
5.3.8. Effect of loop depth	119
5.3.8.1. Loop depth change effect within layer structure of TEM foil.....	119
5.3.8.2. Loop depth change across whole TEM foil thickness.....	120
5.3.9. Anisotropy ratio effect	121
5.3.10. Loop radius effect	121
5.3.11. Zone axis effect.....	122
5.3.11.1. Simulated [100] dislocation loop under [001] zone axis.....	122
5.3.11.2. Simulated [100] dislocation loop under [011] zone axis.....	123
5.3.11.3. Simulated [111] dislocation loop under [111] zone axis.....	124
CHAPTER.6: DISCUSSION	127
6.1. TEM contrast of inclined dislocation	128
6.2. TEM contrast of nanometric dislocation loops	129
6.3. Dislocation loops in bcc Fe thin foil.....	130
6.4. Column approximation	132
6.5. Dislocation core treatment	133
CHAPTER.7: CONCLUSION AND PERSPECTIVES.....	135
7.1 Conclusion	136
7.1.1. Anisotropic image stress method	136
7.1.2. Dislocation loops within thin TEM foil	136
7.1.3. TEM contrast of inclined dislocation.....	136
7.1.4. TEM contrast of nanometric dislocation loops	136

7.2. Perspectives	137
7.2.1. Comparison between MD, isotropic and anisotropic models	137
7.2.2. Further application on HCP crystal.....	138
REFERENCE.....	141
APPENDIX.....	149
ACKNOWLEDGEMENTS	173
CURRICULUM VITAE.....	175

Abbreviation and acronyms

2D	Two Dimensional
3D	Three Dimensional
ALWR	Advanced Light Water Reactor
appm	Atomic Parts Per Million
BC	Boundary Condition
BF	Bright Field
CA	Column Approximation
CEA	Commissariat à l'Energie Atomique et aux énergies alternatives
Comis	A software package for many beam TEM image simulation of defects
CUFOUR	A software package for many beam TEM image simulation of defects
DBTT	Ductile to Brittle Transition Temperature
DD	Dislocation Dynamics
DF	Dark Field
DP	Diffraction Pattern
dpa	Displacement Per Atom
EIA	United States Energy Information Administration
EPFL	École Polytechnique Fédérale de Lausanne
Fe-Cr	Iron Chromium alloy
FFT	Fast Fourier transform
F/M	Ferritic-Martensitic steel
GB	Grain Boundary
Gen-II	Generation II reactor
Gen-III	Generation III reactor
Gen-IV	Generation IV reactor
GFR	Gas cooled Fast Reactor
HB	Howie-Basinski
HCP	Hexagonal close packed crystal
HOLZ	Higher Order Laue Zone
HREM	A software package for TEM simulation
HRTEM	High Resolution Transmission Electron Microscopy
HT	High tension of transmission electron microscope
HV	The Vickers Pyramid Number unit of hardness given by Vickers hardness test
ITER	International Thermonuclear Experimental Reactor
jEMS	A software package for TEM simulation
LFR	Lead cooled Fast Reactor

LHS	Left Hand Screw dislocation
MD	Molecular Dynamics
MN	Meshing number along periodic length
MSR	Molten Salt Cooled Reactor
Non-CA	None Column Approximation
ODS	Oxide Dispersion Strengthened
PBC	Periodic Boundary Condition
PL	Periodic length in 2D space
PRV	Pressure Reducing Valve stainless steel
PSI	Paul Scherrer Institut
R & D	Research and Development
RHS	Right Hand Screw dislocation
SAD	Selected Area Diffraction
SCWR	Supercritical Water cooled Reactor
SFR	Sodium cooled Fast Reactor
SN	Number of segments of the inclined dislocation and dislocation loop
TEM	Transmission Electron Microscopy
TEMACI	A software package for many beam TEM image simulation of defects
UHP	Ultra High Purity
VHTR	Very High Temperature Reactor
WB	Weak Beam
WBDF	Weak Beam Dark Field
WN	Numbers of wave for Fourier series
WSL	Willis–Steeds–Lothe
ZA	Zone Axis of diffraction pattern

List of symbols

B	Beam direction
$B_{ijk}(x, x')$	Boussinesq operators representing the stress tensor at x induced by unit force at x' .
b	Burgers vector
b_n	Component of Burger vector
b_p	Burgers vector component normal to habit plane of dislocation loop
b_z	Component of Burgers vector projected on the image plate plane
C_{ijkl}	4-order stiffness matrix
d	Depth of dislocation loop within thin TEM foil from bottom, or depth of dislocation loop under free surface of half space
E	Elastic modulus
g	diffraction vector representing a Bragg reflection or diffracted beam in reciprocal space
$G_{ij}(x, x')$	The ij-component of the Green's tensor
$G_{ij,k}(x, x')$	First order derivative of ij-component of the Green's tensor
$G_{ij,kl}(x, x')$	Second order derivative of ij-component of the Green's tensor
I	Intensity of TEM image
I_0	Intensity of transmitted beam
I_g	Intensity of diffracted beam
k_x, k_y	Discrete Fourier frequency component
L	L-vector representing black-white coffee bean TEM contrast of dislocation loop
L1	First black-white contrast flip layer of TEM foil along depth direction
L^M	Stiffness matrix for finite solid matrix
L^N	Stiffness matrix for defects within solid matrix
m_e	Mass of electron
mg(ng)	Definition of the imaging and diffraction conditions
n_f	Thin TEM foil normal direction
n_h	Dislocation loop habit plane normal vector
n_l	Inclined dislocation line vector
R	Dislocation loop radius
S_f	Stress boundary condition
S_g	Deviation vector off exact Bragg diffraction condition in reciprocal space
S_u	Displacement boundary condition
t	Foil thickness
T	Temperature

$\mathbf{T}_{\text{dislocation}}$	Transformation matrix between crystal coordinate and dislocation coordinate
\mathbf{T}_{foil}	Transformation matrix between crystal coordinate and thin TEM foil coordinate
\mathbf{T}_{beam}	Transformation matrix between crystal coordinate and electron beam coordinate
T_m	Melting temperature
\mathbf{u}	Dislocation direction in original CUFOUR
\mathbf{u}_k	Displacement component of displacement vector
$\mathbf{u}_{k,l}$	Displacement gradient component of 2 nd -order distortion tensor
$V(\mathbf{r})$	Crystal potential field of TEM thin foil
V^M	3D volume of finite solid matrix
V^N	3D volume of defects within solid matrix
α	Beam convergence angle
\hbar	Planck constant
λ	Wave length of electron
$\psi(\mathbf{r})$	Wave propagation function of the electrons
σ_{ij}	Stress component
μ	Elastic modulus of material
ε_{ij}	Strain component of deformation
ε_{ijk}	Einstein permutation operator
δ_{ij}	Kronecker delta operator
ξ_g	The extinction distance of Bragg reflection \mathbf{g}
ξ_g^{eff}	The effective extinction distance of Bragg reflection \mathbf{g}
ξ'_g	Related to ξ_g through a material-dependent absorption constant

Introduction

In 2011, nuclear power provided 10% of the world's electricity, and nuclear energy is still a promising option for the world energy market in the 21st century. The innovative Generation-IV (Gen-IV) nuclear energy systems and fusion systems are still under continuous research and development, especially concerning the safety, waste treatment and efficiency issues. The combination of high heat load, high thermal neutron flux and corrosive environment could be a major obstacle for the viability of some of the Gen-IV systems and fusion reactors. The safe and reliable performance of such nuclear plants is strongly dependent on the assessment of materials degradation. Changes of mechanical and physical properties of materials during irradiation arise from microstructural changes such as the formation of dislocation loops and cavities, segregation and precipitation that impede dislocation mobility, thus leading to hardening, a shift in the ductile to brittle transition temperature and a reduction of fracture toughness.

Fe-Cr based reduced activation ferritic/martensitic steel has been considered as a promising candidate structural material for Gen-IV reactors and fusion reactors. Even though these materials are used in the nuclear industry since decades, there is still a lack of quantitative understanding of the physical and geometrical features of defects formed under thermo-mechanical and intense flux of energetic neutron flux loads. TEM post-irradiation checking is widely used for studying irradiation defects formed within irradiated materials. It is known that in Fe-Cr alloys, there are $\frac{1}{2} a_0 \langle 111 \rangle$ and $a_0 \langle 100 \rangle$ types of dislocation loops that are formed during irradiation.

TEM imaging using diffraction contrast is one of the most widely used techniques for studying irradiation defects. Observation of small dislocation loops (≤ 5 nm) with TEM is still a challenge today, as the diffraction contrast of the dislocation loop is not directly related to the actual features of the loops, and the widely accepted $g \cdot b = 0$ invisibility criterion for dislocations is of limited utility for small dislocation loops. In addition, there are surface relaxation effect that won't be negligible. In order to make reliable assessments on the characteristics of dislocation loops, TEM image simulation and TEM experimental observation are employed together to understand the structure of the defects. The difficulty in this approach is the lack of knowledge on the image contrast modification induced by the free surfaces. In addition, the synergetic effect of image stress and the strong anisotropy of Fe-Cr alloys will make the contrast more complex. Besides such image contrast analysis difficulties for post-irradiation checking with TEM, the free surface effect of thin TEM foil on the physical behavior of defects during in-situ irradiation experiments is still not well understood. Indeed, the observation of the irradiation induced microstructure is inherently conducted in thin areas of the TEM sample, for they have to be transparent to electrons. This implies that the image contrast of dislocation loops and the physical status of small dislocation loops (≤ 1 nm in radius) formed during in-situ ion irradiation experiments is strongly influenced by the proximity of free surfaces, because of the so-called image forces, as it was recognized long ago [Masters, 1963].

In this work we attempt to quantify some of these pending issues by developing appropriate elasticity models and many beam TEM image simulations using the code CUFOUR. Comparison with TEM experimental investigation of inclined dislocations in ultra high purity (UHP) Fe is made in order to validate simulations, and thus provide a better understanding of free surfaces effect in TEM thin foils on irradiation induced damage in Fe-Cr alloy. The experimental characterization of the dislocation in Fe is performed using diffraction contrast or conventional TEM.

Aims of the work

In view of the described challenges the aims of the current work are the following:

- Development of isotropic and anisotropic elasticity models to describe image forces for a dislocation line inclined in the thin TEM foil and for a dislocation loop.
- Implementation of inclined dislocation and dislocation loop models into CUFOUR code, based on Schaeublin-Stadelmann equations for many beam TEM image simulation.

- Experimental verification with an inclined screw dislocation in ultra high purity Fe, quantitative evaluation of the TEM image contrast intensity profile with the different inclined dislocation elasticity models.
- Investigation of the effect of the diffraction condition, foil physical properties, inclined dislocation and dislocation loop physical and geometrical properties on their simulated TEM image, including image forces.
- Elucidation of the effects of thin TEM foil free surfaces on the black-white contrast of nanometric dislocation loops.
- Qualitative evaluation of the synergistic effects of anisotropy and image stress effect on dislocation loops are studied in a bcc Fe thin TEM foil, especially focusing on an a_0001 loop within (001) foil and a $\frac{1}{2} a_0111$ loop within (111) foil.

Chapter. 1: Background and literature review

In this chapter, dislocation loops in irradiated Fe-Cr alloy are reviewed firstly, then theories on TEM image simulation and micromechanics of defects are briefly reviewed, especially focusing on the image stress of thin foil and free surface effect on TEM image contrast.

1.1. Fe-Cr based alloy application in future nuclear reactors

The International Generation-IV (Gen-IV) initiative was incubated in 2000 to promote the development of a new generation of nuclear energy systems, which hold economics, safety, environmental performance and proliferation resistance advantages over the current Gen II and Gen III reactors. The main physical parameters of the Gen-IV reactors: three thermal neutron reactors and three fast reactors are shown in Table 1.1. In the thermal reactors, almost all neutrons in the reactor core have a low energy (~ 0.025 eV), while in the fast reactors, the neutron energy is much higher (more than 1 MeV).

Table 1.1: Survey of Generation IV nuclear reactors [Mesquita, 2013].

	GFR	SCWR	MSR	SFR	VHTR	LFR
Neutrons energy	Fast	Thermal	Thermal or fast	Fast	Thermal	Fast
Power (MWe)	1200	Up to 1500	1000	50 - 1500	~200	19.8 - 600
Fuel type	Plate or ceramic	UO ₂ pellet	Molten salt	MOX or Metal alloy	TRISO	MOX or Nitrides
Coolant	Helium	Light water	Molten salt	Sodium	Helium	Lead
Moderador	-	Light water	-	-	Graphite	-
Outlet temperature	850°C	625°C	1000°C	~500°C	1000°C	~500°C
Pressure * (MPa)	7	25	~0.1	~0.1	5 - 7	~0.1
Fuel Cycle	Closed	once through	Closed	Closed	once through	Closed

* Primary system pressure.

The promising structural materials for the six types of Gen-IV systems are shown in Table.1.2, and the major service requirements of candidate structural materials for these reactors are summarized in the three following categories [Murty, 2008; Yvon, 2009].

- The in-core materials need to exhibit dimensional stability under irradiation, whether under stress (irradiation creep or relaxation) or without stress (swelling, growth);
- The mechanical properties (tensile strength, ductility, creep resistance, fracture toughness, resilience) of all structural materials have to remain acceptable after aging;
- The materials have to retain their properties in corrosive environments (reactor coolant).

Table 1.2: Summary of candidate materials for Gen-IV reactors [Kuksenko, 2011].

Reactor system	F-M steel	Austenitic stainless steels	ODS steels	Ni-base alloys	Graphite	Refractory alloys	Ceramics
GFR	P	P	P	P	-	P	P
Pb-LFR	P	P	S	-	-	S	S
MSR	-	-	-	P	P	S	S
SFR	P	P	P	-	-	-	-
SCWR	P	P	S	S	-	-	-
VHTR	S	-	-	P	P	S	P

P (primary options) – materials that has a reasonable database but the qualification needs to be carried out.

S (secondary options) – refers to promising materials which need extensive research and development for database generation

Besides the development of the six types of Gen-IV fission reactors, international research cooperation on fusion technology is also on the way. Fusion has very promising energy efficiency, safety and environmental friendly advantages over fission reactors. However, as shown in Fig. 1.1, the cruel thermo-mechanical stress, high temperatures, intense high-energy neutron flux, fusion transmutation (He/dpa, H/dpa) puts the greatest challenge for fusion structural materials development.

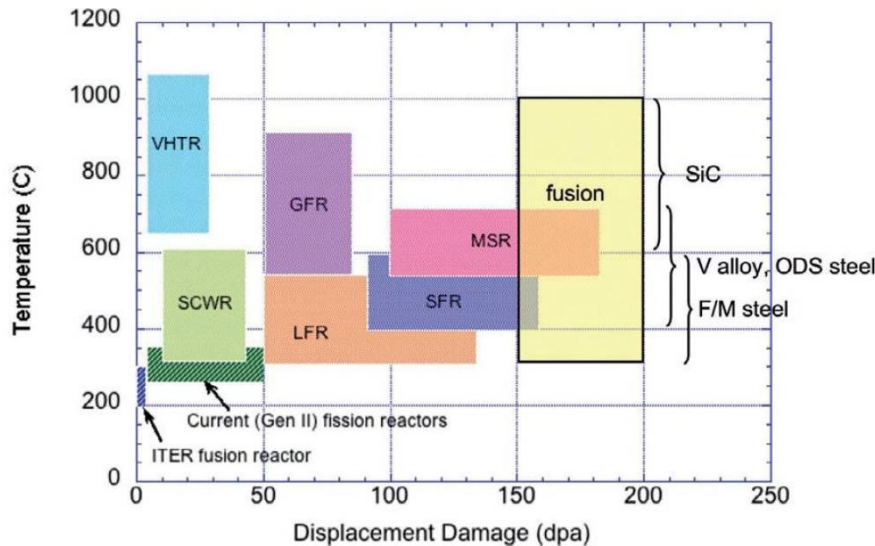


Figure 1.1: Overview operating temperatures and displacement damage dose regimes for current Gen-II and Gen-IV reactors [Zinkle, 2000].

1.1.1. Displacement cascade and defects evolution

Radiation damage event is defined as the transfer of energy from an incident particle to the impacted solid, the resulting distribution of target atoms after completion of the collision event, and the subsequent microstructural evolution process. The radiation damage event is actually composed of several distinct processes: [Was, 2007]

(1) The primary knock-on event:

- The interaction of an energetic incident particle with a lattice atom, resulting in the transfer of kinetic energy to the lattice atom, such energy transfer gives birth to a primary knock on atom (PKA).
- The displacement of the atom from its lattice site.

(2) The displacement cascade:

- The passage of the displaced atom through the lattice and the resulting additional knock-on atoms, trigger a displacement cascade (collection of point defects created by the PKA) event.
- It introduces vacancy and self-interstitial atom (SIA) defects during the collision cascade process. The radiation damage event is terminated when the PKA comes to rest in the lattice as an interstitial. An equal number of vacancies and interstitials, or Frenkel pairs, are created.

(3) The defects post-cascade evolution (migration, annihilation, diffusion)

- These point defects (vacancies and interstitials) will diffuse, annihilate, cluster, and interact with dislocation, grain boundary, foreign elements, thus forming the foundation for all observed macroscopic physical and mechanical properties degradation of materials [Ullmaier, 1980; Was, 2007].

- Point defects can cluster into dislocation loops for SIA and vacancies, and voids for vacancies.

Details of this process and its timescale are given in Table 1.3.

Table 1.3: Approximate time-scale for the production of defects in irradiated metals [Ullmaier, 1980].

Time (s)	Event	Result
10^{-18}	Energy transfer from the incident particle	Creation of a primary knock-on atom (PKA)
10^{-13}	Displacement of lattice atoms by the PKA	Displacement cascade
10^{-11}	Energy dissipation, spontaneous recombination and clustering	Stable Frenkel pairs (single interstitial atoms (SIA) and vacancies) and defect clusters
$> 10^{-8}$	Defect reactions by thermal migration	SIA and vacancy recombination, clustering, trapping, defect emission

Irradiation causes another type of damage. When the energy is sufficient, there are nuclear reactions creating foreign elements, especially a large amount of hydrogen and helium atoms, which precipitate into bubbles and grow by absorption of vacancies [Chen, 2008]. The final defect structure depend strongly on accumulated dose, dose rate, irradiation source, temperature, alloy types, minority alloying elements, and production rate of impurities. The interaction between different types of irradiation defects and dislocation is crucial for understanding the macroscopic mechanical properties degradation of nuclear structural materials, such as hardening, swelling, creeping, embrittlement, segregation, and shift of ductile-brittle transition temperature (DBTT). According to the service temperature and irradiation condition, the main mechanical degradation issues of irradiated nuclear structural materials can be summarized as following:

- At low temperature (up to $0.35 T_m$, dose > 0.1 dpa), there will be radiation embrittlement, hardening, reduction in fracture toughness and increase in DBTT, thus reducing the lifetime of the irradiated materials;
- Within intermediate temperature region (up to $0.45 T_m$, dose > 10 dpa), there will be drastic reduction of ductility, and irradiation creep.
- At high temperature (between $0.35-0.6 T_m$, dose > 10 dpa), there will be radiation induced/enhanced segregation and precipitation, swelling due to void formation (this will happen for most alloys between $0.35-0.55 T_m$), fusion materials exhibit a peculiar He embrittlement.

1.1.2. Fe-Cr based alloy as structural material

As shown in Table 1.2 and Fig. 1.1, Fe-Cr based austenitic steels, ferritic/martensitic (F/M) alloys and their oxide dispersion strengthened (ODS) versions are promising candidates for structural materials in future fusion reactors and Gen-IV, and the Cr content is one of the key parameters to be optimized in order to guarantee favorable properties under irradiation exposure. The application of Fe-Cr based nuclear structural materials cover over a wide range of temperature:

- Low temperature (300-600°C) range: austenitic steels, ferritic/martensitic steels, and ODS alloys;
- Intermediate temperature range (600-800°C): traditional and modified austenitic steels, ODS F/M steels, iron or nickel based super-alloys, refractory alloys;
- High temperature ($> 800^\circ\text{C}$) range: advanced ODS and refractory based systems.

Depending on the irradiation source, the temperature, the accumulated dose and the dose rate, various irradiation experimental schemes are proposed for investigating the mechanical properties degradation of commercial and experimental Fe-Cr alloys, such as hardening, swelling, loss of elongation, creep and DBTT shift. However, making a clear general conclusion on the relationship between mechanical properties and irradiation conditions, namely dose, dose rate and temperature is still very challenging, until present. [Suganuma, 1982; Kohyama, 1996; Garner, 2000; Luppó, 2000; Malerba, 2008]

1.2. Dislocation loops in irradiated Fe-Cr alloy

1.2.1. Dislocation loops formed in Fe-Cr alloy under irradiation

For several decades, a number of experimental studies focused on the formation of dislocation loops in bcc materials under irradiation, including Fe based steel and also other bcc metals, such as Cr, Mo, W, Nb and V [Downey, 1965; Eyre, 1965a; Master, 1965; Meakin, 1965; Haeussermann, 1972; Sikka, 1973; Shiraishi, 1974; Narayan, 1976; Chen, 1978; English, 1980; Little, 1980; Suganuma, 1981; Robertson, 1982; Horton, 1982; Ward, 1989; Muroga, 1996; Schäublin, 2002; Zinkle, 2006; Chen, 2008; Hernández, 2008; Yao, 2008; Kuksenko, 2011; Klimenkov, 2011]. It is generally accepted that the configuration of dislocation loops only depends on the lattice structure. Here, a summary of the defects in bcc metals is given in Table 1.4. Taking these facts into consideration, one can conclude that the irradiation induced dislocation loops in Mo, W, Nb and V are interstitial with a Burger's vector $\frac{1}{2} a_0 \langle 111 \rangle$ and on a habit plane (HN) $\{111\}$. Occasionally, other Burgers vectors and habit planes in W and Nb are reported but seem less reliable. Pure Fe and Fe-based ferritic/martensitic steels were widely investigated at different temperature regimes, and two types of dislocation loops Burgers's vector are found, namely $\frac{1}{2} a_0 \langle 111 \rangle$ or $a_0 \langle 100 \rangle$.

One of the key features is the common observation that a quite large portion of the dislocation loops formed during irradiation at elevated temperatures (300-600°C) are interstitial loops with $\mathbf{b}=a_0 \langle 100 \rangle$, and quite strong evidences confirm that their nature and habit plane are interstitial and $\{100\}$, respectively, in all Fe and Fe-based bcc materials. The situation of the $\frac{1}{2} a_0 \langle 111 \rangle$ loops is somewhat unclear. One recent paper reported that $\frac{1}{2} a_0 \langle 111 \rangle$ loops have both $\{011\}$ and $\{111\}$ habit planes [Zinkle, 2006], while another reported only $\{111\}$ habit planes [Chen, 2008].

Table 1.4: Summary of experimental studies on dislocation loop in bcc structural materials.

	T (K)	<i>b</i>	n_h	nature	specimen	irradiation	ref.
Fe	823	$a_0\langle 001 \rangle$	{001}	I	thin	p, Fe	Master, 1965
	333	$\frac{1}{2}a_0\langle 111 \rangle$	-	-	bulk	n	Eyre, 1965a
	353-593	$\frac{1}{2}a_0\langle 111 \rangle$ $a_0\langle 001 \rangle$		- -	bulk	n	Robertson, 1982
	623-723	$\frac{1}{2}a_0\langle 111 \rangle$ $a_0\langle 001 \rangle$	- {001}	- I	bulk	n	Horton, 1982
	703-763	$\frac{1}{2}a_0\langle 111 \rangle$ $a_0\langle 001 \rangle$	- {001}		thin	e	Ward, 1989
	333	$\frac{1}{2}a_0\langle 111 \rangle$	{111}, {110}		bulk	n	Zinkle, 2006
Fe+10%Cr	653-733	$a_0\langle 001 \rangle$	{001}	I	bulk	n	Little, 1980
	573-773	$\frac{1}{2}a_0\langle 111 \rangle$ $a_0\langle 001 \rangle$	{001}		thin	e	Muroga, 1996
Fe+15%Cr	473-873	$\frac{1}{2}a_0\langle 111 \rangle$ $a_0\langle 001 \rangle$	- -	- -	thin	e	Suganuma, 1981
Fe+19%Cr	573-773	$\frac{1}{2}a_0\langle 111 \rangle$ $a_0\langle 001 \rangle$	{111} {001}	I I	Semi-bulk (100 μm)	α	Chen, 2008
Mo	873	$\frac{1}{2}a_0\langle 111 \rangle$	{111}	I	bulk	n	Meakin, 1965
	333-1473	$\frac{1}{2}a_0\langle 111 \rangle$	{111}, {321}	I	bulk	n	Downey, 1965
	293-673	$\frac{1}{2}a_0\langle 111 \rangle$ $a_0\langle 001 \rangle$	{110}-{111} {110}-{001}	V V	thin ($<10\text{ nm}$)	W, Sb	English, 1980
W	293	$\frac{1}{2}a_0\langle 111 \rangle$ $\frac{1}{2}a_0\langle 011 \rangle$	{011} {011}	V V	thin ($<10\text{ nm}$)	Au	Haeussermann, 1972
	703-853	$\frac{1}{2}a_0\langle 111 \rangle$	{111}		bulk	n	Sikka, 1973
Nb	353	$\frac{1}{2}a_0\langle 111 \rangle$ $\frac{1}{2}a_0\langle 011 \rangle$	{111} {111}		bulk	n	Chen, 1978
	303	$\frac{1}{2}a_0\langle 111 \rangle$ $\frac{1}{2}a_0\langle 011 \rangle$		I, V I, V	bulk	n	Narayan, 1976
V	323-823	$\frac{1}{2}a_0\langle 111 \rangle$	{111}	I, V	bulk	n	Shiraishi, 1974
Fe; Fe+ (5,8,11,9,18%) Cr	300; 573	$\frac{1}{2}a_0\langle 111 \rangle$ $a_0\langle 100 \rangle$	{110}-{111} {001}	I,V	thin (15-85 nm)	Fe+, Xe+	Hernández, 2008
Fe; Fe+8%Cr;	300; 573	$\frac{1}{2}a_0\langle 111 \rangle$	{110}-{111}	I,V	thin ($<100\text{ nm}$)	Fe+	Yao, 2008
Fe+(9,12%)Cr	773	$\frac{1}{2}a_0\langle 111 \rangle$ $a_0\langle 100 \rangle$	{110}-{111} {001}	Not mentioned	Thin(80- 150 nm)	n, Fe+	Kuksenko, 2011
F82H	523; 583	$\frac{1}{2}a_0\langle 111 \rangle$ $a_0\langle 100 \rangle$	- -	I	bulk	p	Schäublin, 2002
Eurofer 97	523-723	$\frac{1}{2}a_0\langle 111 \rangle$	-		bulk	n	Klimenkov, 2011

(Symbols used: T, irradiation/ annealing temperature; b, Burgers vector; -, between; I, interstitial; V, vacancy; p, proton; n, neutron; e, electron; L, low; M, middle and H, high. The results followed by “-” means preliminary or not clear.)

In-situ ion irradiation experiments suggested that the difference in the $a_0\langle 001 \rangle / \frac{1}{2} a_0\langle 111 \rangle$ ratio between Fe and Fe-Cr alloys mainly originates from the fact that dislocations in Fe-Cr alloys are less mobile and more $\frac{1}{2} a_0\langle 111 \rangle$ loops in the Fe TEM foil are lost to the free surfaces than in the Fe-Cr TEM foil [Masters, 1963; Hernandez, 2008; Yao, 2008; Jenkins, 2009]. Loop loss to the surface is thought to occur under the influence of surface image forces, with the gliding along the Burgers vector as the most probable loss mechanism [Masters, 1963]. Prokhodtseva [Prokhodtseva, 2013] studied the effect of the free surfaces of TEM thin foil on the irradiation induced microstructure, and compared the irradiation defects formed in TEM thin foil under in-situ irradiation with that formed in bulk materials irradiated ex situ with single and dual beams. In bulk ultra-high purity (UHP) Fe and Fr(Cr) samples after single and dual beam irradiation, mainly $\frac{1}{2} a_0\langle 111 \rangle$ loops and few $a_0\langle 100 \rangle$ loops were observed, but of smaller size than in thin foils, emphasizing the effects of free surfaces on the type of produced loops. It is thus inferred that $\frac{1}{2} a_0\langle 111 \rangle$ loops dominate the early loop population and visible $a_0\langle 100 \rangle$ loops observed in UHP Fe and Fe-Cr thin foils stem from addition and/or absorption reactions between $\frac{1}{2} a_0\langle 111 \rangle$ loops. The difference between bulk and thin foil irradiation experiments shows that the formation of visible $a_0\langle 100 \rangle$ loops is promoted by the presence

of free surfaces, the more so in the thinnest regions of the sample, leaving a loop population dominated by $a_0\langle 100 \rangle$ loops. Thus, quantification of the ratio of $\frac{1}{2} a_0\langle 111 \rangle / a_0\langle 100 \rangle$ loops appears difficult when performed during TEM in-situ iron irradiation experiments. Moreover, it was experimentally established that chromium decreases the mobility and increases the thermal stability of loops [Arakawa, 2004]. Theoretical works have also shown that Cr atoms decrease the mobility of SIA clusters or small dislocation loops in Fe-Cr alloys [Terentyev, 2005; Terentyev, 2009].

1.2.2. Formation mechanism of $a_0\langle 001 \rangle$ dislocation loop

In order to explain the $a_0\langle 100 \rangle$ loop, which is unique to bcc Fe and Fe-Cr alloys, Eyre and Bullough [Eyre, 1965b] proposed a mechanism to describe the formation of $a_0\langle 100 \rangle$ and $\frac{1}{2} a_0\langle 111 \rangle$ dislocation loops in bcc metals from the shearing of aggregates of $a_0\langle 110 \rangle$ dumbbell self-interstitials. The latter are the most favorable SIAs in Fe, and can form tiny aggregates or dislocation loops on the close packed $\{110\}$ plane. According to extensive molecular dynamics (MD) simulations, an alternative mechanism was proposed based on the reaction of loops initially as $\frac{1}{2} a_0\langle 111 \rangle\{110\}$ [Marian, 2002]. In addition an ab-initio calculations predicted that the most stable interstitial clusters in α -iron with more than 5 atoms are arrangements of parallel $a_0\langle 111 \rangle$ dumbbells on $\{110\}$ habit planes [Willaime, 2005]. More recently, by using a full anisotropic elasticity approximation in the treatment of dislocations, the appearance of $a_0\langle 100 \rangle$ loops in bcc iron at elevated temperatures is explained by the experimentally measured temperature dependence of the elastic constants $(C_{11}-C_{12})/2$ with increasing temperature towards the $\alpha - \gamma$ phase transition temperature of 912°C . This changes the anisotropic elastic free self-energy of the dislocations in iron. As shown in Fig. 1.2, it is expected that the $a_0\langle 100 \rangle$ prismatic loops become increasingly favorable with increasing temperature. The calculation is mainly based on elastic continuum model which could be questionable when applied on the nanometric loops. The influence of Cr, which is vital for the understanding of Fe-Cr alloys, was not taken into account. These investigations demonstrate that additional parameters must influence the loop formation process. One possibility could be the ferromagnetic interaction between atoms which is affected by Cr content, and correspondingly a magnetic potential was developed for MD [Dudarev, 2005], which is not confirmed through experiments yet.

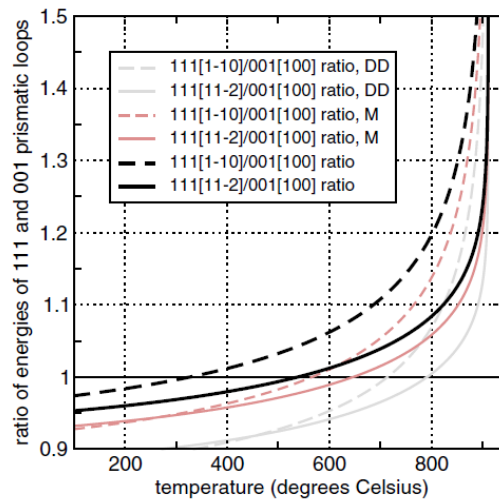


Figure 1.2: Energy of different types of dislocation loops [Dudarev, 2008].

Another formation mechanism derived from Monte Carlo simulations by Xu et al. [Xu, 2013] involves an atomistic process with the reaction product having a Burgers vector that is not the sum of the reacting loops Burgers vectors. Moreover, authors claim that the interaction between interstitial

loops is stochastic in nature and different outcomes can be obtained from the same initial configuration. So, two reacting $\frac{1}{2} a_0\langle 111 \rangle$ loops can lead to the formation of either $a_0\langle 100 \rangle$, or larger $\frac{1}{2} a_0\langle 111 \rangle$ loop with about the same probability. Recently, it was observed in UHP Fe that loops formed under irradiation with He contain both $\frac{1}{2} a_0\langle 111 \rangle\{211\}$ and $a_0\langle 100 \rangle\{100\}$ components which are considered as intermediate stages of transformation of $\frac{1}{2} a_0\langle 111 \rangle$ loops to $a_0\langle 100 \rangle$ [Chen, 2013]. Direct formation of $a_0\langle 100 \rangle$ from the interaction of two $\frac{1}{2} a_0\langle 111 \rangle$ loops has not been experimentally observed yet [Arakawa, 2011], although spontaneous change of the Burgers vector from $\frac{1}{2} a_0\langle 111 \rangle$ into $a_0\langle 100 \rangle$ has been reported [Arakawa, 2006].

1.3. TEM imaging of defects

1.3.1. TEM application for studying irradiation induced dislocation loop

TEM imaging with diffraction contrast is one of the most widely used techniques for studying irradiation defects in irradiated material. The crystal is set at some well-defined diffraction condition, and an objective aperture is used to form an image by selecting only the transmitted beam or one of the diffracted beams. The defect strain field causes local changes in diffraction condition. Indeed, the diffracting planes may be locally bent, causing changes in the excitation of the diffracted beam used to form the image. Under diffraction contrast, only the elastic strain field is thus imaged. Nanometric dislocation loops induced by irradiation gives in such a way a typical black-white contrast. This is the most common mechanism used in radiation-damage studies. However, TEM image characteristics depend sensitively on the selected diffraction conditions.

The various types of irradiation defects, such as small defect clusters, dislocation loops, stacking fault tetrahedra, precipitates, voids and He bubbles can be investigated in TEM using diffraction contrast, Fig. 1.3 shows some of them [Packan, 1979; Prokhodtseva, 2013; Kiritani, 2000].

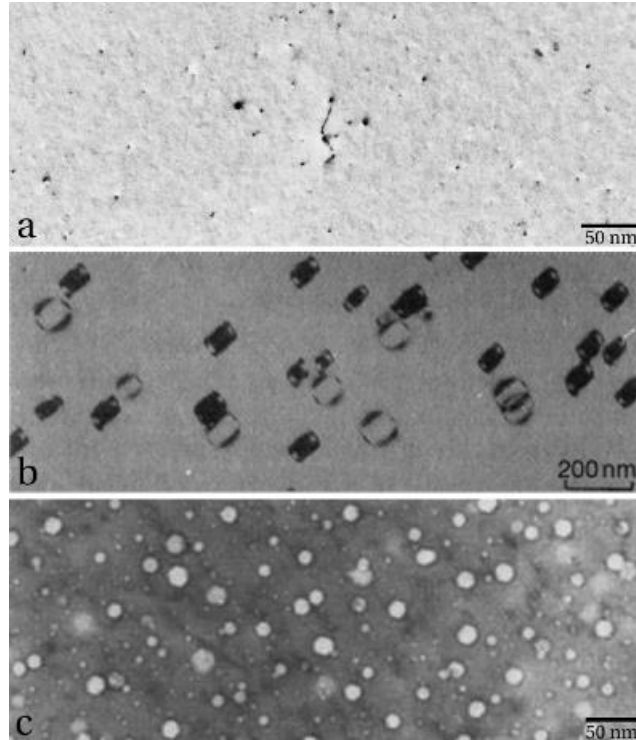


Figure 1.3 Transmission electron micrographs showing typical irradiation induced defects: (a), "black dots" or small dislocation loops in Fe-14Cr after irradiation with heavy ions to 1 dpa at room temperature, [Prokhodtseva, 2013]; (b), dislocation loops in pure Fe following electron irradiation [Kiritani, 2000]; (c), Cavities in austenitic steel irradiated with ions to 70 dpa at 900 K pre-implanted with 1400 appm He [Packan, 1979].(from [Prokhodtseva, 2013])

The invisibility criterion states that when $g \cdot b = 0$ is satisfied for straight dislocation observation in TEM, all the lattice displacement components of a defect lie in the diffraction plane, there will be no diffraction contrast of dislocation. However, complications may arise since the displacement field of a general dislocation will distort any diffracting plane, so that even when $g \cdot b = 0$ there will be residual contrast. Therefore, complete invisibility of a dislocation requires that both $g \cdot b = 0$ and $g \cdot b \times u = 0$ are satisfied simultaneously [Nabarro, 2007]. Different from straight dislocation invisibility criterion, loops with $g \cdot b = 0$ are often still visible when imaged under dynamical two-beam conditions. Under weak-beam imaging conditions, loops usually show invisibility or very weak contrast when $g \cdot b = 0$. However, small loops with $g \cdot b \neq 0$ may also show very weak contrast under weak-beam imaging conditions.

1.3.1.1. Black-white contrast of four types of dislocation loops

As summarized by Eyre from TEM image simulations with two beam dynamic diffraction and isotropic dislocation loop model, depending on the magnitude of $|g \cdot b|$ and dislocation loop orientation, these contrast types have been classified as follows [Jenkins, 2001].

Type 1. $|g \cdot b| = 0$, and the acute angle between the loop normal n_h and the beam direction z is less than about 45° . As an example, two beam TEM DF image of a $\frac{1}{2} a_0011$ loop is shown in Fig. 1.4(a), the diffraction vector is $g=[01\bar{1}]$, and the diffraction condition is $g(1.0g)$ along (011) pole.

Type 2. $|g \cdot b| = 0$, and the acute angle between the loop normal n_h and the beam direction z is equal or close to 90° . As an example, two beam TEM DF image of a $\frac{1}{2} a_001\bar{1}$ loop is shown in Fig. 1.4(b), the diffraction vector is $g=[200]$, and the diffraction condition is $g(1.0g)$ along (011) pole.

Type 3. $0 < |\mathbf{g} \cdot \mathbf{b}| \leq 1$, this is a simple black–white lobe with no interface structure, independent of the angle between loop normal \mathbf{n}_h and z . As an example, two beam TEM DF image of an a_0010 loop is shown in Fig. 1.4(c), the diffraction vector is $\mathbf{g}=[2\bar{1}1]$, and the diffraction condition is $g(1.0g)$ along (011) pole.

Type 4. $|\mathbf{g} \cdot \mathbf{b}| > 1$, this is again a black–white lobe but now the interface between the lobes has structure, for example a small white area of contrast within the dark lobe. As an example, two beam TEM DF image of an a_0100 loop is shown in Fig. 1.4(d), the diffraction vector is $\mathbf{g}=[21\bar{1}]$, and the diffraction condition is $g(1.0g)$ along (011) pole.

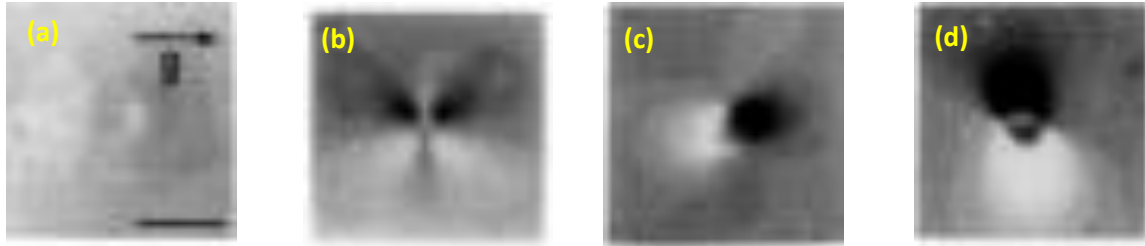


Figure 1.4: Simulated DF images of edge dislocation loops of types $\frac{1}{2} a_0\langle 011 \rangle$ and $a_0\langle 100 \rangle$ in bcc molybdenum foil with normal $z=(011)$. (a), $\frac{1}{2} a_0011$ loop with $\mathbf{g}=[01\bar{1}]$; (b), $\frac{1}{2} a_001\bar{1}$ loop with $g(1.0g)$ under $\mathbf{g}=[200]$; (c), a_0010 loop with $\mathbf{g}=[2\bar{1}1]$; (d), a_0100 loop with $\mathbf{g}=[21\bar{1}]$. Foil thickness $t=121.8$ nm, loop radius $R=1.16$ nm; loop located 118.32 nm from bottom of the foil [Eyre, 1977a].

Type 1 shows quite weak visibility contrast. Type 2, 3 and 4 images are insensitive to a range of practically relevant variables related to the imaging plane, crystal thickness, dislocation loop position within the layer structure (i.e. L1, L2 or L3), dislocation loop size, and also independent of material properties [Eyre, 1977a]. However, despite of such basic classification of the contrast, quantitative judgment of the physical parameters of small dislocation loops is still not feasible for most cases.

1.3.1.2. *L*-vector analysis of dislocation loops black-white contrast and its limit

When performing a TEM analysis of defects, imaging with various diffraction vectors for the same defect is required for a full quantitative analysis. It relies on examining the changes in directions of black–white lobes with the operating diffraction vector \mathbf{g} . The black–white lobes direction is defined by the so-called \mathbf{L} -vector. For a given black–white contrast figure, the \mathbf{L} -vector is defined to run from the center of the black contrast lobe to the center of the white contrast lobe. For defects with symmetrical strain fields, such as spherical precipitates, the \mathbf{L} -vector is found to run approximately parallel to \mathbf{g} vector [Jenkins, 2001].

For dislocation loops, the direction of \mathbf{L} in many situations is parallel to \mathbf{b} , or its projection \mathbf{b}_q on the image plane. For an evaluation of \mathbf{b} , it is then necessary only to evaluate the direction of \mathbf{L} for at least two images taken at different foil orientations [Jenkins, 2001].

For dislocation loops, however, the direction of the \mathbf{L} -vector is usually tied fairly closely to the Burgers vector \mathbf{b} or its projection on the image plane \mathbf{b}_q . \mathbf{L} -vectors do not rotate to follow \mathbf{g} from one micrograph to another. \mathbf{L} -vector analysis generally works well for edge loops if the angle between \mathbf{g} and \mathbf{b} is small. However, the simple \mathbf{L} -vector approach may break down when the angle between \mathbf{g} and \mathbf{b} or \mathbf{b}_q is large, or when non-edge loops are present. Simple \mathbf{L} -vector analysis may therefore fail even in the simple case of edge loops in an isotropic elastic material [Jenkins, 2001]. \mathbf{L} vector analysis is therefore not sufficient for a reliable determination of an unknown type of loop.

1.3.2. The necessity for TEM image simulation

It is known that experimental TEM image of dislocation loops is complex, which depends on beam diffraction condition, TEM foil geometrical and physical properties and defect features, such as foil normal direction, beam direction, loop habit plane, loop Burgers vector, loop depth, loop size, SIA or vacancy loop. In order to make a reliable judgment on the features of dislocation loops quantitatively, experimental observation and TEM image simulation comparison is needed. The image simulations are made using computer programs which integrate the equations of the dynamical theory of electron diffraction. The most extensive simulations have been made using the two-beam Howie–Whelan dynamical equations. [Jenkins, 2001]

- The majority of the simulations in the literature have used two-beam dynamical theory in the column approximation. These approximations appear to work well provided that the Bragg condition is satisfied (i.e. $s_g = 0$). There have been few simulations of loop contrast under kinematical or weak-beam diffraction conditions, where these approximations are less good.
- Most of the simulations have been done for loops located within the first few depth layers, usually the first depth layer L_1 . When dislocation loops are situated within the layer structure, the black-white contrast will be reversed at depth $0.25 \xi_g$, $0.75 \xi_g$ and $1.25 \xi_g$ from free surfaces, and L vector will change direction as well.
- The calculations require knowledge of the displacement field of a loop in a thin foil. Bulk model may work if the loop does not be close to the foil surface, and if this surface is not constrained by an oxide layer, then the strain field of a loop in a semiinfinite medium is required. Most authors, however, have used an expression for the strain field due to a small loop in an infinite medium derived from linear elasticity theory and so neglect the effect of the nearby surface.
- Elastic anisotropy has not been included in most cases.

1.3.2.1 *Dynamic diffraction principle in TEM imaging of defects*

In order to explain the complex black-white contrast of defects, theoretical description of electron scattering through the derivation of the relevant Schroedinger equation is employed. However, when deriving the differential equations from Schroedinger equation, the second order differential terms are omitted under most conditions, and electron energy loss is usually not included in the simulation.

There are mainly lattice image multi-slice simulation and electron dynamical diffraction differential equations simulation schemes for TEM image simulation of defects, as described in the following.

1.3.2.2 *Multislice approach*

The first description of the multislice theory was given in the classic paper by Cowley and Moodie [Cowley, 1957], which originates from a physical optics approach. The development of a computer algorithm from the multislice theory of Cowley and Moodie for numerical computation was summarized by Goodman and Moodie [Goodman, 1974], the crystal foil is divided into thin slices perpendicular to the electron beam, so that the scattering process and the wave propagation can be treated independently. The multislice approach is convenient for interpreting the mechanism of phase contrast imaging of high resolution transmission electron microscopy (HRTEM) and simulations of HRTEM micrographs, but it is not widely used in diffraction contrast image simulations of defects. Since the multislice formula is a kind of numerical integration, there are some continuing discussions on its accuracy. Moreover, there are some open questions on an applicability of the multislice approach when used to calculate diffraction intensities in higher order Laue zones (HOLZ) or in the case of an inclined illumination [Ishizuka, 1998].

1.3.2.3 Differential equations approach

Before elaborating the differential equations approach, a basic concept for electron diffraction contrast imaging is explained. Electron diffraction is essentially a forward scattering process, even after several scattering events in the multi-scattering cases, the scattering angles are still quite small, and most electron travels nearly parallel to the incident beam. An electron which enters the foil at one point will never leave a cylinder column parallel to the incident beam, then so-called column approximation (CA) is introduced by M. Whelan and colleagues [Whelan, 1957], assuming that neighboring columns do not interact, ie. no electrons are exchanged between columns, so that dynamical diffraction equations can be solved for each column independently. CA is essentially equivalent to the high energy approximation. [Graef, 2003]

Differential equations approach can be classified into two categories: CA and non-CA respectively [Howie, 1961; Howie, 1968]. As to CA scheme, the differential equations are reduced into a system of ordinary differential equations. While, a system of coupled partial differential equations will be generated for non-CA scheme [Williams, 2009]. The development history of differential equations approach is simply shown in Fig. 1.5.

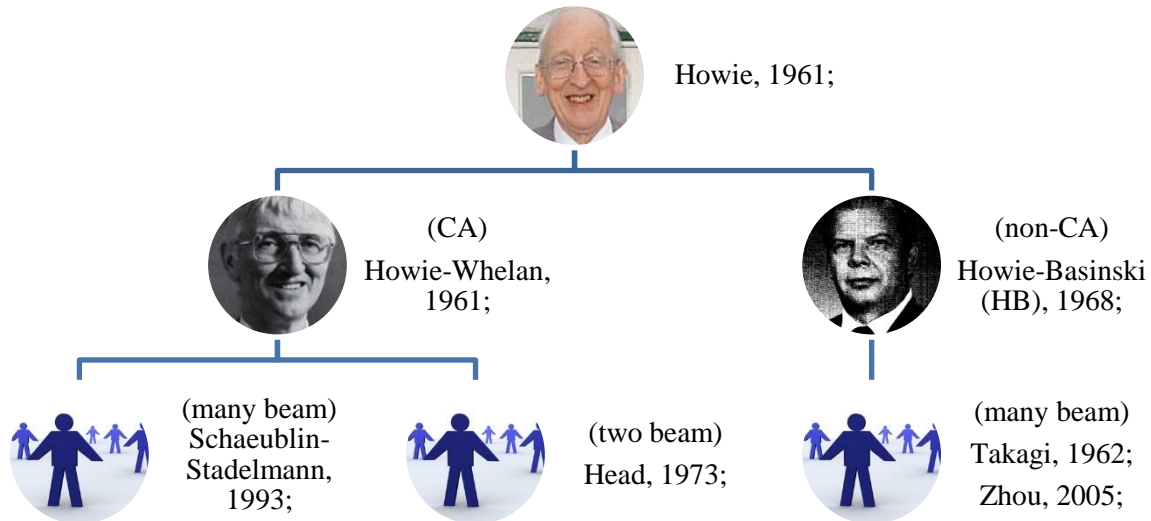


Figure 1.5: Classification of differential equations approach for TEM image simulation of defects [Howie, 1961; Howie, 1968; Takagi, 1962; Head, 1973; Schaeublin, 1993; Zhou, 2005].

Until present, several softwares are reported in literature for TEM image simulation of defects, such as ONEDIS/TWODIS [Head, 1973], CUFOUR [Schaeublin, 1993], TEMACI [Zhou, 2005], SIMCOM [Janssens, 1992], COMIS [Rasmussen, 1991]. The physical models and schemes are summarized in Table.1.5.

Table 1.5: Packages or codes for simulation of diffraction contrast images [Zhou, 2005].

('CA' means column approximation; 'HB' represents Howie-Basinski)

code	model	defects	Fields of defects	Reference
COMIS	CA and HB	Straight dislocations, plane faults, anisotropic	$g \cdot R(r)$	[Rasmussen, 1991]
CUFOUR	CA	Straight dislocations, plane faults, anisotropic	$g \cdot \frac{dR(r)}{dz}$	[Schaeublin, 1993]
ONEDIS/TWODIS	CA and two beam	Straight dislocations, plane faults, isotropic and anisotropic	$g \cdot R(r)$	[Head, 1973]
-	CA and HB	Straight dislocations, anisotropic	-	[Wiezorek, 1995]
-	CA and two beam	Dislocation loops, isotropic	$g \cdot \frac{dR(r)}{dz}$	[Bullough, 1971]
-	CA and two beam	n-sides dislocation loops, isotropic	$g \cdot R(r)$	[Saldin, 1979a; 1979b]
SIMCON	CA and two beam	Straight dislocations, dislocation loops	$g \cdot \frac{dR(r)}{dz}$	[Janssens, 1992]
-	Perturbation	Infinitesimal loops, isotropic and anisotropic	$g \cdot R(r)$	[Wilkens, 1972; Wilkens, 1981]
TEMACI	HB	Dislocation loops, isotropic	$g \cdot \frac{dR(r)}{dz}$	[Zhou, 2005]

Several authors have examined the effects of the CA on both strong beam images and weak beam images of line dislocations, and have generally concluded that these are likely to be small [Jouffrey, 1967; Howie, 1970; Humphreys, 1976]. However, Lewis et al. [Lewis, 1979] have made analytical and numerical studies of Takagi's equations [Takagi, 1962; Takagi, 1969], and claim that the CA is likely to be unreliable in the simulation of weak-beam images of single point-defects and, by inference, small point-defect clusters [Zhou, 2005]. Although Howie [Howie, 1970] concluded that the difference between CA and non-CA calculations for measurements of spacing is negligible for conventional WB-TEM, it was shown that when the partial dislocations do not lie at the same depth in the foil the effect of non-CA can be severe [Wiezorek, 1995]. Schaeublin mentioned that the error of CA amounts to about $10^{-4} g \cdot \lambda$, which is negligible [Schaeublin, 2006].

Lewis argued that the main image detail with non-CA scheme will not be where the CA would predict, but shifted to the left or the right by easily determined amounts. This shifting has the consequence that dislocation images, from two or more dislocations, will not be separated in space by the same lateral distance, as the dislocations themselves unless the dislocations are all the same distance from the exit surface of the crystal [Lewis, 1979].

Zhou made comparison between the WB images of a 10.0nm flat-on vacancy dislocation loop with Burgers vector $1/3 a_0111$ in silicon for $g=(\bar{2}20)$ with CA and HB approaches, the image simulated by the HB approach is shifted by about 1.10nm in a direction opposite to g vector. In general, the magnitude of the displacement depends on both the diffraction conditions and loop depth from bottom of thin TEM foil. The images simulated by the HB approach are broader and of lower maximum intensity than images obtained using CA. Zhou claimed that: CA treatment in HW equation may fail in weak-beam diffraction contrast imaging if the thickness of the foil is relatively large, and the effects associated with a breakdown of the CA are quite serious for very small dislocation loops. For loops smaller than about 3.0nm, there is significant difference between images simulated by the HB and CA approaches. For loops larger than about 5.0nm, the difference is small [Zhou, 2004].

The size of dislocation loops may be divided into three regions: (a), $d > 5.0$ nm; (b), $5.0 \text{ nm} > d > 2.0$ nm; and (c) $d < 2.0$ nm. For defects larger than about 5.0 nm, a combination of dynamical two beam imaging and image contrast simulations has proven very successful for determining defect morphologies [Jenkins, 2001], the contrast is not very sensitive to small changes in diffraction conditions. Under such case, weak-beam imaging and dynamical two-beam imaging are adequate. It has been found experimentally, however, that the visibility of very small clusters of size < 5.0 nm is usually better under weak-beam diffraction conditions [Jenkins, 1999; Kirk, 2000]. MD (in the form of conjugate gradient minimization of the potential energy of a large system of interacting atoms)

models work well for small clusters of defects (≤ 5.0 nm). Comparison between MD and elasticity is important for identifying the limits of elasticity. The use of elasticity theory is likely to be a good approximation for loops of sizes greater than about 2.0 nm, but less feasible for smaller loops [Jenkins, 2001; Zhou, 2006]. In that case, MD would have to be used for the TEM image simulation. Besides, elastic theory has considerable computation speed advantages over MD when defects size is large, as the number of atoms within MD periodic box increases explosively with increase of defects characteristic size. More accurate results obtained using lattice models [Dudarev, 2003; Hudson, 2004] show that deformations remain smooth and continuous even in the core of small defects, and singularities present in solutions found using elasticity can be eliminated by introducing a small regularizing correction in the denominators of the relevant formulas.

As an example, comparison between experimental and simulated TEM images under many beam diffraction condition for small Frank loops in fcc Cu is shown in Fig. 1.6 [Zhou, 2006].

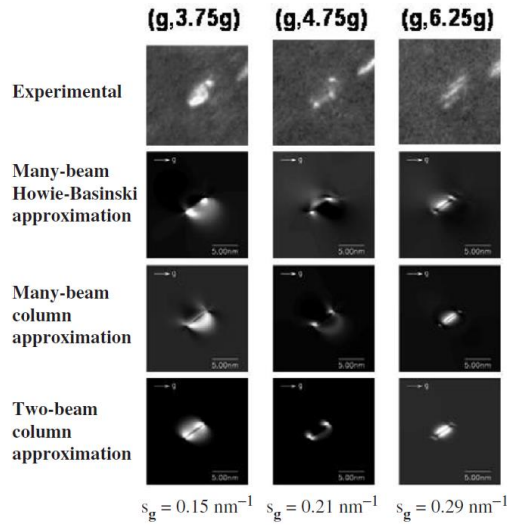


Figure 1.6: TEM experimental and simulated images of a $1/3 a_0 \bar{1}11$ edge-on Frank dislocation loop of diameter 2.5 nm within $[110]$ fcc Cu thin foil for $g=[002]$ with $[110]$ pole. Foil thickness $t=60.0$ nm, located 30.0 nm from bottom of the foil. (a), Experimental observation, many beam; (b), The full Howie–Basinski approach, many beam, non-CA, with Yoffe isotropic dislocation loop employed; (c), The modified Howie–Whelan equations, many beam, CA, with Yoffe isotropic dislocation loop employed; (d), the modified Howie–Whelan equations, two beams, CA, with Yoffe isotropic dislocation loop employed; [Zhou, 2006].

1.4 Free surface effect of defects

1.4.1. Continuum micromechanics of defects

For a perfect finite solid, four basic equations are employed for the description of a deformation field, namely:

(1). Differential equilibrium equation:

$$\sigma_{ij,i} + f_i = 0 \quad (1-1)$$

In which, $\sigma_{ij,i}$ is the first order derivative of the stress component σ_{ij} , and f_i is the external force on the solid.

(2). Geometry equation:

$$\varepsilon_{ij} = \frac{1}{2}(u_{i,j} + u_{j,i}) \quad (1-2)$$

In which, ε_{ij} is the strain component, and $u_{i,j}$ is the displacement gradient component.

(3). Principle of deflections consistency:

$$\begin{aligned} \frac{\partial^2 \varepsilon_{yy}}{\partial x^2} + \frac{\partial^2 \varepsilon_{xx}}{\partial y^2} &= \frac{\partial^2 \varepsilon_{xy}}{\partial x \partial y} \\ \frac{\partial^2 \varepsilon_{zz}}{\partial y^2} + \frac{\partial^2 \varepsilon_{yy}}{\partial z^2} &= \frac{\partial^2 \varepsilon_{yz}}{\partial y \partial z} \\ \frac{\partial^2 \varepsilon_{xx}}{\partial z^2} + \frac{\partial^2 \varepsilon_{zz}}{\partial x^2} &= \frac{\partial^2 \varepsilon_{xz}}{\partial x \partial z} \\ \frac{\partial}{\partial x} \left(-\frac{\partial \varepsilon_{yz}}{\partial x} + \frac{\partial \varepsilon_{xz}}{\partial y} + \frac{\partial \varepsilon_{xy}}{\partial z} \right) &= 2 \frac{\partial^2 \varepsilon_{xx}}{\partial y \partial z} \\ \frac{\partial}{\partial y} \left(\frac{\partial \varepsilon_{yz}}{\partial x} - \frac{\partial \varepsilon_{xz}}{\partial y} + \frac{\partial \varepsilon_{xy}}{\partial z} \right) &= 2 \frac{\partial^2 \varepsilon_{yy}}{\partial y \partial z} \\ \frac{\partial}{\partial z} \left(\frac{\partial \varepsilon_{yz}}{\partial x} + \frac{\partial \varepsilon_{xz}}{\partial y} - \frac{\partial \varepsilon_{xy}}{\partial z} \right) &= 2 \frac{\partial^2 \varepsilon_{zz}}{\partial y \partial z} \end{aligned} \quad (1-3)$$

(4). Displacement and (or) stress boundary condition (BC):

$$\boldsymbol{\sigma} \cdot \mathbf{n} = 0 \quad (1-4)$$

In which, $\boldsymbol{\sigma}$ is the stress tensor, and \mathbf{n} is normal vector at given stress BC S_f .

$$\mathbf{u} = \mathbf{U} \quad (1-5)$$

In which, \mathbf{u} is the displacement vector, and \mathbf{U} is the given displacement BC at S_u .

However, solids are generally imperfect. Micromechanics of defects is fundamental for studying the displacement, stress field of various types of defects (dislocation, dislocation loops, inclusions, precipitates) within solid materials [Mura, 1987].

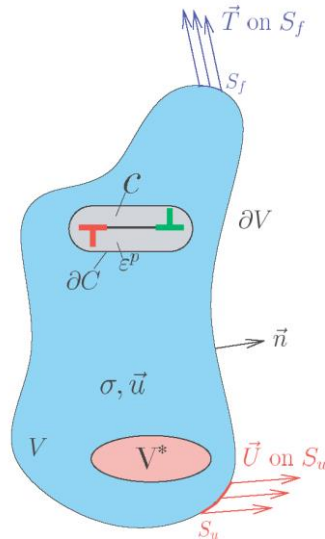


Figure 1.7: Defects within a finite solid [Devincre, 2004].

Compared to the four basic equations for a perfect finite solid, the general description of defects within imperfect finite solid not only needs to satisfy the fundamental relation of elasticity, but also needs to satisfy the constitutive laws of defects and solid matrix respectively. As shown in Fig. 1.7, defects within finite solid can be described as:

$$\nabla \cdot \boldsymbol{\sigma} = 0 \quad (1-6)$$

the stress equilibrium condition.

$$\sigma \cdot n = 0 \quad (1-7)$$

at given stress BC S_f .

$$u = U \quad (1-8)$$

at given displacement BC S_u .

$$\nabla u = \varepsilon \quad (1-9)$$

the constitutive relation equation for solid.

$$\sigma = L^M : (\varepsilon - \varepsilon^p) \quad (1-10)$$

in the continuous solid V^M .

$$\sigma = L^M : \varepsilon \quad (1-11)$$

within the defects region V^* .

As shown in Fig. 1.8, the final stress field of defects within finite body can be considered as the superposition of the stress field of defect in infinite solid, and the virtual displacement and stress field along the boundary, which will satisfy the given displacement and stress BC.

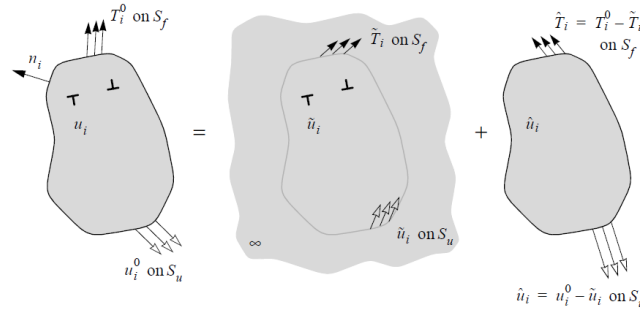


Figure 1.8: Superposition treatment of defects within finite solid [Giessen, 2010].

1.4.2. Anisotropic elasticity of defects in solid

In order to evaluate the displacement field u due to a dislocation within a finite solid, a surface S is defined across which the tractions are continuous, while the displacement has a discontinuity b . [Gosling, 1994]

The anisotropic stress-displacement relation can be written as:

$$\sigma_{ij} = C_{ijkl} u_{k,l} \quad (1-12)$$

In which, C_{ijkl} is the anisotropic elastic modulus.

$$C_{ijpq} = C_{jipq} = C_{ijqp} = C_{pqij} \quad (1-13)$$

Equilibrium equation of solid is written as:

$$C_{ijkl} u_{k,lj} = 0 \quad (1-14)$$

Then, the displacement u in the body B should satisfy (1-14) together with the following displacement and stress BCs (1-15) and (1-16).

$$u \rightarrow 0 \quad (1-15)$$

should be satisfied when $|x| \rightarrow \infty$.

$$[u_i] = b_i \quad \text{and} \quad [C_{ijkl}n_j u_{k,l}] = [f] \quad (1-16)$$

should be satisfied across the surface of defects S .

$$C_{ijkl}n_j u_{k,l} = 0 \quad (1-17)$$

should be satisfied on the boundary of finite body ∂B , where $[f]$ represents the jump in f across S . Equation (1-17) expresses the zero traction BC on the outer surface ∂B of the body B within which the dislocation resides.

The displacement may be expressed as [Volterra, 1907]:

$$u_m(x') = - \int b_i C_{ijkl} G_{mk,l}(x, x') dS_j \quad (1-18)$$

where $G_{mk}(x, x')$ is the mk -component of the Green's tensor for the body B , such Green's function represents the elastic displacement in the m -direction at x induced by a unit point force in k -direction applied at x' .

$$C_{ijkl} G_{mk,lj}(x, x') + \delta_{im} \delta(x - x') = 0 \quad (1-19)$$

together with homogeneous BCs on the boundary B :

$$C_{ijkl} n_j G_{mk,l}(x, x') = 0 \quad (1-20)$$

for $x \in \partial B$.

If B is finite, a modification is needed to ensure overall equilibrium. The simplest would be to require zero displacement on some part of ∂B . However, this is not an issue for a half space.

The stress can be easily written as:

$$\sigma_{pq}(x') = - \int b_s C_{srkl} C_{pqmj} \frac{\partial G_{mk,l}(x, x')}{\partial x'_j} dS_r \quad (1-21)$$

The above area integrals representation is valid for a dislocation in any elastic body, provided that the Green's tensor appropriate for that body is used. If the defects are located in an isotropic and homogeneous full space, the above equation can exactly be reduced to a line integral, as given by Mura [Mura, 1963], and Gosling and Willis [Gosling, 1994]. However, in the inhomogeneous anisotropic finite solid case, it is difficult to convert the involved surface integral into a line integral, since the Green's function does not satisfy the derivative relationship $\partial G(y, x)/\partial x = -\partial G(y, x)/\partial y$, [Chu, 2012].

For isotropic solids, both the 2D and 3D Green's functions are classic and can be found in many text books [Wang, 1997].

For general anisotropic solids, the 2-D Green's functions have been extensively studied, such as Barnett and Lothe [Barnett, 1973; Barnett, 1974], Hwu and Yen [Hwu, 1991], Stroh [Stroh, 1958; Stroh, 1962], Ting [Ting, 1982; Ting, 1992] and Wang [Wang, 1994].

However, derivation of 3D Green's functions within anisotropic finite solid is not easy. In general, six different methods have been proposed to calculate the elastostatic Green's function in 3D anisotropic solid: (a) non-explicit contour-form integrals; (b) numerical integration method; (c) Series expansion technique; (d) Dual reciprocity technique; (e) Eigenvalue and eigenfunction method; and (f) Stroh's formalism [Pan, 2000b].

1.4.3. Half infinite space, thin foil

Accounting for the effects of free surfaces of straight dislocation in half space and thin foil is classically treated in 2D by simply introducing the mirror images with respect to the free surface of all the dislocation lines considered. In 3D, the problem is much more complex for two reasons: (a) dislocation finite segments must be considered; (b) these segments may not necessarily be parallel to the free surface [Fivel, 1996].

Generally speaking, the stress field of finite body containing arbitrary dislocations and dislocation loops, other than the applied external stress, acting on the surface of a stressed body should vanish in order to satisfy the free surface BC:

$$\sigma_{ij}n_j = 0 \quad (1-22)$$

In order to satisfy the free surface BCs, there are two methods that have been used in the literature: (a) those where image dislocations are invoked; (b) those where surface dislocations are used. [Jagannadham, 1978]

When an image dislocation model is used to satisfy the free surface BCs, a dislocation which is a mirror image of the real dislocation is employed, appearing on the other side of the free surfaces. The stress field of the image dislocation cancels with the stress field of the real dislocation only on the surface of the finite body; the total stress field is not zero elsewhere under the free surface within finite solid. Simply employing an image dislocation does not cancel all of the stress components at free surfaces automatically, and therefore additional stress functions must be imposed. [Hirth, 1982; Head, 1953]

As shown in Fig. 1.9, in order to produce traction-free BC, an infinitely long screw dislocation in a free-standing foil of thickness h gives rise to an infinite series of image dislocations, the right hand screw (RHS) dislocation and left hand screw dislocation (LHS) series are mirrored infinite screw dislocations induced by the free surfaces of thin foil, which is similar to a face-to-face amounted mirror pair for the object sitting in-between them [Hartmaier, 1999].

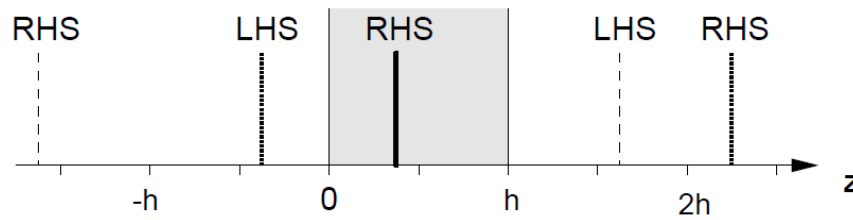


Figure 1.9: Image stress for screw dislocation parallel to free surface within thin foil [Hartmaier, 1999].

As shown in Fig. 1.10, a finite segment can be treated as the subtraction of two semi-infinite segments; the image stress field of such a segment is simply the subtraction of the two image stress fields of the semi-infinite segments [Tang, 2006]. As a source of stress, an arbitrarily shaped dislocation (a) terminating at the free surface is viewed here as a sum of two configurations, i.e. (b) and (c). The Yoffe solution applies directly to (b) and the standard FEM is used to calculate the image stress for (c).

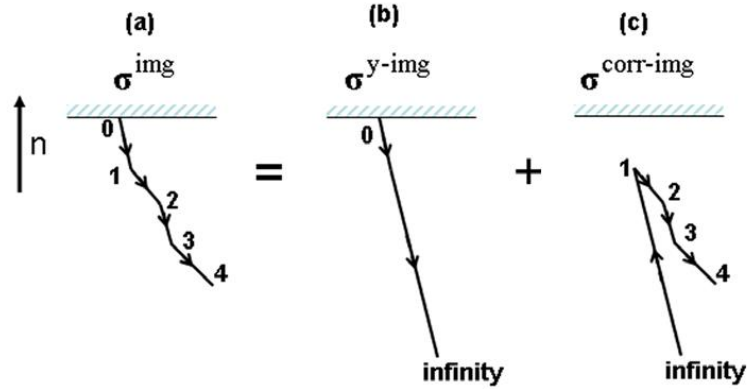


Figure 1.10: Decomposition and superposition used in the hybrid method are illustrated schematically for a half-space [Tang, 2006].

As shown in Fig. 1.11, isotropic elasticity analytical solutions for the elastic fields of a sub-surface rectangular dislocation loop, with any combination of the Burgers vector components, lying below and parallel to a free surface of a half medium have been obtained. The stress around the loop at the free surface is given by $\sigma_{ij} = \sigma_{ij}^I + \sigma_{ij}^{II} + \sigma'_{ij}$, where σ_{ij}^I is the stress around this loop in an unlimited medium, σ_{ij}^{II} is the stress from the image loop in the same medium and σ'_{ij} is the additional stress determined from the condition of the vanishing of the normal and tangential components on the free surface. It can be said that the influence of free surface on the loop is equivalent to the influence of the stress $\sigma_{ij} = \sigma_{ij}^{II} + \sigma'_{ij}$. Thus, the force which the free surface exerts on an unit length of the finite loop has components $f_i = \varepsilon_{ijk} b_n \sigma_{nj} l_k$, where ε_{ijk} is the Levi-Civita tensor; b_n are the components of the Burgers vector of dislocation loop; and l_k are the components of the unit vector of the curve [Baštecká, 1964].

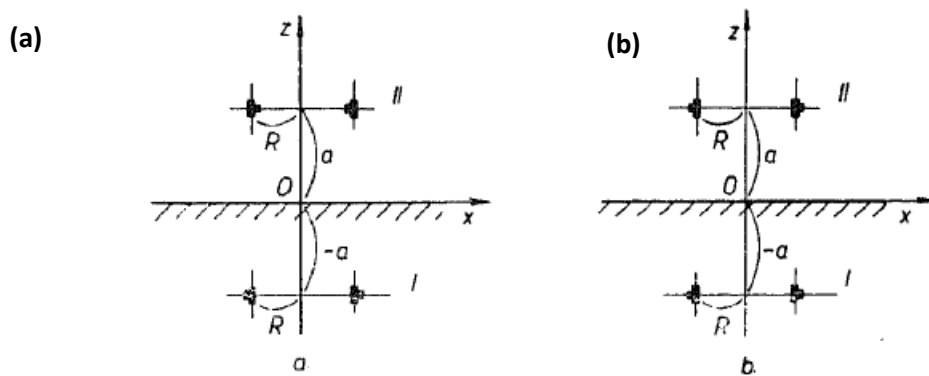


Figure 1.11: Edge prismatic loop and its image edge dislocation loop; a) Burgers vector of image loop II has reverse direction to Burgers vector of loop I; b) Burgers vector of both dislocation loops have the same direction [Baštecká, 1964].

Beyond such simple examples, boundary problems can involve curved surfaces, anisotropy, elastically mismatched interfaces and atomistically mismatched interface. The image stress for these cases are often extremely difficult to deal with [Liu, 2005]. A theorem based on anisotropic Stroh's formula for calculating the image stress of infinite straight dislocations in anisotropic bicrystals has been found by Barnett and Lothe [Barnett, 1974], which was further deployed for the elastic field calculation of dislocations emerging at the free surface of half space [Lothe, 1982]. Integration

solutions based on Gosling and Willis method [Gosling, 1994] and Boussinesq solution [Fivel, 1996] are also developed for dislocation and dislocation loops with complex geometrical and physical configuration within half space and thin foil.

Dislocations cannot terminate inside an infinite medium, and the stress fields of dislocation segments do exist, they only satisfy equilibrium if they form a complete loop, which includes dislocations that continue to infinity. Therefore, in order to compute the stress fields due to dislocations that intersect the free surface, the dislocation segment has to be extended outside the thin foil. As shown in Fig. 1.12(a), these continuations, which are termed virtual dislocations, allow the dislocation to form a complete loop (or go to infinity) and allow the stress field to satisfy equilibrium. The image stress, then, must account for the surface traction generated by all the real dislocations as well as virtual dislocations. The efficient scheme for virtual dislocation implementation is elongating the terminating dislocation segment until infinite far away along the tangential direction of the dislocation segments that intersect the free surface outside thin foil. This choice is made mainly out of convenience, but it also appears to have the best convergence when the image force is computed using spectral methods [Weinberger, 2009]. As shown in Fig. 1.12(b), in order to compute the image stress field of dislocation piercing the half-space, an adaptive meshing process for surface integral calculation in the form of Boussinesq operators has to be performed, which constructs a denser mesh when getting closer to the piercing point [Fivel, 1996].

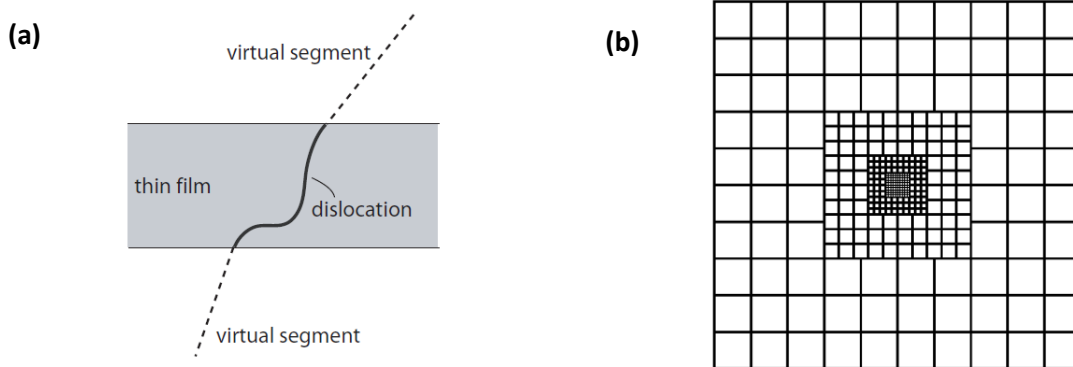


Figure 1.12: Treating of local area around piercing point (a), Virtual dislocation treatment for piercing dislocation (b), Schematic of the local surface grid which is centered on each dislocation intercept point. [Fivel, 1996; Weinberger, 2009].

Alternatively, the image stress due to free surfaces and interfaces can now, owing to computing power, be computed by finite element method.

1.4.4. Surface relaxation effects on TEM contrast

Surface relaxation plays an important role in TEM image contrast, particularly for end-on screws, and sometimes also by affecting their configurations at the surface [Hazzledine, 1975]. The Eshelby twist is well known to make it possible to image end-on screws by diffraction contrast [Tunstall, 1964; Williams, 2009], even though $\mathbf{g} \cdot \mathbf{b} = 0$ and $\mathbf{g} \cdot \mathbf{b} \times \mathbf{u} = 0$.

Tunstall et al. [Tunstall, 1964] have shown that in two-beam conditions the diffraction contrast is in the form of black–white lobes perpendicular to the diffracting vector, with the line of no-contrast parallel to \mathbf{g} . Hirth [Hirth, 2007] shows that the surface relaxation strain field for screws normal to thin foils, as calculated by Eshelby and Stroh [Eshelby, 1951] with isotropic elasticity, gives rise to diffraction contrast in the form of black-white lobes, when imaged in weak-beam dark field under two beam diffraction conditions, with the line of no contrast parallel to \mathbf{g} , and can be used to determine the sign of the dislocations. Unlike weak-beam images of inclined dislocations, the image contrast field is very broad owing to the long-range nature of surface relaxation strain field.

The free surface relaxation effect on TEM diffraction contrast for thin foil containing a loop parallel to the surface can be treated by taking the sum of the displacement fields of the loop and its mirror image in the foil surface [Ruhle, 1965]. Ohr [Ohr, 1977] has reported a more sophisticated technique for handling surface relaxation for finite loops, and has concluded that the image contrast of small loops lying very close to a stress-free surface is indeed sensitive to the presence of the surface. The surface was found to affect the size and detailed shape of the black–white contrast figure. When the distance of the loop from the surface exceeds its diameter, free surface relaxation effect does not appear to be too serious a problem. In practice, the situation is even more complicated, as the conditions at the surface are not well established. For example, a surface oxide layer may be present which constrains the underlying material.

Chapter 2: Experiment

In this chapter, bcc Fe TEM sample preparation and the TEM diffraction contrast of dislocation are described firstly, using many beam Schaeublin-Stadelmann equations for the latter. Then, TEM experimental observation techniques of defects and dislocation quantitative analysis are discussed.

2.1. Preparation of TEM sample

2.1.1. Initial material

Ultra high purity (UHP) Fe for the TEM investigation of the present study was elaborated at Ecole des Mines de Saint-Etienne, France [Coze, 2007]. The material was elaborated by induction melting and subsequent solidification under Ar. It was then forged at 1000°C into a rod that has a hexagonal section and 20 mm in diameter. It was then cooled by air, followed by cold forging down to 11 mm, inducing a reduction of 70%. The rod was annealed between 700°C to 850°C for one hour in Ar. The obtained UHP Fe is single phased and with a body centered cubic (bcc) crystalline structure. The mean grain size is about 4 to 650 μm and the dislocation density is about $1.2 \cdot 10^8 \text{ cm}^{-2}$. Its Vickers hardness is 75 HV. From this rod, delivered to CRPP Materials Group at PSI, slices were cut using a diamond saw to a thickness of 300 μm . These slices were used for TEM sample preparation.

The chemical composition of the UHP Fe [Coze, 2007] employed for TEM experiment is shown in Table 2.1.

Table 2. 1 Chemical composition of UHP Fe after hot forming and in the as-delivered final metallurgical condition [Coze, 2007].

	Reference number	C	S	O	N	P	Cr
Fe	1235	3/4	2/2	5/4	2/1	<5	<2

2.1.2. Mechanical and electrochemical polishing

UHP Fe is ferromagnetic, it causes distortion of the TEM image that can be difficult if not impossible to compensate with the beam shift, beam tilt, condensor and objective astigmatism correctors. In addition, these beam corrections often need to be adjusted when shifting or tilting the TEM sample during the observation, making stable continuous observation of the same defects under different beam condition difficult without further beam correction and optimization. To minimize these side-effects induced by ferromagnetic samples, the volume of the sample was reduced using the method described below.

Firstly, the thickness of the 300 μm thick UHP Fe slice is reduced to 110-150 μm by mechanical polishing with wet SiC papers of, firstly, number 400, then 1000 and finally 2000. Then, the slice is bent back and forth a few times to impose plastic deformation with ball pen cylinder, then made flat by compression between two plates, thus producing a dislocation density within the sample that is sufficient to ensure that a few dislocations are visible in TEM in a typical field of view of 1 μm^2 . As dislocation produces long range displacement and stress field, such limited number of dislocations within the observed region will avoid the influence of neighboring dislocation on the distortion field of considered dislocation. Then, as shown in Fig. 2.1, a 1 mm disk is punched out from the UHP Fe slice with a precision puncher.

Secondly, a supporting disk with 3 mm outer diameter and 1 mm inner diameter is made out of 316L steel plate, which is not ferromagnetic. Its thickness is 100 μm . As shown in Fig. 2.1, a 1 mm hole is punched out of a 100 μm thick 316L sheet with a high precision puncher. Then, the punched 316L sheet is placed on a 3 mm cutting matrix, with a 1mm pin in its 1mm hole. Hammer is again employed to knock out a 3 mm 316L disk out of the 316L sheet.

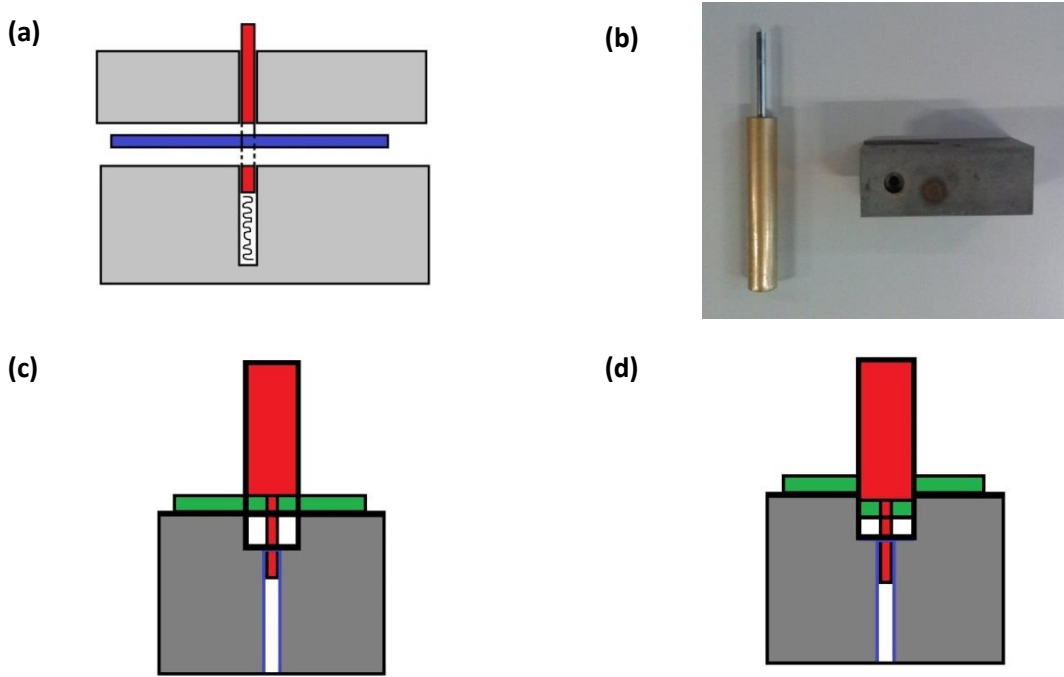


Figure 2.1: Devices employed for 1mm Fe sample fabrication (a), High-resolution Eckert 1mm puncher; (b), The alignment pin and corresponding cutting mold; (c), Alignment of 1mm hole of 316L sheet; (d), Punch 3 mm ring out of 316L sheet.

Thirdly, the 1 mm Fe disk is mounted into the 1 mm hole of the 3 mm supporting 316L disk. The supporting 316L disk with the 1mm TEM Fe sample inside are glued together with G1 glue from GATAN® at 110°C for 4 minutes. Once the glue is hardened and cooled, the specimen is reduced to about 100 μm thickness by mechanical polishing with wet SiC paper of number 2000 and finally 4000.

Finally, the composite specimen is electrochemical polished at -23 °C with Tenupol5 device of STRUERS®. The chemical solution is 7% in volume of 70%-HClO₄ and methanol of 93% purity. The polishing voltage is 50 V, and the jet flow is set to 20 (Tenupol5 setting). It produces a TEM sample with a central hole, whose edges are transparent to electrons. After electrochemical polishing, the TEM sample is cleaned with pure ethanol in three successive bathes, making sure to remove the chemical residues produced during the electrochemical process. In order to reduce oxidization of the TEM sample surfaces, the TEM sample is then mounted onto the TEM sample holder and transferred into TEM chamber as fast as possible.

2.2. Many beam dynamical theory

To calculate the propagation of electrons in a faulted crystal, the dynamical theory of contrast is employed [Hirth, 1969]. The crystal at a point r is described by a faulted potential $V(r)$ that can be written as a Fourier series:

$$V(r) = \frac{\hbar^2}{2m_e} \sum_{\mathbf{g}} [U_{\mathbf{g}} \exp(-2\pi i \mathbf{g} R(r))] \exp(2\pi i \mathbf{g} \cdot r) \quad (2-1)$$

The summation is done over all reciprocal lattice vectors \mathbf{g} , with m_e the electron mass and \hbar the Planck constant. $R(r)$ describes the displacement field around the lattice defect. The Schrödinger's wave equation is:

$$\nabla^2 \psi(r) + \left(\frac{8\pi^2 m_e}{h^2} \right) [E + V(r)] \psi(r) = 0 \quad (2-2)$$

$\psi(r)$ is the function associated to the electron wave that moves through the faulted crystal. The proposed solution to the Schrödinger equation is:

$$\psi(r) = \sum_g \varphi_g \exp(2\pi i(\chi + g + s_g)r) \quad (2-3)$$

The function $\varphi_g(r)$ is associated with the beams that come out of the sample, including the transmitted beam (beam 0) and the diffracted beams (beam 1 to n). The contrast intensity I recorded on the micrographs for a diffraction contrast image, is simply $I = \varphi_g(r) \cdot \varphi_g^*(r)$. Fig. 2.2 shows the crystal and the beams in the reciprocal space. χ is the direction of the transmitted beam; g is the reciprocal lattice vector and s_g the deviation parameter. $(\chi + g + s_g)$ is the direction of the beam with index g and we will take a co-ordinate η_g along this direction.

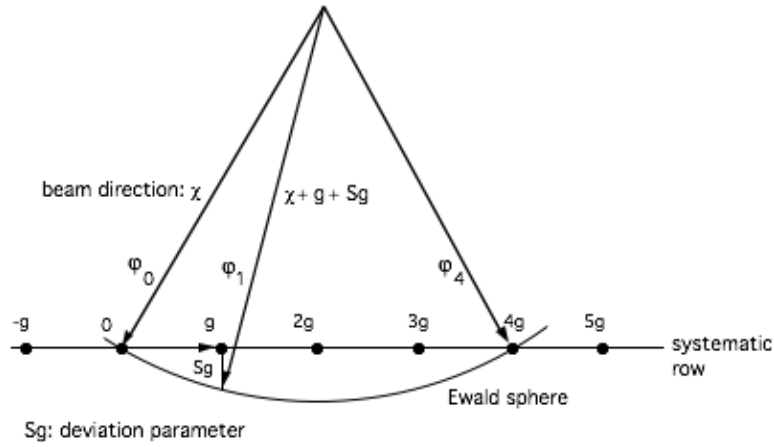


Figure 2.2: Representation in the reciprocal space of a $g(4g)$ weak beam condition [Schaeublin, 1993].

We then substitute $V(r)$ and $\psi(r)$ in the Schrödinger equation. We obtain a system of n differential equations of the first order with n unknowns $\varphi_g(r)$:

$$\frac{\partial \varphi_g(r)}{\partial \eta_g} = \sum_h \frac{\pi i}{\xi_{g-h}} \varphi_h(r) \exp(2\pi i(h - g)R(r) + 2\pi i(s_h - s_g)r) \quad (2-4)$$

The equations are to be integrated along the proper beam direction η_g . This is difficult to solve analytically. To simplify, the column approximation that allows making the integration along the same direction for all beams is employed. Actually the error made with this approximation is relatively small (about $10^{-4} g \cdot \lambda$). Indeed, the scattering angle for high energy electron diffraction is quite small. It is thus reasonable to assume that an electron which enters the foil will never leave a column centered on the point or pixel of interest. This column is parallel to the incident beam direction, and has a diameter of a few Ångstroms at most, depending on the foil thickness and the acceleration voltage, implying that the neighboring column will never interact, or in other words that there is no electron exchange between columns. The column approximation means that the direction of the transmitted beam is employed for making the integration, so that:

$$\frac{\partial}{\partial \eta_g} \cong \frac{d}{dz} \quad (2-5)$$

Then, the equations (2-4) can be written as matrix form:

$$\frac{d\phi(r)}{dz} = M\phi(r) \quad (2-6)$$

and

$$\phi(r) = [\phi_0(r) \quad \phi_1(r) \quad \dots \quad \phi_n(r)]^T \quad (2-7)$$

The matrix M is symmetrical and has the following expression:

$$\begin{bmatrix} A & A_1 & \dots & A_i & \dots & A_n \\ A_1 & B_1 & \dots & C_{1i} & \dots & C_{1n} \\ \vdots & \vdots & \ddots & \vdots & \ddots & \vdots \\ A_i & C_{i1} & \dots & B_i & \dots & C_{in} \\ \vdots & \vdots & \ddots & \vdots & \ddots & \vdots \\ A_n & C_{n1} & \dots & C_{ni} & \dots & B_n \end{bmatrix} \quad (2-8)$$

Where the coefficients are:

$$\begin{aligned} A &= -\frac{\xi_1}{\xi'_0} \\ B_i &= \left[-\frac{\xi_1}{\xi'_0} + 2is_i\xi_1 + 2\pi i \frac{d}{dz}(g_i R(r)) \right] \\ C_{ij} &= i\xi_1 \left(\frac{1}{\xi_{i-j}} + \frac{i}{\xi'_{i-j}} \right) \\ A_i &= i\xi_1 \left(\frac{1}{\xi_i} + \frac{i}{\xi'_i} \right) \end{aligned} \quad (2-9)$$

In which, $R(r)$ is the displacement field, and ξ_i defines the extinction distance which becomes large if beam i becomes far from the transmitted beam; ξ'_i is related to ξ_i through a material-dependent absorption constant. Equation (2-8) shows that the derivative of each beam is a linear combination of all the beams. The contribution of each beam in the linear combination is weighted by the matrix coefficients (2-9). ξ_1 is a scaling factor that was originally introduced by Head et al [Head, 1973]. to avoid convergence problems and save calculation time in the integrations.

Finally, the equation for the transmitted beam $\frac{d\varphi_0}{dz}$ is:

$$\frac{d\varphi_0}{dz} = -\frac{\xi_1}{\xi'_0} \varphi_0 + \dots + i\xi_1 \left(\frac{1}{\xi_i} + \frac{1}{\xi'_i} \right) \varphi_i + \dots + i\xi_1 \left(\frac{1}{\xi_n} + \frac{1}{\xi'_n} \right) \varphi_n \quad (2-10a)$$

The general equation for a diffracted beam $\frac{d\varphi_k}{dz}$ is:

$$\begin{aligned} \frac{d\varphi_k}{dz} &= i\xi_1 \left(\frac{1}{\xi_i} + \frac{1}{\xi'_i} \right) \varphi_0 + \dots + i\xi_1 \left(\frac{1}{\xi_{i-j}} + \frac{1}{\xi'_{i-j}} \right) \varphi_j \\ &+ \dots + \left(-\frac{\xi_1}{\xi'_0} + 2is_i\xi_1 + 2\pi i \frac{d}{dz}(g_i R(r)) \right) \varphi_i + \dots + i\xi_1 \left(\frac{1}{\xi_{i-n}} + \frac{1}{\xi'_{i-n}} \right) \varphi_n \end{aligned} \quad (2-10b)$$

Equations (2-10) show that the derivative of each beam is a linear combination of all the beams. The contribution of each beam in the linear combination is weighted by the matrix coefficients (2-9).

The physical meaning of relations (2-10) is that the contribution of a beam i depends on the associated deviation parameter s_i (diffraction condition), the associated extinction distance ξ_i (material characteristics) and a cross-term ξ_{i-j} that has the expression of an extinction distance. High $|g_i|$ values correspond to large ξ_i and therefore beam i may have a weak contribution; but when this same beam has a small deviation parameter s_i , it may have a strong contribution. It appears that the importance such contribution has a balance between s_i , deduced from the observation conditions and ξ_i , given by the material characteristics. This had to be taken into account in the choice of the beams

included in the calculation. The general rule is the following: beams have to be close to the transmitted beam (small ξ_i) and situated close to the Ewald sphere intersections with the systematic row (small s_i). The dependence on ξ_{i-j} indicates that if we take for instance beam g_i , then beams g_{i-1} and g_{i+1} will contribute strongly to beam g as ξ_{i-j} is small.

2.3. TEM diffraction imaging of defects

2.3.1. BF, DF, WBDF

When performing TEM experimental observation of defects, either the direct beam or some of the diffracted beams in the selected area diffraction (SAD) pattern may be employed to form bright field (BF) and dark field (DF) images, respectively. Conventional bright field is taken by allowing the incident beam to pass through the objective aperture. Conventional dark field imaging involves tilting the incident illumination until a diffracted, rather than the incident, beam passes through a small objective aperture in the objective lens back focal plane. As shown in Fig. 2.3, such bright field or dark field images can be obtained by allowing the infocusing transmitted or diffracted beam to pass through the objective lens, which can be realized by tilting electron beam or tilting the sample. In single crystal specimens, single-reflection dark field images of a specimen tilted just off the Bragg condition allow one to observe only those lattice defects, like dislocations or precipitates, which bend a single set of lattice planes in their neighborhood. Analysis of intensities in such images may then be used to estimate the amount of that local distortion [Williams, 2009].

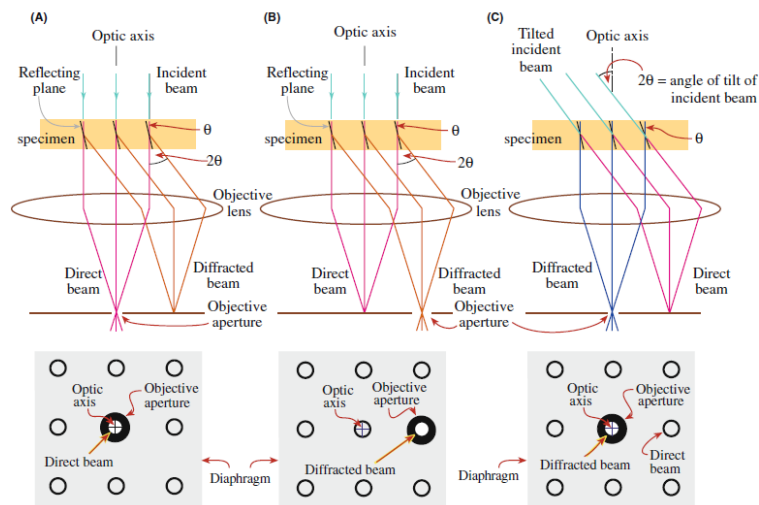


Figure 2.3: Diagram for transmitted beam and diffracted beam [Williams, 2009].

As shown in Fig. 2.4, after tilting the beam (or equivalently tilting the sample) far off exact Bragg diffraction condition, $3g$ beam condition is obtained, when selecting the diffraction beam g for imaging, it will produce a weak beam dark field image. The background will be black, and only the local region of around defects will show strong black-white contrast. The defect free sample area appears dark because of the weak diffraction intensity. However, close to the dislocation core the (hkl) plane is bent back to the Bragg condition, which gives rise to a bright intensity, close to the exact dislocation line. The main challenge is to adjust the tilt conditions in the way that the excitation error of the g reflection used is close to zero only near the dislocation core where the bending of the

(hkl) plane is most prominent. Then a very sharp dislocation line near the dislocation core becomes visible in the WBDF image.

Three conditions have to be satisfied to get a high quality WBDF image:

- Beam tilt to on-axis DF and selection of a Bragg spot by using objective aperture
- Right adjustment of the excitation error
- Two beam conditions to get high contrast

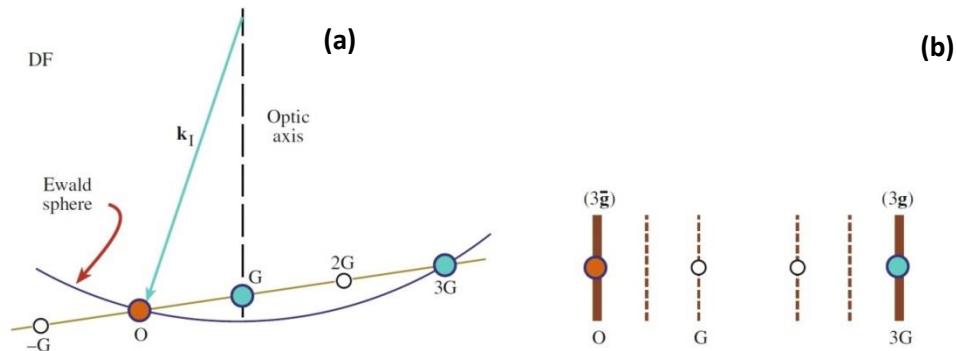


Figure 2.4: Relationship between the orientation of Ewald sphere and position of Kikuchi line for $g(3g)$ WBDF by tilting beam [Williams, 2009].

The contrast of WB images decreases as the thickness increases (due to a corresponding increase in inelastic scattering). However, the orientation of the specimen is accurately set by reference to the Kikuchi lines observed in the DP, and these are not visible in specimens which are too thin. Moreover, if the observations is made on certain defects, their physical behavior within thin TEM foil should not influenced by the surface of the foil, thus TEM foil must not be too thin. In order to maintain the balance between these two naturally controversial geometrical requirements on TEM thin foil: optimizing the image quality under weak beam condition (enough visibility under far off exact Bragg diffraction condition) and keep the physical properties of defects within thin TEM foil (representative of defects physical properties within bulk material), the as-prepared TEM thin foil should have a moderated thickness. Reliable weak beam observation experiments of defect are suggested to be performed within regions where the thickness is about 70 nm [Williams, 2009].

2.3.2. TEM observation technique of crystal defects

It has been found experimentally that the visibility of very small crystal defect clusters of sizes below 5 nm is usually enhanced under the weak-beam diffraction condition, a method that was strongly developed from the 70's, starting with [Cockayne, 1969] and [Stobbs, 1971]. Weak-beam TEM imaging technique has remained a fundamental tool for studying dislocation in the past 40 years.

In current thesis, the experimental characterization of the dislocation in Fe is thus performed using diffraction contrast or conventional TEM, with a JEOL2010 transmission electron microscope situated at PSI Villigen, Switzerland. The microscope, equipped with LaB⁶ electron emission gun, is operated at 200 keV. Bright field, dark field and weak beam dark field methods are deployed to analyze the dislocation.

2.3.3. The deviation vector

The imaging condition in diffraction contrast mode is best described in reciprocal space, see Fig 2.2, showing the Ewald sphere and one row of reciprocal lattice points of the investigated crystal, the so called systematic row, the diffraction condition can be described by the deviation vector \mathbf{S}_g , which is the minimum distance from the Ewald sphere to the reciprocal lattice point. The diffraction condition can be written as $n\mathbf{g}(m\mathbf{g})$, where $n\mathbf{g}$ is the imaging beam and $m\mathbf{g}$ is the excited beam of the systematic row:

$$s_g = m(m - n) \frac{g^2 \lambda}{2} \quad (2-11)$$

As shown in Fig 2.5, in exact Bragg condition, the bright Kikuchi line intersects the systematic row of reciprocal lattice points at $3g$. When tilting the thin foil by a small angle, if the bright Kikuchi line shifts towards the origin of reciprocal space, then the excitation error is negative. Conversely, if tilting towards the opposite direction, a positive excitation error will appear.

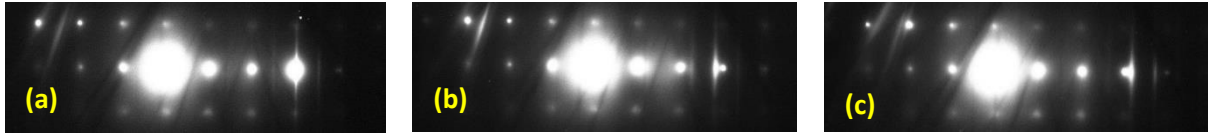


Figure 2.5: Three types of deviation vectors in Fe at 200KV in JEOL 2100 (a), $g(3g)$ with $S_{3g}=0$; (b), $g(3g)$ with $S_{3g}<0$; (c), $g(3g)$ with $S_{3g}>0$.

2.4. Quantitative characterization of dislocation

Before describing the dislocation, the notation for planes and directions in real space is described in Table 2.2. A dislocation is described by dislocation direction and a Burgers vector. A dislocation loop is described by and a Burgers vector and a habit plane.

Table 2.2: Notation for planes and directions in real space.

	General	Particular
Direction	$\langle uvw \rangle$	$[uvw]$
Plane	$\{hkl\}$	(hkl)

2.4.1. Basic $g \cdot b$ analysis principle

The $g \cdot b$ analysis technique is based on the fact that generally the contrast of a dislocation line nearly vanishes when $g \cdot b = 0$. For a pure screw dislocation, whose Burgers vector is parallel to the dislocation line, in an isotropic medium, there is no edge component. The visibility criterion $g \cdot b = 0$ applies well. Thus, the determination of the direction of Burgers vector of a screw dislocation consists in finding two vectors g_1 and g_2 for which the dislocation contrast vanishes. Then, the Burgers vector direction is the cross product of the two g -vectors, thus $b/|b| = \pm g_1 \times g_2 / |g_1 \times g_2|$. A pure edge dislocation is only invisible when $g \cdot b = 0$ and $(b \times u) \cdot g = 0$. However, this special condition exists only for g parallel to dislocation line [Edington, 1975; Graef, 2003].

For a general dislocation in an anisotropic matrix the invisibility principle does not apply completely, which means that in the case $g \cdot b = 0$ there is a residual contrast. Detailed TEM image simulation may be employed to unambiguously and quantitatively determine the dislocation configuration at the origin of this contrast [Edington, 1975; Douin, 1998; Graef, 2003]. This is particularly the case when

the anisotropy ratio is high, for Fe which is 2.4 at room temperature and increases with increasing temperature [Dever, 1972].

Nevertheless, in order to make the quantitative analysis of dislocation's parameters, it is necessary to start with a g·b analysis, as it allows to roughly determine the Burgers vector direction, but not its sign or amplitude. In this work on pure bcc Fe, we have used specific zone axes, those that provide the most useful diffraction vectors for defect analyses.

The g·b value for <111> screw dislocation in bcc Fe for [001], [011] and [111] zone axes conditions are given in Appendix. A.

2.4.2. Determination of sample thickness via EELS

Electron energy loss spectroscopy (EELS), uses the fact that some of the electrons running down the TEM column with a narrow range of kinetic energies will undergo inelastic scattering, which means that they lose energy. The amount of energy loss can be measured via an electron spectrometer and interpreted in terms of what caused the energy loss [Egerton, 1996; Iakoubovskii, 2008a]. EELS allows quick measurement of local thickness in TEM, with 10% accuracy. The most efficient procedure is the following:

Firstly, Measure the energy loss spectrum in the energy range about 5-200 eV (wider is better).

Secondly, extract zero-loss peak (ZLP) using standard routines and calculate the surface under the ZLP (I_0) and under the whole spectrum (I_t).

Finally, the thickness of TEM sample can be calculated out:

$$t = \lambda \cdot \ln(I_0/I_t) \tag{2-12}$$

In which, λ is the mean free path of electron inelastic scattering, which has recently been tabulated for most elemental solids and oxides [Iakoubovskii, 2008b].

Chapter. 3: Elastic image field calculation method

This chapter presents the method to calculate the elastic field in a thin foil in presence of a crystal defect, including the free surface effect. As described in the literature review, this effect induces additional elastic fields that are treated using the free traction BC principle. This chapter starts with (3.1) the general methodology, followed by the detailed description of the calculation of these image fields in Fourier space, starting with (3.2) the solution in the infinite half-space, followed by (3.3) its extension to the thin foil, and (3.4) the image energy of defect within half space and thin foil. Solutions for the displacement field and self energy of a dislocation loop in bulk material are then given in (3.5) and (3.6) respectively.

3.1. General methodology

As described in the literature review, the classical image stress methods in Cartesian coordinate consist basically firstly of superposing an image dislocation beyond free surface, where the surface acts as a mirror to the considered dislocation in the sample, and then secondly of devising a stress function that will cancel the residual shear and normal stresses σ_{i3}^{∞} acting at this surface, thus satisfying the free surface condition. However, such simple “mirror method” is limited to a few dislocation configurations. Thus, it is necessary to develop an alternative solution that can solve the image stress problem for defects with arbitrary configuration, especially when anisotropy is included.

The general methodology consists in calculating separately, on the one hand, the so-called bulk elastic field due to the defect and, on the other hand, the so-called image elastic field, and finally adding them together to obtain the so-called total elastic field, which is the desired solution.

This implies that, concerning for example the stress field of a dislocation within a half space or thin foil, there is a total stress field (σ_{ij}^{total}) that is treated as two superimposed stress fields. There is on the one hand the bulk or infinite stress field (σ_{ij}^{∞}) induced by the same defect in an infinite crystal and on the other hand the image stress field (σ_{ij}^{image}) induced by the presence of the free surfaces, which is employed to satisfy the free traction BC principle. The total stress inside the half space or thin foil can then be written as the superposition of the two stress fields:

$$\sigma_{ij}^{total} = \sigma_{ij}^{image} + \sigma_{ij}^{\infty} \quad (3-1)$$

This is schematically represented in Fig. 3.1.

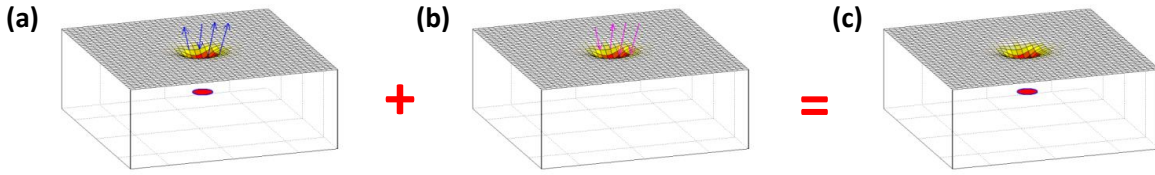


Figure 3.1: Schematics of the method to obtain the stress field of a dislocation loop in presence of free surfaces of foil.(a), bulk stress; (b), image stress; (c), total stress.

Given the geometrical and physical parameters of the defect and of the host crystal, the corresponding stress σ_{ij}^{∞} in the infinite medium at the free surface position can be calculated. The resulting stress field σ_{ij}^{∞} in the infinite medium is then employed for calculating the resultant image displacement, strain and stress field, as described in the following.

The total traction stress components σ_{i3}^{total} should be zero at the free surface position.

(1), The corresponding bulk stress σ_{ij}^{∞} at free surfaces in equation (3-1) can be produced in Cartesian coordinate, and then written into 2D discrete series:

$$\sigma_{ij}^{\infty} = \sum_{k_x} \sum_{k_y} \hat{\sigma}^{\infty}(k_x, k_y) \cdot \exp(ik_x x + ik_y y) \quad (3-2)$$

(2), Due to the completeness of Fourier series, the corresponding image displacement field satisfying the equilibrium of the foil, that is to say the restriction to the free surface or (x,y) in Cartesian coordinate space, can be written as a superposition of the general solutions written in Fourier space, in the form of Fourier series for each (k_x, k_y) mode.

$$u(x, y, z) = \sum_{k_x} \sum_{k_y} [\hat{u}^+(k_x, k_y, z) + \hat{u}^-(k_x, k_y, z)] \cdot \exp(ik_x x + ik_y y) \quad (3-3)$$

(3), The image stress field can be obtained from the anisotropic Hooke's law:

$$\sigma(x, y, z) = \sum_{k_x} \sum_{k_y} [\hat{\sigma}^+(k_x, k_y, z) + \hat{\sigma}^-(k_x, k_y, z)] \cdot \exp(ik_x x + ik_y y) \quad (3-4)$$

The unknown coefficients $\hat{u}^+(k_x, k_y, z)$, $\hat{u}^-(k_x, k_y, z)$, $\hat{\sigma}^+(k_x, k_y, z)$ and $\hat{\sigma}^-(k_x, k_y, z)$ are described as a function of the single parameter z , and the corresponding coefficients can be calculated by matching the image stress field (σ_{i3}^{image}) at the free surface position $z = \pm t/2$ for each Fourier mode between equation (3-2) and (3-4), thus producing the final image displacement, strain and stress field at arbitrary position z within the medium.

The method developed here is based on the solution of Weinberger [Weinberger, 2009], which consists in describing the elastic field in Fourier space. The advantage of the Fourier space is that the developed method is also valid for other types of defects, which is of general application. Conversely, an analytic solution in real space would have to be deduced for each case, one by one.

The numerical algorithm for doing this in a half space or a crystal thin foil is elaborated in the following subsections. Both half space and crystal thin foil are considered to be periodic in both x and y directions, with periodic length L_x and L_y respectively. The wave number in Fourier space is described as $k_x = 2\pi n_x/L_x$ and $k_y = 2\pi n_y/L_y$, where $n_x, n_y = 0, \pm 1, \pm 2, \dots$

In summary, the flowchart for the calculation of the image elastic field in real Cartesian space of a defect in presence of a free surface is shown in Fig 3.2.

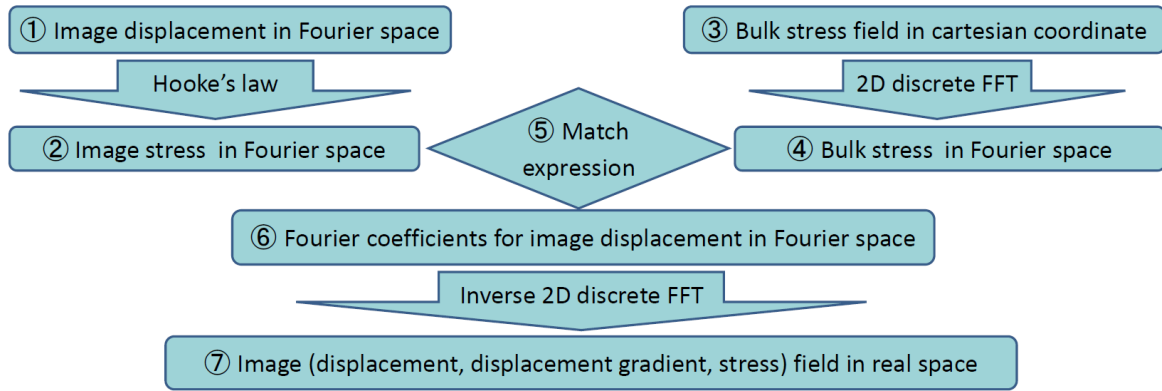


Figure 3.2: Schematics showing the general procedure deployed to find the solution to the components of the image elastic field, for the case of e.g. a dislocation loop in an anisotropic medium.

In order to harvest the image elastic field at given position within thin foil, there are seven steps to be fulfilled, as follows:

- ① Write the arbitrary image displacement field at the free surface in 2D Fourier space.
- ② Generate 2D image stress field via 3D anisotropic Hooke's law in Fourier space. The image stress field σ_{ij}^{image} is written in 2D discrete Fourier series with unknown 2D discrete Fourier coefficients.
- ③ Calculate the bulk stress σ_{ij}^{∞} of the inclined dislocation or the dislocation loop at the free surfaces via known elastic models.
- ④ Perform 2D discrete Fourier transformation for the bulk stress, thus producing the 2D discrete Fourier coefficients for bulk stress field σ_{ij}^{∞} .
- ⑤ Match bulk stress field and image stress field in 2D discrete Fourier space, so as to satisfy the free traction stress BC $\sigma_{i3}^{\infty} + \sigma_{i3}^{image} = 0$.
- ⑥ Produce 2D discrete Fourier coefficients for the arbitrary image displacement field in Fourier space.

- ⑦ Perform inverse 2D discrete Fourier transformation, thus producing image elastic fields, namely the displacement, displacement gradient, and stress fields, in real space.

Finally, the total elastic field is the sum of the bulk elastic field and the image elastic field.

Note that this method was already applied in the case of isotropic materials [Weinberger, 2009], but never for anisotropic once. This is the task we have undertaken in this work. The solution we have developed for that is given in the following.

3.2. Fourier space solution for anisotropic half space problem

Let z direction be perpendicular to the (x, y) free surface of the half space that occupies the region $z \leq 0$. The following image displacement solution is periodic in both x and y directions, and exponential in the z direction, assumed to be of the type $\exp(+qz)$. Hence,

$$(u, v, w) = \sum_{k_x} \sum_{k_y} \left(U(k_x, k_y), V(k_x, k_y), W(k_x, k_y) \right) \cdot \exp(ik_x x + ik_y y + qz) \quad (3-5)$$

In which, (u, v, w) are the image displacement fields in the half space coordinate (x, y, z) . The Fourier coefficients $\left(U(k_x, k_y), V(k_x, k_y), W(k_x, k_y) \right)$ being complex for each Fourier mode (k_x, k_y) , the image displacement components are written in terms of complex exponentials. In the end only the real parts of the solution are retained for the solution. The real parts of the corresponding roots q should be larger than zero for the lower half space.

In order to solve the problem for half space with an arbitrarily oriented crystal surface, two sets of Cartesian coordinate should be employed. There is the original coordinate (x_0, y_0, z_0) , which is related to the basic crystal orientation, such as [100], [010] and [001] for bcc crystals, and the half space coordinate (x, y, z) , where z is along the half space free surface normal direction.

The rotation angles needed to get to the half space coordinate (x, y, z) relative to original coordinate (x_0, y_0, z_0) are (ϕ, θ, ψ) , respectively. The rotation matrix is thus:

$$T_{ij} = \begin{bmatrix} \cos \theta \cos \psi & \cos \phi \sin \psi + \sin \phi \sin \theta \cos \psi & \sin \phi \sin \psi - \cos \phi \sin \theta \cos \psi \\ -\cos \theta \sin \psi & \cos \phi \cos \psi - \sin \phi \sin \theta \sin \psi & \sin \phi \cos \psi + \cos \phi \sin \theta \sin \psi \\ \sin \theta & -\sin \phi \cos \theta & \cos \phi \cos \theta \end{bmatrix} \quad (3-6)$$

The relation between positions (x_0, y_0, z_0) in the original coordinate and positions (x, y, z) in the half space coordinate can be written as:

$$x_i = T_{ij}(x_0)_j \quad (3-7)$$

The stiffness matrix in the half space coordinate can be written as:

$$C_{ijkl} = T_{ig} T_{jh} C_{ghmn}^0 T_{km} T_{ln} \quad (3-8)$$

In which, C_{ghmn}^0 is the four-order elastic matrix in the original coordinate, C_{ijkl} is the four-order elastic matrix in the half space coordinate. The strain displacement relation is:

$$\varepsilon_{ij} = \frac{1}{2} \left(\frac{\partial u_i}{\partial x_j} + \frac{\partial u_j}{\partial x_i} \right) \quad (3-9)$$

Thus, the corresponding stress field in half space coordinate can be calculated through Hooke's law:

$$\sigma_{ij} = C_{ijkl} \varepsilon_{kl} \quad (3-10)$$

The equilibrium equation in half space coordinate is:

$$\sigma_{ij,j} = 0 \quad (3-11)$$

After submitting the displacement field (3-5) into (3-9)-(3-11), the following sextic equation in q is produced:

$$[D_{ij}(q)] \begin{bmatrix} U \\ V \\ W \end{bmatrix} = 0 \quad (3-12)$$

Thus, the determinant of the cofactor matrix of the equation should be zero:

$$\det[D_{ij}(q)] = 0 \quad (3-13)$$

The determinant of the cofactor matrix described by (3-13) will produce a sixth-order equation in q , which will produce the three desired q roots. They can be real or complex roots, and the real part of the roots should be positive for the half space ($z \leq 0$). These roots correspond to the attenuation properties of the displacements when getting far away from the free surface in the medium. For some special cases, the determinant is reduced to the product of two sub-determinants, namely the product of a second-order equation and a fourth-order equation. Then, the image displacement field is described by one independent displacement mode, and the coupled displacement modes in the sagittal plane perpendicular to the independent displacement mode.

After replacing the parameter q in (3-5) with the calculated q from (3-13), the final image displacement field at the free surface of half space is:

$$\begin{bmatrix} u \\ v \\ w \end{bmatrix} = [N^-] \begin{bmatrix} K_1 \\ K_2 \\ K_2 \end{bmatrix} \cdot \exp(ik_x x + ik_y y) \quad (3-14)$$

And the elastic relationship will produce the image stress field at free surface:

$$\begin{bmatrix} \sigma_{xz} \\ \sigma_{yz} \\ \sigma_{zz} \end{bmatrix} = [M^-] \begin{bmatrix} K_1 \\ K_2 \\ K_2 \end{bmatrix} \cdot \exp(ik_x x + ik_y y) \quad (3-15)$$

Following the flowchart in Fig. 3.2, the (K_1, K_2, K_3) for each Fourier mode is produced, thus solving the image displacement field for half space.

In the following, solutions to some special cases are given.

3.2.1. The image stress of a cubic crystal with [001] orientation

In the absence of body forces, the stress equilibrium equation given by the standing Christoffel equation [Dellinger, 1991] for cubic material with a (001) free surface can be written in terms of the displacement field (u, v, w) as:

$$\begin{cases} C_{12}(u_{xx} + v_{xy} + w_{xz}) + (C_{11} - C_{12})u_{xx} + C_{44}(u_{yy} + v_{xy}) + C_{44}(u_{zz} + w_{xz}) = 0 \\ C_{12}(u_{xy} + v_{yy} + w_{yz}) + (C_{11} - C_{12})v_{yy} + C_{44}(u_{xy} + v_{xx}) + C_{44}(v_{zz} + w_{yz}) = 0 \\ C_{12}(u_{xz} + v_{yz} + w_{zz}) + (C_{11} - C_{12})w_{zz} + C_{44}(w_{xx} + u_{xz}) + C_{44}(v_{yz} + w_{yy}) = 0 \end{cases} \quad (3-16)$$

According to the basic properties of cubic crystal, the elastic energy should be larger than zero and the determinant of the stiffness matrix should be positive, thus producing the following conditions:

$$\begin{cases} C_{11} - C_{12} > 0 \\ C_{11} + 2C_{12} > 0 \end{cases} \quad (3-17)$$

By placing the displacement field (3-5) into the equilibrium equation (3-16), one obtains the following equations for each Fourier mode:

$$\begin{bmatrix} [(q^2 C_{44} - k_x^2 C_{11} - k_y^2 C_{44}) & -k_x k_y (C_{12} + C_{44}) & ik_x q (C_{12} + C_{44}) \\ -k_x k_y (C_{12} + C_{44}) & (q^2 C_{44} - k_y^2 C_{11} - k_x^2 C_{44}) & ik_y q (C_{12} + C_{44}) \\ ik_x q (C_{12} + C_{44}) & ik_y q (C_{12} + C_{44}) & (q^2 C_{11} - k_x^2 C_{44} - k_y^2 C_{44}) \end{bmatrix} \cdot \begin{bmatrix} U \\ V \\ W \end{bmatrix} = 0 \quad (3-18)$$

The condition that non-zero roots exist requires that the determinant of the coefficients matrix of equation (3-18) is zero.

(a) Mode ($k_x \neq 0, k_y \neq 0$)

When the determinant of the coefficient matrix in equation (3-18) is zero, a sextic equation in q is produced, which has in general three desired roots with positive real parts. Depending on the attenuation coefficient properties of the three q_j , the ratios of the corresponding (U_j, V_j, W_j) are calculable. After performing the cofactor expansion along the first row of the matrix in equation (3-18), the corresponding (ξ_j, η_j, ζ_j) are the elements along the first row of the cofactor expansion matrix in equation (3-18).

$$\frac{U_j}{\xi_j} = \frac{V_j}{\eta_j} = \frac{W_j}{\zeta_j} = K_j \quad (3-19)$$

the resultant (ξ_j, η_j, ζ_j) is described in Appendix (B-1).

(b) Mode ($k_x = 0, k_y \neq 0$).

The determinant of the matrix in equation (3-18) can be reduced into the product of two sub-determinants, which will produce 3 roots: $q_1 = |k_y|$, and (q_2, q_3) are the roots (with positive real parts) of the following equation.

$$C_{11}C_{44} \cdot (q_j)^4 + (C_{12}C_{12} - C_{11}C_{11} + 2C_{12}C_{44})k_y^2 \cdot (q_j)^2 + k_y^4 \cdot C_{11}C_{44} = 0; (j = 2,3) \quad (3-20)$$

(c) Mode ($k_x \neq 0, k_y = 0$).

The determinant can be reduced into the product of two sub-determinants, which will produce 3 roots: $q_1 = |k_x|$, and (q_2, q_3) . They are the roots with positive real parts of the following equation.

$$C_{11}C_{44} \cdot (q_j)^4 + (C_{12}C_{12} - C_{11}C_{11} + 2C_{12}C_{44})k_x^2 \cdot (q_j)^2 + k_x^4 \cdot C_{11}C_{44} = 0; (j = 2,3) \quad (3-21)$$

(d) Mode ($k_x = 0, k_y = 0$).

The mode ($k_x = 0, k_y = 0$) means constant force and displacement fields. This leads to a uniform stress within the half space. Physically, a dislocation will not be able to exert a constant traction in the half space. The ($k_x = 0, k_y = 0$) mode is thus avoided.

After getting all modes for the Fourier analysis in (a), (b), (c) and (d), the displacement components are related with the coefficients (K_1, K_2, K_3) as follows:

$$\begin{bmatrix} \hat{u} \\ \hat{v} \\ \hat{w} \end{bmatrix} = [N^-] \begin{bmatrix} K_1 \\ K_2 \\ K_3 \end{bmatrix} \quad (3-22)$$

The resultant $[N^-]$ is described in Appendix (B-1). From the displacement field in equation (3-5), it is straightforward to obtain the strain field ε_{ij} through differentiation and the stress field σ_{ij} using Hooke's law. The corresponding tractions composed of the stress components σ_{i3} on the surface $z = 0$ are composed of the coefficients (K_1, K_2, K_3) through the following matrix equation:

$$\begin{bmatrix} \hat{\sigma}_{xz} \\ \hat{\sigma}_{xz} \\ \hat{\sigma}_{xz} \end{bmatrix} = [M^-] \begin{bmatrix} K_1 \\ K_2 \\ K_3 \end{bmatrix} \quad (3-23)$$

The resultant $[M^-]$ is described in Appendix (B-1). Given the surface traction σ_{i3} produced by the defect in infinite medium at the foil surface position, the Fourier coefficients (K_1, K_2, K_3) of any Fourier Mode (k_x, k_y) can be determined from these relationships. Once the Fourier coefficients are obtained, the displacement, stress field of this Fourier mode is completely determined through Fourier analytic expressions.

3.2.2. The image stress of a HCP crystal with [0001] orientation

For a HCP half space with (0001) free surface, the basic crystal cell is defined with the following 4 vectors: $a_1 = [1\bar{2}10]$, $a_2 = [11\bar{2}0]$, $a_3 = [\bar{2}110]$ and $c = [0001]$. The basic coordinate is: $x_0 = [1\bar{1}00]$, $y_0 = [11\bar{2}0]$, $z_0 = [0001]$. The geometrical relation is shown in Fig 3.3.



Figure 3.3: The HCP crystal. (a), crystal index of HCP in the Basal plane; (b), Cartesian coordinate definition.

In the absence of body forces, the equilibrium equation can be written in terms of the displacement field (u, v, w) as:

$$\begin{cases} (C_{11}u_{xx} + C_{12}v_{xy} + C_{13}w_{xz}) + (C_{11} - C_{12})(u_{yy} + v_{xy})/2 + C_{44}(u_{zz} + w_{xz}) = 0 \\ (C_{11} - C_{12})(u_{xy} + v_{xx})/2 + (C_{12}u_{xy} + C_{11}v_{yy} + C_{13}w_{yz}) + C_{44}(v_{zz} + w_{yz}) = 0 \\ C_{44}(u_{xz} + w_{xx}) + C_{44}(v_{yz} + w_{yy}) + (C_{13}u_{xz} + C_{13}v_{yz} + C_{33}w_{zz}) = 0 \end{cases} \quad (3-24)$$

The displacement field (3-5) will be considered as the solution for lower half space, and the following equilibrium equation can be concluded:

$$\begin{bmatrix} (q^2C_{44} - k_x^2C_{11} - \frac{(C_{11}-C_{12})}{2}k_y^2) & -k_xk_y\frac{(C_{11}+C_{12})}{2} & (ik_xq)(C_{13} + C_{44}) \\ -k_xk_y\frac{(C_{11}+C_{12})}{2} & (q^2C_{44} - k_y^2C_{11} - \frac{(C_{11}-C_{12})}{2}k_x^2) & (ik_yq)(C_{13} + C_{44}) \\ (ik_xq)(C_{13} + C_{44}) & (ik_yq)(C_{13} + C_{44}) & (q^2C_{33} - k_y^2C_{44} - k_x^2C_{44}) \end{bmatrix} \begin{bmatrix} U \\ V \\ W \end{bmatrix} = 0 \quad (3-25)$$

This equation can be written as:

$$\begin{bmatrix} D_{11} & D_{12} & D_{13} \\ D_{21} & D_{22} & D_{23} \\ D_{31} & D_{32} & D_{33} \end{bmatrix} \begin{bmatrix} U \\ V \\ W \end{bmatrix} = 0 \quad (3-26)$$

In which the corresponding parameters are described in the Appendix (B-2). In order to produce non-zero roots, the determinant should be set to zero, which will result in a sextic equation producing 6 roots in q_i , but only 3 complex roots (with positive real part) are selected for producing the displacement fields.

(a), the mode $(k_x \neq 0, k_y \neq 0)$.

After doing the cofactor expansion along the first row of the cofactor matrix in equation (3-26), the corresponding (ξ_j, η_j, ζ_j) elements along the first row of the cofactor expansion matrix can be produced. The corresponding displacement field can be written as:

$$\frac{U_j}{\xi_j} = \frac{V_j}{\eta_j} = \frac{W_j}{\zeta_j} = K_j \quad (3-27)$$

The corresponding (ξ_j, η_j, ζ_j) are described in Appendix (B-2).

(b), the mode $(k_x = 0, k_y \neq 0)$.

The determinant of the cofactor matrix will be reduced to the product of two sub-determinants, which will produce the three desired roots: $q_1 = |k_y| \cdot \sqrt{(C_{11} - C_{12})/(2C_{44})}$, and (q_2, q_3) are the roots (with positive real parts) of the following equation:

$$C_{44}C_{33}q_j^4 + (2C_{44}C_{13} + C_{13}C_{13} - C_{11}C_{33})k_y^2q_j^2 + C_{44}C_{11}k_y^4 = 0; (j = 2,3) \quad (3-28)$$

(c), the mode $(k_x \neq 0, k_y = 0)$.

The determinant of the cofactor matrix will be reduced to the product of two sub-determinants, which will produce the three desired roots: $q_1 = |k_x| \cdot \sqrt{(C_{11} - C_{12})/(2C_{44})}$, and (q_2, q_3) are the roots (with positive real parts) of the following equation:

$$C_{44}C_{33}q_j^4 + (2C_{44}C_{13} + C_{13}C_{13} - C_{11}C_{33})k_x^2q_j^2 + C_{44}C_{11}k_x^4 = 0; (j = 2,3) \quad (3-29)$$

(d), the mode $(k_x = 0, k_y = 0)$.

The mode $(k_x = 0, k_y = 0)$ means constant force and displacement fields. This leads to uniform stress inside half space medium, thus leading to infinite energy because the domain is infinite. Physically, a dislocation will not be able to exert a constant traction on the half space, such $(k_x = 0, k_y = 0)$ mode is avoided.

The corresponding $[N^-]$ and $[M^-]$ are described in Appendix (B-2).

3.3. Fourier space solution for anisotropic thin foil problem

For a thin foil with arbitrarily oriented crystal surfaces, a similar procedure can be applied. There is the original coordinate (x_0, y_0, z_0) , which is related to the basic crystal orientation, such as [100], [010] and [001] for bcc crystals, and the thin foil coordinate (x, y, z) , where z is along the foil free surface normal direction. The following image displacement field is employed:

$$\begin{cases} u = \sum_{k_x} \sum_{k_y} [U^S \sinh(q^S \cdot z) + U^A \cosh(q^A \cdot z)] \cdot \exp(ik_x x + ik_y y) \\ v = \sum_{k_x} \sum_{k_y} [V^S \sinh(q^S \cdot z) + V^A \cosh(q^A \cdot z)] \cdot \exp(ik_x x + ik_y y) \\ w = \sum_{k_x} \sum_{k_y} [W^S \cosh(q^S \cdot z) + W^A \sinh(q^A \cdot z)] \cdot \exp(ik_x x + ik_y y) \end{cases} \quad (3-30)$$

The equilibrium equations at the position $\pm z$ can be rewritten into two independent sets of equations on (U^S, V^S, W^S) and (U^A, V^A, W^A) , the symmetrical and the asymmetrical parts respectively. Then, three roots (q_1^S, q_2^S, q_3^S) and three roots (q_1^A, q_2^A, q_3^A) for the symmetrical and asymmetrical matrix equations can be calculated, respectively to these parts.

The symmetrical image displacement solution can be written as:

$$u^S = \frac{1}{2} \begin{bmatrix} u^+ - u^- \\ v^+ - v^- \\ w^+ + w^- \end{bmatrix} = [N^S] \begin{bmatrix} K_1^S \\ K_2^S \\ K_3^S \end{bmatrix} \cdot \exp(ik_x x + ik_y y) \quad (3-31)$$

And the asymmetrical image displacement solution can be written as:

$$u^A = \frac{1}{2} \begin{bmatrix} u^+ + u^- \\ v^+ + v^- \\ w^+ - w^- \end{bmatrix} = [N^A] \begin{bmatrix} K_1^A \\ K_2^A \\ K_3^A \end{bmatrix} \cdot \exp(ik_x x + ik_y y) \quad (3-32)$$

The symmetrical image stress solutions can be written as:

$$T^S = \frac{1}{2} \begin{bmatrix} \sigma_{xz}^+ + \sigma_{xz}^- \\ \sigma_{yz}^+ + \sigma_{yz}^- \\ \sigma_{zz}^+ - \sigma_{zz}^- \end{bmatrix} = [M^S] \begin{bmatrix} K_1^S \\ K_2^S \\ K_3^S \end{bmatrix} \cdot \exp(ik_x x + ik_y y) \quad (3-33)$$

And the asymmetrical image stress solution can be written as:

$$T^A = \frac{1}{2} \begin{bmatrix} \sigma_{xz}^+ - \sigma_{xz}^- \\ \sigma_{yz}^+ - \sigma_{yz}^- \\ \sigma_{zz}^+ + \sigma_{zz}^- \end{bmatrix} = [M^A] \begin{bmatrix} K_1^A \\ K_2^A \\ K_3^A \end{bmatrix} \cdot \exp(ik_x x + ik_y y) \quad (3-34)$$

The corresponding bulk stress field $(\sigma_{lm}^\infty)_0$ produced by dislocation loops or finite dislocation segments at free surfaces of thin foil can be calculated with suitable elasticity models in the original coordinate, which can be converted into thin foil coordinate:

$$\sigma_{ij}^\infty = T_{il} T_{jm} (\sigma_{lm}^\infty)_0 \quad (3-35)$$

The bulk stress field can be also be written in Fourier space, and converted into the symmetrical and asymmetrical parts, as follows:

$$\sigma^\infty(x, y, z) = \sum_{k_x} \sum_{k_y} [(\hat{\sigma}^\infty)^S(k_x, k_y, z) + (\hat{\sigma}^\infty)^A(k_x, k_y, z)] \cdot \exp(ik_x x + ik_y y) \quad (3-36)$$

Then the corresponding coefficients (K_1^S, K_2^S, K_3^S) and (K_1^A, K_2^A, K_3^A) for each Fourier mode in the thin foil coordinate can be calculated by matching each Fourier mode of the image stress and bulk stress at the free surface position. In such a way the corresponding image displacement field, strain field and stress field within the volume can be calculated.

Finally, the image displacements and stress solutions of any point within the foil can be written as:

$$u_j^{image} = u_j^S + u_j^A; \quad (j = 1, 2, 3) \quad (3-37)$$

And the displacement gradient field:

$$u_{j,3}^{image} = u_{j,3}^S + u_{j,3}^A; \quad (j = 1, 2, 3) \quad (3-38)$$

And

$$\sigma_{ij}^{image} = \sigma_{ij}^S + \sigma_{ij}^A \quad (3-39)$$

3.3.1. The image stress of a cubic crystal thin foil with [001] orientation

In the absence of body forces, the stress equilibrium equation for cubic material with a (001) free surface can be written in terms of the displacement field (u, v, w) as:

$$\begin{cases} C_{12}(u_{xx} + v_{xy} + w_{xz}) + (C_{11} - C_{12})u_{xx} + C_{44}(u_{yy} + v_{xy}) + C_{44}(u_{zz} + w_{xz}) = 0 \\ C_{12}(u_{xy} + v_{yy} + w_{yz}) + (C_{11} - C_{12})v_{yy} + C_{44}(u_{xy} + v_{xx}) + C_{44}(v_{zz} + w_{yz}) = 0 \\ C_{12}(u_{xz} + v_{yz} + w_{zz}) + (C_{11} - C_{12})w_{zz} + C_{44}(w_{xx} + u_{xz}) + C_{44}(v_{yz} + w_{yy}) = 0 \end{cases} \quad (3-40)$$

The equilibrium equations can be written in the foil coordinate. Considering the independent properties (U^S, V^S, W^S) and (U^A, V^A, W^A) , the equilibrium equation can be written separately into the symmetrical and asymmetrical parts.

(a) Mode $(k_x \neq 0, k_y \neq 0)$.

When the determinant of the coefficient matrix in equation (3-40) is zero, 3 desired roots (q_1^S, q_2^S, q_3^S) with positive real parts will be produced. After doing the cofactor expansion along the first row of the coefficient matrix, the corresponding $(\xi_j^S, \eta_j^S, \zeta_j^S)$ elements along the first row of the cofactor expansion matrix can be calculated. The ratios of the corresponding (U_j^S, V_j^S, W_j^S) are calculable, which can be written as:

$$\frac{U_j^S}{\xi_j^S} = \frac{V_j^S}{\eta_j^S} = \frac{W_j^S}{\zeta_j^S} = K_j^S \quad (3-41)$$

The resultant $(\xi_j^S, \eta_j^S, \zeta_j^S)$ is described in Appendix (B-3).

Likewise for the asymmetrical part, when the determinant of its coefficient matrix in equation (3-40) is zero, 3 desired roots (q_1^A, q_2^A, q_3^A) with positive real parts will be produced. After doing the cofactor expansion along the first row of the coefficient matrix, the corresponding ($\xi_j^A, \eta_j^A, \zeta_j^A$) elements along the first row of the cofactor expansion matrix can be calculated. The ratios of the corresponding (U_j^A, V_j^A, W_j^A) are calculable, which can be written as:

$$\frac{U_j^A}{\xi_j^A} = \frac{V_j^A}{\eta_j^A} = \frac{W_j^A}{\zeta_j^A} = K_j^A \quad (3-42)$$

The resultant ($\xi_j^A, \eta_j^A, \zeta_j^A$) is also described in Appendix (B-3).

(b) Mode ($k_x = 0, k_y \neq 0$).

The determinant can be reduced into the product of two sub-determinants. For the symmetrical part, this is expressed by the following equation that has three roots, namely $q_1^S = |k_y|$ and (q_2^S, q_3^S), the latter being roots with positive real parts.

$$C_{11}C_{44} \cdot (q_j^S)^4 + (C_{12}C_{12} - C_{11}C_{11} + 2C_{12}C_{44})k_y^2 \cdot (q_j^S)^2 + k_y^4 \cdot C_{11}C_{44} = 0; (j = 2,3) \quad (3-43)$$

For the asymmetrical part this is expressed by the following equation that has three roots, namely $q_1^A = |k_y|$ and (q_2^A, q_3^A), the latter being the roots with positive real parts.

$$C_{11}C_{44} \cdot (q_j^A)^4 + (C_{12}C_{12} - C_{11}C_{11} + 2C_{12}C_{44})k_y^2 \cdot (q_j^A)^2 + k_y^4 \cdot C_{11}C_{44} = 0; (j = 2,3) \quad (3-44)$$

(c) Mode ($k_x \neq 0, k_y = 0$).

The determinant can be reduced into the product of two sub-determinants. For the symmetrical parts, this is expressed by the following equation that has three roots, namely $q_1^S = |k_x|$ and (q_2^S, q_3^S), the latter being the roots with positive real parts.

$$C_{11}C_{44} \cdot (q_j^S)^4 + (C_{12}C_{12} - C_{11}C_{11} + 2C_{12}C_{44})k_x^2 \cdot (q_j^S)^2 + k_x^4 \cdot C_{11}C_{44} = 0; (j = 2,3) \quad (3-45)$$

For the asymmetrical parts, this is expressed by the following equation that has three roots, namely $q_1^A = |k_x|$ and (q_2^A, q_3^A), the latter being the roots with positive real parts.

$$C_{11}C_{44} \cdot (q_j^A)^4 + (C_{12}C_{12} - C_{11}C_{11} + 2C_{12}C_{44})k_x^2 \cdot (q_j^A)^2 + k_x^4 \cdot C_{11}C_{44} = 0; (j = 2,3) \quad (3-46)$$

(d) Mode ($k_x = 0, k_y = 0$).

The mode ($k_x = 0, k_y = 0$) means constant force and displacement fields. This leads to uniform stress inside the thin foil. Physically, a dislocation will not be able to exert a constant traction stress field on the free surface. The ($k_x = 0, k_y = 0$) mode is thus avoided.

Finally, the symmetrical image displacement matrix [N^S] and symmetrical image stress [M^S], and the asymmetrical image displacement matrix [N^A] and asymmetrical image stress [M^A] for each Fourier mode are described in Appendix (B-3).

3.3.2. The image stress of a cubic crystal thin foil with [111] orientation

When cubic foil is following the $[11\bar{2}]$, $[\bar{1}10]$ and $[111]$ coordinate, the equilibrium equation is:

$$\begin{cases} [C'_{11}u_{xx} + C'_{13}v_{xy} + C'_{12}w_{xz} + C'_{16}(2u_{xz} + w_{xx})] + [-C'_{16}(2v_{yz} + w_{yy}) + C'_{55}(u_{yy} + v_{xy})] + [+C'_{44}(u_{zz} + w_{zz})] = 0 \\ [-C'_{16}(2v_{xz} + 2w_{xy}) + C'_{55}(u_{xy} + v_{xx})] + [C'_{13}u_{xy} + C'_{11}v_{yy} + C'_{12}w_{yz} - C'_{16}(2u_{yz})] + [C'_{44}(v_{zz} + w_{yz})] = 0 \\ [C'_{16}u_{xx} - 2C'_{16}v_{xy} + C'_{44}(u_{xz} + w_{xx})] + [C'_{44}(v_{yz} + w_{yy}) - C'_{16}(u_{yy})] + [C'_{12}u_{xz} + C'_{12}v_{yz} + C'_{22}w_{zz}] = 0 \end{cases} \quad (3-47)$$

In which,

$$H = 2C_{44} + C_{12} - C_{11}; C'_{11} = C_{11} + \frac{1}{2}H; C'_{12} = C_{12} - \frac{1}{3}H; C'_{13} = C_{12} - \frac{1}{6}H;$$

$$C'_{44} = C_{44} - \frac{1}{3}H; C'_{55} = C_{44} - \frac{1}{6}H; C'_{16} = \frac{\sqrt{2}}{6}H; C'_{22} = C_{11} + \frac{2}{3}H; \quad (3-48)$$

The equilibrium equations can be written in the foil coordinate. Considering the independent properties (U^S, V^S, W^S) and (U^A, V^A, W^A) , the equilibrium equation can be written separately into the symmetrical and asymmetrical parts.

(1) Mode $(k_x \neq 0, k_y \neq 0)$ and $(k_x = 0, k_y \neq 0)$.

When the determinant of the coefficient matrix in equation (3-47) is zero, 3 desired roots (q_1^S, q_2^S, q_3^S) with positive real parts will be produced. After doing the cofactor expansion along the first row of the coefficient matrix, the corresponding $(\xi_j^S, \eta_j^S, \zeta_j^S)$ elements along the first row of the cofactor expansion matrix can be calculated. The ratios of the corresponding (U_j^S, V_j^S, W_j^S) are calculable, which can be written as:

$$\frac{U_j^S}{\xi_j^S} = \frac{V_j^S}{\eta_j^S} = \frac{W_j^S}{\zeta_j^S} = K_j^S \quad (3-49)$$

The resultant $(\xi_j^S, \eta_j^S, \zeta_j^S)$ is described in Appendix (B-4).

Likewise for the asymmetrical part, when the determinant of its coefficient matrix in equation (3-47) is zero, 3 desired roots (q_1^A, q_2^A, q_3^A) with positive real parts will be produced. After doing the cofactor expansion along the first row of the coefficient matrix, the corresponding $(\xi_j^A, \eta_j^A, \zeta_j^A)$ elements along the first row of the cofactor expansion matrix can be calculated. The ratios of the corresponding (U_j^A, V_j^A, W_j^A) are calculable, which can be written as:

$$\frac{U_j^A}{\xi_j^A} = \frac{V_j^A}{\eta_j^A} = \frac{W_j^A}{\zeta_j^A} = K_j^A \quad (3-50)$$

The resultant $(\xi_j^A, \eta_j^A, \zeta_j^A)$ is also described in Appendix (B-4).

(2) Mode $(k_x \neq 0, k_y = 0)$.

As to the symmetrical part, the determinant will be reduced to the product of two sub-determinant, which will produce the three desired roots: $q_1^S = (ik_x C'_{16} + |k_x| \cdot \sqrt{(C'_{55} C'_{44} - C'_{16} C'_{16})}) / C'_{44}$, and (q_2^S, q_3^S) are the roots with positive real parts of the following equation:

$$C'_{44} C'_{22} (q_j^S)^4 + 2ik_x C'_{16} C'_{22} (q_j^S)^3 + k_x^2 (2C'_{44} C'_{12} + C'_{12} C'_{12} - C'_{11} C'_{22}) (q_j^S)^2 + 2ik_x^3 C'_{12} C'_{16} (q_j^S) + k_x^4 (C'_{11} C'_{44} - C'_{16} C'_{16}) = 0; \quad (j = 2, 3) \quad (3-51)$$

Likewise, the determinant will be reduced to the product of two sub-determinant, which will produce the three desired roots: $q_1^A = (ik_x C'_{16} + |k_x| \cdot \sqrt{(C'_{55} C'_{44} - C'_{16} C'_{16})}) / C'_{44}$, and (q_2^A, q_3^A) are the roots with positive real parts of the following equation:

$$C'_{44} C'_{22} (q_j^A)^4 + 2ik_x C'_{16} C'_{22} (q_j^A)^3 + k_x^2 (2C'_{44} C'_{12} + C'_{12} C'_{12} - C'_{11} C'_{22}) (q_j^A)^2 + 2ik_x^3 C'_{12} C'_{16} (q_j^A) + k_x^4 (C'_{11} C'_{44} - C'_{16} C'_{16}) = 0; \quad (j = 2, 3) \quad (3-52)$$

(3) Mode $(k_x = 0, k_y = 0)$.

The mode $(k_x = 0, k_y = 0)$ means constant force and displacement fields. This leads to a uniform stress inside the half space medium, thus leading to infinite energy because the domain is infinite. Physically this means that a dislocation will not be able to exert a constant traction on the half space, such a mode is thus avoided.

Finally, the symmetrical image displacement matrix $[N^S]$ and symmetrical image stress $[M^S]$, and the asymmetrical image displacement matrix $[N^A]$ and asymmetrical image stress $[M^A]$ for each Fourier mode are described in Appendix (B-4).

3.4. Image energy calculation

3.4.1. Image energy for the half space

Let \bar{T}^- and \bar{u}^- be respectively the traction force and displacement field in the surface of the lower half space for each Fourier mode. They are related to each other through $[M^-]$ and $[N^-]$ matrices as follows:

$$\bar{T}^- = [M^-] \cdot [N^-]^{-1} \cdot \bar{u}^- \quad (3-53)$$

Then, the image energy for half space is:

$$E_h^{image} = -\frac{1}{2} \int_S \bar{T}^- \cdot \bar{u}^- dS \quad (3-54)$$

3.4.2. Image energy for the thin foil

The image energy of the foil can be written as the sum of two contributing parts, namely the upper and lower half spaces, the upper and lower free surfaces of thin foil.

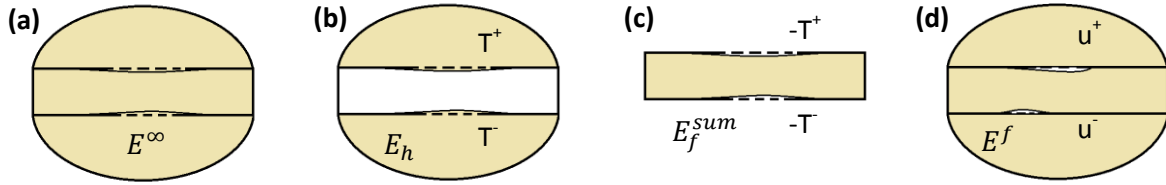


Figure 3.4: Image energy of thin foil (a), bulk material containing defects, the perfect lattice will be bended; (b), two half space with stress field BC, which is equal in magnitude as the stress field induced by defects in bulk material, but in opposite direction; (c), foil containing defects with stress BC, which is equal in magnitude as the stress field induced by defects in bulk material; (d), foil containing defects with free surfaces, after releasing the stress field in (b) and (c), there are no external forces need to be applied to the infinite medium, but there will be a displacement jump across the surfaces of thin foil.

As shown in Fig. 3.4(a), the infinite energy E^∞ of a dislocation loop can be treated as the sum of all the elastic energy stored in two half spaces and the thin foil zones. The displacement, stress field and elastic energy storage in these three regions is equivalent to the sum of Fig. 3.4(b) and Fig. 3.4(c).

$$E^\infty = E_h + E_f^{sum} \quad (3-55)$$

As shown in Fig. 3.4(b), the whole energy E_h^{sum} is the sum of elastic energy E_h^+ and E_h^- stored within the two half spaces, and can be expressed as integral over the foil upper and lower surfaces.

$$E_h = E_h^+ + E_h^- \quad (3-56)$$

and

$$E_h^+ = -\frac{1}{2} \int_{S^+} T^+ \cdot u_h^+ ds^+ \quad (3-57)$$

and

$$E_h^- = -\frac{1}{2} \int_{S^-} T^- \cdot u_h^- ds^- \quad (3-58)$$

As shown in Fig.3.4(c), the whole energy E_f^{sum} can be expressed as the sum of three parts: the elastic energy E^f stored inside the thin foil with free surfaces, which is equivalent to Fig. 3.4(d); and two

boundary stress loading induced additional elastic energy E_f^+ and E_f^- respectively, which can be expressed as integral over the foil upper and lower surfaces.

$$E_f^{sum} = E^f + E_f^+ + E_f^- \quad (3-59)$$

And,

$$E_f^+ = \frac{1}{2} \int_{S^+} T^+ \cdot u_f^+ ds^+ \quad (3-60)$$

and

$$E_f^- = \frac{1}{2} \int_{S^-} T^- \cdot u_f^- ds^- \quad (3-61)$$

As shown in Fig. 3.4(d), the whole elastic energy stored inside the thin foil with free surfaces can be expressed as E^f . Similar to Weinberger [Weinberger, 2007], analytic expressions for the elastic energy of an arbitrary dislocation network in an infinite medium is described as E^∞ , then the elastic energy E^f stored inside the thin foil with free surfaces are decompose into two parts:

$$E^f = E^\infty + E^{image} \quad (3-62)$$

Alternatively, the following equation stands:

$$E^\infty = E^f + E_f^+ + E_f^- + E_h^+ + E_h^- \quad (3-63)$$

Finally, the image energy can be written as:

$$E^{image} = -\frac{1}{2} \int_{-L_x/2}^{L_x/2} \int_{-L_y/2}^{L_y/2} [T^+(x, y) \cdot u^+(x, y) + T^-(x, y) \cdot u^-(x, y)] dx dy \quad (3-64)$$

In which, $u^+(x, y)$ and $u^-(x, y)$ are the displacement jump in the upper and lower surface of thin foil, respectively.

3.5. Displacement field of dislocation loop within bulk material

The general theory of curved dislocations in anisotropic media was developed by Volterra [Volterra, 1907], De Wit [De Wit, 1960] and Mura [Mura, 1963; Mura, 1968]. The special case of curved dislocations in an isotropic medium was attributed to Burgers [Burgers, 1939] and Peach and Koehler [Peach, 1950]. The Burgers formulas for the displacement field of isotropic dislocation loop with Burgers vector \mathbf{b} can be expressed as a sum including curvilinear integrals made along the dislocation line, C :

$$u_m(x) = -\frac{1}{4\pi} b_m \Omega - \frac{1}{8\pi} \int_C b_l \varepsilon_{mlk} R_{,pp} dx'_k - \frac{1}{8\pi(1-\nu)} \int_C b_j \varepsilon_{jpk} R_{,mp} dx'_k \quad (3-65)$$

In which, $R = x - x'$ is the vector from dislocation position x' to the calculated position x .

$$\Omega = -\int_A \frac{R \cdot dA}{R^3} \quad (3-66)$$

is the surface integral taken over the surface, A , of the dislocation loop.

Besides Burgers formula for isotropic dislocation loops, the bulk displacement field of general anisotropic dislocation loops can also be calculated with the surface integration formula of Volterra:

$$u_m(x) = b_i \int_S C_{ijkl} G_{km,l}^\infty(x - x') dS_j \quad (3-67)$$

Where the surface is the dislocation surface, which is a cap of dislocation line, whose boundary is the dislocation loop perimeter, and C_{ijkl} are the elastic constants of the the material and $G_{mk,l}^\infty$ is the first order derivative of Green's function in bulk material.

For an isotropic material, it appears that:

$$b_i C_{ijkl} G_{km,l}^{\infty}(R) = \frac{1}{8\pi\mu} \left[\mu b_m R_{,ppj} + \mu (b_l R_{,ppl} \delta_{jm} - b_j R_{,ppm}) \right. \\ \left. + 2 \left(\frac{\lambda+\mu}{\lambda+2\mu} \right) \mu (b_j R_{,ppm} - b_i R_{,mij}) \right] \quad (3-68)$$

Where $R = x - x'$ is the vector from dislocation position x' to the calculated position x , λ is Lamé's first parameter of isotropic material, and μ is shear modulus of isotropic material, δ_{ij} is the Kronecker delta operator.

For anisotropic materials, a corresponding modulus matrix and the first order derivatives of anisotropic Green's function will be employed for the calculation.

3.6. Self-energy of a dislocation loop within bulk material

3.6.1. Interaction energy between two dislocation loops

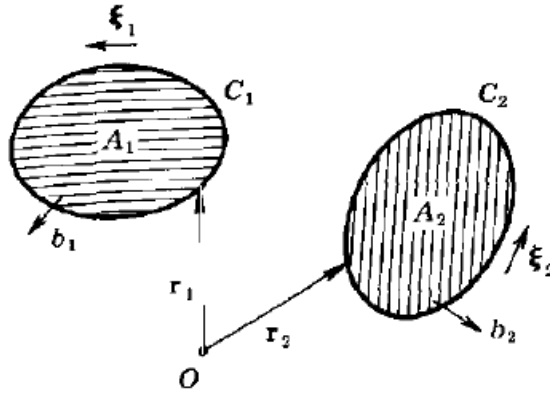


Figure 3.5: Schematics of two interacting dislocation loops [Hirth, 1982].

As shown in Fig. 3.5, if loop 1 is created while loop 2 is present, the stress originating from loop 2 does work, w_{12} , which is the interaction energy between the two loops:

$$w_{12} = \left[-\frac{\mu}{2\pi} \oint_{C_1} \oint_{C_2} \frac{(b_1 \times dl_1) \cdot (b_2 \times dl_2)}{R} + \frac{\mu}{4\pi} \oint_{C_1} \oint_{C_2} \frac{(b_1 \cdot dl_1)(b_2 \cdot dl_2)}{R} \right. \\ \left. + \frac{\mu}{4\pi(1-\nu)} \oint_{C_1} \oint_{C_2} (b_1 \times dl_1) \cdot T \cdot (b_2 \times dl_2) \right] \quad (3-69)$$

In which,

$$T_{ij} = \frac{\partial^2 R}{\partial x_i \partial x_j} \quad (3-70)$$

The above formula was first obtained by Blin [Blin, 1955].

3.6.2. Self-energy of a dislocation loop with isotropic elasticity

In forming the dislocation line, work must also be done against the self-stress of the loop. Each element of the loop feels a force caused by the stress originating from all other parts of the loop, and the work done against all these forces is a work called the self-energy. Only when the total force on each element of the loop is zero is the loop in equilibrium, and only then does one find an extremum in the total energy of the system. [Hirth, 1982]

The self-energy, is obtained when the two involved dislocation loops are overlapped, which means that the double integration is done on the same loop. Finally, the the self-energy of single loop is obtained by dividing the integration by 2.

$$\begin{aligned}
 w_S &= \left[\frac{\mu}{8\pi} \oint_{C_1=C} \oint_{C_2=C} \frac{(b \cdot dl_1) \cdot (b \cdot dl_2)}{R} + \frac{\mu}{8\pi(1-\nu)} \oint_{C_1=C} \oint_{C_2=C} (b \times dl_1) \cdot T \cdot (b \times dl_2) \right] \\
 &= \left[\frac{\mu}{8\pi} \oint_{l_1=C} \oint_{l_1+\rho}^{l_1+2\pi R-\rho} \frac{(b \cdot dl_1) \cdot (b \cdot dl_2)}{R} + \frac{\mu}{8\pi(1-\nu)} \oint_{l_1=C} \oint_{l_1+\rho}^{l_1+2\pi R-\rho} (b \times dl_1) \cdot T \cdot (b \times dl_2) \right]
 \end{aligned} \quad (3-71)$$

As is expected from the discussion of the core region of a straight dislocation, the self-energy diverges as the separation between two finite dislocation elements approaches zero. Cut off procedures must be introduced to avoid the divergence. This problem is characteristic of all types of interaction between two adjacent segments of the same dislocation line, as the separation distance between neighboring segments is at dislocation core radius level. [Hirth, 1982]

3.6.3. Self-energy of a dislocation loop with anisotropic elasticity

As already been mentioned in chapter.1, Green's function can be expressed as:

$$G_{ij}(x) = \frac{1}{8\pi^2|x|} \oint_{S1} N_{ij}(\bar{\xi}) D^{-1}(\bar{\xi}) d\phi \quad (3-72)$$

In which, S1 is an integral path along a unit circle lying on the plane perpendicular to x.

Then, a new function H_{ij} is introduced: [Ohsawa, 2009; Ohsawa, 2011]

$$H_{ij}(x) = \frac{1}{16|x|} \iint_{S2} |x \cdot \bar{\xi}| N_{ij}(\bar{\xi}) D^{-1}(\bar{\xi}) dS(\bar{\xi}) \quad (3-73)$$

In which, $|\xi| = 1$, and S_2 is surface of a unit sphere in Fourier space;

Then, the function H_{ij} satisfies the following relation:

$$G_{ij}(x) = H_{ij,kk}(x) \quad (3-74)$$

As has been developed by Mura, the stress field components produced by closed dislocation loops C' in anisotropic crystals are represented by integral representations:

$$\sigma_{ij}(x) = C_{ijkl} \oint_{C'} \epsilon_{lnh} C_{pqmn} G_{kp,q}(x - x') b'_m dx'_h \quad (3-75)$$

where the line integral with respect to x'_h is performed along the dislocation line C' ; G_{kp} are the Green's functions for anisotropic crystals; C_{ijkl} are the elastic constants; and b'_m is the Burgers vector of the dislocation loop C' .

Similarly, a new stress function χ_{ij} for the stress field produced by dislocation loops in anisotropic crystals can be expressed as:

$$\chi_{ij}(x) = C_{ijkl} \oint_{C'} \epsilon_{lnh} C_{pqmn} H_{kp,q}(x - x') b'_m dx'_h \quad (3-76)$$

Which is simply by replacing G_{kp} with the function H_{kp} .

According to the linear elasticity theory, the energy of interaction between a dislocation loop and an applied stress field σ_{ij} is equal to the work done on the surface S bounded by the dislocation line C' while the dislocation loop is created. Therefore, the interaction energy is expressed as:

$$E_I = b_i \int_S \sigma_{ij} dS_j \quad (3-77)$$

After mathematical operation, the interaction energy in the form of surface integration can be reduced into linear integration along dislocation perimeter line:

$$E_I = -b_i \oint_C \epsilon_{jts} \chi_{ij,s} dx_t \quad (3-78)$$

Then, the interaction energy can be expressed as:

$$E_I = -b_i b'_m \int_C \int_{C'} \epsilon_{jts} \epsilon_{lnh} C_{ijkl} C_{pqmn} H_{kp,qs}(x - x') dx_t dx'_h \quad (3-79)$$

Finally, the self-energy can be expressed as the summation of four double integrals over the two identical dislocation loops (C and C' will be the same dislocation loop perimeter):

$$E_I = b_i b'_m \left\{ \begin{aligned} & C_{ihks} C_{pqmt} \oint_C \oint_{C'} H_{kp,qs}(x-x') dx_t dx'_h - C_{ijks} C_{pqmj} \oint_C \oint_{C'} H_{kp,qs}(x-x') dx_h dx'_t \\ & + C_{ijmj} \oint_C \oint_{C'} \frac{1}{4\pi|x-x'|} dx_h dx'_t - C_{ihmt} \oint_C \oint_{C'} \frac{1}{4\pi|x-x'|} dx_t dx'_h \end{aligned} \right\} \quad (3-80)$$

In which,

$$C_{ijkl} H_{km,lj}(x-x') = \frac{1}{4\pi|x-x'|} \delta_{im} \quad (3-81)$$

$$H_{kp,qs}(x-x') = \frac{1}{8\pi^2|x|} \oint_S \bar{\xi}_q \bar{\xi}_s N_{kp}(\bar{\xi}) D^{-1}(\bar{\xi}) d\phi$$

The following parameters are used for $H_{kp,qs}$ function calculation:

$$D(\xi) = \mu^2 \cdot (\lambda + 2\mu + \mu') \cdot \xi^6 + \mu \cdot \mu' \cdot (2\lambda + 2\mu + \mu') \cdot \xi^2 \cdot (\xi_1^2 \cdot \xi_2^2 + \xi_2^2 \cdot \xi_3^2 + \xi_3^2 \cdot \xi_1^2) + \mu'^2 \cdot (3\lambda + 3\mu + \mu') \cdot \xi_1^2 \cdot \xi_2^2 \cdot \xi_3^2 \quad (3-82)$$

and

$$N_{11}(\xi) = \mu^2 \cdot \xi^4 + \beta \cdot \xi^2 \cdot (\xi_2^2 + \xi_3^2) + \gamma \cdot \xi_2^2 \cdot \xi_3^2$$

$$N_{12}(\xi) = -(\lambda + \mu) \cdot \xi_1 \cdot \xi_2 \cdot (\mu \cdot \xi^2 + \mu' \cdot \xi_3^2) \quad (3-83)$$

and the other components are obtained by the cyclic permutation of (1, 2, 3) and where

$$\begin{aligned} \xi^2 &= \xi_1 \cdot \xi_1 \\ \beta &= \mu \cdot (\lambda + \mu + \mu') \\ \gamma &= \mu' \cdot (2\lambda + 2\mu + \mu') \\ \lambda &= C_{12} \\ \mu &= C_{44} \\ \mu' &= C_{11} - C_{12} - 2C_{44} \end{aligned} \quad (3-84)$$

Chapter. 4: TEM image simulation method

In this chapter, the TEM image simulation method using CUFOUR code is described. Then, the simulation schemes for the inclined dislocation and dislocation loop are presented, together with the different corresponding elasticity models implemented in CUFOUR.

4.1. General methodology

In order to study the free surface effect on TEM image contrast of inclined dislocation and dislocation loops, different types of elasticity models are developed. Each elasticity model has its special physical meaning and can be compared with each other for studying the impact image stress effect, anisotropy, and the synergetic effect of image stress and anisotropy on TEM image contrast of inclined dislocation and dislocation loop. What is more, two very important approximations are employed for the TEM image simulation, and will be briefly discussed in chapter 6.

(1), the column approximation (CA) impact on TEM image is not studied.

(2), the dislocation core contribution to TEM image contrast is not considered.

The displacement gradient field models of different types of inclined dislocation and dislocation loop are implemented into many beam TEM image simulation code CUFOUR for simulating diffraction contrast TEM image, based on Schaeublin-Stadelmann equations. As shown in Fig.4.1, the general structure of CUFOUR consists of three main parts:

- Pre-processing of geometrical and physical parameters input.
- Solving Schaeublin-Stadelmann equations in CUFOUR.
- Post-processing of the simulated TEM diffraction contrast image.

Firstly, the subroutine “forems.f” in CUFOUR is employed for producing input parameters, including beam condition, TEM thin foil properties, and defect properties. These parameters are stored in “CUFOUR.inp”, containing diffraction vector, deviation parameter, beams number included, image size, foil thickness, lattice parameter, material element type and beam convergence angle.

Secondly, depending on the simulation purpose, one of the physical model of either inclined dislocation or the dislocation loop will be selected, together with the input parameters in “CUFOUR.inp”, many beam TEM image simulation will be performed in CUFOUR, thus producing the transmitted or diffracted beam intensity at the pixel corresponding to the column position in the image. The dislocation core of inclined dislocation and dislocation loops are all ignored in the current work.

Finally, the simulated diffraction contrast TEM image “*.ima” is generated, which contains the intensity information, ranging from 0 to 1 at each pixel and the corresponding scale bar.

Following the flowchart of Fig. 4.1, the simulation schemes of inclined dislocation and dislocation loop are elaborated in details as follows. The geometrical and physical parameters for describing foil, electron beam and inclined dislocation are defined in CUFOUR for obtaining a TEM image comparable to experiment. These parameters can be divided into four categories: Defects Model Selection, Materials Data, Geometry Data and Diffraction Condition Data respectively.

The Material Data specifies the material physical properties of thin TEM foil for CUFOUR, consists of the following parameters:

- Space Group
- Lattice Parameter
- Atomic Positions
- Elastic Constants

The Geometry Data specifies the beam, foil and inclined dislocation or dislocation loop geometrical parameters for CUFOUR, consists of the following parameters:

- Foil normal
- Electron beam Direction
- Direction vector of inclined dislocation or normal vector of dislocation loop habit plane
- Burgers vector of inclined dislocation or dislocation loop
- Image size
- Thickness of the thin foil

Diffraction Condition Data specifies the beam diffraction conditions for CUFOUR, consists of the following parameters:

- Transmitted image or diffracted image
- Diffraction vector
- Included beam number
- Laue circle center
- Beam convergence angle

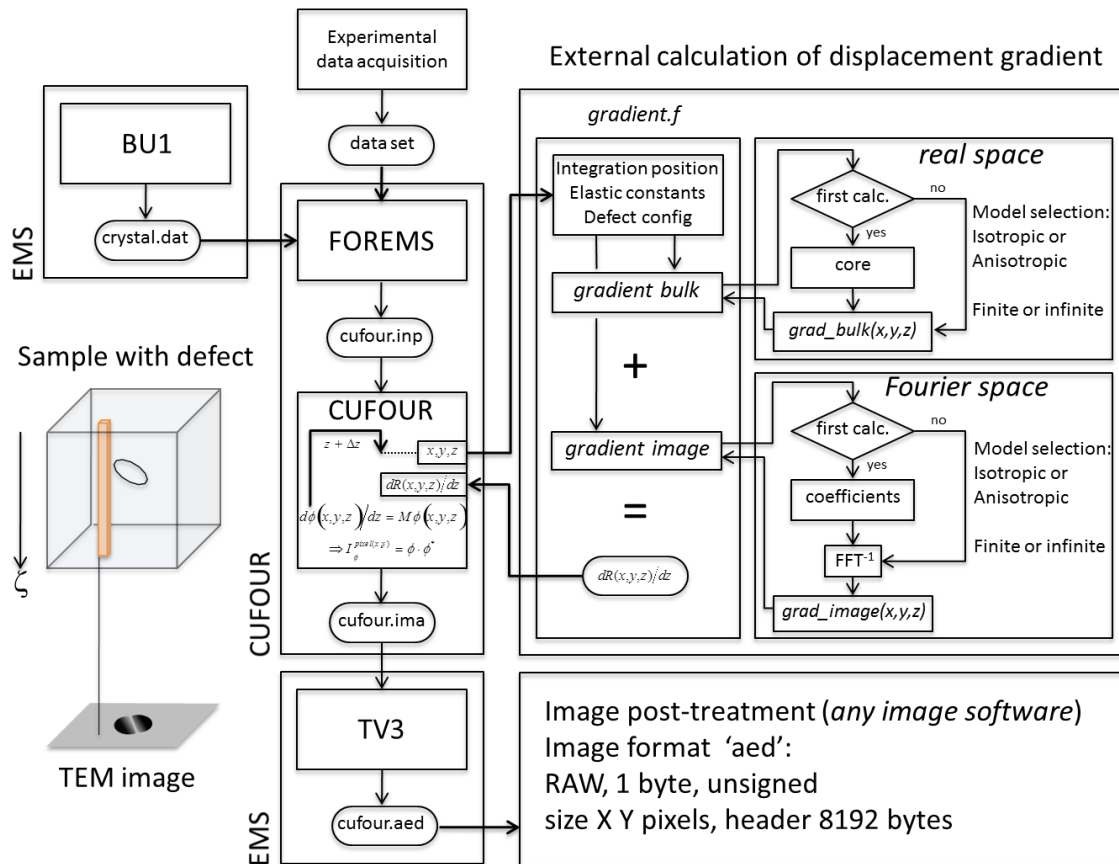


Figure 4. 1: CUFOUR TEM image simulation flowchart

4.1.1. Simulation scheme for inclined dislocation

The Defects Model Selection specifies which type of inclined dislocation model will be employed for the TEM image simulation. Ten types of inclined dislocation models have been implemented in CUFOUR, they are classified into the following four categories:

- Image stress effect of inclined dislocation
- Finite dislocation segment integration of inclined dislocation
- Image stress effect plus finite dislocation segment integration of inclined dislocation
- Infinite dislocation models

As to the image stress effect implementation schemes, the stress field at free surfaces is calculated from dislocation segments integration, which is prolonged outside thin foil, because dislocation can not terminate inside finite solid. Such prolonged dislocation is called virtual dislocation. It implies that the inclined dislocation is prolonged outside the thin foil on both sides. These outer segments are

each 2.5 times the length of the dislocation within the thin TEM foil. This length has been chosen arbitrarily.

In summary, the ten candidate isotropic/anisotropic inclined dislocation models are shown in Table 4.1.

Table 4. 1 Candidate models for inclined dislocation in thin foil [Stroh, 1958; Hirth, 1982; Mura, 1987; Devincere, 1995; Li, 2008; Akarapu, 2009; Weinberger, 2009; Yin, 2010; Wu, 2012].

Model type	Image gradient	Finite gradient	Total gradient	Bulk gradient
Isotropic	Image gradient via Devincere formula	Finite gradient via Mura formula	Total gradient via Devincere Image gradient plus Mura finite gradient	Bulk gradient via Hirth and Lothe formula
	Image gradient via Mura formula		Total gradient via Mura Image gradient plus Mura finite gradient	
Anisotropic	Image gradient via Willis–Steeds–Lothe (WSL) formula	Finite gradient via Willis–Steeds–Lothe formula	Total gradient via Willis–Steeds–Lothe image gradient plus Willis–Steeds–Lothe finite gradient	Bulk gradient via Stroh’s formula

4.1.2. Simulation scheme for dislocation loops

The Defects Model specifies which type of dislocation loop model will be employed for the TEM image simulation. Ten types of dislocation loop models implemented in CUFOUR, they are classified into the following three categories:

- Image stress effect of dislocation loop
- Bulk dislocation loop
- Image stress effect of dislocation loop plus infinite dislocation loop

As to the circular loop calculation, the elastic field induced by the circular loop is obtained using linear superposition of the ones induced by straight dislocation segments describing the loop. The loop is approximated by a regular polygon, made here of 30 to 40 straight dislocation segments of equal size.

In summary, the five isotropic/anisotropic dislocation loop models are shown in Table 4.2 and Table 4.3 respectively.

Table 4.2: Candidate models for isotropic dislocation loop in thin TEM foil [Stroh, 1958; Hirth, 1982; Mura, 1987; Devincere, 1995; Li, 2008; Akarapu, 2009; Weinberger, 2009; Yin, 2010; Wu, 2012].

Model type	Image gradient	Bulk gradient	Total gradient
Isotropic	Image gradient via Devincere’ formula	Bulk gradient via Mura’s formula	Total gradient via Devincere image gradient plus Mura infinite gradient
Isotropic	Image gradient via Mura’ formula		Total gradient via Mura image gradient plus Mura infinite gradient

Table 4. 3 Candidate models for anisotropic dislocation loop in thin TEM foil [Stroh, 1958; Hirth, 1982; Mura, 1987; Devincere, 1995; Li, 2008; Akarapu, 2009; Weinberger, 2009; Yin, 2010; Wu, 2012].

Model type	Image gradient	Bulk gradient	Total gradient
Anisotropic	Image gradient via Willis–Steeds–Lothe formula	Bulk gradient via Willis–Steeds–Lothe formula	Total gradient via Willis–Steeds–Lothe image gradient plus Willis–Steeds–Lothe infinite gradient
Anisotropic	Image gradient via Mura formula		Total gradient via Mura image gradient plus Willis–Steeds–Lothe infinite gradient

4.2. Inclined dislocation

4.2.1. Image solution of inclined dislocation

4.2.1.1. Isotropic Devinre-Weinberger model

As shown in the flowcharts in Fig. 3.2 and Fig. 4.1, when calculating the image gradient value at given point, the corresponding bulk stress field at free surfaces should be cancelled by its corresponding image stress field.

The geometrical relation for bulk stress calculation via Devinre [Devinre, 1995] dislocation segment integration is shown in Fig.4.2, the unit vector t' is parallel to the dislocation line AB , R is the vectorial distance between a point r' of the dislocation line and an arbitrary point r at which the stress produced by the segment AB is calculated. ρ is the component of R normal to t' . Devinre's formula for isotropic stress field induced by dislocation segment t' within space can be written as:

$$\sigma_{ij}(r) = \frac{\mu}{\pi Y^2} \left[[b'Yt']_{ij}^S - \frac{1}{(1-\nu)} [b't'Y]_{ij}^S - \frac{(b',Y,t')}{2(1-\nu)} \left[\delta_{ij} + t'_i t'_j + \frac{2}{Y^2} [\rho_i Y_j + \rho_j Y_i + \frac{L'}{R} Y_i Y_j] \right] \right] \quad (4-1)$$

In which, r is the position vector of calculated point within thin TEM foil, r' is the position vector of dislocation segments, b is Burgers vector of inclined dislocation, and ν is Poisson ratio and μ is isotropic modulus of TEM thin foil material.

In the above-mentioned formulas, the following relations will apply:

$$\begin{aligned} Y^2 &= 2R(L' + R) \\ r' &= a' + l't' \\ R &= r - r' \\ L' &= R \cdot t' \\ \rho &= R - L't' \\ Y_i &= (L' + R)t_i + \rho_i \end{aligned} \quad (4-2)$$

The specific definition may be described as:

$$[abc]_{ij}^S = \frac{1}{2} ((a \times b)_i c_j + (a \times b)_j c_i) \quad (4-3)$$

The following definition will be applied:

$$\begin{aligned} (b', \rho, t') &= (b', Y, t') \\ (a, b, c) &= (a \times b) \cdot c \end{aligned} \quad (4-4)$$

Then, the stress field can be written as:

$$\sigma_{ij}^{AB}(r) = \left((\sigma_{ij}(r))_{r'=B} - (\sigma_{ij}(r))_{r'=A} \right) \quad (4-5)$$

Finally, the stress field at free surfaces can be produced.

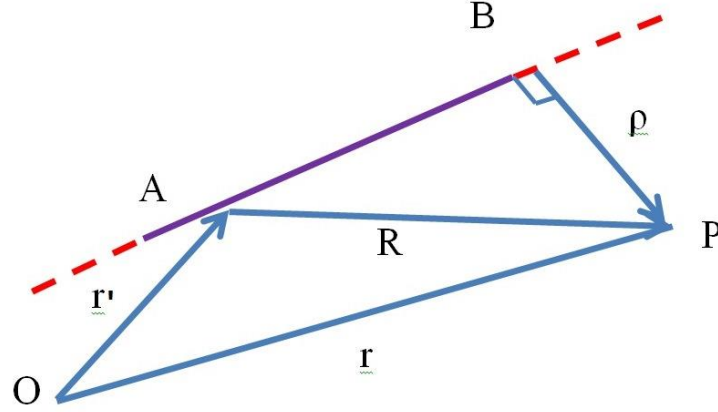


Figure 4.2: The geometrical relationship for finite (bulk) stress calculation with Devincere formula

The isotropic image stress calculation in Fourier space is described by Weinberger [Weinberger, 2009]. The details for isotropic Devincere-Weinberger model implementation into CUFOUR are described in Algorithm 4.1 of Appendix C.

4.2.1.2. Isotropic Mura-Weinberger model

As shown in the flowcharts in Fig. 3.2 and Fig. 4.1, when calculating the image gradient value at given point, the corresponding bulk stress field at free surfaces should be cancelled by its corresponding image stress field.

The stress field induced by dislocation segments in isotropic material can be produced via Mura's formula [Akarapu, 2009]. Firstly, the gradient field can be written as:

$$u_{i,j}(x) = \int \varepsilon_{jnh} C_{pqmn} G_{ip,q}(x - x') b'_m dx'_h \quad (4-6)$$

The integration is performed along inclined dislocation line within thin foil, and the virtual dislocation parts of the inclined dislocation outside thin foil. In which,

$$C_{pqmn} G_{ip,q}(x - x') = \frac{-1}{8\pi(1-\nu)} \left[\begin{aligned} &(1-2\nu) \frac{\delta_{ni}(x_m - x'_m) + \delta_{im}(x_n - x'_n) + \delta_{mn}(x_i - x'_i)}{R^3} \\ &+ 3 \frac{(x_m - x'_m)(x_n - x'_n)(x_i - x'_i)}{R^5} \end{aligned} \right] \quad (4-7)$$

$$R = |x - x'|$$

In which, the strain-gradient relation is:

$$\varepsilon_{ij} = \frac{1}{2} \cdot (u_{i,j} + u_{j,i}) \quad (4-8)$$

The isotropic stress-strain relation is:

$$\sigma_{ij} = \lambda \cdot \varepsilon_{kk} \cdot \delta_{ij} + 2\mu\varepsilon_{ij} = C_{ijkl} \cdot \varepsilon_{ij} \quad (4-9)$$

Then, the stress field at free surfaces can be produced.

The isotropic image stress calculation in Fourier space is described by Weinberger [Weinberger, 2009]. The details for isotropic Devincere-Weinberger model implementation into CUFOUR are described in Algorithm 4.2 of Appendix C.

4.2.1.3. Anisotropic Willis-Steeds-Lothe (WSL) and Wu model

As shown in the flowcharts in Fig. 3.2 and Fig. 4.1, when calculating the image gradient value at given point, the corresponding bulk stress field at free surfaces should be cancelled by its corresponding image stress field.

The bulk stress field of an anisotropic finite dislocation segment can be obtained through the Willis–Steeds–Lothe [Yin, 2010] formula:

$$\frac{\partial u_m}{\partial x_s} = \frac{1}{4\pi d} \varepsilon_{jsn} b_i C_{ijkl} t_n \{-m_l Q_{mk} + n_l [(nn)^{-1} \cdot (nm) \cdot Q]_{mk} + n_l [(nn)^{-1} \cdot S^T]_{mk}\} \Big|_{AP}^{BP} \quad (4-10)$$

where d is the shortest distance from field point P to the dislocation line pointing along t .

As shown in Fig 4.3, an infinitely long dislocation line passing through the origin along unit vector t is studied, and a local right-hand Cartesian coordinate system $m - n - t$ is employed for calculating its stress field. To obtain the stress field of this dislocation requires the solution of the following eigenvalue problem,

$$N\xi^\alpha = p_\alpha \xi^\alpha \quad (4-11)$$

Where N is a 6*6 matrix,

$$N = - \begin{bmatrix} (nn)^{-1}(nm) & (nn)^{-1} \\ (mn)(nn)^{-1}(nm) & (mn)(nn)^{-1} \end{bmatrix} \quad (4-12)$$

In which, $(mn)_{jk} = m_i C_{ijkl} n_l$ and $(mn)^{-1}$ is its inverse. The intrinsic matrix Q, B, S for anisotropic crystal is written into integral formulas format:

$$\begin{aligned} Q_{js} &= -\frac{1}{2\pi} \int_0^{2\pi} (nn)_{js}^{-1} d\omega \\ B_{ij} &= \frac{1}{2\pi} \int_0^{2\pi} \{(mm)_{ij} - (mn)_{ik} (nn)_{kp}^{-1} (nm)_{pj}\} d\omega \\ S_{ij} &= -\frac{1}{2\pi} \int_0^{2\pi} (nn)_{ik}^{-1} (nm)_{kj} d\omega \end{aligned} \quad (4-13)$$

Where ω measures the rotation angle of the local coordinate system $m - n - t$ around unit vector along dislocation line t direction.

Even though the matrix N depend on the choices of m and n , the matrices Q, B, S only depend on vector t , i.e. they are independent of m and n . This can be seen from their expressions in the integral formalism. Because all integrands have a period of π , the matrices can be rewritten as integrals from 0 to π , decreasing the domain of numerical integration.

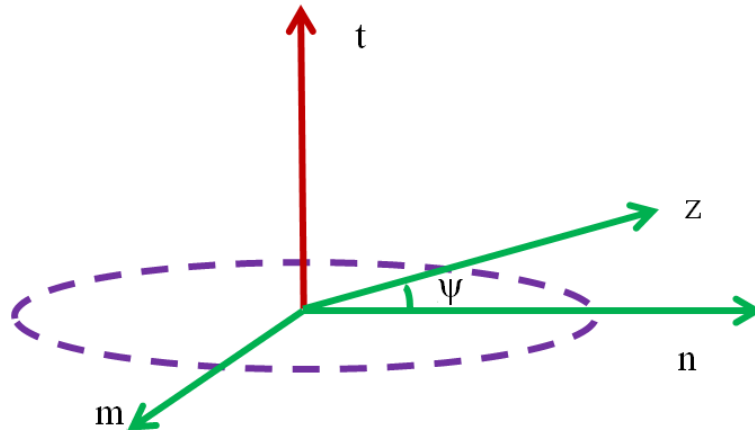


Figure 4.3: The geometrical relation around inclined dislocation for calculation

As shown in Fig.4.3, the geometric setup to derive the stress field using the Willis–Steeds–Lothe formula in the collinear case. z is an arbitrary unit vector in the $m - n$ plane at an angle ψ from n .

$$r_1 = |AP|, r_2 = |BP| \quad (4-14)$$

The displacement gradient at collinear point P is:

$$\frac{\partial u_i}{\partial x_p}(P) = \left(\frac{1}{|AP|} - \frac{1}{|BP|} \right) g_{ip}(t) \quad (4-15)$$

In which,

$$g_{ip}(t) = \frac{1}{8\pi^2} \varepsilon_{p j w} b_m C_{w m r s} t_j \int_0^{2\pi} \left(t_s (z z)_{i r}^{-1} - z_s [(z z)^{-1} ((t z) + (z t)) (z z)^{-1}]_{i r} \right) d\psi \quad (4-16)$$

In which, the strain-gradient relation is:

$$\varepsilon_{ij} = \frac{1}{2} \cdot (u_{i,j} + u_{j,i}) \quad (4-17)$$

Thus, anisotropic stress-strain relation is:

$$\sigma_{ij} = C_{ijkl} \cdot \varepsilon_{ij} \quad (4-18)$$

Then, the bulk stress field at free surfaces can be produced.

The details of anisotropic image stress calculation in Fourier space is described by Wu [Wu, 2012]. The details for anisotropic Willis-steeds-Lothe and Wu model implementation into CUFOUR are described in Algorithm 4.3 of Appendix C.

4.2.2. Bulk solution via finite dislocation segment

4.2.2.1. Isotropic Mura model

Firstly, the displacement gradient field of isotropic dislocation segment via Mura formula [Akarapu, 2009] is calculated with formulas (4-6) and (4-7). Then, the bulk gradient via Mura dislocation segment integration is performed along inclined dislocation line within thin foil.

The details for isotropic Mura model implementation into CUFOUR are described in Algorithm 4.4 of Appendix C.

4.2.2.2. Anisotropic Willis-steeds-Lothe model

Firstly, the displacement gradient field of anisotropic dislocation segment via Willis–Steeds–Lothe formula [Yin, 2010] is calculated with formulas from (4-10) to (4-16). Then, the bulk gradient via Willis–Steeds–Lothe dislocation segment integration is performed along inclined dislocation line within thin foil.

The details for anisotropic Willis–Steeds–Lothe model implementation into CUFOUR are described in Algorithm 4.5 of Appendix C.

4.2.3. Total solution, as image + bulk solutions

4.2.3.1. Isotropic Devincere-Weinberger-Mura model

The total gradient can be calculated out by adding isotropic Devincere-Weinberger model and isotropic Mura model together. Isotropic Devincere-Weinberger model is described in Part 4.2.1.1. of this chapter, and isotropic Mura model is described in Part 4.2.2.1. of this chapter. [Devincere, 1995; Akarapu, 2009; Weinberger, 2009]

The details for isotropic Devincere-Weinberger-Mura model implementation into CUFOUR are described in Algorithm 4.6 of Appendix C.

4.2.3.2. Isotropic Mura-Weinberger-Mura model

The total gradient can be calculated out by adding isotropic Mura-Weinberger model and isotropic Mura model together. Isotropic Mura-Weinberger model is described in Part 4.2.1.2. of this chapter, and isotropic Mura model is described in Part 4.2.2.1. of this chapter. [Akarapu, 2009; Weinberger, 2009]

The details for isotropic Mura-Weinberger-Mura model implementation into CUFOUR are described in Algorithm 4.7 of Appendix C.

4.2.3.3. Anisotropic WSL-Wu-WSL model

The total gradient can be calculated out by adding anisotropic WSL-Wu model and anisotropic WSL model together. Anisotropic WSL-Wu model is described in Part 4.2.1.3. of this chapter, and anisotropic WSL model is described in Part 4.2.2.2. of this chapter. [Yin, 2010; Wu, 2012]

The details for anisotropic WSL-Wu-WSL model implementation into CUFOUR are described in Algorithm 4.8 of Appendix C.

4.2.4. Bulk solution via infinite dislocation

4.2.4.1. Isotropic Hirth-Lothe model

The displacement field induced by an isotropic screw dislocation [Hirth, 1982] is:

$$u_z(x, y) = \frac{b}{2\pi} \tan^{-1} \left(\frac{y}{x} \right) \quad (4-19)$$

Then, the gradient field can be written as:

$$\frac{\partial u_z}{\partial x} = -\frac{b}{2\pi} \frac{y}{x^2+y^2} \quad (4-20)$$

and

$$\frac{\partial u_z}{\partial y} = +\frac{b}{2\pi} \frac{x}{x^2+y^2} \quad (4-21)$$

The details for isotropic Hirth-Lothe model implementation into CUFOUR are described in Algorithm 4.9 of Appendix C.

4.2.4.2. Anisotropic Stroh model

The displacement field of anisotropic dislocation [Stroh, 1958] is written as:

$$u_k = A_k f(\eta) \quad (4-22)$$

In which,

$$\eta = x_1 + p \cdot x_2 \quad (4-23)$$

Considering the equilibrium condition, the following equilibrium equations can be produced:

$$[C_{i1k1} + (C_{i1k2} + C_{i2k1}) \cdot p + C_{i2k2} \cdot p^2] \cdot A_k = 0 \quad (4-24)$$

It can be written into matrix formula,

$$a_{ik} A_k = 0 \quad (4-25)$$

In which,

$$a_{ik} = C_{i1k1} + (C_{i1k2} + C_{i2k1}) \cdot p + C_{i2k2} \cdot p^2 \quad (4-26)$$

Final, the displacement field can be written as:

$$u_k = Re \left[-\frac{1}{(2\pi i)} \sum_{n=1}^3 A_k(n) D(n) \ln \eta_n \right] \quad (4-27)$$

The gradient can be written as:

$$u_{k,l} = Re \left[-\frac{1}{(2\pi i)} \sum_{n=1}^3 A_k(n) D(n) \frac{1}{\eta_n} [\delta_{l1} + p_n \delta_{l2}] \right] \quad (4-28)$$

$$\eta_n = x_1 + p_n x_2;$$

The details for anisotropic Stroh model implementation into CUFOUR are described in Algorithm 4.10 of Appendix C.

4.3. Dislocation loop

4.3.1. Image solution

4.3.1.1. Isotropic Devincere-Weinberger model

As shown in the flowcharts in Fig. 3.2 and Fig. 4.1, when calculating the image gradient value at given point, the corresponding bulk stress field at free surfaces should be cancelled by its corresponding image stress field.

In order to implement image stress effect efficiently, isotropic dislocation loop can be segmented into many segments, and the bulk stress field at free surfaces of thin foil can be produced from Devincere dislocation segment integration [Dvincere, 1995] around dislocation loop perimeter.

The isotropic image stress calculation in Fourier space is described by Weinberger [Weinberger, 2009]. The details for isotropic Devincere-Weinberger model implementation into CUFOUR are described in Algorithm 4.11 of Appendix C.

4.3.1.2. Isotropic Mura-Weinberger model

As shown in the flowcharts in Fig. 3.2 and Fig. 4.1, when calculating the image gradient value at given point, the corresponding bulk stress field at free surfaces should be cancelled by its corresponding image stress field.

In order to implement image stress effect efficiently, isotropic dislocation loop can be segmented into many segments, and the bulk stress field can be produced from Mura dislocation segment integration [Akarapu, 2009] around dislocation loop perimeter.

The isotropic image stress calculation in Fourier space is described by Weinberger [Weinberger, 2009]. The details for isotropic Mura-Weinberger model implementation into CUFOUR are described in Algorithm 4.12 of Appendix C.

4.3.1.3. Anisotropic WSL-Wu model

As shown in the flowcharts in Fig. 3.2 and Fig. 4.1, when calculating the image gradient value at given point, the corresponding bulk stress field at free surfaces should be cancelled by its corresponding image stress field.

In order to implement image stress effect efficiently, anisotropic dislocation loop can be segmented into many segments, and the bulk stress field can be produced from Willis–Steeds–Lothe dislocation segment integration [Yin, 2010] around dislocation loop perimeter.

The anisotropic image stress calculation in Fourier space is described by Wu [Wu, 2012]. The details for anisotropic WSL-Wu model implementation into CUFOUR are described in Algorithm 4.13 of Appendix C.

4.3.1.4. Anisotropic Mura-Wu model

As shown in the flowcharts in Fig. 3.2 and Fig. 4.1, when calculating the image gradient value at given point, the corresponding bulk stress field at free surfaces should be cancelled by its corresponding image stress field.

The stress field of dislocation loop in anisotropic infinite medium can be calculated by integration of Green's function. The stress field of dislocation loop in infinite medium is described as [Mura, 1987]:

$$\sigma_{ij}(x) = C_{ijkl} \oint_{C'} \varepsilon_{lnh} C_{pqmn} G_{kp,q}(x - x') b'_m dx'_h \quad (4-29)$$

(Note. 1: Stress field components produced by closed dislocation loops C' in anisotropic crystals are represented by integral representations: where the line integral with respect to x'_h is performed along the dislocation line C' , $G_{kp,q}$ are the first derivative of Green's functions for anisotropic crystals, and the derivative of Green's function is different for different anisotropic crystal; C_{pqmn} are the elastic constants; and b'_m is the Burgers vector of dislocation loop C')

In which,

$$G_{ij,k}(x) = \frac{1}{8\pi^2 x^2} \int_{S^1} [-\bar{x}_k N_{ij}(\bar{\xi}) D^{-1}(\bar{\xi}) + \bar{\xi}_k C_{lpmq} (\bar{x}_p \bar{\xi}_q + \bar{\xi}_p \bar{x}_q) N_{li} N_{mj} D^{-2}] d\phi \quad (4-30)$$

The integration is performed in the plane normal to $x - x'$ vector for a round. x is the calculated position vector in space, x' is the dislocation loop position vector on the loop perimeter when performing integration around dislocation loop.

For cubic crystals:

$$\begin{aligned} D(\xi) &= \mu^2 \cdot (\lambda + 2\mu + \mu') \cdot \xi^6 + \mu \cdot \mu' \cdot (2\lambda + 2\mu + \mu') \cdot \xi^2 \cdot \\ &(\xi_1^2 \cdot \xi_2^2 + \xi_2^2 \cdot \xi_3^2 + \xi_3^2 \cdot \xi_1^2) + \mu'^2 \cdot (3\lambda + 3\mu + \mu') \cdot \xi_1^2 \cdot \xi_2^2 \cdot \xi_3^2 \\ N_{11}(\xi) &= \mu^2 \cdot \xi^4 + \beta \cdot \xi^2 \cdot (\xi_2^2 + \xi_3^2) + \gamma \cdot \xi_2^2 \cdot \xi_3^2 \\ N_{12}(\xi) &= -(\lambda + \mu) \cdot \xi_1 \cdot \xi_2 \cdot (\mu \cdot \xi^2 + \mu' \cdot \xi_3^2) \end{aligned} \quad (4-31)$$

And the other components are obtained by the cyclic permutation of 1, 2 and 3, where,

$$\begin{aligned} \xi^2 &= \xi_1 \cdot \xi_1 \\ \beta &= \mu \cdot (\lambda + \mu + \mu') \\ \gamma &= \mu' \cdot (2\lambda + 2\mu + \mu') \\ \lambda &= C_{12} \\ \mu &= C_{44} \\ \mu' &= C_{11} - C_{12} - 2C_{44} \end{aligned} \quad (4-32)$$

For Hexagonal crystals (transversely isotropic):

$$\begin{aligned} D(\xi) &= (\alpha' \cdot \eta^2 + \gamma \cdot \xi_3^2) \cdot \{\alpha\gamma\eta^4 + (\alpha\beta + \gamma^2 - \gamma'^2)\eta^2 \cdot \xi_3^2 + \beta\gamma \cdot \xi_3^4\} \\ &= (\alpha' \cdot \eta^2 + \gamma \cdot \xi_3^2) \cdot \{(\gamma \cdot \eta^2 + \beta \cdot \xi_3^2) \cdot (\alpha \cdot \eta^2 + \gamma \cdot \xi_3^2) - \gamma'^2 \cdot \eta^2 \cdot \xi_3^2\} \end{aligned} \quad (4-33)$$

and

$$\begin{aligned} N_{11}(\xi) &= (\alpha' \cdot \xi_1^2 + \alpha \cdot \xi_2^2 + \gamma \cdot \xi_3^2) \cdot (\gamma \cdot \eta^2 + \beta \cdot \xi_3^2) - \gamma'^2 \cdot \xi_2^2 \cdot \xi_3^2 \\ N_{12}(\xi) &= \gamma'^2 \cdot \xi_1 \cdot \xi_2 \cdot \xi_3^2 - (\alpha - \alpha') \cdot \xi_1 \cdot \xi_2 \cdot (\gamma \cdot \eta^2 + \beta \cdot \xi_3^2) \\ N_{13}(\xi) &= (\alpha - \alpha') \cdot \gamma' \cdot \xi_1 \cdot \xi_2^2 \cdot \xi_3 - \gamma' \cdot \xi_1 \cdot \xi_3 \cdot (\alpha' \cdot \xi_1^2 + \alpha \cdot \xi_2^2 + \gamma \cdot \xi_3^2) \\ N_{22}(\xi) &= (\alpha \cdot \xi_1^2 + \alpha' \cdot \xi_2^2 + \gamma \cdot \xi_3^2) \cdot (\gamma \cdot \eta^2 + \beta \cdot \xi_3^2) - \gamma'^2 \cdot \xi_1^2 \cdot \xi_3^2 \end{aligned} \quad (4-34)$$

$$N_{23}(\xi) = (\alpha - \alpha') \cdot \gamma' \cdot \xi_1^2 \cdot \xi_2 \cdot \xi_3 - \gamma' \cdot \xi_2 \cdot \xi_3 \cdot (\alpha \cdot \xi_1^2 + \alpha' \cdot \xi_2^2 + \gamma \cdot \xi_3^2)$$

$$N_{33}(\xi) = (\alpha \cdot \xi_1^2 + \alpha' \cdot \xi_2^2 + \gamma \cdot \xi_3^2) \cdot (\alpha' \cdot \xi_1^2 + \alpha \cdot \xi_2^2 + \gamma \cdot \xi_3^2)$$

$$-(\alpha - \alpha')^2 \cdot \xi_1^2 \cdot \xi_2^2$$

In which,

$$\alpha = C_{11} = C_{22}, \alpha' = C_{66} = \frac{1}{2}(C_{11} - C_{12}),$$

$$\beta = C_{33}, \gamma' - \gamma = C_{13} = C_{23}$$

$$\gamma = C_{44} = C_{55}, \eta^2 = \xi_1^2 + \xi_2^2$$

(4-35)

The anisotropic image stress calculation in Fourier space is described by Wu [Wu, 2012]. The details for anisotropic Mura-Wu model implementation into CUFOUR are described in Algorithm 4.14 of Appendix C.

4.3.2. Bulk solution

4.3.2.1. Isotropic Mura model

Firstly, the displacement gradient field of isotropic dislocation segment via Mura formula [Akarapu, 2009] is calculated with formulas (4-6) and (4-7). Then, the bulk gradient via Mura dislocation segment integration is performed along dislocation loop perimeter.

The details for isotropic Mura model implementation into CUFOUR are described in Algorithm 4.15 of Appendix C.

4.3.2.2. Anisotropic WSL model

Firstly, the displacement gradient field of anisotropic dislocation segment via Willis–Steeds–Lothe formula [Yin, 2010] is calculated with formulas from (4-10) to (4-16). Then, the bulk gradient via Willis–Steeds–Lothe dislocation segment integration is performed along dislocation loop perimeter.

The details for anisotropic WSL model implementation into CUFOUR are described in Algorithm 4.16 of Appendix C.

4.3.3. Total solution, as image + bulk solutions

4.3.3.1. Isotropic Devincere-Weinberger-Mura model

The total displacement gradient can be calculated out by adding isotropic Devincere-Weinberger model and isotropic Mura model together. Isotropic Devincere-Weinberger model is described in Part 4.3.1.1. of this chapter, and isotropic Mura model is described in Part 4.3.2.1. of this chapter [Devincere, 1995; Akarapu, 2009; Weinberger, 2009].

The details for isotropic Devincere-Weinberger-Mura model implementation into CUFOUR are described in Algorithm 4.17 of Appendix C.

4.3.3.2. Isotropic Mura-Weinberger-Mura model

The total displacement gradient can be calculated out by adding isotropic Mura-Weinberger model and isotropic Mura model together. Isotropic Mura-Weinberger model is described in Part 4.3.1.2. of this chapter, and isotropic Mura model is described in Part 4.3.2.1. of this chapter [Akarapu, 2009; Weinberger, 2009].

The details for isotropic Mura-Weinberger-Mura bulk gradient model implementation into CUFOUR are described in Algorithm 4.18 of Appendix C.

4.3.3.3. *Anisotropic WSL-Wu-WSL model*

The total displacement gradient can be calculated out by adding anisotropic WSL-Wu model and anisotropic WSL model together. Anisotropic WSL-Wu model is described in Part 4.3.1.3. of this chapter, and anisotropic WSL model is described in Part 4.3.2.3. of this chapter [Yin,2010; Wu,2012].

The details for anisotropic WSL-Wu-WSL model implementation into CUFOUR are described in Algorithm 4.19 of Appendix C.

4.3.3.4. *Anisotropic Mura-Wu-WSL model*

The total displacement gradient can be calculated out by adding anisotropic Mura-Wu model and anisotropic WSL model together. Anisotropic Mura-Wu model is described in Part 4.3.1.4. of this chapter, and anisotropic WSL model is described in Part 4.3.2.3. of this chapter [Mura,1982; Li,2008; Yin,2010; Wu,2012].

The details for anisotropic Mura-Wu-WSL model implementation into CUFOUR are described in Algorithm 4.20 of Appendix C.

4.4. *General considerations on the different models*

Some considerations are made on the different models used to describe the dislocation line and the dislocation loop. Concerning the dislocation line, models consider an infinite or a finite dislocation line. For the simulation using the infinite dislocation line, the isotropic Hirth-Lothe model and the anisotropic Stroh model are convenient for speed. One typical calculation of the present work can be calculated within less than 10 seconds.

For the simulation using the finite dislocation line, the calculation time depends on the model employed. For to anisotropy calculation, the Willis–Steeds–Lothe expression can be used, which is based on a matrix formalism. It can faster than the anisotropic Mura’s formula, which is based on double integral formalism, based on anisotropic Green’s function. As to the isotropic calculation, Devincre model is slightly faster than isotropic Mura’s model, depending on the segmentation number. The larger the number the faster Devincre’s model is.

As to the image stress model and total model, the total calculation time depends on both the dislocation segment models employed, and the image stress Fourier wave number $k_x = k_y$ and meshing density MN. With their increase, the calculation time increases fast.

From the experimental verification, we can see that anisotropy can change the contrast remarkably. Also, the image stress effect cannot be ignored, especially the contrast of the inclined dislocation tips. Our experience indicate that the anisotropic WSL-Wu-WSL total model is the closest to the experimental observation, but calculation speed is slower than with anisotropic Stroh bulk model.

Concerning the models for dislocation loops, the simulation with anisotropic WSL bulk model is slower than with isotropic Mura bulk model. As to the image stress model and total model:

The total calculation time depends also on the dislocation segment models employed, and the image stress Fourier wave number $k_x = k_y$ and meshing density MN. the calculation speed thus increases fast with their increase. For to anisotropic calculation, the Willis–Steeds–Lothe expression can be used, which is based on matrix formalism. It’s faster than anisotropic Mura’s formula, as for the inclined dislocation. Also, as to the isotropic calculation with the dislocation loop, Devincre’s model is slightly faster than isotropic Mura’s model, depending on the segmentation number.

Chapter.5: Results

In this chapter, the displacement, displacement gradient and stress field of the inclined dislocation, and the dislocation loop within half space and thin foil are shown firstly. Then, their TEM image for the thin foil simulated with CUFOUR are presented. TEM image simulations are performed mainly in Fe, but also in Cu and Mo, for there are well know detailed studies in the latter materials. They are used here as reference.

The details of many beam Schaeublin-Stadelmann equations, and dislocation and dislocation loop elastic field models employed here are described in chapter 2 and chapter 4, respectively. There are two types of cubic crystals employed for the calculation in this chapter, namely Fe and Cu. Their mechanical properties are shown in Table 5.1 and Table 5.2 respectively. The elastic constants of α -Fe single crystal are shown in Table 5.1 with their dependence on temperature.

Table 5.1: Elastic parameters of pure bcc Fe [Voigt, 1889; Reuss, 1929; Dever, 1972].

T(°C)	C11 (GPa)	C12 (GPa)	C44 (GPa)	Anisotropy ratio (-)	Voigt modulus (GPa)	Voigt Poisson ratio (-)	Reuss modulus (GPa)	Lattice Parameter (nm)
25	232.20	135.60	117.00	2.4224	89.5200	0.2735	74.5724	a=0.2866
300	214.20	132.00	111.10	2.7032	83.1000	0.2779	66.0812	
600	186.70	126.50	105.30	3.4983	75.2200	0.2809	52.6675	
900	148.60	122.20	99.00	7.4436	64.7200	0.2880	27.6734	

Table 5.2: Elastic parameters of pure fcc Cu at room temperature [Voigt, 1889; Straumanis, 1969; Ledbetter, 1974].

T(°C)	C11 (GPa)	C12 (GPa)	C44 (GPa)	Anisotropy ratio (-)	Voigt modulus (GPa)	Voigt Poisson ratio (-)	Lattice Parameter (nm)
25	169.1	122.2	75.42	3.2162	54.632	0.3249	a=0.36149

5.1. Elastic field calculation

5.1.1. Energy of dislocation loop

There are mainly two known types of dislocation loops formed in irradiated Fe-Cr alloy, namely a_0001 and $\frac{1}{2} a_0111$ dislocation loops, and one less known, the $\frac{1}{2} a_0[111](110)$ loop. The energy of dislocation loops consist of two parts, namely the elastic self-energy and the dislocation core energy. The isotropic and anisotropic self-energy of these three types of circular dislocation loop is calculated with the methods described in the part 3.5 of chapter 3. Following the treatment method of dislocation core by Aubry [Aubry, 2011], the core cut-off parameter is equal to the norm of the Burgers vector b , and a core energy per unit length of $\mu|b|^2/4\pi$ [Aubry, 2011] is added to the elastic self-energy of dislocation loops in both isotropic and anisotropic cases. For isotropic model, the value of μ in the core energy expression equals to Voigt isotropic modulus, while for anisotropic model, the value of μ in the core energy expression is chosen to be the Reuss isotropic modulus. The corresponding Voigt and Reuss isotropic moduli for bcc Fe at different temperature are shown in Table 5.1. Figs. 5.1 (a), (c) and (e) show the isotropic and anisotropic energy of a_0001, $\frac{1}{2} a_0[111](011)$ and $\frac{1}{2} a_0111$ dislocation loops at 25, 300, 600 and 900°C as a function of loop radius. Figs. 5.1 (b), (d) and (f) show the anisotropic to isotropic energy ratio in the same condition. The isotropic energy is higher than anisotropic models for all three types of dislocation loops. The ratio between anisotropic and isotropic energy of all three types of dislocation loops of the same loop radius always decrease with increasing anisotropic ratio. With the increase of temperature, the isotropic and anisotropic energy decreases in all cases. It should be noted that when loop size is relatively small, smaller than 4 to 6 nm, their dislocation core energy constitutes a remarkable share of the total energy,.

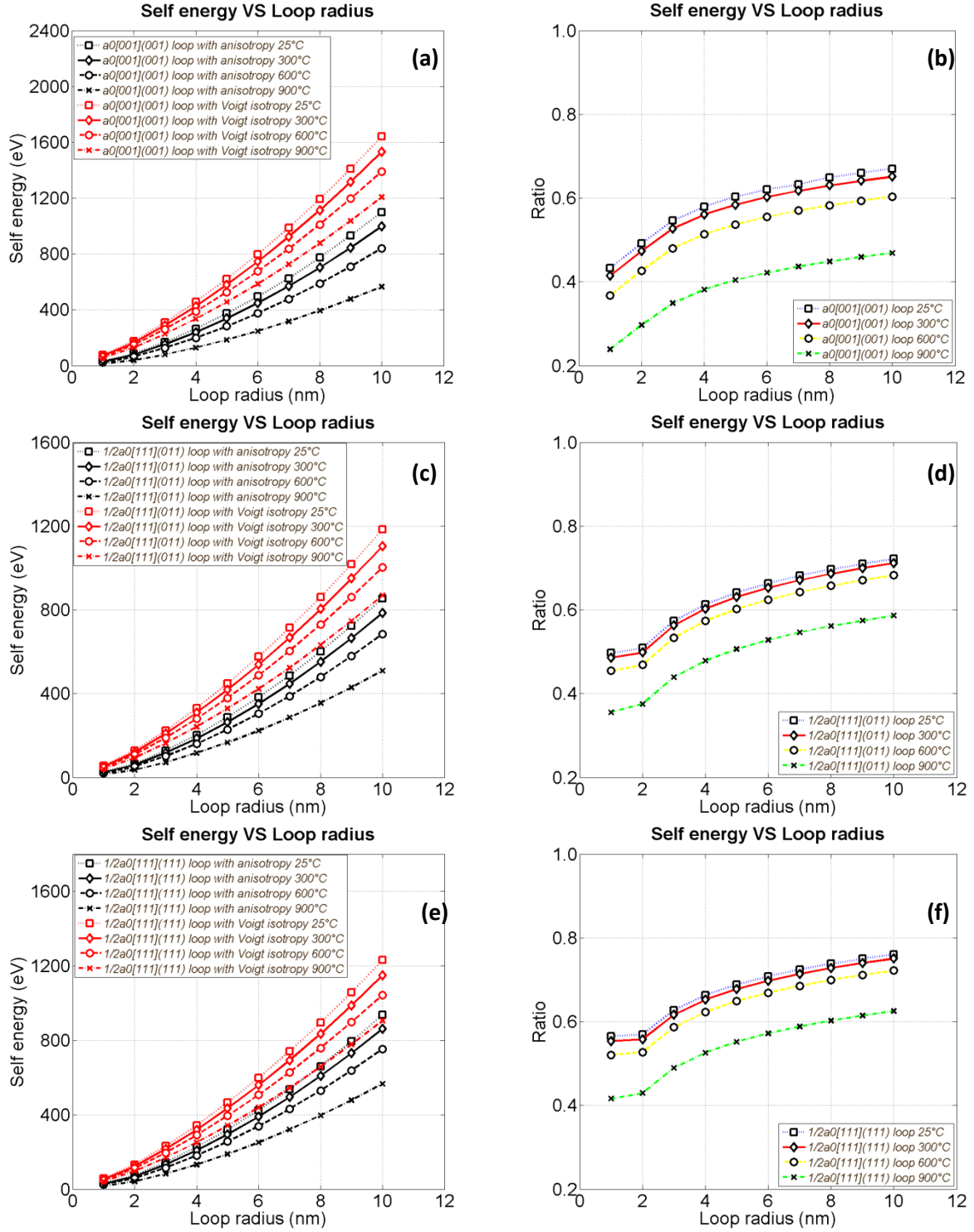


Figure 5.1: Energy of a dislocation loop in bulk material as a function of its radius at different temperatures calculated with Voigt isotropic and anisotropic models. for a_0001 loop (a), energy; (b), anisotropic to isotropic energy ratio; for $\frac{1}{2} a_0[111](011)$ loop (c), energy; (d), anisotropic to isotropic energy ratio; for $\frac{1}{2} a_0111$ loop (e), energy; (f), anisotropic to isotropic energy ratio.

5.1.2. The relative error of image stress calculation for half space and thin foil

The calculation method is optimized with respect to the number of waves and the number of meshes in Fourier space. The relative errors in the image displacement amplitude at free surface and image

energy of a dislocation loop within bcc Fe half space and thin foil are calculated with isotropic Devincere and anisotropic WSL dislocation loop models, as a function of the wave number and meshing number. They are calculated for a nanometric $\frac{1}{2} a_0111$ loop in (111) bcc Fe half space and thin foil with (x,y,z) crystallographic orientations as $[11\bar{2}]$, $[\bar{1}10]$ and $[111]$, respectively. The nanometric a_0001 loop in (001) bcc Fe half space and thin foil with (x,y,z) crystallographic orientations as $[001]$, $[010]$ and $[001]$, respectively is also considered.

Fig. 5.2 (a), (b), (c) and (d) show the relation with the meshing number or wave number of the relative error of the image energy, E_{image} , and the surface out-of-plane image displacement amplitude, $\Delta d = |\max(u_z) - \min(u_z)|$, induced by the same dislocation loop within half space or a thin foil using Voigt equivalent isotropy and anisotropy. Simulation parameters are given in Table 5.4.

Table 5.3: Simulation parameters for studying the relative error of the image energy and surface out-of-plane image displacement amplitude versus meshing number or wave number within half space or a thin foil. (PL: Periodic length in 2D space; MN: Meshing number along periodic length; WN: Wave of numbers for Fourier series; SN: Number of segments of the inclined dislocation and dislocation loop; t: Thickness of thin TEM foil; d: Depth of dislocation loop within thin TEM foil from bottom, or depth of dislocation loop under free surface of half space; R: Dislocation loop radius; T: Temperature)

Fig	Periodic Boundary condition (PBC)			Dislocation loop physical parameters				
	PL (nm)	MN	WN	SN	t (nm)	d (nm)	R (nm)	T (°C)
(a)	120	10, 20, 30, 40, 50, 60, 70, 80, 90, 100	30	40	-	25	5	25
(b)	120	10, 20, 30, 40, 50, 60, 70, 80, 90, 100	30	40	30	15	5	25
(c)	120	80	5, 10, 15, 20, 25, 30	40	-	25	5	25
(d)	120	80	5, 10, 15, 20, 25, 30	40	30	15	5	25

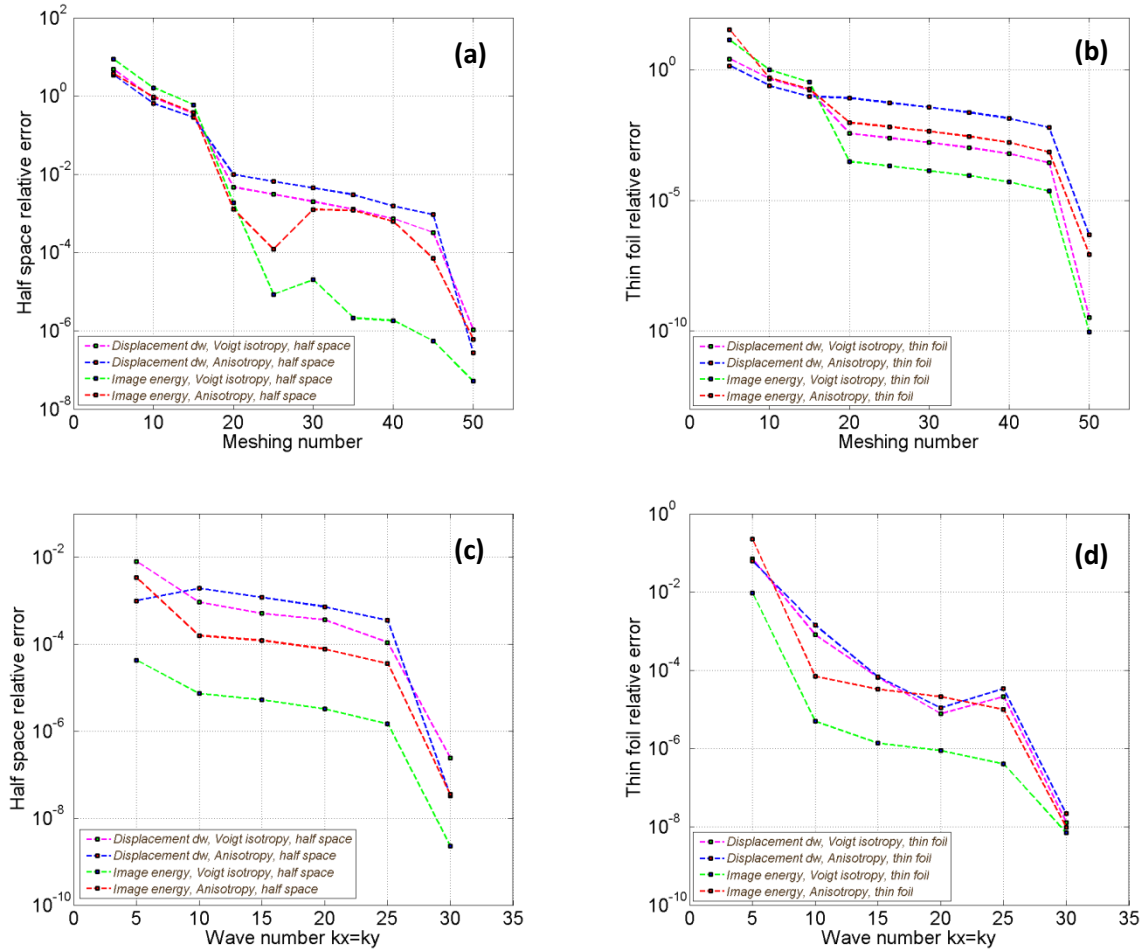


Figure 5.2: Relative errors in the calculation using Voigt isotropic and anisotropic elasticity of the image displacement and image energy of pure bcc Fe containing a nanometric a_0001 dislocation loop within anisotropic (001) half space and (001) thin film and a nanometric $\frac{1}{2}a_0111$ dislocation loop within isotropic (111) half space and (111) thin film. Relative error of, (a) the image displacement and the image energy of half space versus meshing number; (b) the image displacement and the image energy of thin foil versus meshing number; (c) the image displacement and the image energy of half space versus wave number; (d) the image displacement and the image energy of thin foil versus wave number.

All relative error results in Fig. 5.2 show convergence as the wave number or meshing number increase. The image energy calculation converges faster than the displacement convergence rate for both half space and thin foil. Voigt isotropy calculation converges faster than the anisotropy case. It appears that for free surfaces of half space and thin foil with periodic length (PL) of 120 nm, a meshing number (MN) and wave number (WN) of respectively 80 and 25 is reasonable in terms of computing time and relative error.

5.1.3. Image force for half space

5.1.3.1. Inclined dislocation

In this part, the image stress of an inclined $\frac{1}{2}a_0111$ screw dislocation within (001) bcc Fe half space is calculated with Voigt isotropic and anisotropic image stress models, with (x,y,z) crystallographic orientations as [001], [010] and [001], respectively. The simulation parameters are shown in Table 5.4, and the simulation results are shown in Fig. 5.3 and Fig. 5.4 respectively.

Table 5.4: Simulation parameters for an inclined $\frac{1}{2} a_0111$ screw dislocation within (001) bcc Fe half space.

Meshing PBC			Dislocation physical parameters		
PL (nm)	MN	WN	\mathbf{b}	\mathbf{n}_l	T (°C)
40	100	30	$\frac{1}{2} a_0[111]$	(111)	25

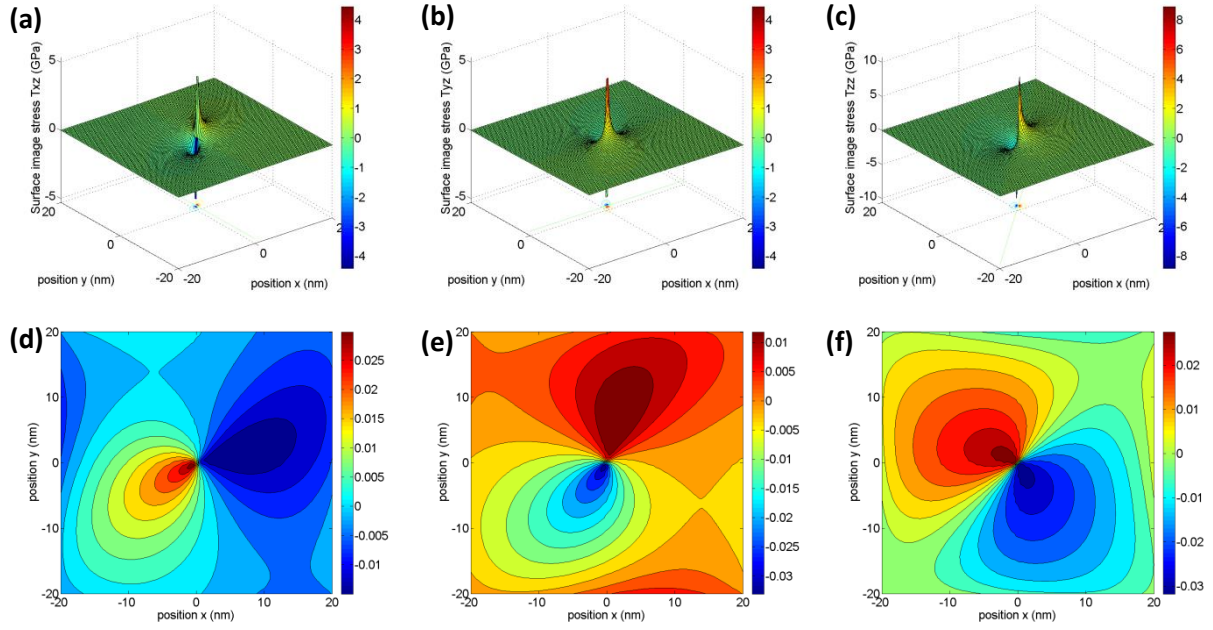


Figure 5.3: Surface image elastic field for an inclined $\frac{1}{2} a_0111$ screw dislocation within (001) bcc Fe half space, calculation with isotropic Devincere model. Image stress (a) T_{xz} ; (b) T_{yz} ; (c) T_{zz} ; Image displacement (nm) along (d) X; (e) Y; and (f) Z.

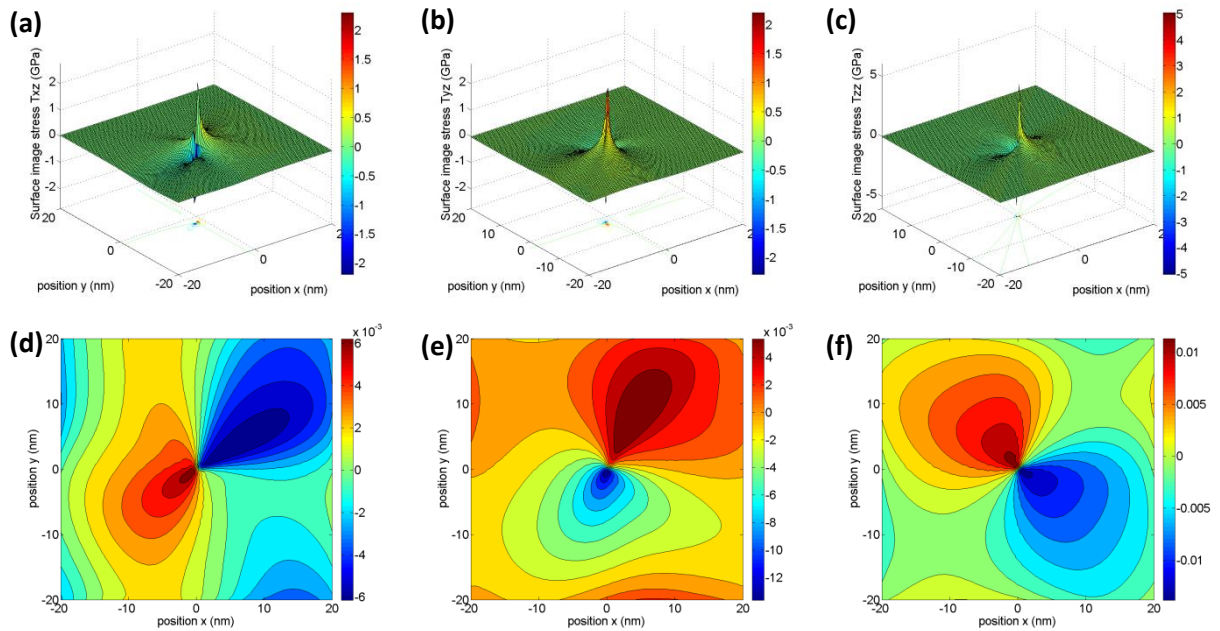


Figure 5.4: Surface image elastic field for an inclined $\frac{1}{2} a_0111$ screw dislocation within (001) bcc Fe half space, calculation with anisotropic WSL model. Image stress (a) T_{xz} ; (b) T_{yz} ; (c) T_{zz} ; Image displacement (nm) along (d) X; (e) Y; and (f) Z.

Fig. 5.3 and Fig. 5.4 show that the image stress field amplitude with isotropy is around 2 times higher than the one with anisotropy. The amplitude of the resulting out-of-plane and in plane image displacement field with isotropy is around 3 times higher than the amplitude of anisotropy, with a dependence on x, y, or z direction.

5.1.3.2. Dislocation loop

In this part, the image stress of a $\frac{1}{2} a_0111$ dislocation loop within (111) bcc Fe half space is calculated with Voigt isotropy and anisotropy image stress models, with (x,y,z) crystallographic orientations as $[11\bar{2}]$, $[\bar{1}10]$ and $[111]$, respectively. The simulation parameters are given in Table 5.5, and the simulation results are shown in Fig. 5.5 and Fig. 5.6 respectively.

Table 5.5: Simulation parameters for a $\frac{1}{2} a_0111$ dislocation loop within (111) bcc Fe half space.

PBC			Dislocation loop physical parameters					
PL (nm)	MN	WN	SN	b	n_h	d (nm)	R (nm)	T (°C)
80	80	30	40	$\frac{1}{2} a_0[111]$	(111)	10	5	25

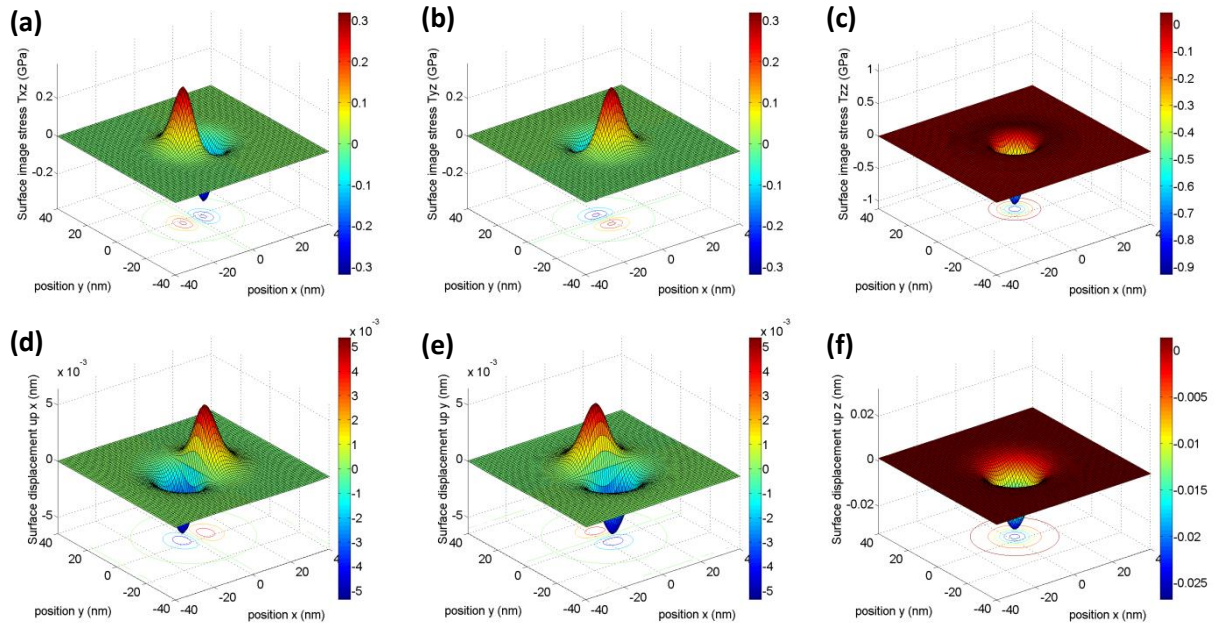


Figure 5.5: Surface elastic field of a $\frac{1}{2} a_0111$ dislocation loop within (111) bcc Fe half space, calculation with isotropic Devincere model. Image stress (a) T_{xz} ; (b) T_{yz} ; (c) T_{zz} ; Image displacement (nm) along (d) X; (e) Y; and (f) Z.

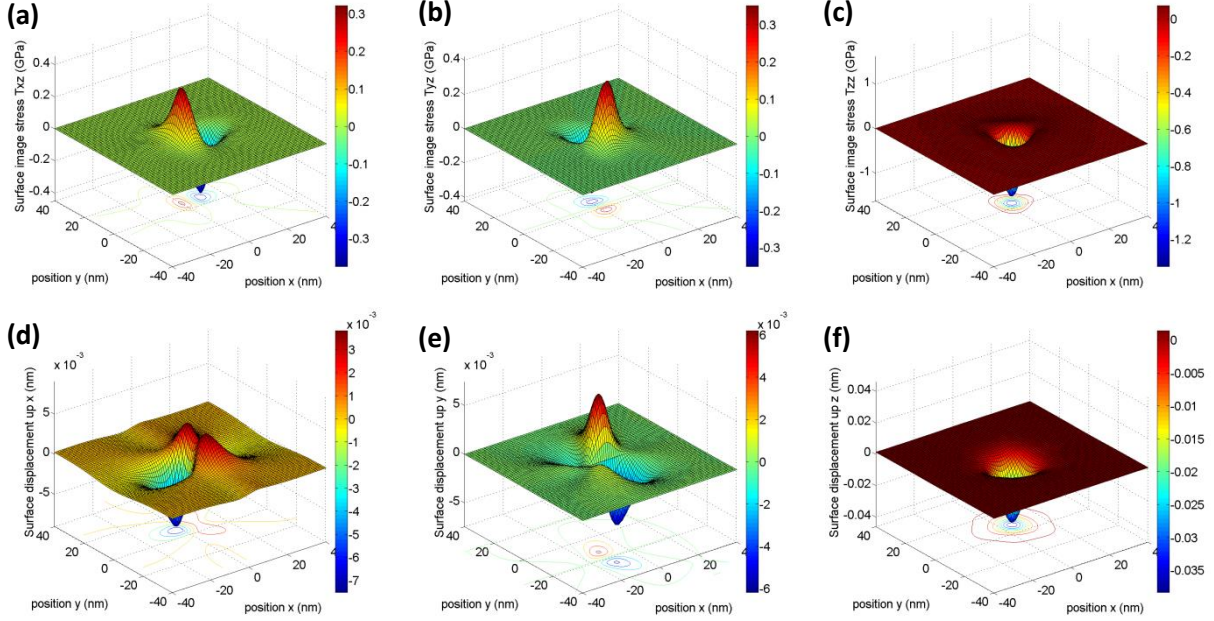


Figure 5.6: Surface elastic field of a $\frac{1}{2} a_0111$ dislocation loop within (111) bcc Fe half space, calculation with anisotropic WSL model. Image stress (a) T_{xz} ; (b) T_{yz} ; (c) T_{zz} ; Image displacement (nm) along (d) X; (e) Y; and (f) Z.

Fig. 5.5 and Fig. 5.6 show that the in plane image stress amplitude (T_{xz}, T_{yz}) is nearly the same for both isotropic and anisotropic, while the out of plane image stress field amplitude T_{zz} with anisotropy is around 1.35 times the amplitude with isotropy. The resulting in plane image displacement amplitude with isotropy is nearly the same as with anisotropy. While the displacement field essential feature is different. The out-of-plane image displacement amplitude of anisotropic calculation is around 1.35 times the amplitude of isotropic Devincere calculation case. The image displacement field also evolves, from circular to triangular shape with rounded corners.

5.1.3.3. Factors influencing the effect of dislocation loop image stress

In this part, the impact of anisotropy ratio which relates to the effect of temperature, loop depth under free surface, loop radius on the in plane and out-of-plane image displacement amplitude and image energy of a $\frac{1}{2} a_0111$ dislocation loop within (111) bcc Fe half space and an a_0001 dislocation loop within (001) bcc Fe half space is evaluated. The employed dislocation loop models are the isotropic Devincere and the anisotropic WSL ones.

In the following, the effect of the anisotropy ratio is described. The elastic modulus of bcc Fe is shown in Table 5.1. The simulation parameters are shown in Table 5.6, and the simulation results are shown in Fig. 5.7.

Table 5.6: Simulation parameters for anisotropy ratio effect of a $\frac{1}{2} a_0111$ dislocation loop within (111) bcc Fe half space and an a_0001 dislocation loop within (001) bcc Fe half space.

PBC			Dislocation loop physical parameters					
PL (nm)	MN	WN	SN	b	n_h	d (nm)	R (nm)	T (°C)
80	80	30	40	-	-	10	5	25, 300, 600, 900

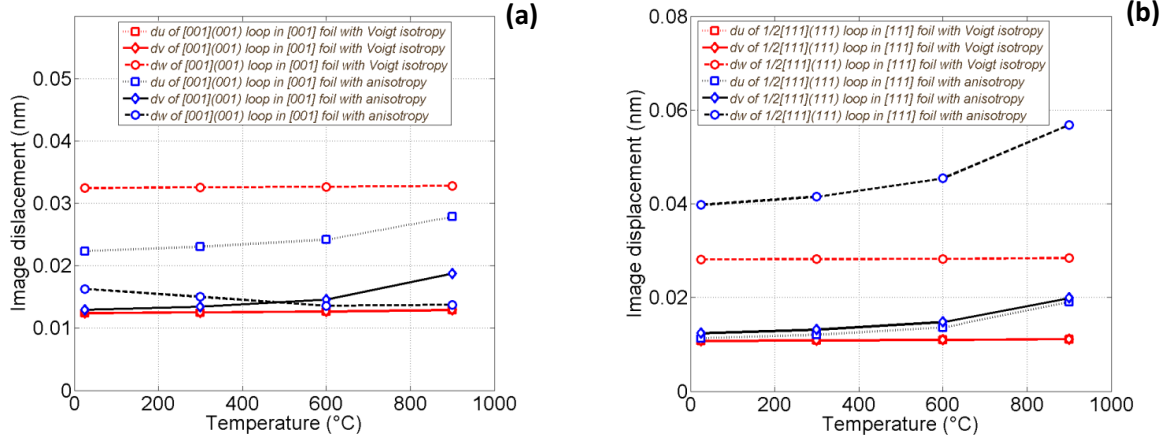


Figure 5.7: Image displacement versus temperature of (a) an a_0001 dislocation loop within (001) bcc Fe half space; and (b) a $\frac{1}{2} a_0111$ dislocation loop within (111) bcc Fe half space.

As shown in Fig. 5.7, when comparing anisotropic calculation results for a $\frac{1}{2} a_0111$ dislocation loop within (111) bcc Fe half space and an a_0001 dislocation loop within (001) bcc Fe half space, the in plane and out-of-plane image displacement amplitudes with anisotropy show increasing or decreasing trend with the increase of temperature, while the in plane and out-of-plane image displacement amplitudes with isotropy remains nearly the same. The image displacement amplitude for the a_0001 dislocation loop does not changes so much with increasing temperature, while the impact for the $\frac{1}{2} a_0111$ dislocation loop is remarkable. It is interesting to notice that the out-of-plane image displacement amplitude for a $\frac{1}{2} a_0111$ dislocation loop calculated with anisotropy is much stronger than with isotropy, while the one for a_0001 dislocation loop calculated with isotropy is larger than with anisotropy.

The effect of the dislocation loop radius effect is now described. The anisotropic image displacement field is calculated with WSL-Wu anisotropic image stress model. The simulation parameters are shown in Table 5.7, and the simulation results are shown in Fig. 5.8.

Table 5.7: Simulation parameters for studying loop radius effect of a $\frac{1}{2} a_0111$ dislocation loop within (111) bcc Fe half space and an a_0001 dislocation loop within (001) bcc Fe half space.

PBC			Dislocation loop physical parameters					
PL (nm)	MN	WN	SN	d (nm)	b	n_h	R (nm)	T (°C)
80	80	30	40	10	-	-	1,2,3,4,5,6,7,8,9,10, 11	25°C

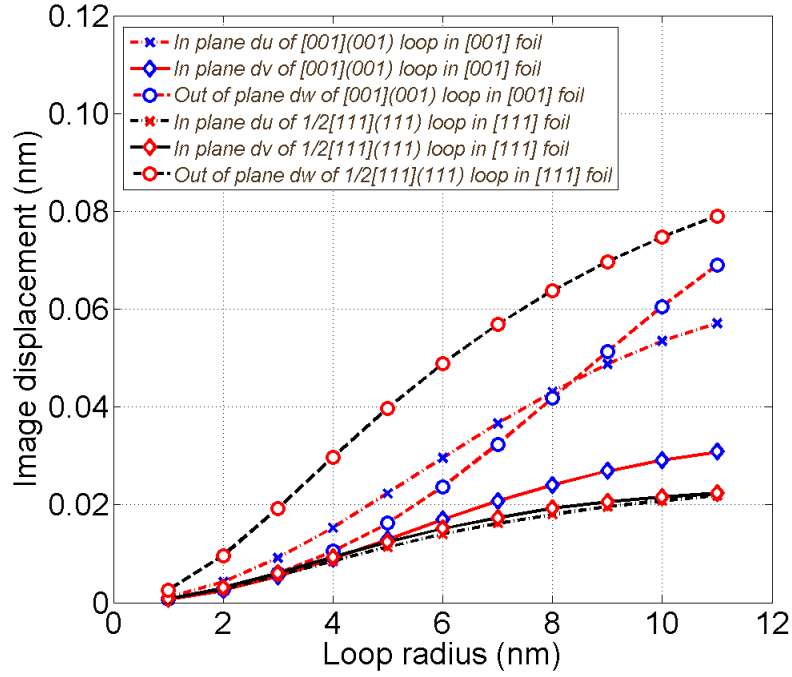


Figure 5.8: Image force induced surface displacement as a function of loop radius of a $\frac{1}{2} a_0111$ dislocation loop within (111) bcc Fe half space and an a_0001 dislocation loop within (001) bcc Fe half space, calculated with anisotropic WSL dislocation loop model. Loop depth is 10 nm.

Fig. 5.8 shows that when loop radius is smaller than 4 to 5 nm, the in-plane image displacement amplitude for the $\frac{1}{2} a_0111$ dislocation loop within (111) bcc Fe half space and for the a_0001 dislocation loop within (001) bcc Fe half space calculated with anisotropic WSL model are nearly the same. However, when loop size is larger than 4 to 5 nm, the in plane image displacement amplitude for the a_0001 dislocation loop increases sharply with loop radius, and is much larger than for the $\frac{1}{2} a_0111$ dislocation loop of the same size. While the out-of-plane image displacement amplitude for the a_0001 dislocation loop is always smaller than for the $\frac{1}{2} a_0111$ dislocation loop. In other words, with the increase of loop radius, the out-of-plane image displacement amplitude for the $\frac{1}{2} a_0111$ dislocation loop within (111) bcc Fe half space is always larger than for the corresponding a_0001 dislocation loop of the same size within (001) bcc Fe half space, but their difference decreases. Conversely, the in plane image displacement for the a_0001 dislocation loop within (001) bcc Fe half space is larger than for the corresponding $\frac{1}{2} a_0111$ dislocation loop of the same size within (111) bcc Fe half space, when loop radius is relatively large.

In the following, the effect of the dislocation loop depth is described. The anisotropic image displacement field is calculated with WSL-Wu anisotropic image stress model. The simulation parameters are shown in Table 5.8, and the simulation results are shown in Fig. 5.9.

Table 5.8: Simulation parameters for studying loop depth effect of a $\frac{1}{2} a_0111$ dislocation loop within (111) bcc Fe half space and an a_0001 dislocation loop within (001) bcc Fe half space.

PBC			Dislocation loop physical parameters					
PL (nm)	MN	WN	SN	b	n_h	d (nm)	R (nm)	T (°C)
40,60,80,100,120	80,100	30	40	-	-	5,10,15,20,25	5	25°C

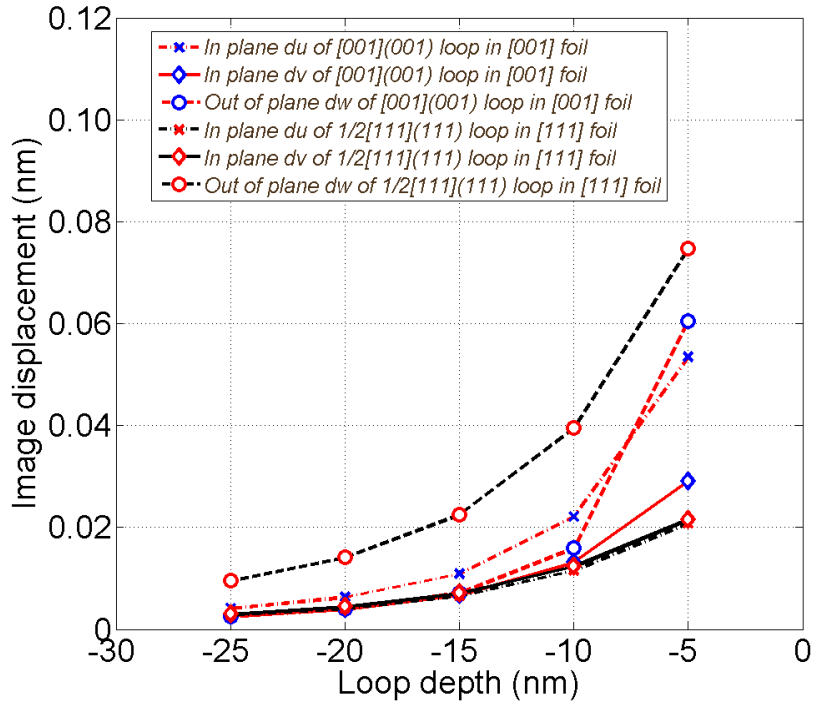


Figure 5.9: Simulation results for studying loop depth effect of a $\frac{1}{2} a_0111$ dislocation loop within (111) bcc Fe half space and an a_0001 dislocation loop within (001) bcc Fe half space, calculated with anisotropic WSL dislocation loop model. Loop radius is 5 nm.

As shown in Fig. 5.9, the in plane and out-of-plane image displacement amplitudes for both dislocation loops decrease with the increase of loop depth. However, with the increase of loop depth, the in plane and out-of-plane image displacement amplitude for a_0001 dislocation loop decreases more steeply than for the $\frac{1}{2} a_0111$ dislocation loop within (111) bcc Fe half space. In summary, the out of plane image displacement amplitude of $\frac{1}{2} a_0111$ dislocation loop is larger than for the corresponding a_0001 dislocation loop, and decreases slowly with the increase of loop depth. Conversely, the in plane image displacement amplitude for the a_0001 dislocation loop is stronger than for the corresponding $\frac{1}{2} a_0111$ dislocation loop when relatively close to free surface, but decreases rapidly with increasing loop depth. It remains then nearly of the same amplitude, as for the corresponding $\frac{1}{2} a_0111$ dislocation loop.

It can be concluded from the calculation results regarding the impact of temperature, loop radius, and loop depth on the image displacement of $\frac{1}{2} a_0111$ dislocation loop within (111) bcc Fe half space and a_0001 dislocation loop within (001) bcc Fe half space that (1) the out-of-plane image displacement is more important than in plane image displacement for $\frac{1}{2} a_0111$ dislocation loop within (111) bcc Fe half space, and (2) the in plane image displacement is more important than out-of-plane image displacement for a_0001 dislocation loop within (001) bcc Fe half space.

5.1.4. Image force for thin foil

5.1.4.1. Inclined dislocation

The thin foil relates to the TEM thin foil, and for the purpose of the TEM image simulation we remind here that it is the displacement gradient that is considered, because it is the input for CUFOUR code.

In this subsection, the image stress induced displacement gradient fields are calculated, with a study of the difference between Voigt isotropic method and anisotropic method for a $\frac{1}{2} a_0111$ inclined screw dislocation within (001) bcc Fe thin foil. The isotropic and anisotropic image

displacement gradient field is calculated respectively from Devincire-Weinberger isotropic image stress and WSL-Wu anisotropic image stress models in Fourier space. The simulation parameters are shown in Table 5.9, and the simulated results are shown in Fig. 5.10 and Fig. 5.11 respectively.

Table 5.9: Simulation parameters for a $\frac{1}{2} a_0111$ inclined dislocation within (001) bcc Fe thin foil.

PBC			Dislocation physical parameters				
PL (nm)	MN	WN	SN	t (nm)	b	n_l	T (°C)
60	120	30	10	30	$\frac{1}{2} a_0[111]$	[111]	25

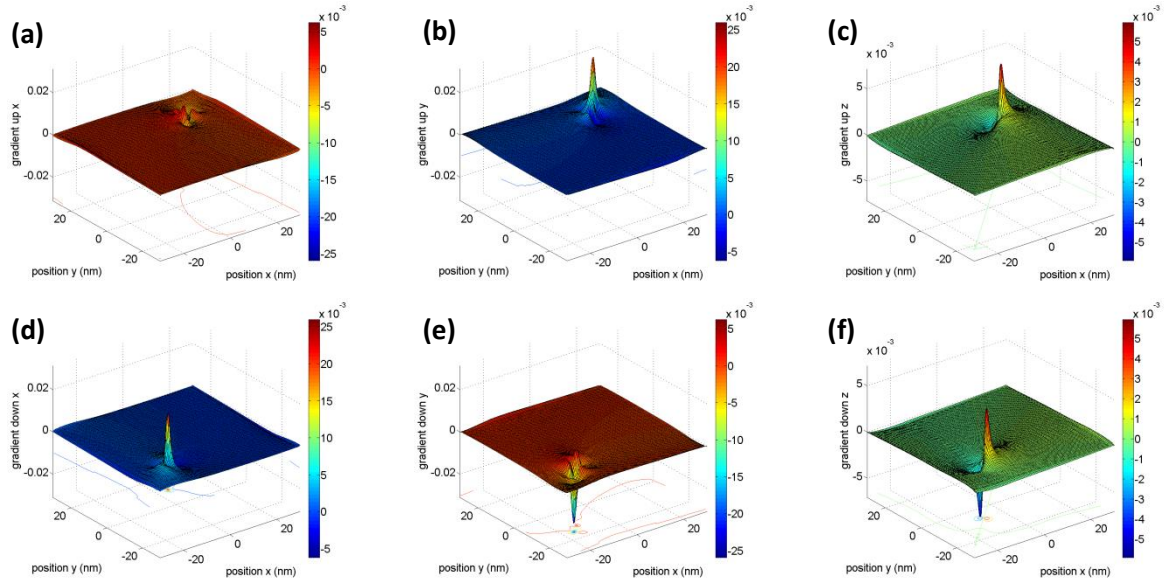


Figure 5.10: Image force induced displacement gradient for a $\frac{1}{2} a_0111$ inclined screw dislocation within (001) bcc Fe thin foil via isotropic Devincire model in the upper surface (a), (du/dz); (b), (dv/dz); (c), (dw/dz); and lower surface (d), (du/dz); (e), (dv/dz); (f), (dw/dz).

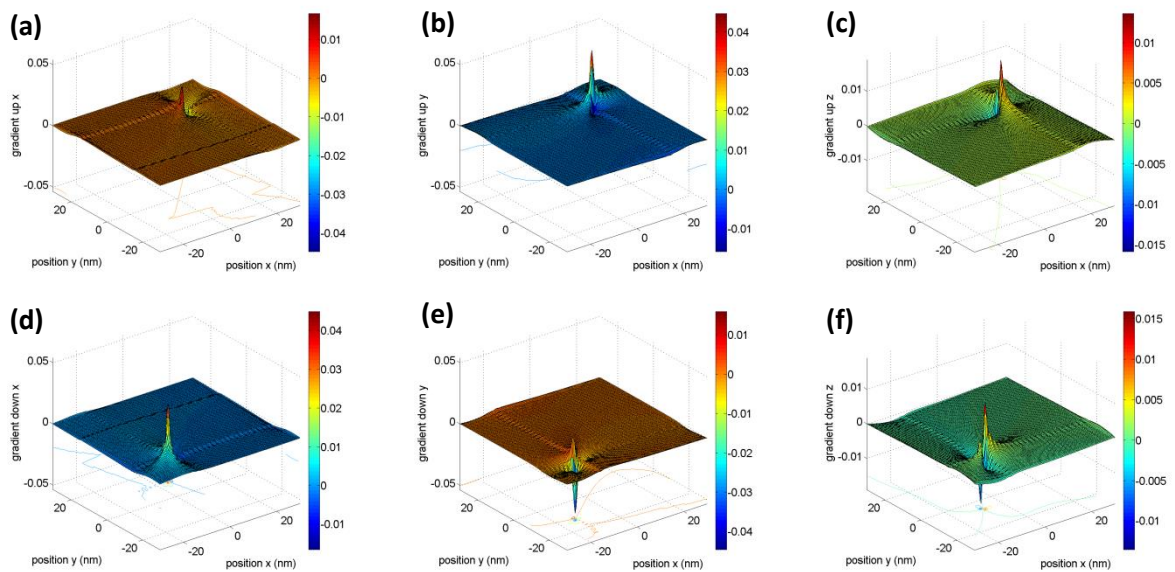


Figure 5.11: Image force induced displacement gradient for a $\frac{1}{2} a_0111$ inclined screw dislocation within (001) bcc Fe thin foil via anisotropic WSL model in the upper surface (a), (du/dz); (b), (dv/dz); (c), (dw/dz); and lower surface (d), (du/dz); (e), (dv/dz); (f), (dw/dz).

It appears in Fig. 5.10 and Fig. 5.11 that (1) the image gradient amplitude of a $\frac{1}{2} a_0111$ inclined screw dislocation with anisotropy is stronger than the corresponding image displacement gradient amplitude with isotropy, and (2) the image gradient via anisotropy shows stronger asymmetrical properties than with isotropy.

5.1.4.2. Dislocation loop

In this subsection, a prismatic $\frac{1}{2} a_0111$ dislocation loop situated in the middle of a (111) bcc Fe thin foil is employed to study the image displacement field difference with Voigt isotropic and anisotropic models. The crystallographic orientations are: $[11\bar{2}]$, $[\bar{1}10]$ and $[111]$ respectively. The isotropic and anisotropic image displacement field is calculated respectively with Devincre-Weinberger isotropic image stress and WSL-Wu anisotropic image stress models in Fourier space. The simulation parameters are shown in Table 5.10, and the corresponding image stress and image displacement field are shown in Fig. 5.12 and Fig. 5.13 respectively.

Table 5.10: Simulation parameters for a $\frac{1}{2} a_0(111)[111]$ dislocation loop within (111) thin foil.

PBC			Dislocation loop physical parameters						
PL (nm)	MN	WN	SN	t (nm)	b	n_h	d (nm)	R (nm)	T (°C)
120	80	30	40	28	$\frac{1}{2} a_0[111]$	[111]	14	3.0	25

Fig. 5.12 shows the isotropic image stress as induced in-plane and out-of-plane displacement fields, and Fig. 5.13 shows the anisotropic case.

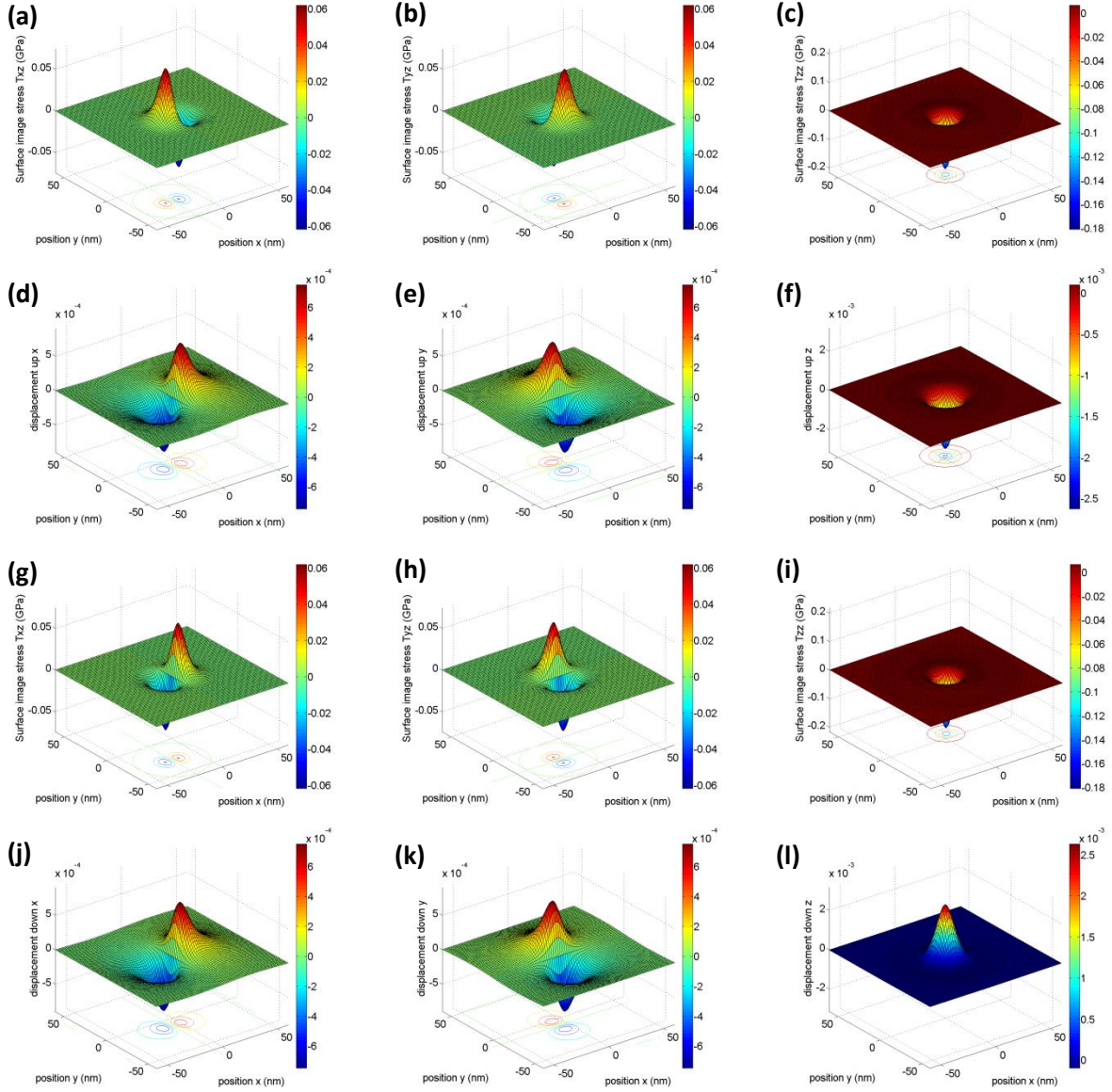


Figure 5.12: Image force induced in plane and out-of-plane displacement fields for a $\frac{1}{2} a_0111$ loop within (111) bcc Fe isotropic thin foil, calculated with isotropic Devincere dislocation model. Upper surface image stress (a), T_{xz} ; (b), T_{yz} ; (c), T_{zz} ; Upper surface image displacement (a) du (nm); (e), dv (nm); (f), dw (nm); Lower surface image stress (g), T_{xz} ; (h), T_{yz} ; (i), T_{zz} ; Lower surface image displacement (j), du (nm); (k), dv (nm); (l), dw (nm).

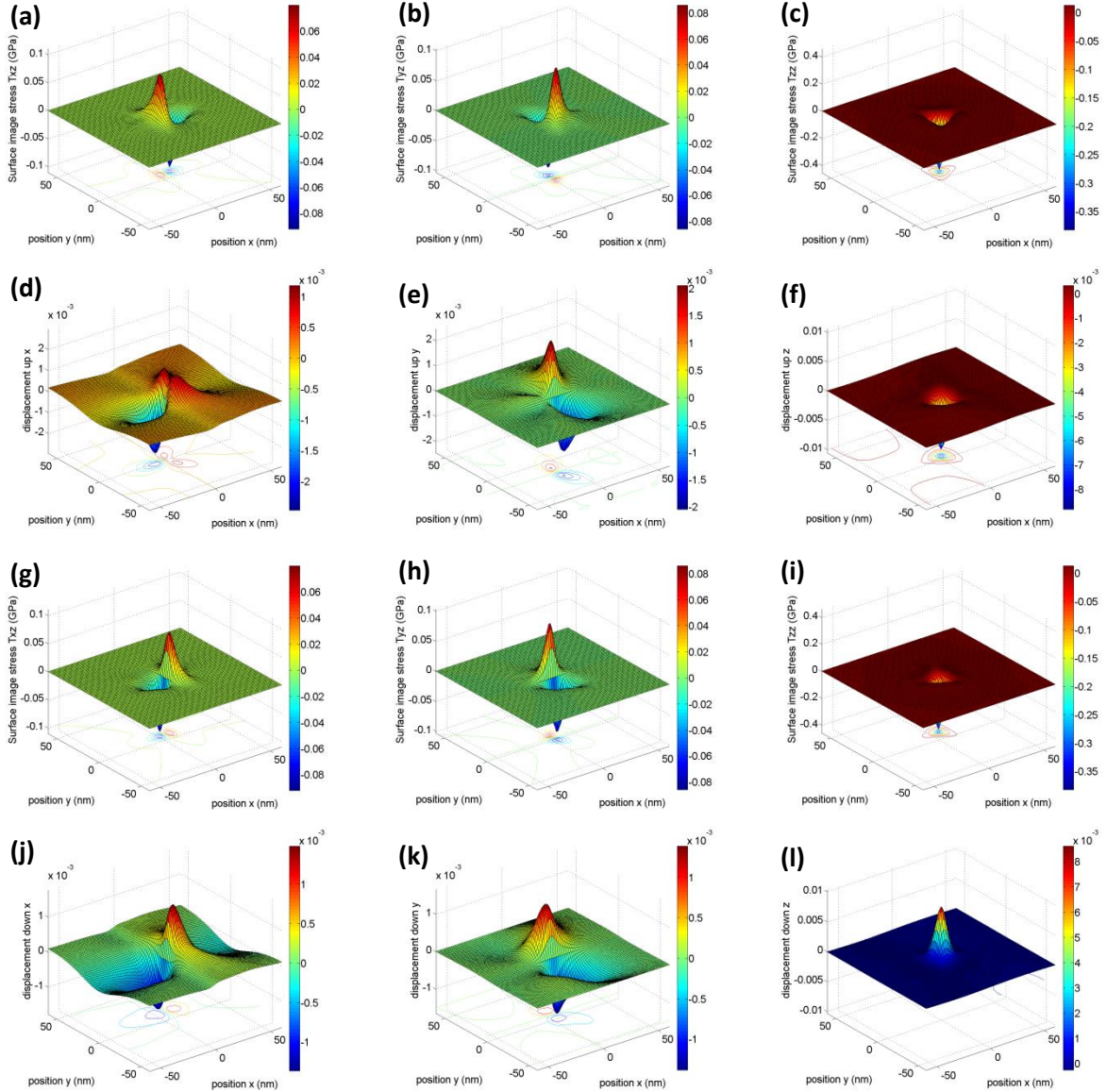


Figure 5.13: Image force induced in plane and out-of-plane displacement fields for a $\frac{1}{2} a_0111$ loop within (111) bcc Fe anisotropic thin foil, calculated with anisotropic WSL dislocation model. Upper surface image stress (a), T_{xz} ; (b), T_{yz} ; (c), T_{zz} ; Upper surface image displacement (a) du (nm); (e), dv (nm); (f), dw (nm); Lower surface image stress (g), T_{xz} ; (h), T_{yz} ; (i), T_{zz} ; Lower surface image displacement (j), du (nm); (k), dv (nm); (l), dw (nm).

It can be concluded from the calculation results shown in Fig. 5.12 and Fig.5.13 that a stronger image stress induced in plane and out-of-plane image displacement amplitude is produced with anisotropy, relative to the amplitude calculated by Voigt isotropy. Especially, the out of plane image displacement amplitude with anisotropy is several times the amplitude of the isotropic calculation case. The image displacement field characteristic features with anisotropy model are quite different from Voigt isotropic model. In effect, the image displacement field evolves from a circular to a triangular shape with rounded corners. It can be concluded that anisotropy cannot be neglected when calculating the image stress of dislocation loops within anisotropic bcc Fe thin foil.

5.1.4.3. Comparison between bulk, image and total displacement field

In order to study the impact of anisotropic image stress on the displacement field of dislocation loops within a thin foil, a prismatic $\frac{1}{2} a_0111$ dislocation loop situated in the middle of (111) bcc Fe thin foil and a prismatic a_0001 dislocation loop situated in the middle of (001) bcc Fe thin foil are employed. The corresponding anisotropic bulk displacement and image displacement field are shown in Fig. 5.14 and Fig. 5.15, respectively. The anisotropic bulk displacement is calculated with Mura area integration described in chapter.3, and the anisotropic image displacement field is calculated with WSL-Wu anisotropic image stress method in Fourier space as described in chapter 3 as well. The simulation parameters are shown in Table 5.11, and the simulated results are shown in Fig. 5.14 and Fig. 5.15 respectively.

Table 5.11: Simulation parameters for studying the impact of image stress effect on the modification of the bulk displacement field for a prismatic $\frac{1}{2} a_0111$ dislocation loop situated in the middle of (111) bcc Fe a thin foil of 30.0 nm thickness and a prismatic a_0001 dislocation loop situated in the middle of (001) bcc Fe thin foil, 30.0 nm thick.

PBC			Dislocation loop physical parameters				
PL (nm)	MN	WN	SN	t (nm)	d (nm)	R (nm)	T (°C)
80	80	30	40	30	15	5.0	25

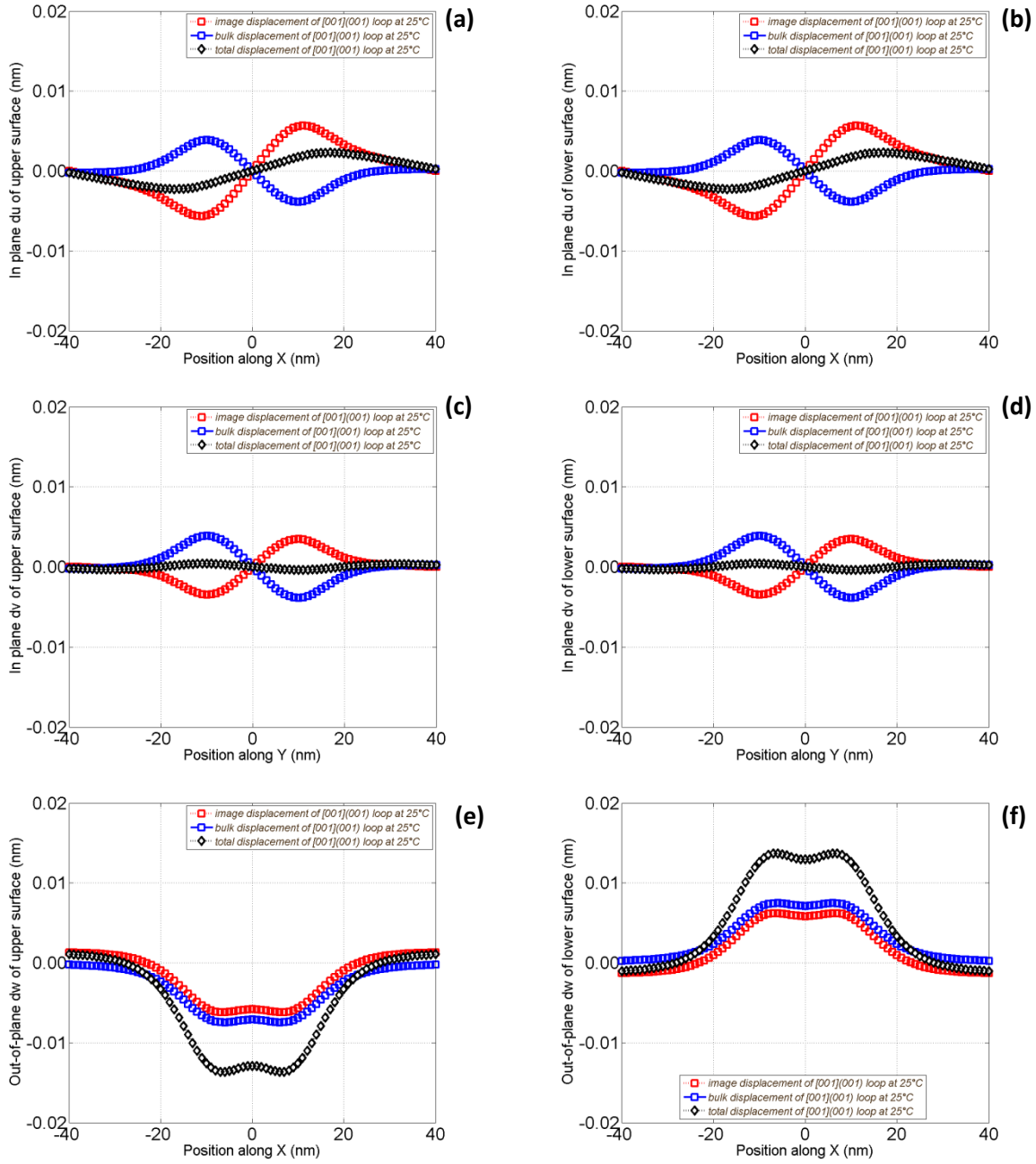


Figure 5.14: Bulk, image and total displacement fields for a prismatic a_0001 dislocation loop situated in the middle of a (001) bcc Fe thin foil, 30.0 nm thick. In plane displacement du of (a), upper surface; (b), lower surface; In plane displacement dv of (c), upper surface; (d), lower surface; Out-of-plane displacement dw of (e), upper surface; (f), lower surface.

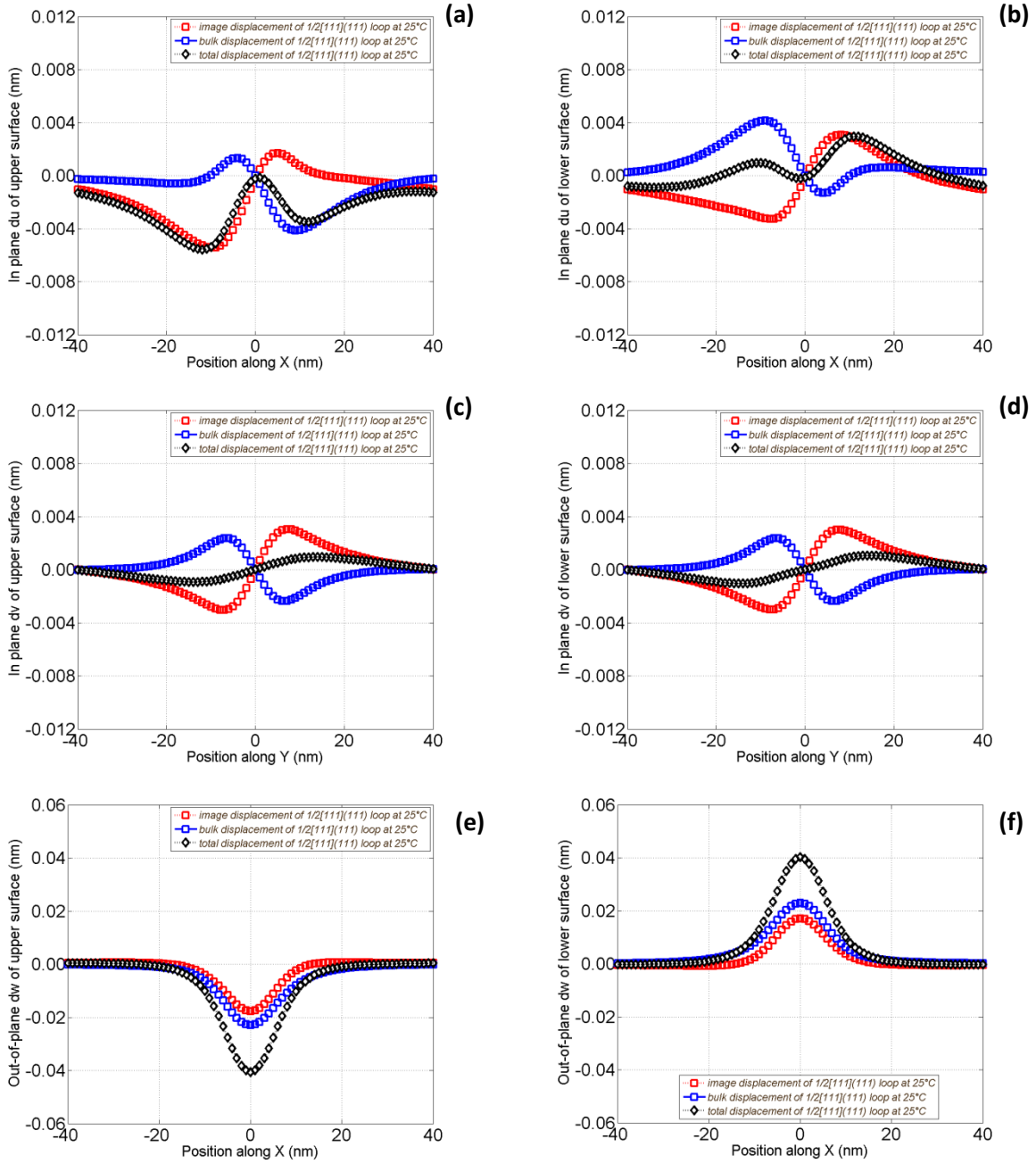


Figure 5.15: Bulk, image stress and total displacement field for a prismatic $\frac{1}{2} a_0111$ dislocation loop situated in the middle of a (111) bcc Fe thin foil, 30.0 nm thick. In plane displacement du of (a), upper surface; (b), lower surface; In plane displacement dv of (c), upper surface; (d), lower surface; Out-of-plane displacement dw of (e), upper surface; (f), lower surface.

It is shown in Fig. 5.14 and Fig. 5.15 that the bulk displacement amplitude is comparable to the corresponding image displacement amplitude, with a dependence on foil orientation and dislocation loop properties. The out-of-plane bulk displacement field is strengthened remarkably. A $\frac{1}{2} a_0111$ dislocation loop within (111) bcc Fe thin foil shows strongest out-of-plane image displacement amplitude, while an a_0001 dislocation loop within (001) bcc Fe thin foil shows weaker out-of-plane displacement. As to the in plane bulk displacement field, it is remarkable to notice that the impact of image stress is to cancel it, thus recovering the distorted lattice in the plane parallel to the free surfaces of the thin foil.

5.1.4.4. Factors influencing thin foil effect

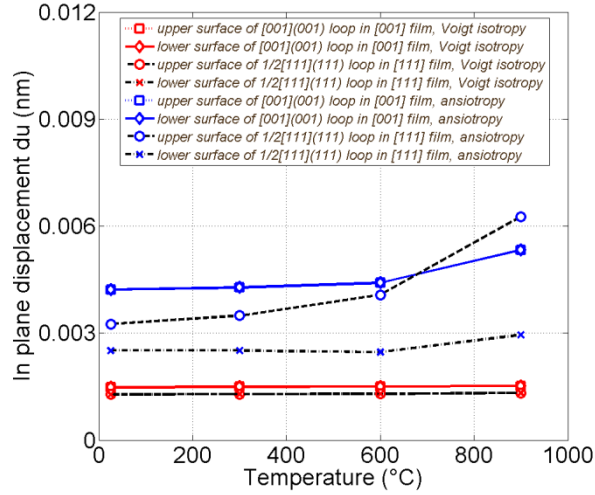
As shown in Figs. 5.12, 5.13, 5.14, and Fig. 5.15, the difference between isotropic and anisotropic image stress effect is remarkable, with a dependence on the orientation of bcc Fe thin foil, anisotropy ratio and dislocation loop type.

In the following the effect of the anisotropy ratio on the image stress induced displacement is studied. The elastic modulus of bcc Fe for the calculation is chosen from Table 5.1. The isotropic and anisotropic image displacement field is calculated from Devincere-Weinberger isotropic image stress and WSL-Wu anisotropic image stress models in Fourier space respectively. The simulation parameters are shown in Table 5.12, and the simulation results are shown in Fig. 5.16.

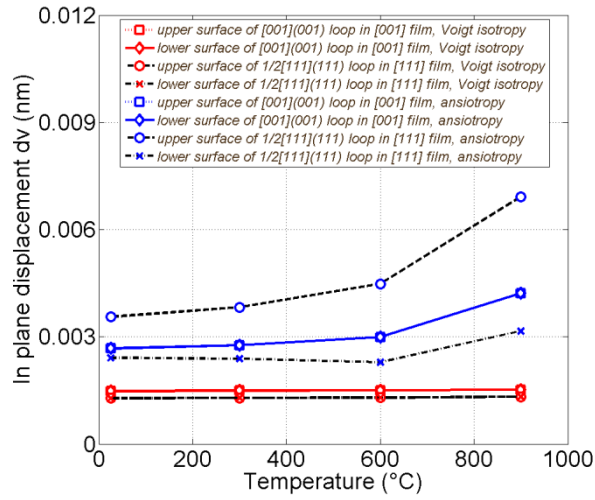
Table 5.12: Simulation parameters for a prismatic $\frac{1}{2} a_0111$ dislocation loop situated in the middle of (111) bcc Fe thin foil of 50.0 nm thickness and for a prismatic a_0001 dislocation loop situated in the middle of (001) bcc Fe thin foil, 50.0 nm thick.

PBC			Dislocation loop physical parameters				
PL (nm)	MN	WN	SN	t (nm)	d (nm)	R (nm)	T (°C)
120	100	30	40	50	25	5.0	25, 300, 600, 900

(a)



(b)



(c)

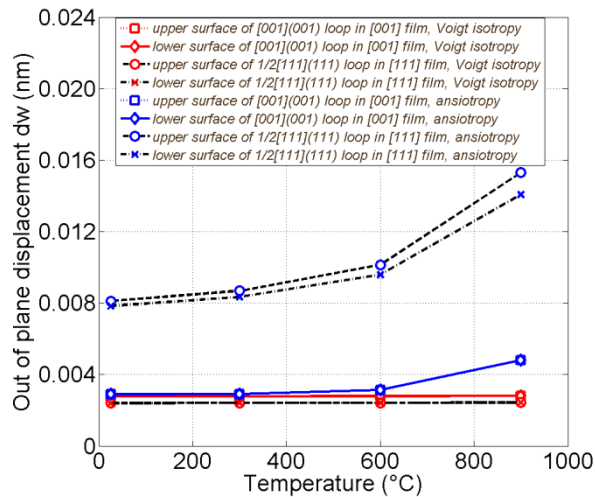


Figure 5.16: Temperature dependence of the image force induced displacement for a prismatic $1/2 a_0111$ dislocation loop situated in the middle of (111) bcc Fe thin foil, 50.0 nm thick, and for a prismatic a_0001 dislocation loop situated in the middle of a (001) bcc Fe thin foil, 50.0 nm thick, calculated with isotropic Devincere and anisotropic WSL dislocation loop model. In plane image displacement (a), du ; and (b), dv ; and out-of-plane image displacement (c), dw .

It is shown in Fig. 5.16 that the in plane and out-of-plane displacements with Voigt isotropy show little change with temperature for both dislocation loops. However, both the in plane and out-of-plane image displacement fields with anisotropy show increasing trends with temperature. The upper and lower free surfaces show the same displacement field feature and magnitude for the a_0001 dislocation loop, while the upper surface for the $\frac{1}{2} a_0111$ dislocation loop shows stronger displacement magnitude than the lower surface. The in-plane displacement magnitude for $\frac{1}{2} a_0111$ dislocation loop is nearly the same as for a_0001 dislocation loop, depending on upper or lower surface, and temperature. Conversely, the out-of-plane displacement magnitude for $\frac{1}{2} a_0111$ dislocation loop is always several times larger than for a_0001 dislocation loop.

In the following the effect of dislocation loop radius on the image stress induced displacement field is presented. The anisotropic image displacement field is calculated with WSL-Wu anisotropic image stress models in Fourier space. The elastic modulus of bcc Fe for the calculation is chosen from Table 5.1. The simulation parameters are shown in Table 5.13, and the simulation results are shown in Fig. 5.17.

Table 5.13: Simulation parameters for a prismatic $\frac{1}{2} a_0111$ dislocation loop situated in the middle of (111) bcc Fe thin foil of 50.0 nm thickness and for a prismatic a_0001 dislocation loop situated in the middle of (001) bcc Fe thin foil, 50.0 nm thick, calculated with anisotropic WSL dislocation loop formula.

PBC			Dislocation loop physical parameters				
PL (nm)	MN	WN	SN	t (nm)	d (nm)	R (nm)	T (°C)
120	100	30	40	50	25	2, 4, 6, 8, 10	25

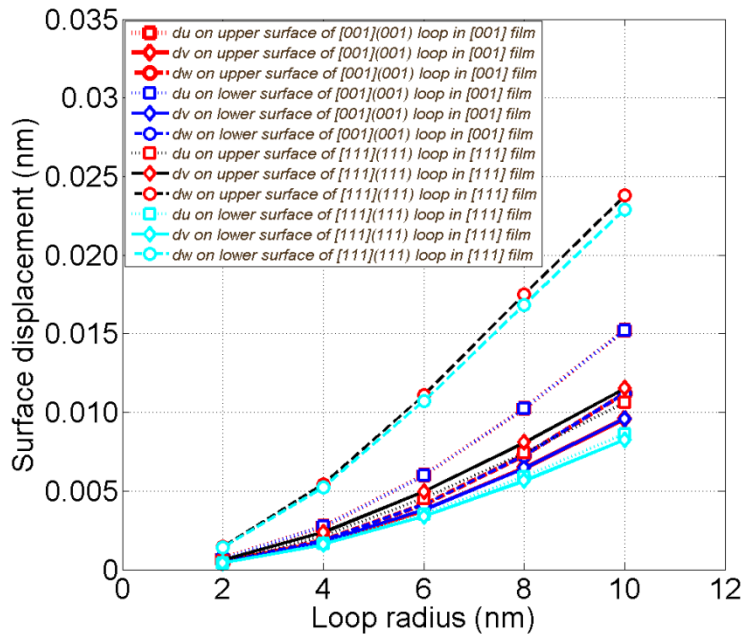


Figure 5.17: Dislocation loop radius effect on the image force induced surface displacement for a prismatic $\frac{1}{2} a_0111$ dislocation loop situated in the middle of (111) bcc Fe thin foil, 50.0 nm thick, and for a prismatic a_0001 dislocation loop situated in the middle of (001) bcc Fe thin foil of 50.0 nm thickness, calculated with anisotropic WSL dislocation loop formula.

As shown in Fig. 5.17, the in-plane image displacement amplitude for a_0001 dislocation loop is nearly the same as $\frac{1}{2} a_0111$ dislocation loops, while the out-of-plane image displacement

amplitude for a_0001 dislocation loop is smaller than for the $\frac{1}{2} a_0111$ dislocation loop of the same size. In other words, with the increase of loop radius, the $\frac{1}{2} a_0111$ dislocation loop within (111) foil shows the largest out-of-plane image displacement amplitude, while a_0001 dislocation loop within (001) foil shows remarkable in-plane image displacement. As shown in Fig. 5.14 and Fig. 5.15, the corresponding out-of-plane image displacement of upper and lower surfaces for a_0001 dislocation loop in (001) foils shows symmetrical properties. However, for $\frac{1}{2} a_0111$ dislocation within (111) thin foil, the corresponding out-of-plane image displacement at upper and lower surfaces within (111) foil still loses symmetrical properties, the image displacement amplitude on the upper surface is a little stronger than on the lower surface.

In the following the effect of dislocation loop depth on the image induced displacement field is presented. A $\frac{1}{2} a_0111$ dislocation loop within (111) thin foil and an a_0001 dislocation loop within (001) thin foil with dislocation loop radius 1.0 and 5.0 nm respectively are employed for the calculation. The simulation parameters are shown in Table 5.14, and the simulated results are shown in Fig. 5.18 and 5.19 respectively.

Table 5.14: Simulation parameters for a $\frac{1}{2} a_0111$ dislocation loop within (111) thin foil and for an a_0001 dislocation loop within (001) thin foil.

PBC			Dislocation loop physical parameters				
PL (nm)	MN	WN	SN	t (nm)	d (nm)	R (nm)	T (°C)
20, 40, 80, 120, 150, 200	80	30	40	50	2, 5, 10, 15, 20, 25, 30, 35, 40, 45, 48	1.0, 5.0	25

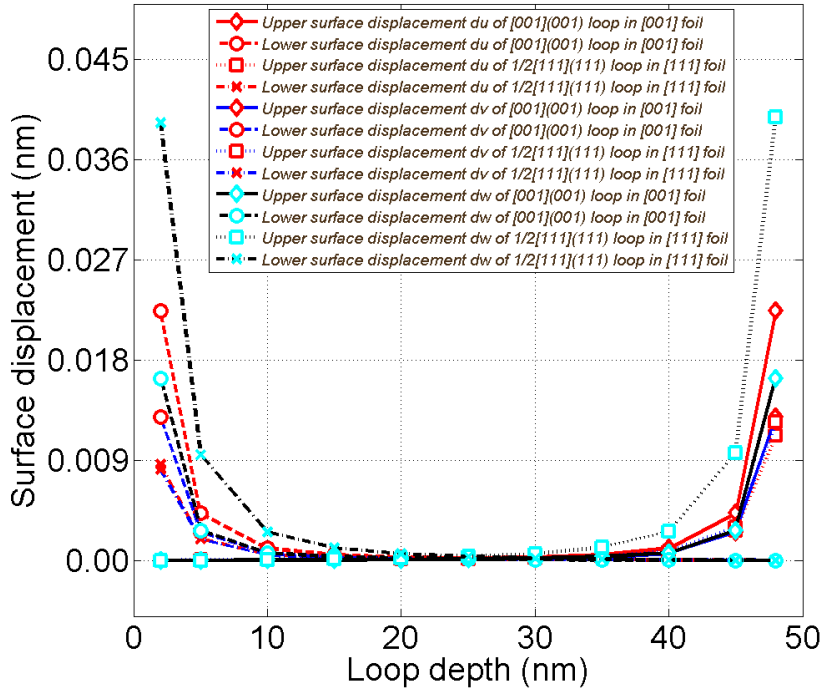


Figure 5.18: The dependence of surface image displacement on loop depth within thin foil for $\frac{1}{2} a_0111$ dislocation loop within (111) thin foil and for a_0001 dislocation loop within (001) thin foil with dislocation loop $R=1.0$ nm.

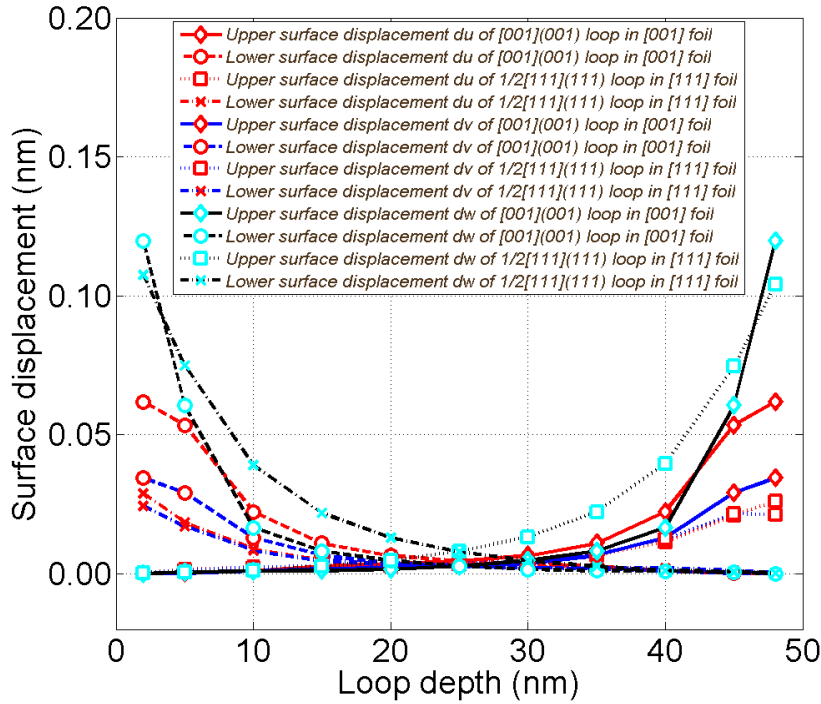


Figure 5.19: The dependence of surface image displacement on loop depth within thin foil for $\frac{1}{2} a_0111$ dislocation loop within (111) thin foil and for a_0001 dislocation loop within (001) thin foil with dislocation loop $R=5.0$ nm.

As shown in Fig. 5.18 and Fig. 5.19, when comparing results for $\frac{1}{2} a_0111$ dislocation loop and for a_0001 dislocation loop, with the increase of loop depth under free surface, the in plane image displacement amplitude and out-of-plane image displacement amplitude for both $\frac{1}{2} a_0111$ dislocation and for a_0001 dislocation loop decrease. Moreover, the in plane and out-of-plane image displacement amplitudes for a_0001 dislocation loop drop sharply with loop depth, more steeply than for the $\frac{1}{2} a_0111$ dislocation loop. In other words, with the increase of loop depth within bcc Fe thin foil, the $\frac{1}{2} a_0111$ dislocation loop within (111) foil shows the largest out of plane distortion amplitude, and decreases more slowly with depth. Conversely, the a_0001 dislocation loop within (001) foil shows stronger in-plane image displacement, and decreases sharply, finally reaching nearly the same amplitude as $\frac{1}{2} a_0111$ dislocation loop within (111) foil.

In summary, it can be concluded from the calculation regarding the impact of anisotropy ratio, loop radius and loop depth within thin foil on the image displacement for $\frac{1}{2} a_0111$ dislocation loop within (111) thin foil and for the a_0001 dislocation loop within (001) thin foil that (1) the out-of-plane image displacement is more important than in plane image displacement for $\frac{1}{2} a_0111$ dislocation loop within the (111) foil. While (2) the in plane image displacement is more important than out-of-plane displacement for the a_0001 dislocation loop in (001) foil.

5.2. TEM image simulation results for inclined dislocation

Before starting many beam TEM image simulation with CUFOUR, some elements about the employed diffraction condition are reminded.

The $ng(mg)$ notation is adopted to describe the diffraction condition, where ng is the imaging beam, and mg is the position where the Ewald sphere cuts the systematic rows. The diffraction conditions employed for the diffraction contrast TEM image simulations in this chapter are the following:

- (1) If two beam simulation schemes are employed, only $0g$ and $1g$ are included in the calculation.

(2) If many beam simulation schemes are employed, the included beams for diffraction condition are shown in Table 5.15.

Table 5.15: Many beam TEM image simulation condition employed in CUFOUR.

Beam diffraction condition	Beam number	Included beams
g(1.10g)	6	-2g, -1g, 0g, 1g, 2g, 3g
g(2.10g)	5	-1g, 0g, 1g, 2g, 3g
g(3.10g)	6	-1g, 0g, 1g, 2g, 3g, 4g
g(3.75g)	8	0g, 1g, 2g, 3g, 4g, 5g, 6g, 7g
g(4.10g)	7	-1g, 0g, 1g, 2g, 3g, 4g, 5g
g(4.75g)	8	0g, 1g, 2g, 3g, 4g, 5g, 6g, 7g
g(6.25g)	8	0g, 1g, 2g, 3g, 4g, 5g, 6g, 7g

Note that the effect of beam convergence angle is not studied in the current thesis, and all the simulation tasks are performed at a fixed convergence angle of 10 mrad [Schaeublin, 2000].

The study of the dislocation core impact on the simulation TEM images is not included in all the following TEM simulations of inclined dislocation and dislocation loop.

5.2.1. Comparison between elasticity models

TEM BF many beam image simulation for a $\frac{1}{2} a_0[111]$ inclined screw dislocation within (001) bcc Fe thin foil along (001) pole is performed for studying the efficiency and reliability of different isotropic and anisotropic inclined dislocation line models as described in chapter 4. The diffraction vector is: $g=(020)$, and the diffraction condition is: $0g(1.1g)$. The simulation parameters are given in Table 5.16, and the simulated images are shown in Fig. 5.20 and Fig. 5.21 respectively.

Table 5.16: Simulation parameters for a $\frac{1}{2} a_0[111]$ inclined screw dislocation within (001) bcc Fe thin foil.

PBC			Dislocation physical parameters					
PL (nm)	MN	WN	SN	t (nm)	b	n_l	T (°C)	CR (nm)
100	100	30	20	70	$\frac{1}{2} a_0[111]$	[111]	25	0.2

Beam	Models					
0g(1.1g), BF, g=(020)	(a)	(b)	(c)	(d)	(e)	(f)
	(g)	(h)	(i)	(j)		

Figure 5.20: Simulated TEM images of a $\frac{1}{2} a_0[111]$ inclined screw dislocation within (001) bcc Fe thin foil along (001) pole. The diffraction vector is: $g=(020)$, and the diffraction condition is: $g(1.1g)$. (a), anisotropic WSL finite model; (b), anisotropic infinite Stroh model; (c), anisotropic WSL-Wu-WSL total model, virtual dislocation outside thin foil not included; (d), anisotropic WSL-Wu-WSL total model, virtual dislocation outside thin foil included; (e), isotropic Mura finite model; (f), isotropic infinite Hirth-Lothe model; (g), isotropic Devincere-Weinberger-Mura total model, virtual dislocation outside thin foil not included; (h), isotropic Devincere-Weinberger-Mura total model, virtual dislocation outside thin foil included; (i), isotropic Mura-Weinberger-Mura total model, virtual dislocation outside thin foil not included; (j), isotropic Mura-Weinberger-Mura total model, virtual dislocation outside thin foil included.

beam	(a)	(b)	(c)	(d)	(e)	(f)
0g(1.1g), BF, g=(020)						

Figure 5.21: Simulated many beam TEM images of a $\frac{1}{2} a_0111$ inclined screw dislocation within (001) bcc Fe thin foil along (001) pole. The diffraction vector is (020), and the diffraction condition is: $g(1.1g)$. (a), anisotropic WSL-Wu image gradient model, virtual dislocation outside thin foil not included; (b), anisotropic WSL-Wu image gradient model, virtual dislocation outside thin foil included; (c), isotropic Devincere-Weinberger image gradient model, virtual dislocation outside thin foil not included; (d), isotropic Devincere-Weinberger image gradient model, virtual dislocation outside thin foil included; (e), isotropic Mura-Weinberger image gradient model, virtual dislocation outside thin foil not included; (f), isotropic Mura-Weinberger image gradient model, virtual dislocation outside thin foil included.

Figs. 5.20 (c), (d), (g), (h), (i) and (j) show that the essential contrast features of the six total gradient models match each other; Figs. 5.20 (a) and (e) show that the essential contrast features of the two finite gradient models match each other; Figs. 5.21 (b) and (f) show that the essential contrast features of the two bulk gradient models match each other; Fig. 5.21 (a), (b), (c), (d), (e) and (f) show that the essential contrast features of the six image stress effect models match each other. These models show that the contrast details difference between isotropy and anisotropy models is remarkable, and the black-white contrast via anisotropy shows elongated and rotated contrast features, compared to isotropy one. As shown in Figs. 5.20 (a), (b), (c) and (d), when $g \cdot b \neq 0$ is satisfied for inclined dislocation, the image stress effect on the contrast is not remarkable.

Considering the anisotropy feature of most crystal and the calculation efficiency, if free surface effect is not included for inclined dislocation, Fig. 5.20 (b) anisotropic infinite Stroh model is the most

reasonable models for simulation. If free surface effect is included for inclined dislocation, Fig. 5.20 (c) anisotropic WSL-Wu-WSL total model will be the best option.

5.2.2. Verification by TEM experiments with intensity profile information

In order to assess the reliability of CUFOUR displacement gradient field implementation schemes, a comparison between a 200 kV TEM experimental image and simulated image of an inclined screw dislocation in bcc Fe is performed. The TEM sample preparation and TEM bright field experiments are performed following the procedures described in chapter 2. The thickness of TEM thin foil was calculated with EELS as described in chapter 2. TEM BF experimental observation is performed on a 200 kV TEM JOEL2010, at PSI Villigen.

5.2.2.1. Inclined dislocation within $[001]$ bcc Fe thin foil

The experimental TEM imaging of a $\frac{1}{2} a_0[111]$ inclined dislocation within a (001) bcc Fe thin foil along (001) pole is performed with $g=(020)$, close to a two beam dynamical diffraction condition, and the experimental image is shown in Fig. 22(d). The thickness measured by EELS is 88 nm.

TEM BF two beam image simulation is performed for $g=(020)$. The simulation parameters are shown in Table 5.17, and the images simulated with two beams for the $0g(0.65g)$ diffraction condition are shown in Fig. 5.22. The corresponding intensity profile comparison between simulated and experimental image is shown in Fig. 5.23. It should be noted that when producing the profile along the dashed yellow line, normalization process should be performed for both the intensity and the position firstly. The intensity of experimental image in Fig. 5.22(d) is linearly scaled and shifted within $[0, 1]$ region, thus the maximum and minimum intensity of experimental image is the same as the maximum and minimum intensity of simulated TEM images via anisotropic Stroh infinite model in Fig. 5.22 (c). The actual profile line position of the experimental TEM image is also scaled and shifted within $[0, 1]$ normalized position region. Thus, the intensity profile can be compared between experimental and simulated TEM images at the same position, and real TEM image observation can be verified reliably.

Table 5.17: Simulation parameters for a $\frac{1}{2} a_0[111]$ inclined dislocation within (001) bcc Fe thin foil, with two beams $g(0.65g)$ diffraction conditions included in CUFOUR.

PBC					Dislocation physical parameters					
ZA	n_f	PL (nm)	MN	WN	SN	t (nm)	b	n_t	T (°C)	CR (nm)
[001]	[001]	180	120	30	50	88	$\frac{1}{2} a_0[111]$	[111]	25	0.2

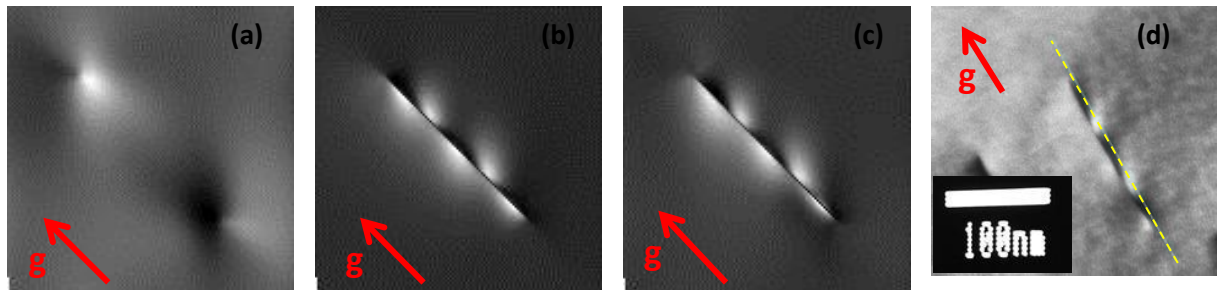


Figure 5.22: Experimental and simulated TEM images of a $\frac{1}{2} a_0[111]$ inclined dislocation within a (001) thin foil along (001) pole, with two beams, $g=(020)$, $g(0.65g)$ diffraction condition. (a), anisotropic WSL-Wu image gradient model; (b), anisotropic WSL-Wu-WSL total gradient model; (c), anisotropic Stroh infinite gradient model; (d), Experimental TEM image. The intensity profile, taken along the marked line, is around 7.0 nm away from the dislocation line. It is shown in Fig. 5.21.

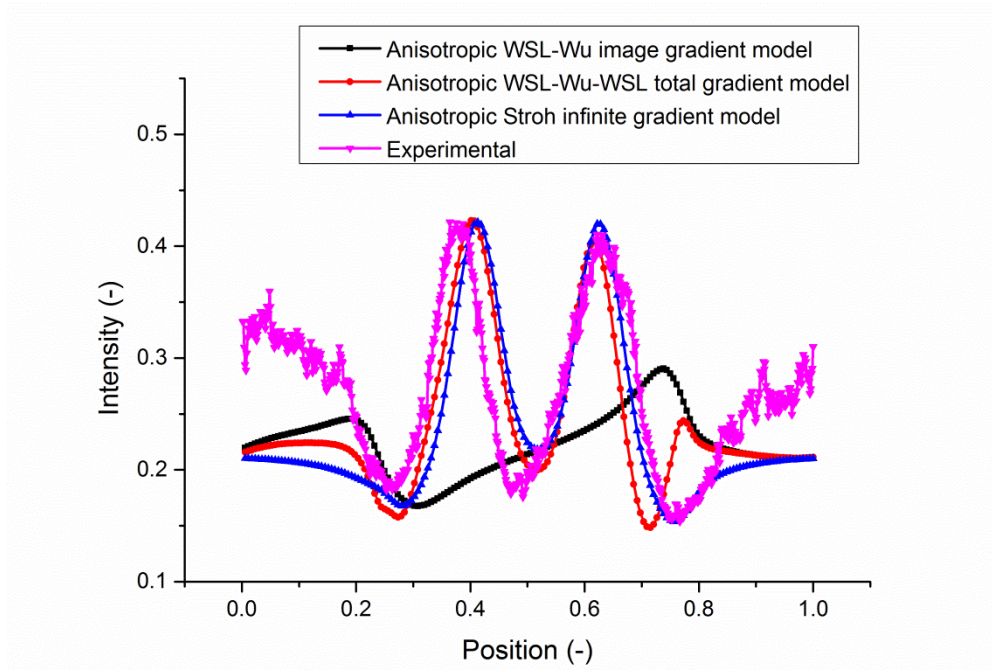


Figure 5.23: Intensity profile of experimental and simulated TEM image for a $\frac{1}{2} a_0[111]$ inclined dislocation within (001) bcc Fe thin foil along the yellow dashed line shown in Fig. 5.20(d).

It can be concluded from Fig. 5.22 and 5.23 that the experimental and simulated TEM images match quite well. The intensity profile within the black-white oscillations of the dislocation also matches each other. However, the background intensity of the simulated TEM image profile differs from the experimental one in the regions away from the dislocation. As shown in Fig. 5.23, the black-white oscillations simulated via WSL-Wu-WSL model will be slightly shifted along the inclined dislocation direction, compared to the anisotropic Stroh infinite model.

5.2.2.2. Verification of inclined dislocation within [011] bcc Fe thin foil

The experimental TEM imaging of a $\frac{1}{2} a_0[111]$ inclined dislocation within (011) bcc Fe thin foil along [011] pole is performed with $g=(200)$, close to two beam dynamical diffraction condition, and the experimental image is shown in Fig. 5.24(d). The thickness measured by EELS is 57 nm.

TEM BF imaging is performed with $g=(200)$ for $g(0.6g)$ diffraction condition. The simulation parameters are shown in Table 5.18, and the images simulated with two beams for the $g(0.6g)$ diffraction condition are shown in Fig. 5.24. The corresponding intensity profile of simulated and experimental image is shown in Fig. 5.25 and Fig. 5.26 respectively.

Table 5.18: Simulation parameters for a $\frac{1}{2} a_0[111]$ inclined dislocation within (011) bcc Fe thin foil, with two beams $g(0.60g)$ diffraction condition included in CUFOUR.

PBC					Dislocation physical parameters					
ZA	n_f	PL (nm)	MN	WN	SN	t (nm)	b	n_t	T (°C)	CR (nm)
[011]	[011]	105.0	120	30	20	57.1338	$\frac{1}{2} a_0[111]$	[111]	25	0.2

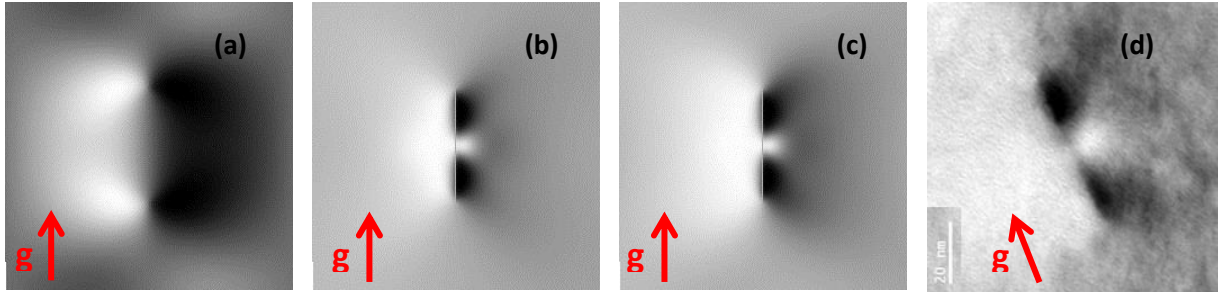


Figure 5.24: Experimental and simulated TEM image of a $\frac{1}{2} a_0[111]$ inclined dislocation within (011) bcc Fe thin foil along (011) pole, with $g=(200)$, $g(0.60g)$ diffraction condition. (a), anisotropic WSL-Wu image gradient model; (b), anisotropic WSL finite gradient model; (c), anisotropic WSL-Wu-WSL total gradient model; (d), Experimental TEM image.

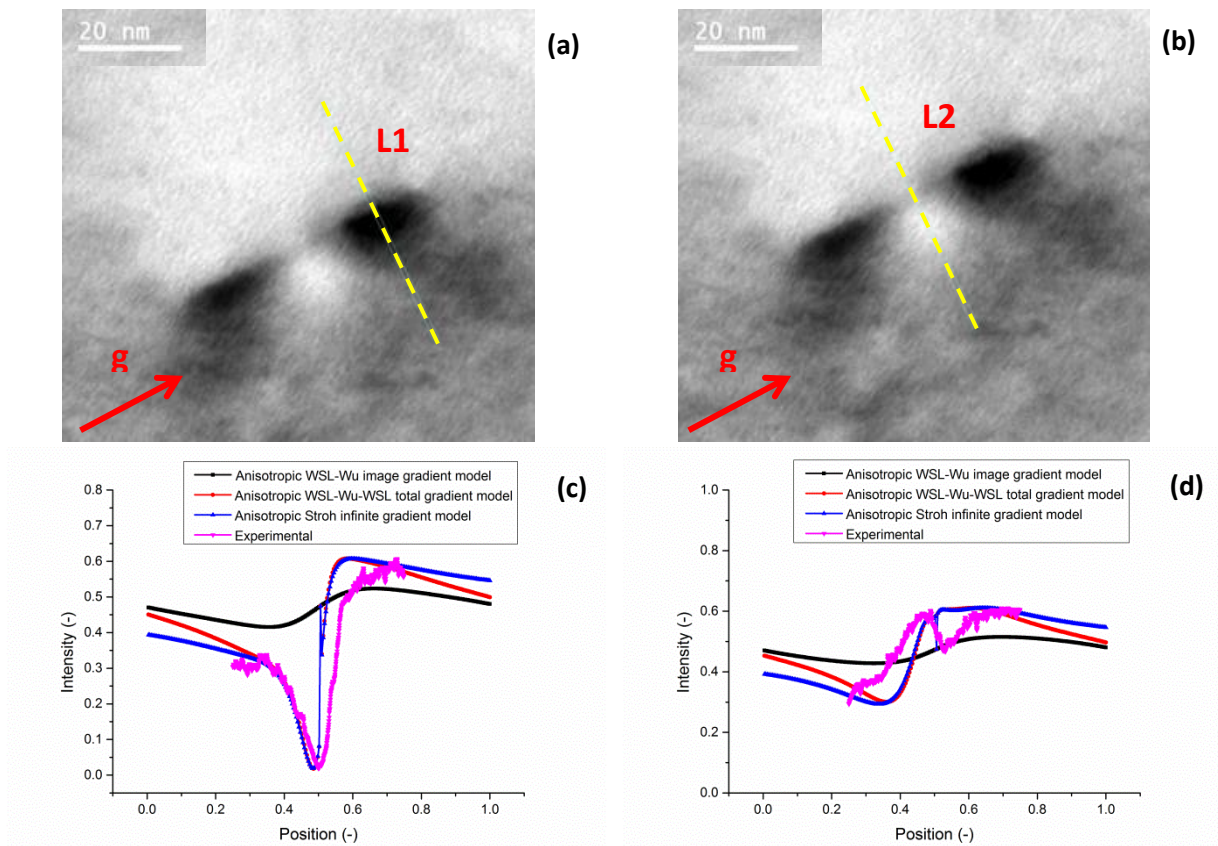


Figure 5.25: Intensity profile of experimental and simulated TEM image with two beam $g=(200)$, $g(0.60g)$ diffraction condition for a $\frac{1}{2} a_0111$ inclined dislocation within (011) bcc Fe thin foil along (011) pole. Intensity profile taken along (a), L1; (b), L2; Intensity profile of (c), experimental and simulated TEM image simulated with anisotropic elasticity along L1; (d), experimental and simulated TEM image simulated with anisotropic elasticity along L2.

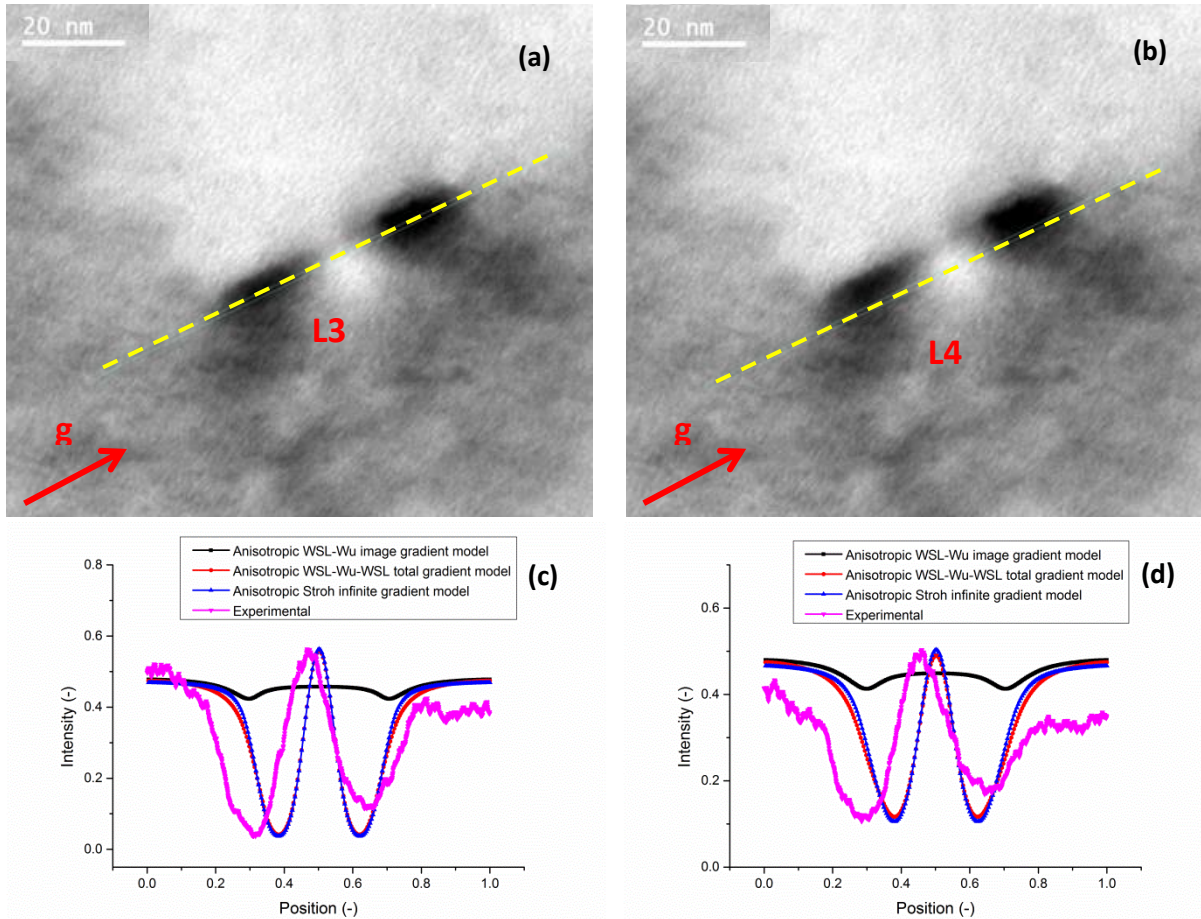


Figure 5.26: Intensity profile of experimental and simulated TEM image with two beam $g=(200)$, $g(0.60g)$ diffraction condition for a $\frac{1}{2} a_0111$ inclined dislocation within (011) bcc Fe thin foil along (011) pole. Intensity profile taken along (a), L3, around 3.0 nm away from the dislocation line; (b), L4, around 5.5 nm away from the dislocation line. Intensity profile of experimental and simulated TEM image simulated with anisotropic elasticity along (c), L3; (d), L4.

It can be concluded from Fig. 5.24, 5.25 and 5.26 that the experimental and simulated TEM images matches each other reasonably well, and that the essential features of the intensity profile along L1, L3 and L4 also match each other quite well. However, the background intensity of the simulated TEM image profile differs from experimental intensity profile along L2. It could be due to the fact that the absolute contrast amplitude along L2 is rather weak, and thus drown into the background noise. As shown in Fig. 5.25, the difference between the intensity amplitudes simulated via anisotropic WSL-Wu-WSL model and the anisotropic Stroh infinite model along L1 and L2 is quite small in the region near to dislocation line, while their intensity amplitudes differ a lot in the region far away from dislocation line. As shown in Fig. 5.26, the difference between the intensity amplitudes simulated via anisotropic WSL-Wu-WSL model and the anisotropic Stroh infinite model along L3 and L4 is quite small.

5.2.3. Image force effect induced end-on contrast

Surface relaxation plays an important role in the TEM image of crystal defects, as is well known for end-on screw dislocations. Indeed, the so-called Eshelby twist induced by the free surface is able to generate a black-white contrast image for end-on screw dislocations in TEM diffraction contrast imaging.

Tunstall et al [Tunstall, 1964] showed that in two beam conditions the diffraction contrast is in the form of black–white lobes perpendicular to the diffracting vector, with the line of no contrast parallel to \mathbf{g} . Hirth [Hirth, 2007] shows that the surface relaxation for screws normal to thin foils, calculated by Eshelby and Stroh [Eshelby, 1951] on isotropic elasticity, gives rise to diffraction contrast in the form of black-white lobes, when imaged in weak beam dark field under two beam diffraction conditions, with the line of no contrast parallel to \mathbf{g} , and can be used to determine the sign of the dislocation. Unlike weak beam images of inclined dislocations, the image contrast field in bright and dark field is very broad owing to the long range nature of the displacement field of a dislocation.

TEM many beam image simulation for an $a_0[001]$ end-on dislocation within (001) bcc Fe thin foil along (001) pole is performed. The diffraction vector is: $\mathbf{g}=(110)$, and the diffraction conditions are: $0\mathbf{g}(1.1\mathbf{g})$, $1\mathbf{g}(1.1\mathbf{g})$ and $1\mathbf{g}(3.1\mathbf{g})$. The simulation parameters for the thin TEM foil are shown in Table 5.19, and the simulated images are shown in Fig. 5.27.

Table 5.19: Simulation parameters for an a_0001 end-on screw dislocation in (001) bcc Fe thin foil.

PBC			Dislocation physical parameters					
PL (nm)	MN	WN	SN	t (nm)	\mathbf{b}	n_l	T (°C)	CR (nm)
70	80	30	20	30, 31, 32, 33, 34, 35	$a_0[001]$	[001]	25	0.2

Beam	t (nm)					
	30	31	32	33	34	35
$0\mathbf{g}(1.1\mathbf{g})$, $\mathbf{g}=(110)$, BF						
$1\mathbf{g}(1.1\mathbf{g})$, $\mathbf{g}=(110)$, DF						
$1\mathbf{g}(3.1\mathbf{g})$, $\mathbf{g}=(110)$, DF						

Figure 5.27: Simulated TEM images of an $a_0[001]$ end-on screw dislocation within (001) bcc Fe thin foil along (001) pole. The diffraction vector is: $\mathbf{g}=(110)$, and the diffraction conditions are: $\mathbf{g}(1.1\mathbf{g})$ and $\mathbf{g}(3.1\mathbf{g})$. The dislocation model is anisotropic WSL-Wu image model.

It can be concluded from Fig. 5.27 when $\mathbf{g} \cdot \mathbf{b} = 0$ invisibility criterion is satisfied for end-on dislocation, the image stress effect on the contrast is remarkable, with the emergency of a broad black-white contrast field.

5.2.4. Image force effect relation to TEM foil thickness

TEM DF image simulation for a $\frac{1}{2} a_0[111]$ inclined screw dislocation within (001) bcc Fe thin foil along (001) pole is performed for studying TEM foil thickness effect on its contrast. The diffraction vector is: $\mathbf{g}=(110)$, and the diffraction condition is: $1\mathbf{g}(3.1\mathbf{g})$. The simulation parameters for the thin TEM foil are shown in Table 5.20, and the simulated images are shown in Fig. 5.28.

Table 5.20: Simulation parameters for a $\frac{1}{2} a_0[111]$ inclined screw dislocation within (001) bcc Fe thin foil along (001) pole with diffraction vector $g=(110)$.

PBC			Dislocation physical parameters					
PL (nm)	MN	WN	SN	t (nm)	b	n_l	T (°C)	CR (nm)
100	100	30	20	40,45,46,47,48,49,50,55	$\frac{1}{2} a_0[111]$	[111]	25	0.4

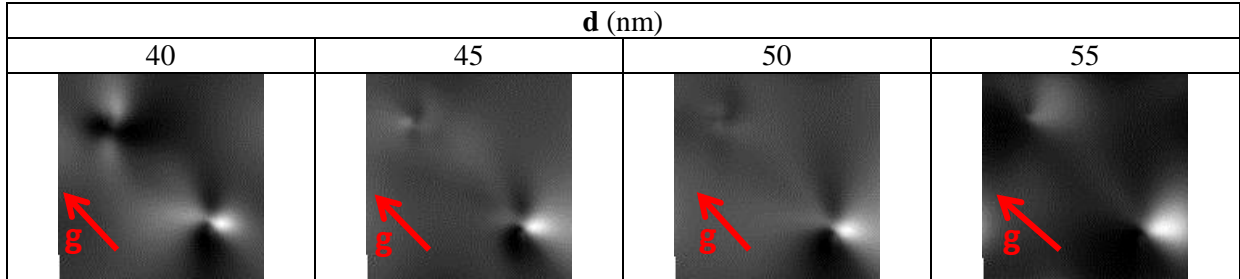


Figure 5.28: Simulated many beam TEM images of a $\frac{1}{2} a_0[111]$ inclined screw dislocation within (001) bcc Fe thin foil along (001) pole. The diffraction vector is: $g=(110)$, and the diffraction condition is: $1g(3.1g)$. The employed model is anisotropic WSL-Wu image gradient model;

It can be concluded from Fig. 5.28 that when increasing TEM foil thickness from 40 to 55 nm gradually, the contrast evolves remarkably. The contrast around the piercing region of inclined dislocation at upper free surfaces will have oscillation features, and the black-white contrast flips with increasing TEM foil thickness, which is similar to the contrast oscillations of small dislocation loop within layer structure of thin TEM foil.

5.2.5. Effect of anisotropy

TEM BF many beam image simulation for a $\frac{1}{2} a_0[111]$ inclined screw dislocation within (001) bcc Fe thin foil along (001) pole is performed for studying the anisotropy ratio effect with various elasticity models. The diffraction vector is: $g=(020)$, and the diffraction condition is: $0g(1.1g)$. The simulation parameters are given in Table 5.21, and the simulated images are shown in Fig. 5.29.

Table 5.21: Simulation parameters for a $\frac{1}{2} a_0[111]$ inclined screw dislocation within (001) bcc Fe thin foil for studying the anisotropy ratio effect on the black-white contrast of simulated TEM images.

PBC			Dislocation physical parameters					
PL (nm)	MN	WN	SN	t (nm)	b	n_l	T (°C)	CR (nm)
100	100	30	20	70	$\frac{1}{2} a_0[111]$	[111]	25	0.2

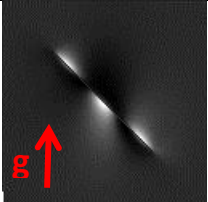
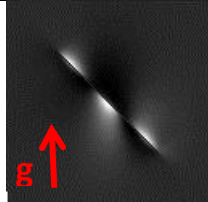
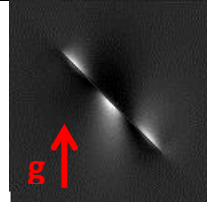
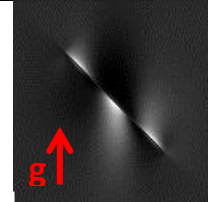

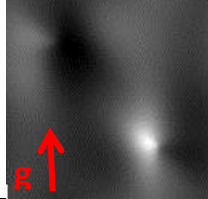
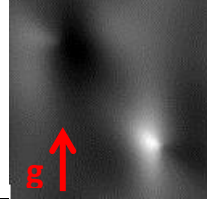
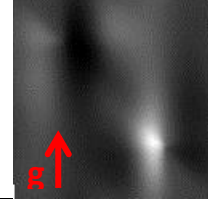
Beam	Model	T (°C)			
		25	300	600	900
0g(1.1g), g=(020); BF	(a)				
	(b)				

Figure 5.29: Simulated many beam TEM images of a $\frac{1}{2} a_0111$ inclined screw dislocation within (001) bcc Fe thin foil along (001) pole for studying the effect of anisotropy ratio. The diffraction vectors is $\mathbf{g}=(020)$, and the diffraction condition is: 0g(1.1g). (a), anisotropic WSL finite model; (b), anisotropic WSL-Wu image gradient model, virtual dislocation outside thin foil included.

It can be concluded from Fig. 5.29 that the essential black-white contrast oscillation features of inclined dislocation via isotropy and anisotropy models match each other and anisotropy ratio have remarkable effect on the simulated TEM image, making the black-white oscillations contrast elongated and rotated. The image stress induced contrast around the piercing points at free surfaces also evolves with anisotropy ratio.

5.2.6. Effect of zone axis

[001] and [011] poles of bcc crystal are the most employed zone axes in TEM imaging observation of dislocation. TEM image simulation for a $\frac{1}{2} a_0[111]$ inclined screw dislocation within bcc Fe thin foil under different zone axes is performed. The diffraction conditions employed for each diffraction vector and zone axis are $g(1.1g)$ BF and DF, $g(2.1g)$ DF and $g(4.1g)$ DF.

5.2.6.1. Simulated $\frac{1}{2} a_0[111]$ dislocation line under [001] zone axis

TEM image simulation for a $\frac{1}{2} a_0[111]$ inclined screw dislocation within (001) bcc Fe thin foil along (001) pole is performed. The diffraction vectors are: $\mathbf{g}=(110)$ and (200), and the diffraction conditions are: $g(1.1g)$, $g(2.1g)$ and $g(4.1g)$. The simulation parameters are shown in Table 5.22, and the simulated images are shown in Fig. 5.30.

Table 5.22: Simulation parameters for a $\frac{1}{2} a_0[111]$ inclined screw dislocation within (001) bcc Fe thin foil along (001) pole, with $g(1.1g)$, $g(2.1g)$ and $g(4.1g)$ diffraction conditions. The diffraction vectors are $\mathbf{g}=(110)$ and (200).

Dislocation physical parameters							
n_f	ZA	SN	t (nm)	\mathbf{b}	n_l	T (°C)	CR (nm)
[001]	[001]	50	40	$\frac{1}{2} a_0[111]$	(111)	25	0.2

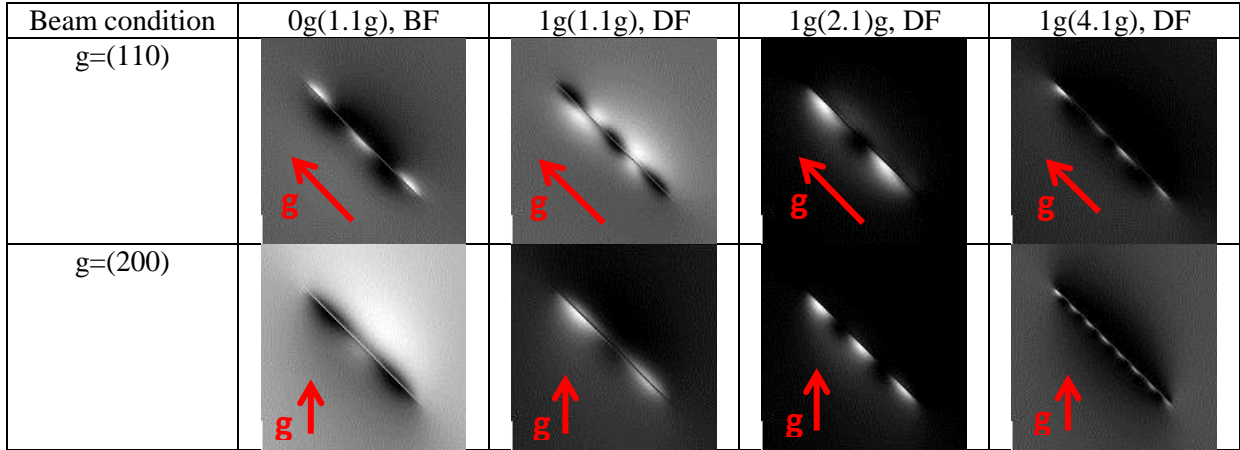


Figure 5.30: Simulated TEM images of a $\frac{1}{2} a_0111$ inclined screw dislocation within (001) bcc Fe thin foil along (001) pole. The diffraction vector are: $g=(110)$ and (200), with 0g(1.1g), 1g(1.1g), 1g(2.1g) and 1g(4.1g) diffraction conditions. The employed model is anisotropic WSL finite gradient model.

It can be concluded from Fig. 5.30 that when high-order beams are excited for g(4.1g) diffraction condition, the number of black-white contrast oscillations will increase sharply.

5.2.6.2. Simulated $\frac{1}{2} a_0[111]$ dislocation line under [011] zone axis

TEM image simulation for a $\frac{1}{2} a_0[111]$ inclined screw dislocation within (011) bcc Fe thin foil along (011) pole is performed. The diffraction vectors are: $g=(0\bar{1}1)$ and (200), and the diffraction conditions are: g(1.1g), g(2.1g) and g(4.1g). The simulation parameters are shown in Table 5.23, and the simulated images are shown in Fig. 5.31.

Table 5.23: Simulation parameters for a $\frac{1}{2} a_0[111]$ inclined screw dislocation within (011) bcc Fe thin foil along (011) pole, with g(1.1g), g(2.1g) and g(4.1g) diffraction conditions. The diffraction vectors are $g=(0\bar{1}1)$ and (200).

Dislocation physical parameters							
n_f	ZA	SN	t (nm)	b	n_l	T (°C)	CR (nm)
[011]	[011]	50	40	$\frac{1}{2} a_0[111]$	(111)	25	0.2

Beam condition	Models	0g(1.1g), BF	1g(1.1g), DF	1g(2.1)g, DF	1g(4.1g), DF
$g=(0\bar{1}1)$	(a)				
	(b)				
$g=(200)$	(c)				
	(d)				

Figure 5.31: Simulated TEM images for a $\frac{1}{2} a_0[111]$ inclined screw dislocation within (011) bcc Fe thin foil. The diffraction vectors are: $g=(0\bar{1}1)$ and (200) along (011) pole. (a), anisotropic WSL finite gradient model; (b), isotropic Mura finite gradient model; (c), anisotropic WSL finite gradient model; (d), isotropic Mura finite gradient model;

It can be concluded from Fig. 5.31 that when $g \cdot b = 0$ invisibility criterion for $g=(0\bar{1}1)$ is satisfied, anisotropy models and isotropy finite model are still able to generate some residual contrast, and the difference between isotropy and anisotropy finite models are remarkable. Conversely, when $g \cdot b \neq 0$ invisibility criterion for $g=(200)$ is not satisfied, the TEM image contrast difference between isotropy and anisotropy models is also remarkable for $g(1.1g)$ diffraction condition, but their difference is not so drastic as the $g \cdot b = 0$ case.

5.3. TEM image simulation results for dislocation loop

5.3.1. Comparison between elasticity models

There are ten types of dislocation loop models for TEM image simulation in CUFOUR as described in chapter 4, including four dislocation loop image gradient models, two infinite gradient models, and four total gradient models, via image gradient model plus infinite gradient model. TEM DF two beam image simulation for a $\frac{1}{2} a_011\bar{1}$ edge-on dislocation loop within (011) bcc Fe thin foil along (011) pole is performed for studying the efficiency and reliability of these ten dislocation loop models. The diffraction vectors is: $g=(21\bar{1})$, and the diffraction condition is: $g(1.1g)$. The simulation parameters are shown in Table 5.24, and the simulated images are shown in Fig. 5.32.

Table 5.24: Simulation parameters for a $\frac{1}{2} a_011\bar{1}$ edge-on dislocation loop of diameter 2.32 nm within (011) bcc Fe thin foil along (011) pole for $g=(21\bar{1})$. Foil thickness $t=50.0$ nm, loop located 40.0 nm from bottom surface of the foil.

PBC and TEM image simulation physical parameters												
HT (KV)	PL (nm)	MN	WN	SN	n_f	ZA	t (nm)	b	n_h	d (nm)	R (nm)	T (°C)
200	100	80	25	40	[011]	[011]	50	$\frac{1}{2} a_0[11\bar{1}]$	[11 $\bar{1}$]	40	1.16	25

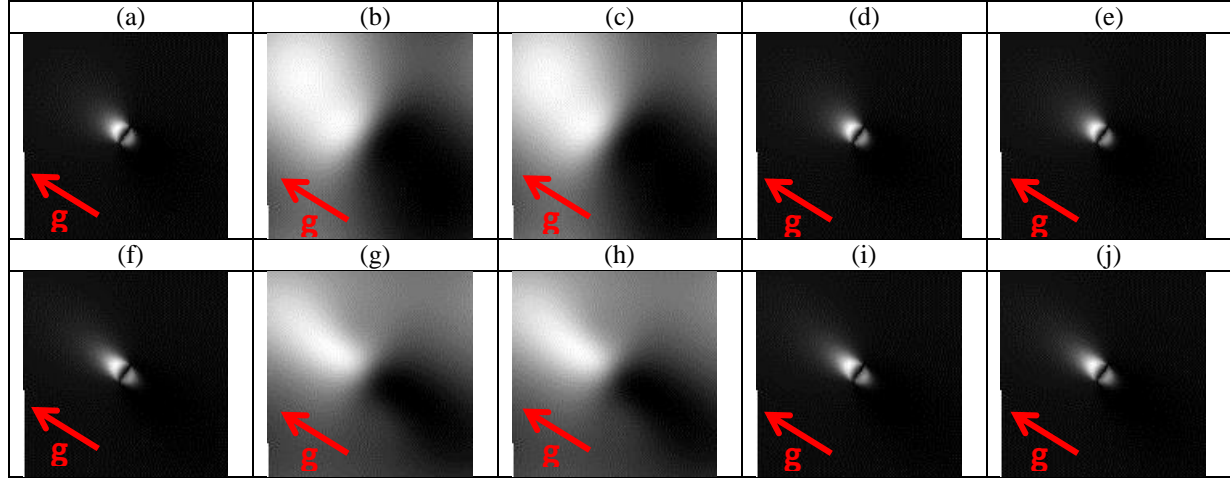


Figure 5.32: Simulated TEM images of a $\frac{1}{2} a_011\bar{1}$ edge-on dislocation loop of diameter 2.32 nm within (011) bcc Fe thin foil along (011) pole for $g=(21\bar{1})$. Foil thickness $t=50.0$ nm, loop located 40.0 nm from bottom of the foil. Comparison between ten dislocation loop models: (a), isotropic Mura bulk model; (b), isotropic Devincere-Weinberger image model; (c), isotropic Mura-Weinberger image model; (d), isotropic Devincere-Weinberger-Mura total model; (e), isotropic Mura-Weinberger-Mura total model; (f), anisotropic WSL bulk model; (g), anisotropic WSL-Wu image model; (h), anisotropic Mura-Wu image model; (i), anisotropic WSL-Wu-WSL total model; (j), anisotropic Mura-Wu-WSL total model.

Figs. 5.32 (b), (c), (g) and (h) show that the essential contrast features of the four image stress effect models match each other, but the anisotropy will make the isotropy black-white lobes elongated and slightly bended; Figs. 5.32 (d), (e), (i) and (j) show that the essential contrast features of the four total gradient models match each other, but the anisotropy will make the isotropy black-white lobes elongated; Figs. 5.32 (a) and (f) show that the essential contrast features of the two bulk gradient models match each other, but the anisotropy will make the isotropy black-white lobes elongated. When image stress effect models and total gradient models are employed, the calculation speed for isotropic Mura and Devincere models are more or less the same, while the calculation speed of anisotropic WSL models are much faster than Mura models. Considering the anisotropy feature of most crystal and the calculation efficiency, if free surface effect is not included, Fig. 5.32 (f) anisotropic WSL bulk model is the most reasonable models for simulation. If free surface effect is included, Fig. 5.32 (i) anisotropic WSL-Wu-WSL total model will be the best option.

5.3.2. Comparison between CA and non-CA TEM image simulation schemes

As there is continuous discussion over the limits and reliability of the column approximation (CA) for TEM image simulation, TEM DF images for $\frac{1}{2} a_001\bar{1}$ edge-on dislocation loop within (011) fcc Cu thin foil along (011) pole are simulated with two beam diffraction condition in CUFOUR, with the various elasticity models, because it is well documented in the literature. The elastic modulus for fcc Cu at room temperature is shown in Table 5.2. The diffraction vectors are: $g=(200)$, $(11\bar{1})$, $(1\bar{1}1)$

and $(0\bar{2}2)$, and the diffraction condition is: $g(1.0g)$. The simulation parameters are shown in Table 5.25, and the simulated images are shown in Fig. 5.33.

Table 5.25: Simulation parameters for a $\frac{1}{2}a_001\bar{1}$ edge-on dislocation loop of diameter 4.86 nm within (011) fcc Cu thin foil along (011) pole for $g=(200)$, $(11\bar{1})$, $(1\bar{1}1)$ and $(0\bar{2}2)$. The foil thickness $t=127.575$ nm, loops located 123.93 nm from bottom surface of the foil.

Dislocation loop physical parameters									
HT (KV)	n_f	ZA	SN	t (nm)	b	n_h	R (nm)	d (nm)	CR (nm)
100	[011]	[011]	40	127.575	$\frac{1}{2}a_0[01\bar{1}]$	$(01\bar{1})$	2.43	123.93	0.1

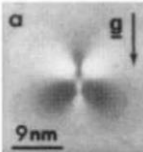
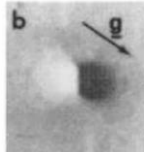
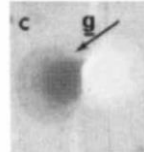
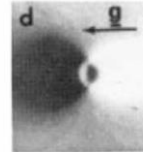
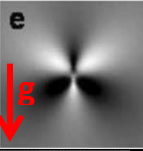
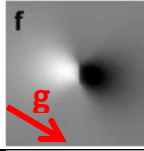
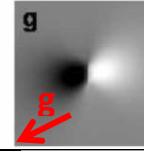
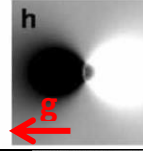
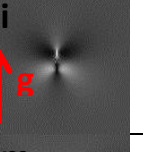
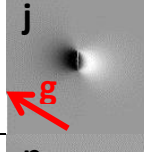
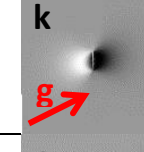
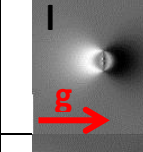
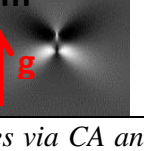
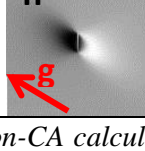
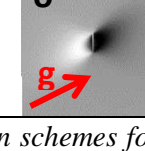
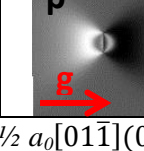
CA/non-CA	Model	Diffraction vector for imaging			
		$g=(200)$	$g=(11\bar{1})$	$g=(1\bar{1}1)$	$g=(0\bar{2}2)$
CA, Howie-Wehlan	Isotropy				
Non-CA, Howie-Basinski	Isotropy				
CA, Schaeublin- Stadelmann	Isotropy				
CA, Schaeublin- Stadelmann	Anisotropy				

Figure 5.33: Simulated TEM images via CA and non-CA calculation schemes for a $\frac{1}{2}a_001\bar{1}$ edge-on dislocation loop of diameter 4.86 nm within (011) fcc Cu thin foil along (011) pole. Foil thickness $t=127.575$ nm, loop located 123.93 nm from bottom of the foil. The original images of Eyre [Eyre, 1977b] via CA with isotropic Bullough dislocation loop model [Bullough, 1960] are shown in (a–d), the images of Zhou [Zhou, 2005] via non-CA with isotropic Yoffe dislocation loop models [Yoffe, 1960] are shown in (e–h), the images of CUFOUR via CA with isotropic Mura dislocation loop models [Schaeublin, 1993; Mura, 1987] are shown in (i–l), and the images of CUFOUR via CA with anisotropic WSL dislocation loop models [Schaeublin, 1993; Yin, 2010] are shown in (m–p). The diffraction conditions are: (a), (e), (i) and (m), $g=(200)$, $g \cdot b = 0$; (b), (f), (j) and (n), $g=(11\bar{1})$, $g \cdot b = 1$; (c), (g), (k) and (o), $g=(1\bar{1}1)$, $g \cdot b = 1$; (d), (h), (l) and (p), $g=(0\bar{2}2)$, $g \cdot b = 2$.

It can be concluded from the simulated TEM images in Fig. 5.33 that CA does not exhibit remarkable difference from non-CA calculation results, when the thickness of TEM foil is 121.8 nm. While anisotropy has a remarkable impact on the simulated TEM image. Indeed, the simulated TEM images via anisotropy model are more elongated along the black-white lobe direction, compared to corresponding Voigt isotropy model. Thus, it can be concluded that simulated TEM image via CA is reliable, and the impact of CA on the final black-white contrast modification is negligible, when compared to anisotropy effect.

5.3.3. The convergence of anisotropy towards isotropy

It has been demonstrated in Fig. 5.34 that the difference between simulated TEM images of dislocation loop via Voigt isotropy and anisotropy models is remarkable. Here, TEM DF images of $\frac{1}{2} a_011\bar{1}$ edge-on dislocation loop within (011) bcc Fe thin foil along [011] pole are simulated with two beam diffraction condition in CUFOUR to demonstrate the impact of anisotropy ratio on its TEM image contrast, with the various elasticity models. The artificial elastic modulus for bcc Fe simulation is shown in Table 5.26, with increasing anisotropy ratio from 1.05 to 5.0. The diffraction vectors is: $g=(2\bar{1}1)$, and the diffraction condition is: $g(2.0g)$. The simulation parameters are shown in Table 5.27, and the simulated images are shown in Fig. 5.34.

Table 5.26: Artificial elastic modulus for studying anisotropy effect on TEM image contrast.

C_{11} (GPa)	150	150	150	150	150	150
C_{12} (GPa)	100	100	100	100	100	100
C_{44} (GPa)	26.5	30	37.5	50	62.5	125
$2C_{44}/(C_{11}-C_{12})$	1.05	1.2	1.5	2.0	2.5	5.0

Table 5.27: Simulation parameters for a $\frac{1}{2} a_011\bar{1}$ dislocation loop of diameter 2.32 nm within (011) bcc Fe thin foil along (011) pole with $g=(2\bar{1}1)$. Foil thickness $t=121.8$ nm, loops located 118.32 nm from bottom surface of the foil.

Dislocation loop physical parameters									
HT (KV)	n_f	ZA	SN	t (nm)	b	n_h	R (nm)	d (nm)	CR (nm)
100	[011]	[011]	40	121.8	$\frac{1}{2} a_0[11\bar{1}]$	(11 $\bar{1}$)	1.16	118.32	0.1

Beam	Model	Anisotropy ratio					
		(a)	(b)	(c)	(d)	(e)	(f)
$g(2.0g)$, DF, $g=(2\bar{1}1)$	Isotropy						
$g(2.0g)$, DF, $g=(2\bar{1}1)$	Anisotropy						

Figure 5.34: Simulation images for $\frac{1}{2} a_011\bar{1}$ edge-on dislocation loop of diameter 2.32 nm within (011) bcc Fe thin foil along (011) pole with increasing anisotropy ratio for $g=(2\bar{1}1)$. Foil thickness $t = 121.8$ nm, loops located 118.32 nm from bottom of the foil. Anisotropy ratio (a) 1.05; (b) 1.20; (c) 1.50; (d) 2.00; (e) 2.50; (f) 5.00.

It is concluded from Fig. 5.34 that when changing the anisotropy ratio, the essential image feature is retained, but the black-white contrast magnitude and size of each wing of the butterfly evolves sharply with increasing anisotropy ratio. The convergence of simulated TEM image black-white contrast via anisotropy model towards isotropy model is confirmed when anisotropy ratio is close to 1.0.

5.3.4. Comparison between two beam and many beam simulation schemes

It has been estimated [Head, 1973] that about 90% of the total intensity was contained in the first two beams and it was deduced that the two-beam simulation was suitable for many situations. TEM DF image simulation are performed for $\frac{1}{2} a_011\bar{1}$ edge-on dislocation loop within (011) bcc Fe thin foil along (011) pole with two beam and many beam diffraction condition in CUFOUR to study the impact of diffraction beam number included on the simulated TEM image black-white contrast,

with the various elasticity models. The elastic modulus for Fe at room temperature is shown in Table 5.1. The diffraction vectors are: $g=(2\bar{1}1)$, (200) , $(21\bar{1})$ and $(22\bar{2})$, and the diffraction condition is: $g(1.1g)$. The simulation parameters are shown in Table 5.28, and the simulated images are shown in Fig. 5.35.

Table 5.28: Simulation parameters for a $\frac{1}{2} a_011\bar{1}$ edge-on dislocation loop of diameter 2.32 nm within (011) bcc Fe thin foil along (011) pole for $g=(2\bar{1}1)$, (200) , $(21\bar{1})$ and $(22\bar{2})$. Foil thickness $t=121.8$ nm, loop located 118.32 nm from bottom surface of the foil.

Dislocation loop physical parameters									
HT (KV)	n_f	ZA	SN	t (nm)	b	n_h	R (nm)	d (nm)	CR (nm)
100	[011]	[011]	40	121.8	$\frac{1}{2} a_0[11\bar{1}]$	$(11\bar{1})$	1.16	118.32	0.1

Beam	Model	Diffraction vector for imaging			
		(a)	(b)	(c)	(d)
g(1.1g), DF, two beam	Isotropy				
g(1.1g), DF, many beam	Isotropy				
g(1.1g), DF, two beam	Anisotropy				
g(1.1g), DF, many beam	Anisotropy				

Figure 5.35: Comparison between two beams and many beams via isotropic and anisotropic dislocation loop models for a $\frac{1}{2} a_011\bar{1}$ dislocation loop of diameter 2.32 nm within (011) bcc Fe thin foil along (011) pole. Foil thickness $t=121.8$ nm, located 118.32 nm from bottom of the foil. Diffraction vector (a) $g=(2\bar{1}1)$; (b) $g=(200)$; (c) $g=(21\bar{1})$; (d) $g=(22\bar{2})$.

It is concluded from Fig. 5.35 that the essential features of these simulated TEM images are retained, which is independent of anisotropy and number of beams. The black-white contrast of simulated image with many beam scheme is however slightly broader than the corresponding two beam case. The latter confirms that when the diffraction condition is close to a Bragg condition, a two beam calculation is sufficient. [Head, 1973]

5.3.5. Experimental verification with Frank edge-on loop within irradiated copper

A study of the black-white contrast of TEM images of small Frank loops in fcc Cu is performed to further validate simulation. This case is selected as it is well documented in the literature. Thus, TEM DF many beam image simulation for a $\frac{1}{3} a_0\bar{1}11$ edge-on dislocation loop within (110) fcc Cu thin foil along (110) pole are performed with the various elasticity models. The elastic modulus for

Cu at room temperature is shown in Table 5.2. The diffraction vector is: $g=(002)$, and the diffraction conditions are: $g(3.75g)$, $g(4.75g)$ and $g(6.25g)$ along $[110]$ pole. The simulation parameters are shown in Table 5.29, and the simulated images are shown in Fig. 5.36.

Table 5.29: Simulation parameters for a $1/3 a_0\bar{1}11$ edge-on Frank dislocation loop of diameter 2.5 nm within (110) fcc Cu thin foil along (110) pole for $g=(002)$. Foil thickness $t=60.0$ nm, located 30.0 nm from bottom surface of the foil.

Dislocation loop physical parameters									
HT (KV)	n_f	ZA	SN	t (nm)	b	n_h	R(nm)	d (nm)	CR (nm)
100	[110]	[110]	40	60	$1/3 a_0[\bar{1}11]$	$(\bar{1}11)$	2.5	30	0.1

Models	(g, 3.75g)	(g, 4.75g)	(g, 6.25g)
(a) many beam, Experimental			
(b) Many beam Howie-Basinski, Non-CA, Yoffe isotropy			
(c) Many beam modified Howie-Whelan [Zhou, 2005], CA, Yoffe isotropy			
(d) Two beam, modified Howie-Whelan [Zhou, 2005], CA, Yoffe isotropy			
(e). Many beam, Schaeublin-Stadelmann, CA, Mura isotropy			
(f). Many beam, Schaeublin-Stadelmann, CA, WSL anisotropy			

Figure 5.36: Simulation images of a $1/3 a_0\bar{1}11$ edge-on Frank dislocation loop of diameter 2.5 nm within (110) fcc Cu thin foil along (110) pole for $g=(002)$. Foil thickness $t=60.0$ nm, located 30.0 nm from bottom of the foil. (a), experimental observation [Zhou, 2005]; (b), the full Howie-Basinski approach, many beam, non-CA, with Yoffe isotropic dislocation loop model [Zhou, 2005; Yoffe, 1960]; (c), the modified Howie-Whelan equations, many beam, CA, with Yoffe isotropic dislocation loop model [Yoffe, 1960; Zhou, 2005]; (d), the modified Howie-Whelan equations, two beams, CA, with Yoffe isotropic dislocation loop model [Yoffe, 1960; Zhou, 2005]; (e), the Schaeublin-Stadelmann equation, many beam, CA, with isotropic Mura infinite dislocation loop model employed in CUFOUR [Mura, 1987; Schaeublin, 1993]; (f), the Schaeublin-Stadelmann equation, many beam, CA, with anisotropic WSL infinite dislocation loop model employed in CUFOUR [Mura, 1987; Schaeublin, 1993].

The simulated TEM images in Fig. 5.36 show that routines (b) and (c) for the $g(3.75g)$ beam condition produce similar contrast features, while routines (d), (e) and (f) produces another set of

similar contrast features. Although the details of the simulated weak beam images are more complex when the higher-order diffraction conditions $g(4.75g)$ and $g(6.25g)$ are achieved, the essential features are always the same, there is little to distinguish them and all seem to reasonably match the experimental images.

Zhou explained that many beam calculations suggest that complex image structures not directly related to the loop geometry may appear if higher-order reflections are satisfied ($n=4, 5$ or 6 , in particular for $n=5, 6$). These effects occur as a result of interference involving higher-order beams, and are absent in a two-beam calculation [Zhou, 2005].

5.3.6. The \mathbf{L} , \mathbf{g} and \mathbf{b} vectors relation analysis

It is widely accepted that $\mathbf{g} \cdot \mathbf{b} = 0$ invisibility criterion for inclined dislocation is valid if the investigated crystal is isotropic or its anisotropy ratio is not high. However, such invisibility criterion is of limited utility for small dislocation loops, as loops with that $\mathbf{g} \cdot \mathbf{b} = 0$ invisibility criterion are often not invisible under dynamical two beam condition. For example, the butterfly visible contrast shown in Fig 5.35 and Fig. 5.36 is produced under $\mathbf{g} \cdot \mathbf{b} = 0$ invisibility criterion condition. On one hand, loops with $\mathbf{g} \cdot \mathbf{b} = 0$ usually show invisibility or very weak contrast under weak-beam imaging conditions; On the other hand, loops with that $\mathbf{g} \cdot \mathbf{b} \neq 0$ may also show very weak contrast under weak-beam imaging conditions. Such complex situation of $\mathbf{g} \cdot \mathbf{b} = 0$ invisibility criterion for small dislocation loops will make reliable judgment of Burgers vector difficult from single TEM diffraction imaging experiment. So-called “L-vector” is proposed as an alternative means for Burgers vector determination for small dislocation loops [Eyre, 1977a]. This method relies on checking of changes of black-white streaking direction with the operating diffraction vector \mathbf{g} , and the \mathbf{L} vector is following the black-white streaking direction, running from the center of black contrast lobe to the center of the white contrast lobe [Eyre, 1977a]. However, as mentioned in chapter 1, the \mathbf{L} vector method works well only under very limited conditions, and it may cause some misleading judgment for reliable Burger vector determination for small dislocation loops.

TEM DF two beam image simulation of $\frac{1}{2} a_001\bar{1}$ edge-on dislocation loop within (011) fcc Cu thin foil along (011) pole are performed for studying the reliability and limits of \mathbf{L} vector method for Burgers vector \mathbf{b} judgment of small dislocation loop, with the various elasticity models. The elastic modulus for fcc Cu at room temperature is shown in Table 5.2. The diffraction vectors are: $\mathbf{g} = \pm(0\bar{1}1)$, $\pm(11\bar{1})$ and $\pm(1\bar{1}1)$ respectively, and the diffraction condition is: $\mathbf{g}(1.0\mathbf{g})$. The simulation parameters are shown in Table 5.30, and the simulated images are shown in Fig. 5.37 and Fig. 5.38 respectively.

Table 5.30: Simulation parameters for a $\frac{1}{2} a_001\bar{1}$ edge-on dislocation loop of diameter 4.86 nm within (011) fcc Cu thin foil along (011) pole for $g=\pm(0\bar{1}1)$, $\pm(11\bar{1})$ and $\pm(1\bar{1}1)$. Foil thickness $t=127.575$ nm, located 123.93 nm from bottom surface of the foil.

Dislocation loop physical parameters									
HT (KV)	n_f	ZA	SN	t (nm)	b	n_h	R (nm)	d (nm)	CR (nm)
100	[011]	[011]	40	127.575	$\frac{1}{2} a_0[01\bar{1}]$	(011)	2.43	123.93	0.1

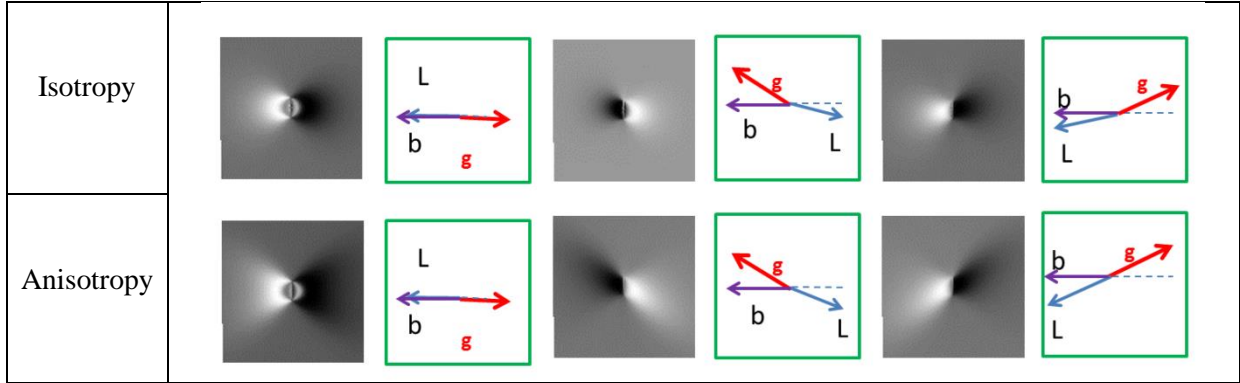


Figure 5.37: The $\mathbf{l-g-b}$ relation for a $\frac{1}{2} a_001\bar{1}$ edge-on dislocation loop of diameter 4.86 nm within (011) fcc Cu thin foil along (011) pole for $g=+(0\bar{1}1)$, $+(11\bar{1})$ and $+(1\bar{1}1)$. Foil thickness $t=127.575$ nm, located 123.93nm from bottom surface of the foil.

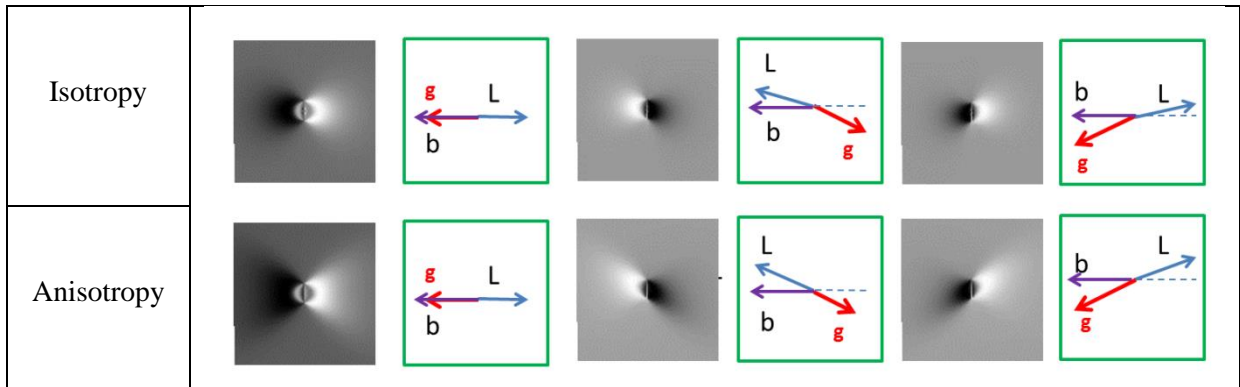


Figure 5.38: The $\mathbf{l-g-b}$ relation for a $\frac{1}{2} a_001\bar{1}$ edge-on dislocation loop of diameter 4.86 nm within (011) fcc Cu thin foil along (011) pole for $g=-(0\bar{1}1)$, $-(11\bar{1})$ and $-(1\bar{1}1)$. Foil thickness $t=127.575$ nm, located 123.93nm from bottom surface of the foil.

It can be concluded Fig. 5.37 and Fig. 5.38 that the angle ($\leq 90^\circ$) between \mathbf{L} (or $-\mathbf{L}$) and \mathbf{b} will increase with the increase of the angle between \mathbf{g} and \mathbf{b} slowly, but lags behind. When anisotropic is considered, the \mathbf{L} vector direction of the black-white lobe will be larger than corresponding isotropic cases, and the black-white lobe will be elongated or compressed. These results clearly indicate that predicting the direction of \mathbf{b} from knowledge of \mathbf{L} will lead to ambiguities even in the simple case of edge dislocation loops in elastically isotropic materials. This will be especially true when the number of possible Burgers vector directions is large (e.g. 14 in the BCC lattice), since then there will be few (possibly no) imaging orientations where a unique assignment of \mathbf{b} can be made from experimentally observed \mathbf{L} directions. [Jenkins, 2001]

5.3.7. Image force dependencies

In order to investigate free surface effect on TEM image black-white contrast of dislocation loops, the displacement field near upper and lower free surfaces are relaxed in order to make the surfaces stress free. This is difficult to do exactly but the condition may be partially fulfilled for a loop parallel to the surface by taking the sum of the displacement fields of the loop and its mirror image in the foil surface [Ruhle, 1965]. However, such investigations mainly focused on effects of the surface on the layer structure of thin TEM foil for dislocation loops. Surface effects on loop contrast were thus not investigated systematically. Ohr [Ohr, 1977] reported a more sophisticated technique for handling surface relaxation for finite loops, and concluded that the image stress induced contrast of small loops lying very close to a stress free surface is indeed sensitive to the presence of the surface. The free surface was found to affect the size and detailed shape of the black-white contrast image [Ohr, 1977].

In this part, the various isotropic and anisotropic image stress models of dislocation loops are compared with each other to study the effect of image stress on their TEM image black-white contrast.

5.3.7.1. Zone axis effect

(1) [001] zone axis.

TEM DF image simulations of an a_0001 edge-on dislocation loop within (001) bcc Fe thin foil along (001) pole are performed. The diffraction vectors are $g=(110)$ and (200), and the diffraction condition is: $g(1.1g)$. The simulation parameters are shown in Table 5.31, and the simulated images are shown in Fig. 5.39.

Table 5.31: Simulation parameters for an a_0001 edge-on dislocation loop of diameter 10.0 nm within (001) bcc Fe thin foil along (001) pole for $g=(110)$ and (200). Foil thickness $t=50.0$ nm, located 5.0 nm from bottom of the foil.

PBC and TEM image simulation physical parameters													
HT (KV)	PL (nm)	MN	WN	SN	n_f	ZA	t (nm)	b	n_h	d (nm)	R (nm)	T (°C)	CR (nm)
200	100	80	25	40	[001]	[001]	50	$a_0[001]$	(001)	5.0	5.0	25	0.2

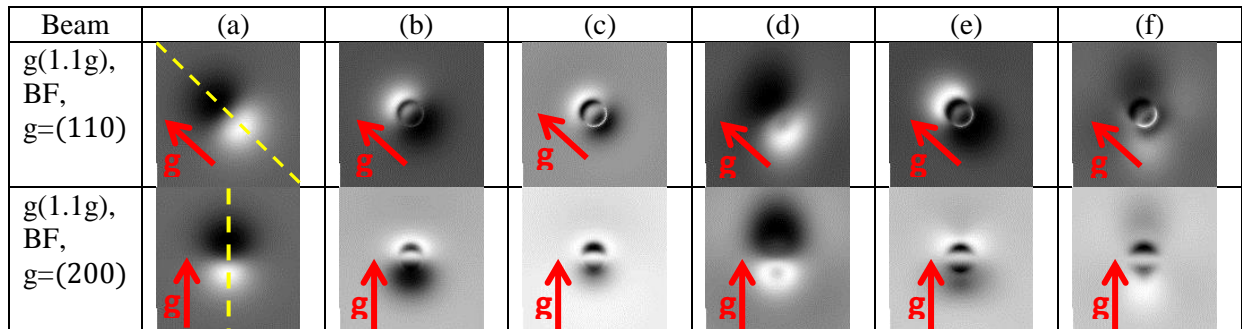


Figure 5.39: Simulated TEM images of an a_0001 edge-on dislocation loop of diameter 10.0 nm within (001) bcc Fe thin foil along (001) pole for $g=(110)$ and (200). Foil thickness $t=50.0$ nm, located 5.0 nm from bottom surface of the foil. (a), isotropic Mura-Weinberger image model; (b), isotropic Mura bulk model; (c), isotropic Mura-Weinberger-Mura total model; (d), anisotropic WSL-Wu image model; (e), anisotropic WSL bulk model; (f), anisotropic WSL-Wu-WSL total model.

The intensity profiles for such a_0001 edge-on dislocation loops for $g=(110)$ and (200) are shown in Fig. 5.40 and Fig. 5.41 respectively, and the yellow marked line in Fig. 5.39 (a) is extracted for the profile comparison between models.

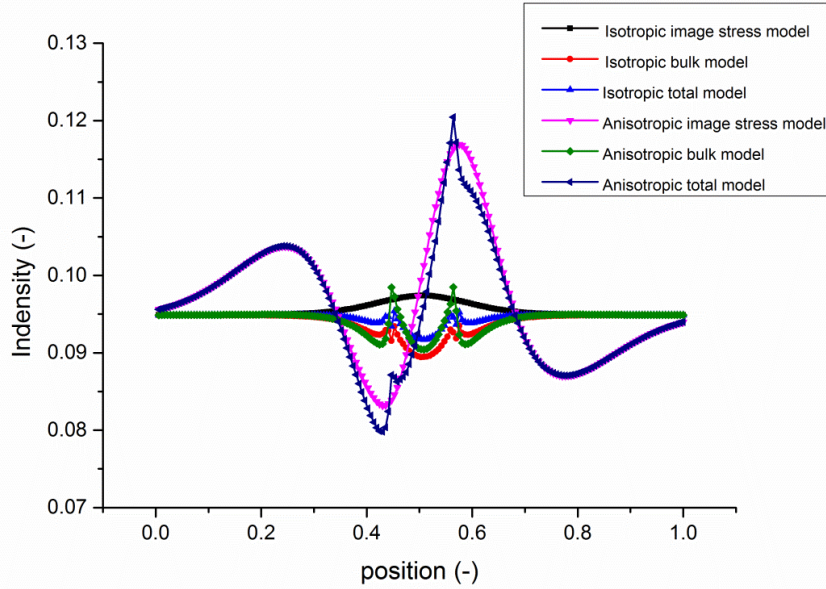


Figure 5.40: Profile across the TEM image of an a_0001 edge-on dislocation loop of diameter 10.0 nm within (001) bcc Fe thin foil along (001) pole for $g=(110)$. Foil thickness $t=50.0$ nm, located 5.0 nm from bottom surface of the foil. Profile taken along the line marked in yellow in Fig. 5.40(a).

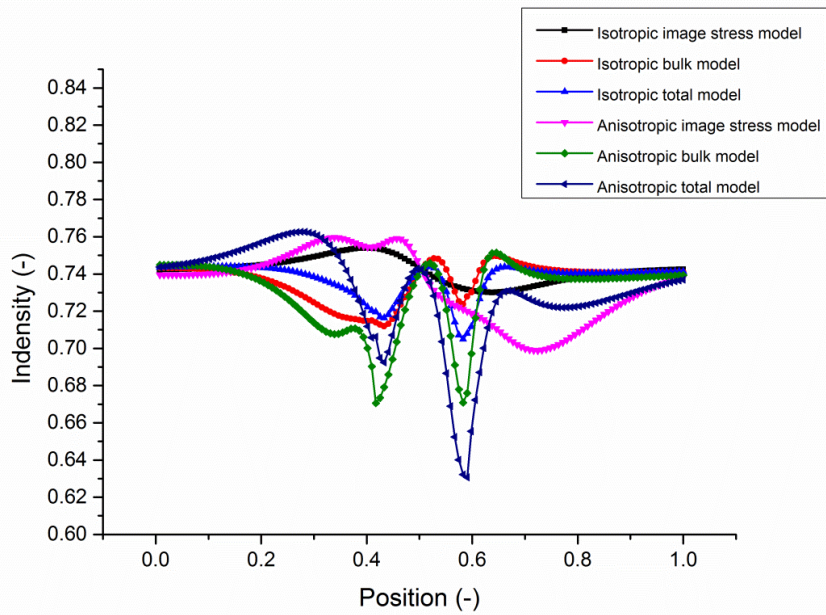


Figure 5.41: Profile across the TEM image of an a_0001 edge-on dislocation loop of diameter 10.0 nm within (001) bcc Fe thin foil along (001) pole for $g=(200)$. Foil thickness $t=50.0$ nm, located 5.0 nm from bottom surface of the foil. Profile taken along the line marked in yellow in Fig. 5.40(a).

(2) [011] zone axis.

TEM DF image simulations for $\frac{1}{2} a_011\bar{1}$ edge-on dislocation loop within (011) bcc Fe thin foil along (011) pole are performed. The diffraction vectors are: $g=(2\bar{1}1)$, (200), $(21\bar{1})$ and $(22\bar{2})$, and the diffraction condition is: $g(1.1g)$. The simulation parameters are shown in Table 5.32, and the simulated images are shown in Fig 5.42.

Table 5.32: Simulation parameters for a $\frac{1}{2} a_011\bar{1}$ edge-on dislocation loop of diameter 2.0 nm within (011) bcc Fe thin foil along (011) pole for $g=(2\bar{1}1)$, (200), $(21\bar{1})$ and $(22\bar{2})$. Foil thickness $t=40.0$ nm, located 35.0 nm from bottom of the foil.

PBC and TEM image simulation physical parameters													
HT (KV)	PL (nm)	MN	WN	SN	n_f	ZA	t (nm)	b	n_h	d (nm)	R (nm)	T (°C)	CR (nm)
200	80	80	20	40	[011]	[011]	40	$\frac{1}{2} a_0 [11\bar{1}]$	[11 $\bar{1}$]	35	1.0	25	0.1

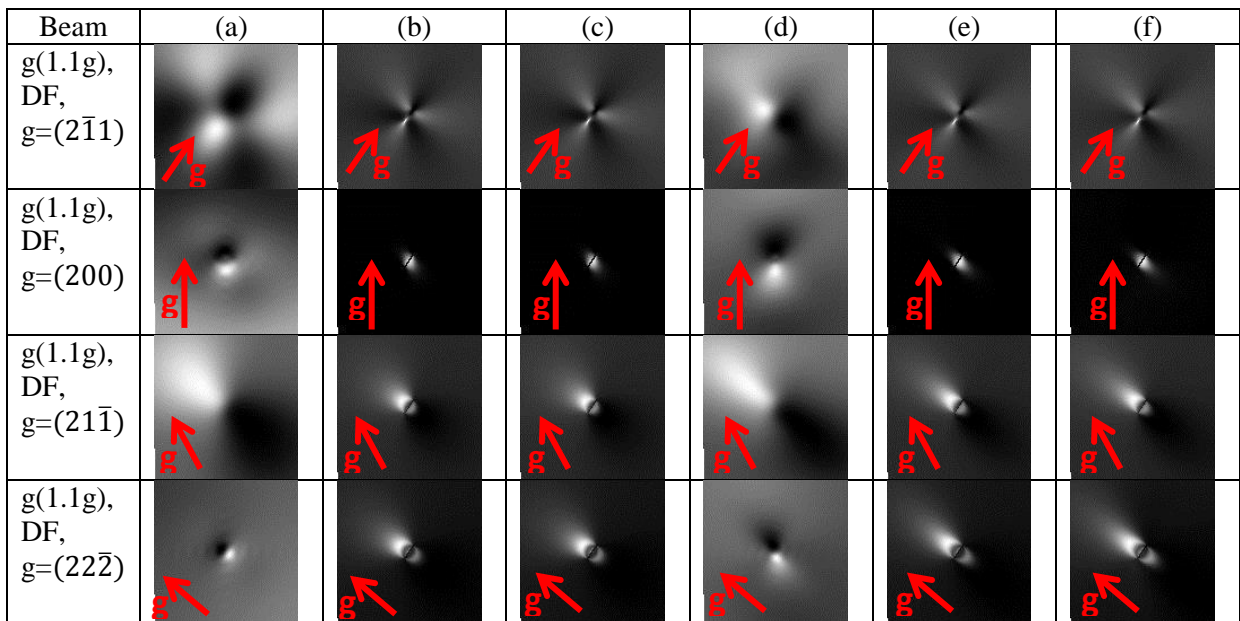


Figure 5.42: Simulated TEM images of a $\frac{1}{2} a_011\bar{1}$ edge-on dislocation loop of diameter 2.0 nm within (011) bcc Fe thin foil along (011) pole for $g=(2\bar{1}1)$, (200), $(21\bar{1})$ and $(22\bar{2})$. Foil thickness $t=40.0$ nm, located 35.0 nm from bottom of the foil. (a), isotropic Mura-Weinberger image model; (b), isotropic Mura bulk model; (c), isotropic Mura-Weinberger-Mura total model; (d), anisotropic WSL-Wu image model; (e), anisotropic WSL bulk model; (f), anisotropic WSL-Wu-WSL total model.

(3). [111] zone axis.

TEM DF image simulations of an a_0100 edge-on dislocation loop within (111) bcc Fe thin foil along (111) pole are performed. The selected diffraction vector is: $g=(\bar{1}01)$, and the diffraction condition is: $g(2.1g)$. The simulation parameters are shown in Table 5.33, and the simulated images are shown in Fig. 5.43.

Table 5.33: Simulation parameters for an a_0100 edge-on dislocation loop of diameter 6.0 nm within (111) bcc Fe thin foil along (111) pole for $g=(\bar{1}01)$. Foil thickness $t=30.0$ nm, located 15.0 nm from bottom of the foil.

PBC and TEM image simulation physical parameters													
HT (KV)	PL (nm)	MN	WN	SN	n_f	ZA	t (nm)	b	n_h	d (nm)	R (nm)	T (°C)	CR (nm)
200	70	70	25	40	[111]	[111]	30	$a_0[100]$	(100)	15	3.0	25	0.1

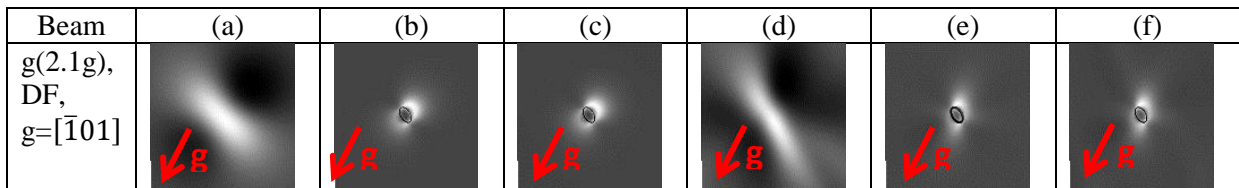


Figure 5.43: Simulated TEM images of an a_0100 edge-on dislocation loop of diameter 6.0 nm within (111) bcc Fe thin foil along (111) pole for $g=(\bar{1}01)$. Foil thickness $t=30.0$ nm, located 15.0 nm from bottom of the foil. (a), isotropic Mura-Weinberger image model; (b), isotropic Mura bulk model; (c), isotropic Mura-Weinberger-Mura total model; (d), anisotropic WSL-Wu image model; (e), anisotropic WSL bulk model; (f), anisotropic WSL-Wu-WSL total model.

It can be concluded from Figs. 5.39, 5.42 and 5.43 that when the loop size is comparable to the distance to free surfaces, the image stress effect on the TEM image contrast becomes important, which is able to change the contrast remarkably. When the loop is very small ($R=1$ nm), the image stress effect on the contrast is ignorable. Anisotropy also has strong impact on the image stress contrast of TEM images. Thus, the impact of image stress on the black-white contrast should be studied systematically. In the following, the relation between loop radius, depth, anisotropy and upper/lower surface and image contrast of TEM images will be investigated systematically for an a_0001 edge-on dislocation loop within (001) bcc Fe thin foil along (001) pole.

5.3.7.2. Loop depth within thin TEM foil effect

In this part, various isotropic and anisotropic dislocation loop models are compared with each other to study the relation between loop depth and image stress effect on its TEM image black-white contrast. TEM BF image simulations for an a_0001 edge-on dislocation loop within (001) bcc Fe thin foil along (001) pole are performed. The diffraction vector is: $g=(110)$, and the diffraction condition is: $g(1.1g)$. The simulation parameters are shown in Table 5.34, and the simulated images are shown in Fig. 5.44.

Table 5.34: Simulation parameters for an a_0 001 edge-on dislocation loop of diameter 10.0 nm within (001) bcc Fe thin foil along (001) pole for $g=(110)$. Foil thickness $t=50.0$ nm, located 5.0, 10.0, 15.0 and 20.0 nm from bottom surface of the foil.

PBC and TEM image simulation physical parameters													
HT (KV)	PL (nm)	MN	WN	SN	n_f	ZA	t (nm)	b	n_h	d (nm)	R (nm)	T (°C)	CR (nm)
200	100	80	25	40	[001]	[001]	50	a_0 [001]	(001)	5,10,15,20	5	25	0.2

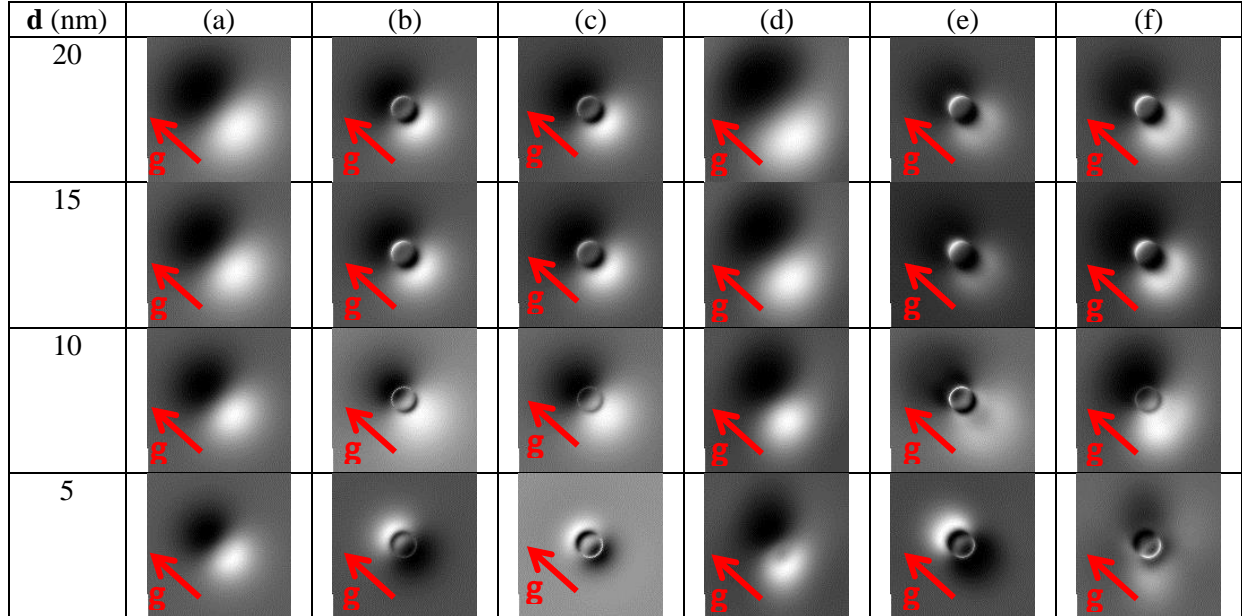


Figure 5.44: Simulated TEM images of an a_0 001 edge-on dislocation loop of diameter 10.0 nm within (001) bcc Fe thin foil along (001) pole for $g=(110)$. Foil thickness $t=50.0$ nm, located 5.0, 10.0, 15.0 and 20.0 nm from bottom of the foil. (a), isotropic Mura-Weinberger image model; (b), isotropic Mura bulk model; (c), isotropic Mura-Weinberger-Mura total model; (d), anisotropic WSL-Wu image model; (e), anisotropic WSL bulk model; (f), anisotropic WSL-Wu-WSL total model.

The following conclusions can be made from the simulation results in Fig. 5.44 when dislocation loop depth is 10.0, 15.0, and 20.0 nm from bottom surface of thin TEM foil (far away from free surface), image stress is strengthening the black-white contrast of dislocation loop contrast generated with bulk model. When dislocation loop depth is 5.0 nm from bottom surface of thin TEM foil (close to free surface), image stress is weakening the black-white contrast of dislocation loop contrast generated with bulk model.

When changing the dislocation loop depth within the thin TEM foil, its black-white contrast of with bulk models flips from layer L1 to L2, layer structure of thin foil. This is because the bulk gradient field of bulk model will be always around dislocation loops. However, the black-white contrast of dislocation loop image model never flips, as the image gradient field will be always generated at the free surfaces, and distributed under free surfaces of thin TEM foil. Thus, image stress effect on TEM contrast is independent of dislocation loop depth within thin TEM foil.

It can be concluded that when TEM foil thickness is constant, dislocation loop black-white contrast via bulk model flips with its depth, while its contrast modification by image stress never flips with its depth within thin TEM foil. Finally, the total TEM image contrast may be flipped. Indeed, image stress effect will have strengthening or weakening effect on the TEM image black-white contrast intensity via bulk models, with a swelling or shrinking the black-white contrast distribution area. It depends on the relative intensity distribution comparison between image stress effect induced contrast

modification on the black-white contrast generated via bulk model, thin TEM foil properties, loop depth, and diffraction condition.

5.3.7.3. Loop radius effect

In this part, various isotropic and anisotropic dislocation loop models are compared with each other to study the relation between loop radius and image stress effect on its TEM image black-white contrast. TEM BF image simulations for a_0001 edge-on dislocation loop within (001) bcc Fe thin foil along (001) pole are performed. The diffraction vector is: $g=(110)$, and the diffraction condition is: $g(1.1g)$. The simulation parameters are shown in Table 5.35, and the simulated images are shown in Fig. 5.45.

Table 5.35: Simulation parameters for an $a_0 001$ dislocation loop of diameter 2.0, 5.0, 8.0 and 11.0 nm within (001) bcc Fe thin foil along (001) pole for $g=(110)$. Foil thickness $t = 50.0\text{nm}$, loops located 5.0 nm from bottom surface of the foil.

PBC and TEM image simulation physical parameters													
HT (KV)	PL (nm)	MN	WN	SN	n_f	ZA	t (nm)	b	n_h	d (nm)	R (nm)	T (°C)	CR (nm)
200	100	80	25	40	[001]	[001]	50	$a_0[001]$	(001)	5	2, 5, 8, 11	25	0.2

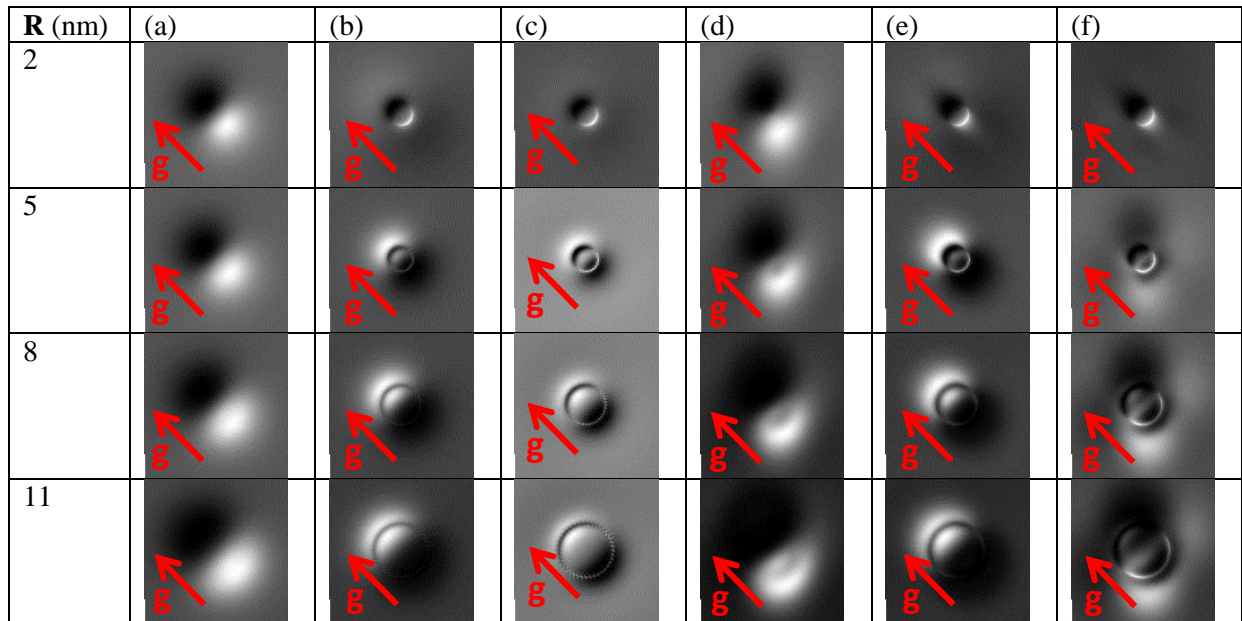


Figure 5.45: Simulated TEM images of an $a_0 001$ dislocation loop of diameter 2.0, 5.0, 8.0 and 11.0 nm within (001) bcc Fe thin foil along (001) pole for $g=(110)$. Foil thickness $t = 50.0\text{nm}$, loops located 5.0nm from bottom of the foil. (a), isotropic Mura-Weinberger image model; (b), isotropic Mura bulk model; (c), isotropic Mura-Weinberger-Mura total model; (d), anisotropic WSL-Wu image model; (e), anisotropic WSL bulk model; (f), anisotropic WSL-Wu-WSL total model.

The following conclusions can be made from the simulation results in Fig. 5.45. When loop radius is 5.0, 8.0 and 11.0 nm, the image stress weakens the contrast of TEM image. When loop radius is 2.0 nm, the image stress strengthens the contrast of TEM image.

5.3.7.4. Anisotropy ratio effect

In this part, various isotropic and anisotropic dislocation loop models are compared with each other to study the relation between anisotropy ratio and image stress effect on its TEM image black-white contrast. TEM BF image simulations for a_0001 edge-on dislocation loop within (001) bcc Fe thin foil along (001) pole are performed. The diffraction vector is: $g=(110)$, and the diffraction condition is: $g(1.1g)$. The simulation parameters are shown in Table 5.36, and the simulated images are shown in Fig. 5.46.

Table 5.36: Simulation parameters for an a_0001 edge-on dislocation loop of diameter 10.0 nm within (001) bcc Fe thin foil along (001) pole at 25, 300, 600 and 900 °C for $g=(110)$. Foil thickness $t=50.0$ nm, loop located 5.0 nm from bottom surface of the foil.

PBC and TEM image simulation physical parameters													
HT (KV)	PL (nm)	MN	WN	SN	n_f	ZA	t (nm)	b	n_h	d (nm)	R (nm)	T (°C)	CR (nm)
200	100	80	25	40	[001]	[001]	50	$a_0[001]$	(001)	5.0	5.0	25, 300, 600, 900	0.2

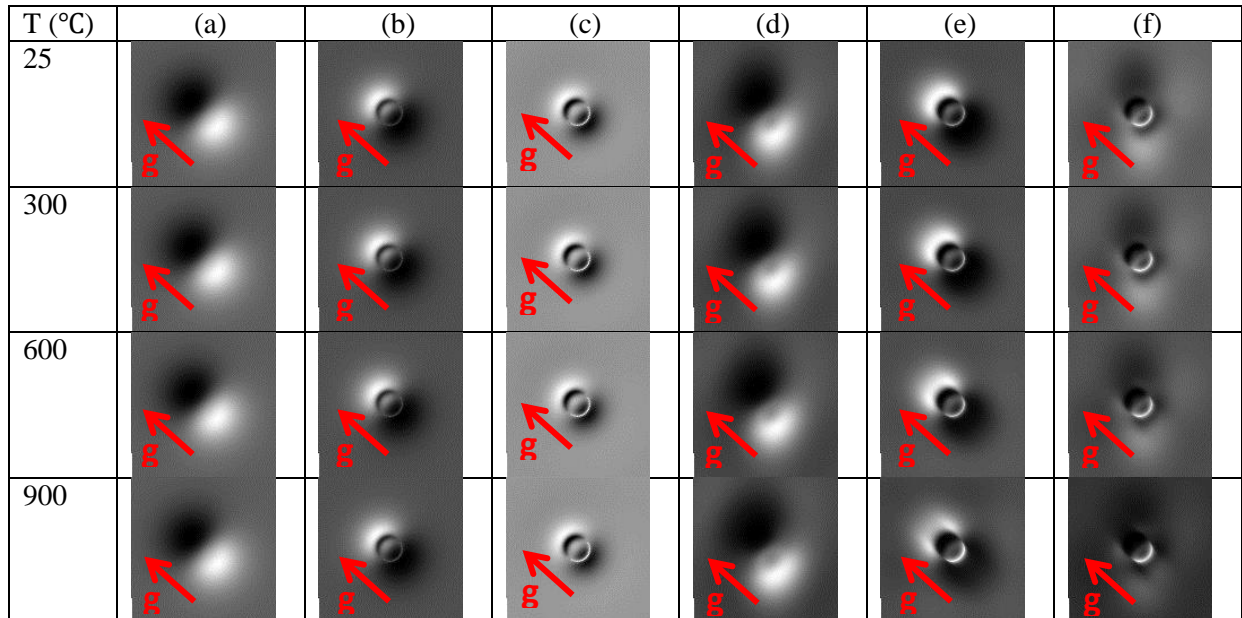


Figure 5.46: Simulated TEM images of an a_0001 edge-on dislocation loop of diameter 10.0 nm within (001) bcc Fe thin foil along (001) pole at 25, 300, 600 and 900 °C for $g=(110)$. Foil thickness $t=50.0$ nm, loop located 5.0 nm from bottom of the foil. (a), isotropic Mura-Weinberger image model; (b), isotropic Mura bulk model; (c), isotropic Mura-Weinberger-Mura total model; (d), anisotropic WSL-Wu image model; (e), anisotropic WSL bulk model; (f), anisotropic WSL-Wu-WSL total model.

The following conclusions can be made from the simulation results in Fig. 5.46. When changing the temperature from 25°C to 900°C, the image stress always weakens the contrast of TEM image of dislocation loops; However, when Voigt isotropy theory is employed, the effect will not show remarkable evolution of the TEM black-white image contrast. Conversely, when anisotropy theory is employed, the effect will show remarkable evolution of the TEM black-white image, and the shape of total effect evolves from two black and white half rings to two black and white half-moons.

5.3.7.5. Image stress effect at upper and lower surfaces

When loop is situated at the same distance to the upper or lower free surfaces, their impact on the simulated TEM image black-white contrast may be different. In this part, isotropic and anisotropic image stress effect, bulk gradient and total gradient field models of dislocation loops are compared with each other to study the individual contribution of image stress effect induced by upper and lower surfaces on the TEM image black-white contrast of a dislocation loop. TEM DF image simulations are employed for a_0001 edge-on dislocation loop within (001) bcc Fe thin foil along (001) pole, situated close to the upper and lower free surfaces. The diffraction vectors are: $g=(110)$ and (200), and the diffraction conditions are: $g(1.1g)$ and $g(3.1g)$.

(a). Image stress effect by upper surface on $a_0 001$ dislocation loop

The simulation parameters are shown in Table 5.37, and the simulated TEM images are shown in Fig. 5.47.

Table 5.37: Simulation parameters for an $a_0 001$ dislocation loop of diameter 10.0 nm within (001) bcc Fe thin foil along (001) pole for $g=(110)$ and (200). Foil thickness $t=50.0$ nm, loop located 45.0 nm from top surface of the foil.

PBC and TEM image simulation physical parameters													
HT (KV)	PL (nm)	MN	WN	SN	n_f	ZA	t (nm)	b	n_h	d (nm)	R (nm)	T (°C)	CR (nm)
200	100	80	25	40	[001]	[001]	50	$a_0[001]$	(001)	45	5	25	0.2

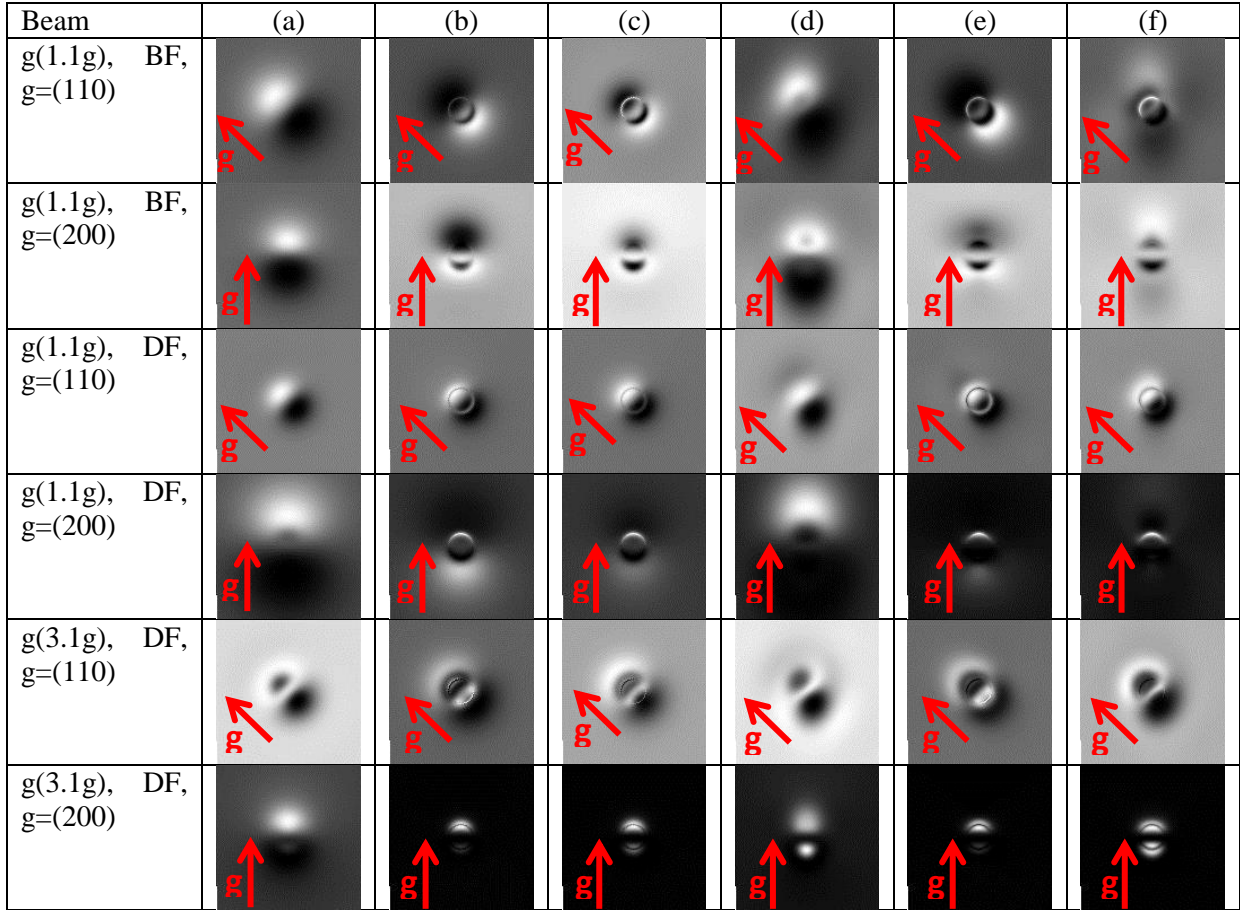


Figure 5.47: Simulated TEM images of an a_0 001 dislocation loop of diameter 5.0 nm within (001) bcc Fe thin foil along (001) pole for $g=(110)$. Foil thickness $t=50.0$ nm, loop located 45.0 nm from bottom of the foil. (a), isotropic Mura-Weinberger image model; (b), isotropic Mura bulk model; (c), isotropic Mura-Weinberger-Mura total model; (d), anisotropic WSL-Wu image model; (e), anisotropic WSL bulk model; (f), anisotropic WSL-Wu-WSL total model.

(b). Image stress effect by lower surface on a_0 001 dislocation loop

The simulation parameters are shown in Table 5.38, and the simulated TEM images are shown in Fig. 5.48.

Table 5.38: Simulation parameters for an a_0 001 dislocation loop of diameter 10.0 nm within (001) bcc Fe thin foil along (001) pole for $g=(110)$ and (200). Foil thickness $t=50.0$ nm, loop located 5.0 nm from bottom of the foil.

PBC and TEM image simulation physical parameters												
HT (KV)	PL (nm)	MN	WN	SN	n_f	ZA	t (nm)	b	n_h	d (nm)	R (nm)	T (°C)
200	100	80	25	40	[001]	[001]	50	$a_0[001]$	(001)	5	5	25

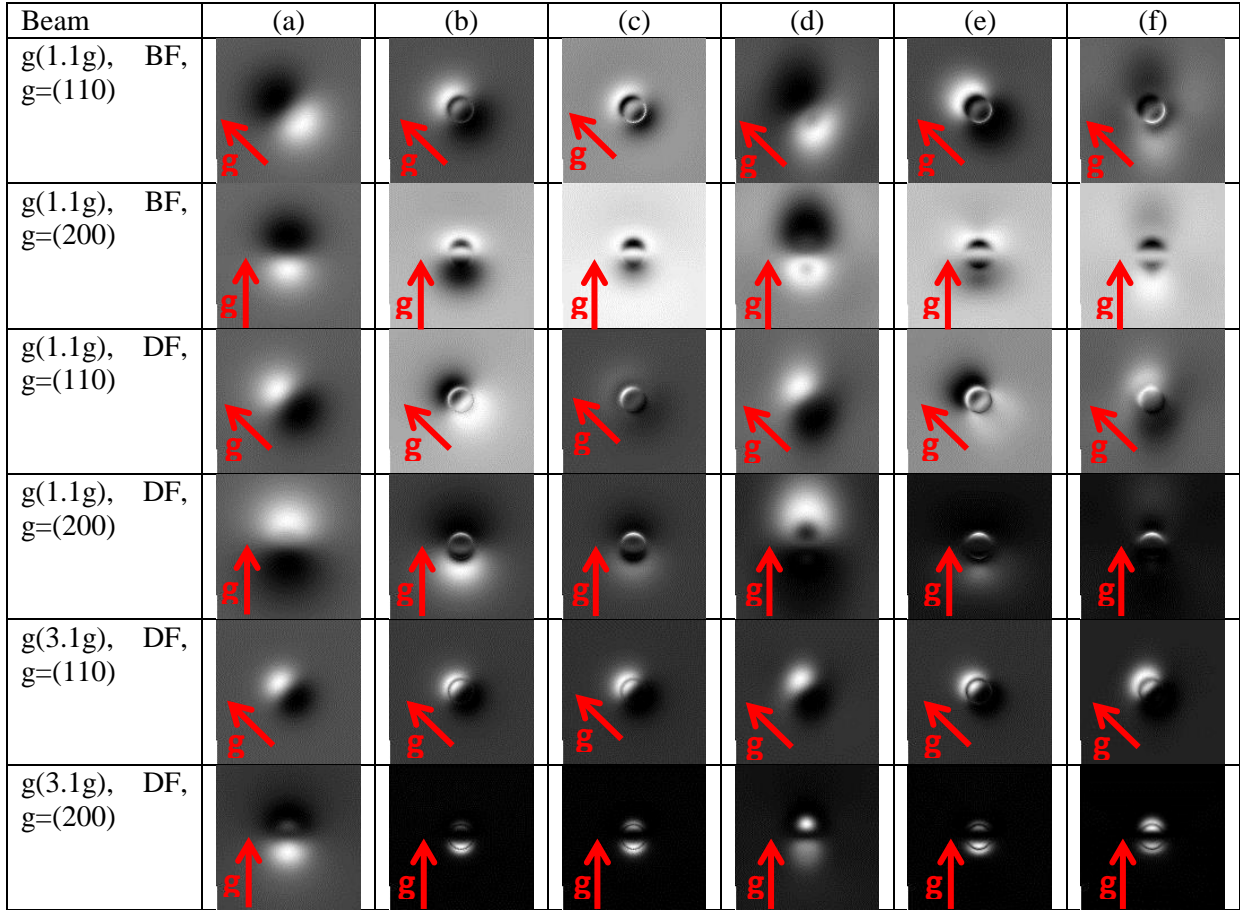


Figure 5.48: Simulated TEM images of an a_0 001 dislocation loop of diameter 5.0 nm within (001) bcc Fe thin foil along (001) pole for $g=(110)$ and (200). Foil thickness $t=50.0$ nm, loop located 5.0 nm from bottom of the foil. (a), isotropic Mura-Weinberger image model; (b), isotropic Mura bulk model; (c), isotropic Mura-Weinberger-Mura total model; (d), anisotropic WSL-Wu image model; (e), anisotropic WSL bulk model; (f), anisotropic WSL-Wu-WSL total model.

5.3.8. Effect of loop depth

TEM DF image simulation of a $\frac{1}{2} a_0$ 01 $\bar{1}$ edge-on dislocation loop within (011) fcc Cu thin foil along (011) pole is performed for studying the effect of loop depth on its black-white contrast, with the various elasticity models. The elastic modulus for Cu at room temperature is shown in Table 5.2. The diffraction vectors is: $g=(1\bar{1}1)$, and the diffraction condition is: $g(1.0g)$. The simulation parameters are shown in Table 5.39, and the simulated images with a loop depth within layer structure and transition zone are shown in Fig. 5.49 and Fig. 5.50 respectively.

Table 5.39: Simulation parameters for a $\frac{1}{2} a_0$ 01 $\bar{1}$ edge-on dislocation loop of diameter 4.86 nm within (011) fcc Cu thin foil along (011) pole for $g=(1\bar{1}1)$.

Dislocation loop physical parameters									
HT (KV)	n_f	ZA	SN	t (nm)	\mathbf{b}	n_h	d (nm)	R(nm)	T (°C)
200	[011]	[011]	40	127.575	$\frac{1}{2} a_0$ [01 $\bar{1}$]	[01 $\bar{1}$]	-	2.43	25

5.3.8.1. Loop depth change effect within layer structure of TEM foil

The effect of changing the loop depth within the layer structure of a fcc Cu thin foil is shown in Fig. 5.49.

Beam	Model	d (nm)				
		123.93	118.93	113.93	108.93	103.93
g(1.0g) , DF, g=(111)	Isotropic					
g(1.0g) , DF, g=(111)	Anisotropic					

Figure 5.49: Simulated TEM images of a $\frac{1}{2} a_001\bar{1}$ edge-on dislocation loop of diameter 4.86 nm within (011) fcc Cu thin foil along (011) pole for $g=(1\bar{1}1)$. Foil thickness $t=127.575$ nm, loop located at 123.93, 118.93, 113.93, 108.93, and 103.93 nm respectively from the bottom surface of the foil.

It can be concluded from Fig. 5.49 that when changing the loop depth within the layers structure (L1, L2, L3) near thin TEM foil free surface, the essential contrast features do not change so much, except for the oscillatory nature of the black-white contrast. Note that, anisotropy will not change such oscillatory nature. Similar conclusions are obtained for $g=(200)$, $(11\bar{1})$, $(1\bar{1}1)$ and $(0\bar{2}2)$ diffraction vectors along (011) pole. The essential features of these images are retained. However, the size and shape of simulated TEM image evolves remarkably with loop depth across whole TEM foil thickness. The simulated images provide solid support for the conclusion given by Eyre via isotropic model that all loops located within the layer structure keep the oscillatory nature of the black-white contrast when changing depth; while the essential features of these image types are unchanged. [Eyre, 1977b]

5.3.8.2. Loop depth change across whole TEM foil thickness

The effect of changing loop depth across the whole TEM foil thickness of a fcc Cu thin foil is shown in Fig. 5.50.

Beam	Model	d (nm)				
		13.7875	33.7875	53.7875	73.7875	93.7875
g(1.0g) , DF, g=(111)	Isotropic					
g(1.0g) , DF, g=(111)	Anisotropic					

Figure 5.50: Simulated TEM images of a $\frac{1}{2} a_001\bar{1}$ edge-on dislocation loop of diameter 4.86 nm within (011) fcc Cu thin foil along (011) pole for $g=(1\bar{1}1)$. Foil thickness $t=127.575$ nm, loop located at 13.7875, 33.7875, 53.7875, 73.7875, and 93.7875 nm from the bottom surface of the foil.

Fig. 5.50 shows essentially the same that was concluded from Fig. 5.49. The difference is that the size of the loop image contrast features does not change so much as for the loop in the layer structure, very close to a free surface.

5.3.9. Anisotropy ratio effect

TEM DF two beam image simulation for a $\frac{1}{2} a_0 11\bar{1}$ edge-on dislocation loop within (011) bcc Fe thin foil along (011) pole is performed in CUFOUR for studying the effect of anisotropic ratio on its black-white contrast with the different elasticity models. The elastic modulus for Fe at different temperature is shown in Table 5.1. The diffraction vectors is: $g=(200)$, and the diffraction condition is: $g(1.1g)$. The simulation parameters are shown in Table 5.40, and the simulated images are shown in Fig. 5.51.

Table 5.40: Simulation parameters for a $\frac{1}{2} a_0 11\bar{1}$ edge-on dislocation loop of diameter 2.32 nm within (011) bcc Fe thin foil along (011) pole at 25, 300, 600, 900 °C for $g=(200)$. Foil thickness $t=121.8$ nm, loop located 118.32 nm from bottom surface of the foil.

Dislocation loop physical parameters									
HT (KV)	n_f	ZA	SN	t (nm)	b	n_h	d (nm)	R (nm)	T (°C)
200	[011]	[011]	40	121.8	$\frac{1}{2} a_0 [11\bar{1}]$	$[11\bar{1}]$	118.32	1.16	25, 300, 600, 900

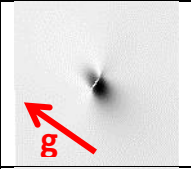
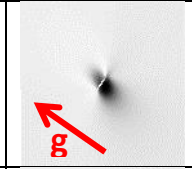
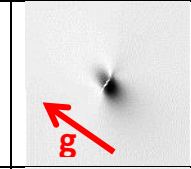
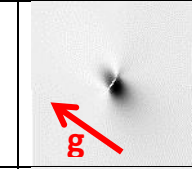
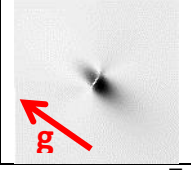
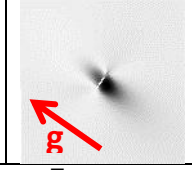
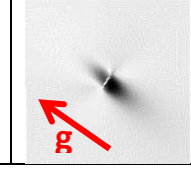
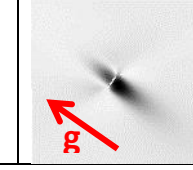
Beam	Model	T			
		25 °C	300 °C	600 °C	900 °C
g(1.1g) , DF, g=(200)	Isotropic				
g(1.1g) , DF, g=(200)	Anisotropic				

Figure 5.51: Simulated TEM images for a $\frac{1}{2} a_0 11\bar{1}$ edge-on dislocation loop of diameter 2.32 nm within (011) bcc Fe thin foil along (011) pole at 25, 300, 600, 900 °C for $g=(200)$. Foil thickness $t=121.8$ nm, loop located 118.32 nm from bottom surface of the foil.

It can be concluded from Fig. 5.51 that when increasing temperature from 25°C to 900°C, the essential double-arc image contrast feature of small dislocation loops within L1 layer of thin foil does not change. However, the shape of anisotropic DF image evolves sharply with increasing temperature, while the shape of corresponding Voigt isotropy DF image remains nearly the same. Therefore, it is concluded that simulated DF images with anisotropy are remarkably different from the ones with Voigt isotropy, and the anisotropy ratio has a strong impact on the simulated TEM image contrast. Similar conclusions are obtained for $g=\pm(2\bar{1}1)$, $\pm(200)$, $\pm(21\bar{1})$ and $\pm(22\bar{2})$ diffraction vectors along (011) pole. The essential features of these image types are retained, but the size and shape evolves remarkably with temperature.

5.3.10. Loop radius effect

TEM DF many beam diffraction image simulation for a $\frac{1}{2} a_0 11\bar{1}$ edge-on dislocation loop within (011) bcc Fe thin foil along (011) pole is performed for studying loop radius effect on the black-white contrast with the various elasticity models. The diffraction vectors is: $g=(200)$, and the diffraction condition is: $g(1.1g)$. The simulation parameters are shown in Table 5.41, and the simulated images are shown in Fig. 5.52.

Table 5.41: Simulation parameters for a $\frac{1}{2} a_011\bar{1}$ edge-on dislocation loop of diameter 2.0, 3.0, 4.0, 5.0 and 6.0 nm within (011) bcc Fe thin foil along (011) pole at 25 °C for $g=(200)$. Foil thickness $t=121.8$ nm, loop located 118.32 nm from bottom surface of the foil.

Dislocation loop physical parameters									
HT (KV)	n_f	ZA	SN	t (nm)	b	n_h	d (nm)	R (nm)	T (°C)
200	[011]	[011]	40	121.8	$\frac{1}{2} a_0 [11\bar{1}]$	[11 $\bar{1}$]	118.32	1.0, 1.5, 2.0, 2.5, 3.0	25

Beam	Model	R (nm)				
		1.0	1.5	2.0	2.5	3.0
g(1.1g), DF, g=(200)	Isotropic					
g(1.1g), DF, g=(200)	Anisotropic					

Figure 5.52: Simulated TEM images of a $\frac{1}{2} a_011\bar{1}$ edge-on dislocation loop of diameter 2.0, 3.0, 4.0, 5.0 and 6.0 nm within (011) bcc Fe thin foil along (011) pole at 25 °C for $g=(200)$. Foil thickness $t=121.8$ nm, loop located 118.32 nm from bottom surface of the foil.

It can be concluded from Fig. 5.52 that when changing loop radius within the first layer of thin foil, the essential image black-white contrast feature does not change so much, and the double-arc contrast feature is retained. Similar loop size effect is also simulated for $g=\pm(2\bar{1}1)$, $\pm(200)$, $\pm(21\bar{1})$, and $\pm(22\bar{2})$ diffraction vectors along (011) pole, and the essential contrast feature of these simulated TEM images are retained. The loop radius effect for simulated TEM images of dislocation loops within L1 layer can be considered as typical for all loops located within the layer structure when changing dislocation loop size. As mentioned by Zhou [Zhou, 2005], the use of elasticity theory is likely to be a good approximation for loops of sizes greater than about 2.0 nm, but less good for smaller loops where molecular dynamics (in the form of conjugate gradient minimization of the potential energy of a large system of interacting atoms) would have to be used to find displacement fields.

5.3.11. Zone axis effect

[001], [011] and [111] poles of bcc crystal are the most employed zone axes in TEM diffraction imaging observation of irradiation defects. TEM image simulations of dislocation loops under different zone axis are performed in CUFOUR. Results are shown in the following.

5.3.11.1. Simulated [100] dislocation loop under [001] zone axis

TEM image simulations of an a_0100 edge-on dislocation loop within (001) bcc Fe thin foil along (001) pole are performed with isotropic and anisotropic models. The diffraction vectors are: $g=(110)$ and (200), and the diffraction conditions are: $g(1.1g)$, $g(2.1g)$ and $g(4.1g)$. The simulation parameters are shown in Table 5.42, and the simulated images are shown in Fig. 5.53 and Fig. 5.54.

Table 5.42: Simulation parameters for an a_0100 edge-on dislocation loop of diameter 2.0 nm within (001) bcc Fe thin foil along (001) pole for $g=(200)$ and (110). Foil thickness $t=40.0$ nm, loop located 20.0 nm from bottom surface of the foil.

Dislocation loop physical parameters									
HT (KV)	n_f	ZA	SN	t (nm)	b	n_h	d (nm)	R (nm)	T (°C)
200	[001]	[001]	40	40	$a_0[100]$	[100]	20	1.0	25

Dislocation loop	Model	$g=(110)$			
		(a)	(b)	(c)	(d)
$a_0 [100] (100)$	Isotropic				
	Anisotropic				

Figure 5.53: Simulated TEM images of an a_0100 edge-on dislocation loop of diameter 2.0 nm within (001) bcc Fe thin foil along (001) pole for $g=(110)$. Foil thickness $t=40.0$ nm, loop located 20.0 nm from bottom surface of the foil. Diffraction condition (a) $g(1.1g)$, BF; (b) $g(1.1g)$, DF; (c) $g(2.1g)$, DF; (d) $g(4.1g)$, DF.

Dislocation loop	Model	$g=(200)$			
		(a)	(b)	(c)	(d)
$a_0 [100] (100)$	Isotropic				
	Anisotropic				

Figure 5.54: Simulated TEM images of an a_0100 edge-on dislocation loop of diameter 2.0 nm within (001) bcc Fe thin foil along (001) pole for $g=(200)$. Foil thickness $t=40.0$ nm, loop located 20.0 nm from bottom surface of the foil. Diffraction condition (a) $g(1.1g)$, BF; (b) $g(1.1g)$, DF; (c) $g(2.1g)$, DF; (d) $g(4.1g)$, DF.

5.3.11.2. Simulated [100] dislocation loop under [011] zone axis

TEM image simulations of an a_0100 edge-on dislocation loop within (011) bcc Fe thin foil along (011) pole are performed with isotropic and anisotropic models. The diffraction vectors are: $g=(200)$ and $(0\bar{1}1)$, and the diffraction conditions are: $g(1.1g)$, $g(2.1g)$ and $g(4.1g)$. The simulation parameters are shown in Table 5.43, and the simulated images are shown in Fig. 5.55 and Fig. 5.56.

Table 5.43: Simulation parameters for an a_0100 edge-on dislocation loop of diameter 2 nm within (011) bcc Fe thin foil along (011) pole for $g=(200)$ and $(0\bar{1}1)$. Foil thickness $t=40.0$ nm, loop located 20.0 nm from bottom surface of the foil.

Dislocation loop physical parameters									
HT (KV)	n_f	ZA	SN	t (nm)	b	n_h	d (nm)	R (nm)	T (°C)
200	[011]	[011]	40	40	$a_0 [100]$	[100]	20	1.0	25

Dislocation loop	Model	$g=(200)$			
		(a)	(b)	(c)	(d)
$a_0 [100] (100)$	Isotropic				
	Anisotropic				

Figure 5.55: Simulated TEM images of an a_0100 edge-on dislocation loop of diameter 2.0 nm within (011) bcc Fe thin foil along (011) pole for $g=(200)$. Foil thickness $t=40.0$ nm, loop located 20.0 nm from bottom surface of the foil. Diffraction condition (a) $g(1.1g)$, BF; (b) $g(1.1g)$, DF; (c) $g(2.1g)$, DF; (d) $g(4.1g)$, DF.

Dislocation loop	Model	$g=(0\bar{1}1)$			
		(a)	(b)	(c)	(d)
$a_0 [100] (100)$	Isotropic				
	Anisotropic				

Figure 5.56: Simulated TEM images of an a_0100 edge-on dislocation loop of diameter 2.0 nm within (011) bcc Fe thin foil along (011) pole for $g=(0\bar{1}1)$. Foil thickness $t=40.0$ nm, loop located 20.0 nm from bottom surface of the foil. Diffraction condition (a) $g(1.1g)$, BF; (b) $g(1.1g)$, DF; (c) $g(2.1g)$, DF; (d) $g(4.1g)$, DF.

5.3.11.3. Simulated [111] dislocation loop under [111] zone axis

TEM image simulations of a $\frac{1}{2} a_0111$ edge-on dislocation loop within (111) bcc Fe thin foil along (111) pole are performed with isotropic and anisotropic models. The diffraction vectors are: $g=(0\bar{1}1)$ and $(\bar{1}01)$, and the diffraction conditions are: $g(1.1g)$, $g(2.1g)$ and $g(4.1g)$. The simulation parameters are shown in Table 5.44, and the simulated images are shown in Fig. 5.57 and Fig. 5.58.

Table 5.44: Simulation parameters for a $\frac{1}{2} a_0111$ edge-on dislocation loop of diameter 2.0 nm within (111) bcc Fe thin foil along (111) pole for $g=(0\bar{1}1)$ and $(\bar{1}01)$. Foil thickness $t=40.0$ nm, loop located 20.0 nm from bottom surface of the foil.

Dislocation loop physical parameters									
HT (KV)	n_f	ZA	SN	t (nm)	b	n_h	d (nm)	R (nm)	T (°C)
200	[111]	[111]	40	40	$\frac{1}{2} a_0 [111]$	[111]	20	1.0	25

Dislocation loop	Model	$g=(0\bar{1}1)$			
		(a)	(b)	(c)	(d)
$\frac{1}{2} a_0 [111] (111)$	Isotropic				
	Anisotropic				

Figure 5.57: Simulated TEM images of a $\frac{1}{2} a_0111$ edge-on dislocation loop of diameter 2.0 nm within (111) bcc Fe thin foil along (111) pole for $g=(0\bar{1}1)$. Foil thickness $t=40.0$ nm, loop located 20.0 nm from bottom surface of the foil. Diffraction condition (a) $g(1.1g)$, BF; (b) $g(1.1g)$, DF; (c) $g(2.1g)$, DF; (d) $g(4.1g)$, DF.

Dislocation loop	Model	$g=(\bar{1}01)$			
		(a)	(b)	(c)	(d)
$\frac{1}{2} a_0 [111] (111)$	Isotropic				
	Anisotropic				

Figure 5.58: Simulated TEM images of a $\frac{1}{2} a_0111$ edge-on dislocation loop of diameter 2.0 nm within (111) bcc Fe thin foil along (111) pole for $g=(\bar{1}01)$. Foil thickness $t=40.0$ nm, loop located 20.0 nm from bottom surface of the foil. Diffraction condition (a) $g(1.1g)$, BF; (b) $g(1.1g)$, DF; (c) $g(2.1g)$, DF; (d) $g(4.1g)$, DF.

It can be concluded from the simulated TEM contrast of dislocation loops under different zone axes and diffraction conditions that reliable judgment on the nature and physical parameters of dislocation loops formed in irradiated nuclear materials can be made by comparison between simulation and experimental observation. For example, Chen [Chen, 2013] investigated the habit plane of dislocation loops formed in irradiated UHP Fe through experimental TEM observation with different diffraction conditions under several zone axes, which can be further improved and quantified through comparison with simulated TEM images.

Chapter.6: Discussion

In this chapter, TEM contrast of inclined dislocation and dislocation loop are discussed, especially focusing on the image stress effect on TEM contrast. Then, the image energy of dislocation loops within thin TEM foil are explored. Finally, The effect of column approximation (CA), dislocation core gradient on TEM image simulation is briefly discussed.

6.1. TEM contrast of inclined dislocation

Complete invisibility of a dislocation requires that both $g \cdot b = 0$ and $(g \cdot b) \times u = 0$ are satisfied simultaneously. Image simulations suggest that a perfect dislocation will exhibit weak residual contrast and effectively is indistinguishable from the background when the parameter $m = \frac{1}{8}(g \cdot b) \times u \leq 0.08$ [Nabarro, 2007].

It should be noted that the elastic distortion field induced by the defects is following a linear superposition principle, while the intensity in the TEM image is not. Indeed the electron waves going through the thin foil follow a complex exponential function, $\exp\left(-2\pi i g \cdot \frac{dR}{dz}\right)$, which indicates that the distortion field, R , actually introduces a phase shift to the electron waves. Thus, when the incident transmitted beam is set to an arbitrary value of 1.0, the final amplitude of the electron waves in the TEM image is always between 0.0 and 1.0. Thus, such image intensity amplitude is not following superposition principle. However, it can be used qualitatively when comparing the contribution to the image contrast from image force field and from bulk field.

(a) Image stress effect on inclined dislocation contrast under $g \cdot b \neq 0$ condition.

Verification between experimental and simulated TEM images of $\frac{1}{2} a_0[111]$ inclined dislocation with different elasticity models was performed, the corresponding TEM images and profile comparison are shown in Fig. 5.22, Fig. 5.23, Fig. 5.24, Fig. 5.25 and Fig. 5.26 respectively. Simulation suggested that the black-white contrast oscillation will be shifted along inclined dislocation direction slightly, if image stress effect is considered, but image stress effect will not be able to influence the basic g, b analysis principle. The image stress effect induced absolute intensity amplitude is around 0.00 to 0.20, relative to the 1.0 intensity of incident transmitted beam, which is low compared to corresponding bulk intensity amplitude under $g \cdot b \neq 0$ dislocation visibility condition. Experimentally, it may become difficult to discriminate it from background noise.

(b) Image stress effect on inclined dislocation contrast under $g \cdot b = 0$ condition.

In order to test this condition, an experimental TEM observation of a $\frac{1}{2} a_0[111]$ inclined dislocation within (001) bcc Fe thin foil along [001] pole was performed with $g=(1\bar{1}0)$, close to a two beam dynamical diffraction condition. It is shown in Fig. 6.1(e).

TEM BF and DF two beam image simulation is performed for $g=(1\bar{1}0)$, with $g(1.1g)$ diffraction condition. The simulation parameters are shown in Table 6.1, and the simulated images are shown in Fig. 6.1. There are four black-white oscillations in the experimental TEM image along dislocation line.

The effective extinction distance is: $\xi_g^{eff} = \xi_g / \sqrt{1 + s_g^2 \cdot \xi_g^2}$, in which ξ_g is about 37 nm. the thickness is: $4 \cdot \xi_g^{eff}$, giving 148 nm. By changing the thickness around this value, a good match between the simulated image Fig. 1.6 (c) and the experimental image one in Fig. 6.1(e) is found for a thickness of 123 nm.

Table 6.1: Simulation parameters for a $\frac{1}{2} a_0[111]$ inclined screw dislocation within (001) bcc Fe thin foil along (001) pole with diffraction vector $g=(1\bar{1}0)$.

PBC			Dislocation physical parameters					
PL (nm)	MN	WN	SN	t (nm)	b	n_l	T (°C)	CR (nm)
250	120	30	50	123	$\frac{1}{2} a_0[111]$	[111]	25	0.2

Beam	(a)	(b)	(c)	(d)	(e)
BF, $g=(1\bar{1}0)$, $g(1.1g)$					
DF, $g=(1\bar{1}0)$, $g(1.1g)$					

Figure 6.1: Experimental and simulated TEM images of a $\frac{1}{2} a_0[111]$ inclined dislocation within a (001) thin foil along (001) pole, with two beams, $g=(1\bar{1}0)$, $g(1.1g)$ diffraction condition. (a), anisotropic WSL-Wu image gradient model; (b), anisotropic WSL finite gradient model; (c), anisotropic WSL-Wu-WSL total gradient model; (d), anisotropic Stroh infinite gradient model; (e), Experimental TEM image.

It can be seen from the difference between Fig. 6.1(b), Fig. 6.1(c) and Fig. 6.1(d) that the image stress effect is remarkable near the tips of inclined dislocation under $g \cdot b = 0$ condition, as the absolute amplitude of residual contrast of anisotropy models is quite low (0.00-0.20), which is comparable to image stress induced contrast amplitude (0.00-0.20). This is valid for both BF and DF images.

(c) Image stress effect on end-on dislocation contrast.

As shown in Fig. 5.27, many beam TEM image simulation for studying end-on black-white contrast is performed, and the end-on TEM contrast is quite sensitive to foil thickness. As mentioned by Mendis [Mendis, 2008], the absolute intensity of the diffraction contrast in the simulated many beam images is too low to be detectable in experimental images which have higher levels of background noise [Mendis, 2008].

In summary, this comparison between experimental and simulated images confirms that image forces have a remarkable impact on the TEM images of inclined dislocation for weak visibility conditions, that is to say $g \cdot b = 0$. This opens the field to experiments allowing to probe and quantify image forces in thin TEM foil.

6.2. TEM contrast of nanometric dislocation loops

As we have seen in chapter 5 surface relaxation has an effect on the extent of the first black-white depth layer L1. The reason for this is clear. Surface relaxation tends to make ($\beta = d(g \cdot R)/dz$) symmetrical, and so expands the first layer. For a finite loop, the first layer is predicted to be of thickness $0.3\xi_g$ when surface relaxation is included, compared with $0.25\xi_g$ when it is not. Jenkins noted that it is not always clear if surface relaxation occurs in practice. This may introduce some uncertainty about the extent of the first layer which has some implications when the black-white stereo technique is used to determine the nature of the loop [Jenkins, 2001].

When image stress effect was included, the in-plane distortion field near free surface of bulk model will be reduced to a great degree, thus inducing additional modification on simulated TEM image based on bulk gradient model. The systematic study on the image stress effect of an a_0001 dislocation loop within (001) bcc Fe thin foil along [001] pole indicate that the contrast intensity amplitude of image stress models and bulk models is within [0.0, 0.2], and total models is within [0.0, 0.25] for most simulation cases. According to the simulated TEM images of dislocation loops with

different models in chapter 5, the following four basic image stress effect modification modes are proposed for the first time, as shown in Fig. 6.2:

- Image stress effect is strengthening the image contrast, and swelling/shrinking the shape of bulk model at the same time. For example, as shown in Fig. 5.44, when $d=10, 15$ and 20 nm, the contrast is strengthened.
- Image stress effect is weakening the image contrast, and swelling/shrinking the shape of bulk model at the same time. For example, as shown in Fig. 5.44, when $d=5$ nm, the contrast is strengthened.
- Image stress effect is weakening the image contrast of bulk model and flipping the black-white essential feature of bulk model, swelling/shrinking the shape at the same time, as image stress effect is stronger than bulk model. For example, as shown in Fig. 5.45, when $R=11$ nm, the contrast is weakened and flipped for the anisotropy case.
- Image stress effect is weakening the image contrast of bulk model and sometimes even flipping the black-white essential feature of bulk model, swelling/shrinking the shape at the same time, as bulk model and image stress effect are both quite weak. For example, as shown in Fig. 5.45, when $R=5$ and 8 nm, the contrast is weakened for the anisotropy case.

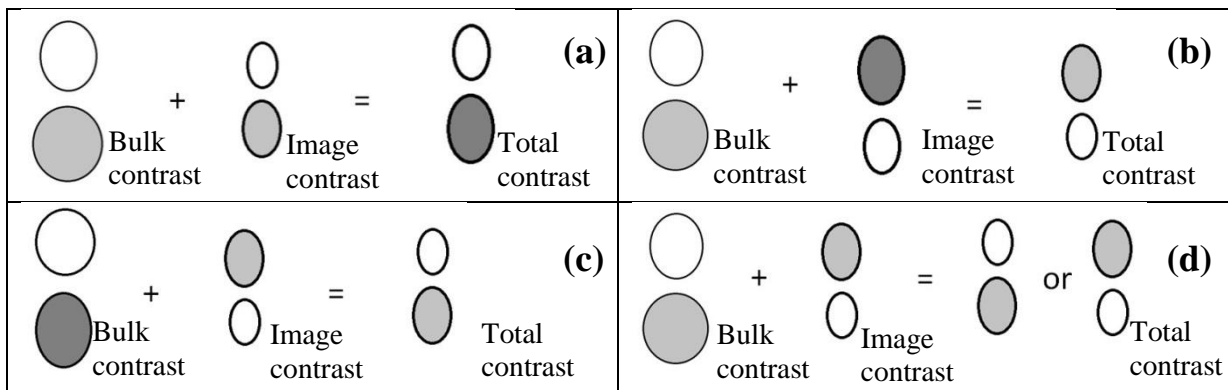


Figure 6.2: The impact of image stress on TEM contrast of dislocation loop.

However, the study for arbitrary oriented dislocation loops within TEM foil under arbitrary diffraction condition should be done in the future.

6.3. Dislocation loops in bcc Fe thin foil

As presented in the literature review, it is known that $\frac{1}{2} \langle 111 \rangle$ loops can run out of thin foil during in situ experiments. It should be noted however that this was not reported yet for the $\langle 001 \rangle$ loops. Actually, the traction force on dislocation loop towards free surface may be described simply by $-dE_{\text{image}}/dz$, which is denoted here as 'attraction force'. Note that it is not strictly speaking the total traction force, which would involve the additional cross terms related to dx and dy , but it is proportional to it. It allows to qualitatively compare the impact of free surfaces induced traction force on the different types of dislocation loops and orientations.

The elastic energy of a dislocation loop in an Fe thin foil as a function of depth is considered. For this, a $\frac{1}{2} a_0111$ dislocation loop within (111) thin film and an a_0001 dislocation loop within (001) thin film with dislocation loop radius 1.0 and 5.0 nm are employed. The simulation parameters are given in Table 6.2, and the simulated results are shown in Fig. 6.3.

Table 6.2: Simulation parameters for $\frac{1}{2} a_0111$ dislocation loop within (111) thin film and for a_0001 dislocation loop within (001) thin film.

PBC				Dislocation loop physical parameters				
PL (nm)	MN	WN	SN	t (nm)	d (nm)	R (nm)	T (°C)	
20, 40, 80, 120, 150, 200	80	30	40	50	2, 5, 10, 15, 20, 25, 30, 35, 40, 45, 48	1, 5	25	

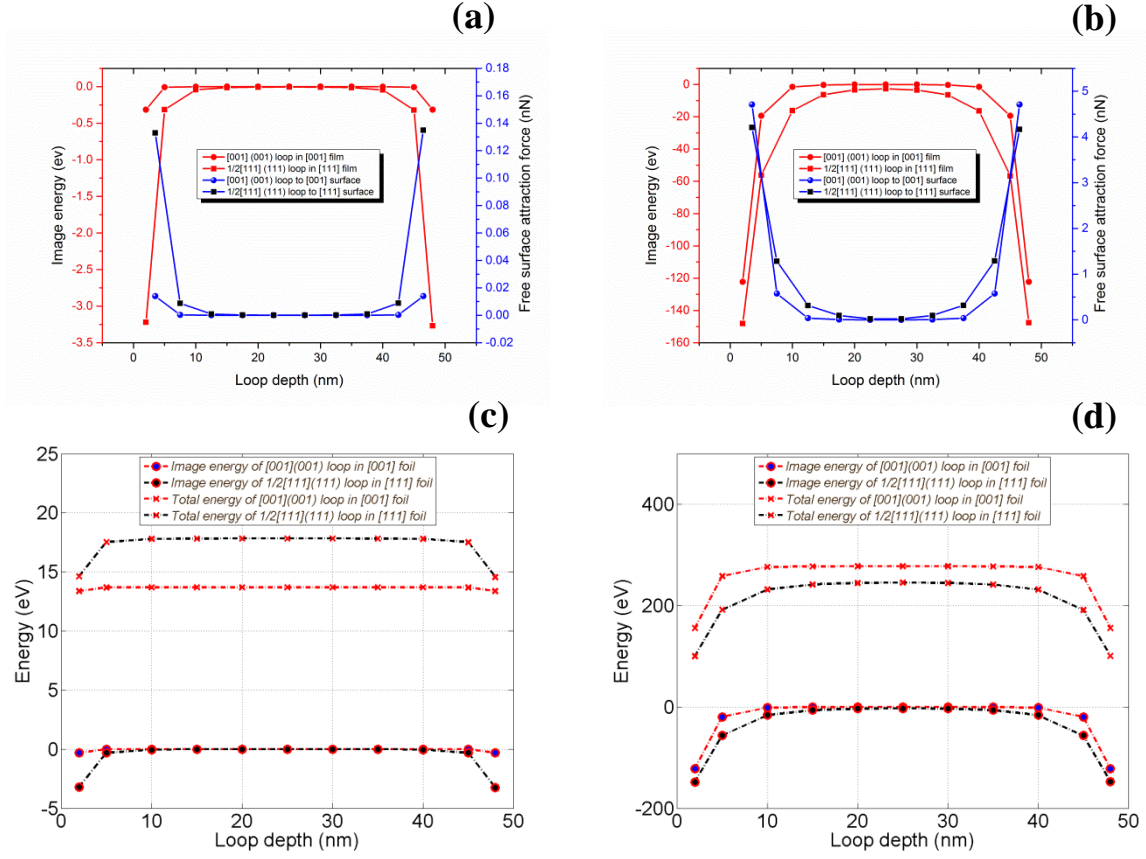


Figure 6.3: The dependence of energy and attraction force to free surface with loop depth within thin foil (a). Image energy and attraction force versus depth ($R=1$ nm); (b), ($R=5$ nm); Energy versus depth (c). ($R=1$ nm); (d), ($R=5$ nm).

It can be concluded from Fig. 6.3 that for a_0001 prismatic dislocation loop parallel to [001] free surface case, the image energy of a_0001 loop drops sharply with the increase of depth under free surface. However, it is amazing to notice that the image energy of $\frac{1}{2} a_0111$ dislocation loops is quite remarkable, and decreasing much flatter than a_0001 dislocation loop with depth. The influencing depth of $\frac{1}{2} a_0111$ dislocation loops within (111) thin TEM foil is much longer than a_0001 dislocation loop within (001) thin TEM foil.

Here, the study is limited within very special cases, mainly a $\frac{1}{2} a_0111$ dislocation loop within (111) bcc Fe thin TEM foil and an $a_0[111](001)$ dislocation loop within (001) bcc Fe thin TEM foil. In order to understand better about the synergetic effect of anisotropy and image stress effect on TEM black-white contrast and physical behavior of dislocation loops better, further systematical research should be carried out. Fitzgerald explained that: Currently, there are no reliable electronic or atomistic approaches to modelling dislocations in Fe at high temperature, and the theoretical resolution of the question of $a_0\langle 100 \rangle$ mobility will have to await their development. Further studies, involving large scale DD simulations and in situ straining at high temperatures in the TEM, are required to further elucidate this mechanism of the formation and evolution of $a_0\langle 100 \rangle$ type of loops [Fitzgerald, 2013].

As pointed out by Masters [Masters, 1963], $\frac{1}{2} a_0\langle 111 \rangle$ dislocation loops is able to run out of thin foil easily, It has also been estimated by MD calculation that a shear stress of a few MPa to 20 MPa is

sufficient to move an edge dislocation [Haghighat, 2010]. At low temperatures at least, $a_0\langle 100\rangle$ dislocations have a much lower mobility than their $\frac{1}{2} a_0\langle 111\rangle$ counterparts, by virtue of their much higher Peierls barrier [Fitzgerald, 2013]. Such remarks has been supported by in-situ ion irradiation experiments and corresponding simulations by Aubry [Aubry, 2011], Prokhodtseva [Prokhodtseva, 2013], Fitzgerald [Fitzgerald, 2009], Yao [Yao, 2008], Hernández [Hernández, 2008] and Moll [Moll, 2013]. In the experiments by Yao [Yao, 2008], it was demonstrated that $\frac{1}{2} a_0\langle 111\rangle$ dislocation loop will run out of thin foil quite easily in pure iron material during in-situ heavy ion irradiation experiments, and the bulk/thin foil irradiation comparison experiments performed by Prokhodtseva [Prokhodtseva, 2013] shows that the formation of visible $a_0\langle 100\rangle$ loops is promoted by the presence of free surfaces, the more so in the thinnest regions of the sample leaving a loop population dominated by $a_0\langle 100\rangle$ loops, both experiments confirmed that free surfaces has a much stronger effect on $\frac{1}{2} a_0\langle 111\rangle$ loop than $a_0\langle 001\rangle$ loops.

Although in situ TEM irradiation experiments has several advantages over post-irradiation TEM investigation of bulk irradiated material, the present investigation of anisotropy and image stress effect of thin foil provides some insight into these. In particular, it sheds some lights on their representativeness of corresponding post-irradiation TEM investigation of bulk irradiated material, especially when the defects density is high, or anisotropy ratio is high.

6.4. Column approximation

As shown in Fig. 5.33, comparison between simulated TEM images via HB, CA and Schaeublin-Stadelmann dynamic diffraction schemes are performed for a $\frac{1}{2} a_001\bar{1}$ dislocation loop of diameter 4.86 nm located 123.93 nm from bottom of a 127.575 nm thick Cu TEM foil along $[011]$ pole. It can be concluded that: the simulated TEM image via CA is reliable, and the impact of CA on the final black-white contrast modification is not remarkable, when compared to anisotropy effect.

However, there are some special cases that non-CA should not be ignored any more. As shown in Fig. 6.4 (a), if two straight dislocations are sitting nearly along beam direction, then the side shift of profile along g (or opposite to g) direction will not be the same amplitude, the intensity overlap will become complex, and there will be big difference between simulated TEM images via CA and non-CA respectively. As shown in Fig. 6.4 (b), if the left edge of loop L2 is nearly below loop the right edge of loop L1, then the side shift of intensity for these two loops will be different, and the final intensity profile will also becomes complex if non-CA is considered. If free surface effect is also considered, things will become more complex, which needs further study in the future. It should also be noted that when there is global bending of the thin TEM foil, the local effective deviation parameter S_g is changed gradually over the observation zone.

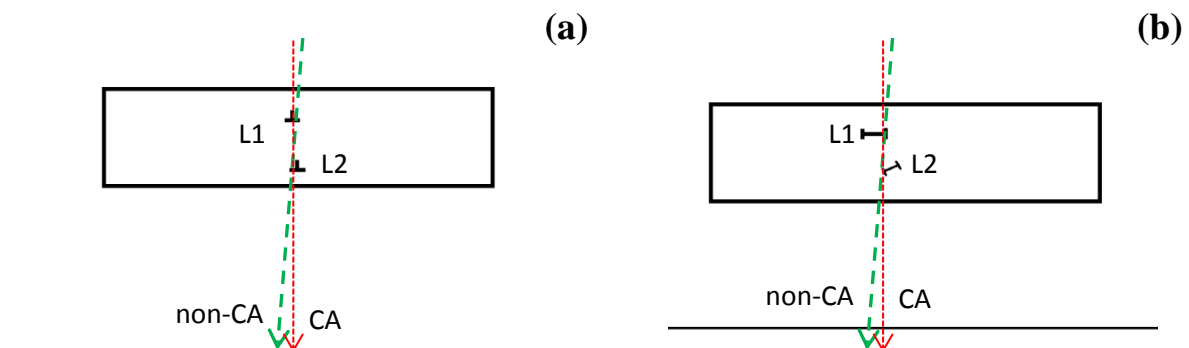


Figure 6.4: Special cases for CA (a), two dislocation lines situated nearly along the beam direction; (b), two dislocation loops situated nearly along the beam direction.

6.5. Dislocation core treatment

Current knowledge on dislocation core is still quite limited, even though a lot HRTEM experimental and theoretical investigation on dislocation core configuration has been made in recent years. For example, a non-singularity dislocation theory is developed by Cai, and dislocation core of pure aluminum is investigated with HRTEM by Mills [Cai, 2006; Mills, 1989]. Here, the dislocation core of inclined dislocation on simulated TEM image is studied briefly. The stress field around piercing point is quite high and the piercing point constitutes a mathematical singularity. In order to represent the stress field of an inclined dislocation precisely, it is necessary to refine the meshing of free surfaces. Surface meshing is refined to study its effect on the simulated TEM images. TEM many beam simulation for $\frac{1}{2} a_0[111]$ inclined dislocation within (001) bcc Fe thin foil along [001] pole is performed. The diffraction vector is: $g=(110)$; and the diffraction conditions are $g(1.1g)$ BF and $g(3.1g)$ DF. The simulation parameters are given in Table 6.3, and the simulated images are shown in Fig. 6.5.

Table 6.3: Simulation parameters for [001] end-on dislocation in [001] thin foil.

Periodic boundary condition (PBC)			Dislocation physical parameters					
PL (nm)	MN	WN	SN	t (nm)	b	n_l	T (°C)	CR (nm)
70	10, 20, 30, 40, 60	30	20	32	$a_0[001]$	[001]	25	0.2868

Beam condition	MN				
	10	20	30	40	60
$g(1.1g)$, BF					
$g(3.1g)$, DF					

Figure 6.5: Simulated TEM images of an $a_0[001]$ (001) end-on dislocation within [001] thin bcc Fe TEM foil along [001] pole for studying meshing number effect on black-white contrast, the diffraction vector is: $g=(110)$, and the diffraction conditions are $g(1.1g)$ and $g(3.1g)$. The inclined dislocation model employed for calculation is inclined anisotropic WSL-Wu image gradient model.

It can be seen from Fig. 6.5 that with the increase of meshing number, the simulated TEM image becomes stable, showing black-white lobe contrast.

Chapter.7: Conclusion and perspectives

In this chapter, general conclusion of the thesis is given. Then, perspectives for further research on elastic calculation TEM image simulation including image forces for hcp crystals are given and briefly elaborated.

In this work we have studied in detail the impact of the free surfaces of a TEM bcc Fe thin foil containing a dislocation line and dislocation loop, including elastic field, elastic energy and TEM images contrast. For that purpose, a new method has been developed, and the resulting displacement field including anisotropy was successfully used to simulate the TEM image of the defect, namely a straight inclined dislocation or a dislocation loop.

7.1 Conclusion

7.1.1. Anisotropic image stress method

- The anisotropy image stress method for dealing with the free surfaces problems of defects within a crystalline thin foil was successfully developed, in Fourier space.

7.1.2. Dislocation loops within thin TEM foil

- Qualitative evaluation of the synergistic effects of anisotropy and image stress was made, especially focusing on an a_0001 loop within (001) foil and a $\frac{1}{2} a_0111$ loop within (111) foil.
- For the a_0001 loop within (001) foil case, image stress induced in plane image displacement is quite remarkable, and such in-plane relaxation is closely related to TEM image diffraction contrast modification. The corresponding image energy drops sharply with the increase of depth under free surfaces of thin TEM foil, and such feature does not change so much with increasing anisotropy ratio.
- For the $\frac{1}{2} a_0111$ loop within (111) foil case, image stress induced out-of-plane image displacement is quite remarkable. The corresponding image energy of $\frac{1}{2} a_0111$ loop within (111) foil is quite remarkable, and decreases much flatter than for the a_0001 loop within (001) foil.

7.1.3. TEM contrast of inclined dislocation

- The various types of elasticity models are successfully implemented into many beam TEM image simulation code CUFOUR. Each model has its special physical meaning and can be compared with each other for studying the impact image stress effect, anisotropy, and the synergetic effect of image stress and anisotropy on TEM image contrast of inclined dislocation.
- The effect of beam conditions, zone axis, foil physical properties are studied systematically for $\frac{1}{2} a_0111$ inclined dislocation within bcc Fe thin foil. Simulations indicate that the difference between isotropy and anisotropy models is remarkable. Anisotropy thus cannot be ignored. The comparison to experimental images of screw dislocations in UHP Fe indicates that while anisotropy has indeed a remarkable impact, image forces seem to have a negligible impact when $g \cdot b \neq 0$ but a strong impact when $g \cdot b = 0$. The latter opens very interesting perspectives, as it would allow quantifying them.

7.1.4. TEM contrast of nanometric dislocation loops

- The various types of elasticity models are successfully implemented into many beam TEM image simulation code CUFOUR. Each model has its special physical meaning and can be compared with each other for studying the impact image stress effect, anisotropy, and the synergetic effect of image stress and anisotropy on TEM image contrast of dislocation loops.
- The simulated TEM image via CA is reliable, and the impact of CA on the final black-white contrast modification is not remarkable, when compared to anisotropy effect.

- The classical \mathbf{L} -vector analysis is quite limited for quantitative judgment on Burgers vector \mathbf{b} via only one diffraction experiments. The angle between \mathbf{L} and \mathbf{b} will increase with the increase of the angle between \mathbf{g} and \mathbf{b} , but more slowly. When anisotropy is considered, the \mathbf{L} vector will be rotated slightly, and the black-white lobe will be elongated or compressed.
- When image stress effect is included, additional modification on simulated TEM image based on bulk gradient model is remarkable for $g \cdot b = 0$ weak visibility condition.

7.2. Perspectives

7.2.1. Comparison between MD, isotropic and anisotropic models

There are elasticity and MD based defect models employed for describing the deformation field of a loop. However the capability of these models for very small loops ($R \leq 1$ nm) is still under investigation. Here, following case study from the literature, TEM two beam DF image simulations are performed for $\frac{1}{2} a_0 11\bar{1}$ head-on dislocation loop within (011) bcc Mo thin foil along [011] pole, with different models. The elastic modulus for bcc Mo at room temperature is shown in Table 7.1. The diffraction vectors is $g = (\bar{2}1\bar{1})$, and the diffraction condition is $g(1.0g)$. The simulation parameters are given in Table 7.2, and the simulated images are shown in Fig. 7.1.

Table 7.1: Elastic parameters of pure bcc Mo at room temperature [Featherstone, 1963].

T(°C)	C_{11} (GPa)	C_{12} (GPa)	C_{44} (GPa)	Anisotropy ratio (-)	Shear modulus (GPa)	Poisson ratio (-)	Lattice Parameter (nm)
25	440.77	172.43	121.65	0.9067	54.632	0.3249	a=b=c=0.315

Table 7.2: Simulation parameters for a $\frac{1}{2} a_0 11\bar{1}$ dislocation loop of diameter 2.32 nm within (011) bcc Mo thin foil for $g = (\bar{2}1\bar{1})$ along [011] pole. Foil thickness $t = 121.8$ nm, loops located 118.32 nm from bottom of the foil.

Dislocation loop physical parameters									
HT (KV)	n_f	ZA	SN	t (nm)	\mathbf{b}	n_h	R (nm)	d (nm)	CR (nm)
100	[011]	[011]	40	121.8	$\frac{1}{2} a_0 [11\bar{1}]$	[11 $\bar{1}$]	1.16	118.32	0.1

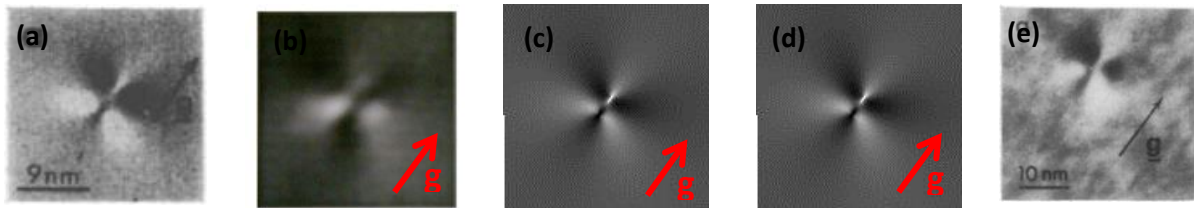


Figure 7.1: Simulated TEM images of a $\frac{1}{2} a_0 11\bar{1}$ dislocation loop of diameter 2.32 nm within (011) bcc Mo thin foil for $g = (\bar{2}1\bar{1})$ along [011] pole. Foil thickness $t = 121.8$ nm, loop located 118.32 nm from bottom of the foil. (a). Isotropy, Eyre, 2B [Eyre, 1977b]; (b). MD, EMS, Multi slice FFT [Stadelmann, 1987; Schaeublin, Private communication, 2014]; (c). Isotropy, CUFOUR, 2B; (d). Anisotropy, CUFOUR, 2B; (e). TEM DF, experimental image, 2B [Eyre, 1977b].

It can be concluded from Fig. 7.1 that the essential “butterfly” contrast features of edge-on dislocation loop via elasticity and MD are preserved, and qualitatively coincide with the ones in the experimental observation. However, this would require further quantitative assessment, in particular for the MD calculation, which exhibits the largest difference relative to the experimental image.

7.2.2. Further application on HCP crystal

The methodology was applied to hcp Zr to study the impact of the image forces via isotropic and anisotropic elasticities for dislocation loops within a half space. The elastic modulus for hcp Zr at room temperature is given in Table 7.3. The image stress effect of a prismatic $c0001$ dislocation loop with $R=5.0$ nm in a $[0001]$ oriented single crystal hcp Zr half space is studied. The crystallographic orientations of (x, y, z) coordinates are $[1\bar{1}00]$, $[11\bar{2}0]$ and $[0001]$ respectively. The simulation parameters are given in Table 7.4, and the simulated image stress and image displacement results are shown in Fig. 7.2 and Fig. 7.3.

Table 7.3: Elastic parameters of pure hcp Zr at room temperature. [Fischer, 1964]

T(°C)	C_{11} (GPa)	C_{12} (GPa)	C_{13} (GPa)	C_{33} (GPa)	C_{44} (GPa)	Shear modulus (GPa)	Poisson ratio (-)	Lattice Parameter (nm)
25	143.4	72.8	65.3	164.8	32.0	36.4067	0.3307	a=b=0.34 c=0.551454

Table 7.4: Simulation parameters for a $c0001$ dislocation loop within (0001) hcp Zr half space.

PBC			Dislocation loop physical parameters					
PL (nm)	MN	WN	SN	\mathbf{b}	\mathbf{n}_h	\mathbf{d} (nm)	\mathbf{R} (nm)	T (°C)
80	80	30	40	$c[0001]$	(0001)	10	5	25

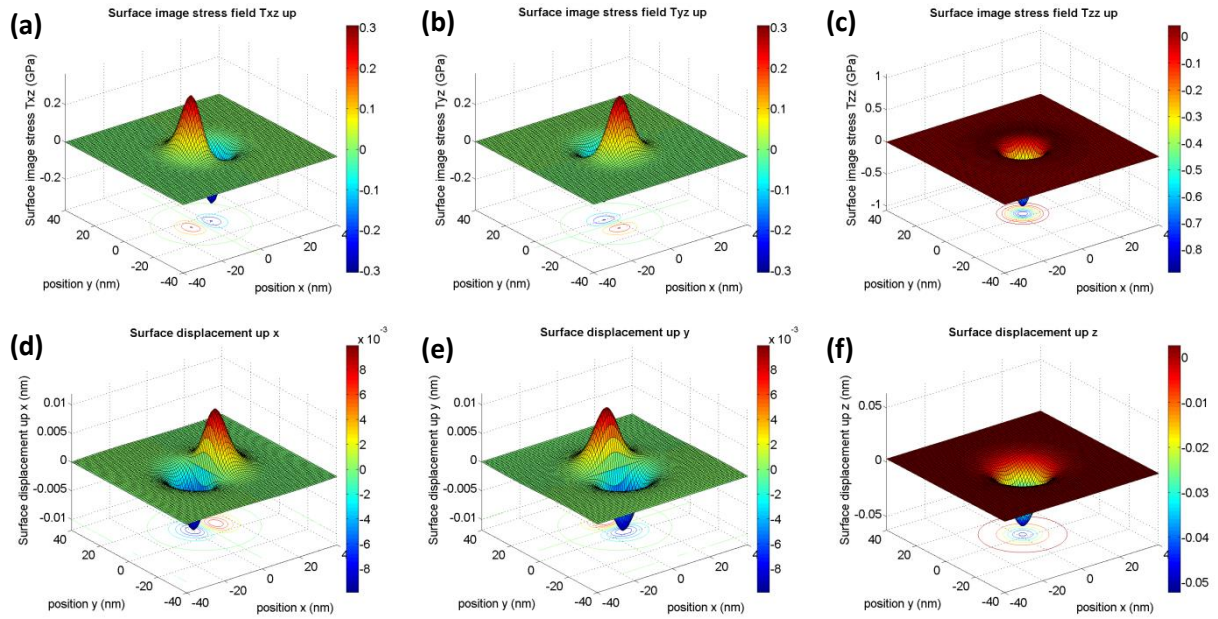


Figure 7.2: Image elastic fields by a $c0001$ loop within a (0001) Zr anisotropic half space, calculated with isotropic Devincere model. Image stress (a), T_{xz} ; (b), T_{yz} ; (c), T_{zz} . Image displacement along (d), X; (e), Y; (f), Z.

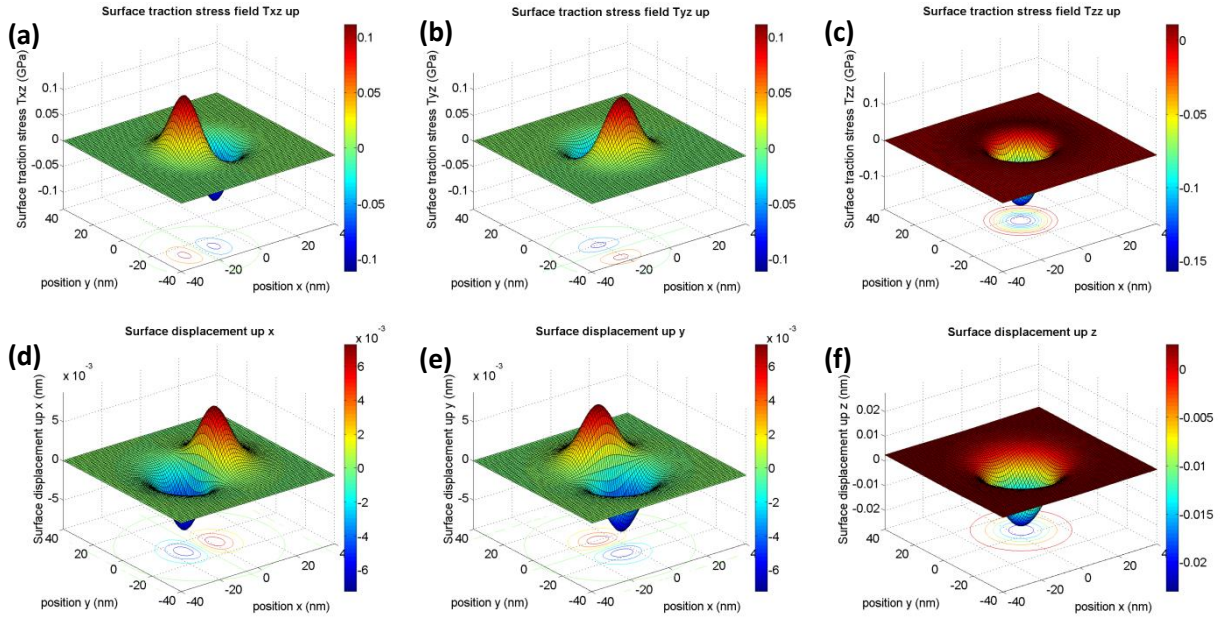


Figure 7.3: Image elastic fields by a $c0001$ loop within a (0001) Zr anisotropic half space, calculated with anisotropic WSL model. Image stress (a), T_{xz} ; (b), T_{yz} ; (c), T_{zz} . Image displacement along (d), X; (e), Y; (f), Z.

From the calculation results shown in Fig. 7.2 and Fig. 7.3, one can conclude that anisotropy cannot be neglected when calculating the image stress induced 3D displacement fields of free surfaces. When comparing the isotropic and anisotropic calculation results for $c0001$ dislocation loop within (0001) hcp Zr half space, the resulting in-plane and out-of-plane image displacement amplitude are (0.0258 nm, 0.0258 nm, 0.0610 nm) and (0.0240 nm, 0.0240 nm, 0.0778 nm) respectively. Hcp Zr gives stronger in plane displacement amplitude with Voigt isotropy model than anisotropy model, and a weaker out-of-plane image displacement with Voigt isotropy model than anisotropy model, thus proving the importance of anisotropic image stress of HCP thin TEM foil.

Reference

- [Akarapu, 2009] Sreekanth Akarapu, Hussein M. Zbib. Line-integral solution for the stress and displacement fields of an arbitrary dislocation segment in isotropic bimetals in 3D space. *Phil. Mag.*, 89(25): 2149-2166, 2009.
- [Arakawa, 2004] K. Arakawa, M. Hatanaka, H. Mori, K. Ono. Effects of chromium on the one-dimensional motion of interstitial-type dislocation loops in iron. *Journal of Nuclear Materials*, 329-333: 1194-1198, 2004.
- [Arakawa, 2006] K. Arakawa, M. Hatanaka, E. Kuramoto, K. Ono, and H. Mori. Changes in the Burgers Vector of Perfect Dislocation Loops without Contact with the External Dislocations. *Phys. Rev. Lett.*, 96: 125506, 2006.
- [Arakawa, 2011] Arakawa, K., Amino, T., Mori, H. Direct observation of the coalescence process between nanoscale dislocation loops with different Burgers vectors. *Acta Materialia*, 59(1): 141-145, 2011.
- [Aubry, 2011] S Aubry, S P Fitzgerald, S L Dudarev and W Cai. Equilibrium shape of dislocation shear loops in anisotropic α -Fe. *Modelling Simul. Mater. Sci. Eng.*, 19: 065006, 2011.
- [Barnett, 1973] D.M. Barnett and J. Lothe. Synthesis of the sextic and the integral formalism for dislocations, Green's functions and surface waves in anisotropic elastic solids. *Phys. Norv.*, 7: 13-19, 1973.
- [Barnett, 1974] D.M. Barnett and J. Lothe. An image force theorem for dislocations in anisotropic bicrystals. *J. Phys. F*, 4: 1618-1635, 1974.
- [Baštecká, 1964] J. Baštecká. Interaction of dislocation loop with free surface. *Czechoslovakij fiziceskij zurnal B*, 14(6): 430-442, 1964.
- [Blin, 1955] J. Blin. Energie Mutuelle de Deux Dislocations. *Acta. Met.*, 3: 199-200, 1955.
- [Bullough, 1960] R. Bullough and R. C. Newman. The spacing of prismatic dislocation loops. *Phil. Mag.*, 5: 921-926, 1960.
- [Bullough, 1971] R. Bullough, D. M. Maher, and R. C. Perrin. Electron microscope image contrast from dislocation loops. *Phys. Stat. Sol. B*, 43: 689-706, 1971.
- [Burgers, 1939] Burgers, J.M. Some considerations on the fields of stress connected with dislocations in a regular crystal lattice. *Proc. Kon. Ned. Akad. Wetenschap*, 42: 293-325, 1939.
- [Cai, 2006] Wei Cai, Athanasios Arsenlis, Christopher R. Weinberger, Vasily V. Bulatov. A nonsingular continuum theory of dislocations. *Journal of the Mechanics and Physics of Solids*, 54: 561-587, 2006.
- [Chen, 1978] C. W. Chen, C. P. Chang, J. D. Elen and A. Mastenbroek. Transmission electron microscopy observation of interstitial clusters in neutron irradiated niobium. *Radiation Effects*, 38: 211-220, 1978.
- [Chen, 2008] J. Chen, P. Jung, W. Hoffelner, H. Ullmaier. Dislocation loops and bubbles in oxide dispersion strengthened ferritic steel after helium implantation under stress. *Acta Materialia*, 56: 250-258, 2008.
- [Chen, 2013] J. Chen, N. Gao, P. Jung, and T. Sauvage. A new mechanism of loop formation and transformation in bcc iron without dislocation reaction. *Journal of Nuclear Materials*, 441(1-3): 216 - 221, 2013.
- [Chu, 2012] H.J. Chu, E. Pan, X. Han, J. Wang, I.J. Beyerlein. Elastic fields of dislocation loops in three-dimensional anisotropic biomaterials. *Journal of the Mechanics and Physics of Solids*, 60: 418-431, 2012.
- [Cockayne, 1969] D. J. H. Cockayne, I. L. F. Ray and M. J. Whelan. Investigations of dislocation strain fields using weak beams. *Phil Mag*, 20(168), 1265-1270, 1969.
- [Cockayne, 1973] Cockayne D J H. The principles and practice of the weak-beam method of electron microscopy. *J. Microscopy*, 98(2): 116-134, (1973).
- [Cowley, 1957] J. M. Cowley and A. F. Moodie. The scattering of electrons by atoms and crystals. I. A new theoretical approach. *Acta Cryst.*, 10: 609-619, 1957.
- [Coze, 2007] J. Le Coze. EFDA contract "Procurement of pure Femetal and Fe-based alloys with controlled chemical alloying element contents and microstructure". Technical Report 06-1901 TW6-TTMS 007-PUREFE, ARMINES Ecole Nationale Supérieure des Mines, 2007.

- [Dellinger, 1991] Joe A. Dellinger. Anisotropic Seismic Wave Propagation. Ph.D thesis, Stanford University, 1991.
- [Dever, 1972] D. J. Dever. Temperature dependence of the elastic constants in α iron single crystals: relationship to spin order and diffusion anomalies. *J. Appl. Phys.*, 43: 3293-3301, 1972.
- [Devincre, 1995] B. Devincré. Three dimensional stress field expressions for straight dislocation segments. *Solid State Communications*, 93(11): 875-878, 1995.
- [Devincre, 2004] Devincré. Recent progress on discrete dislocation dynamics simulations: Discrete Dislocation Plasticity, Cambridge, Thursday 1 July - Friday 2 July, 2004.
- [De Wit, 1960] de Wit R. Continuum Theory of Stationary Dislocations. (Solid State Physics, vol.10, F.Seitz, D.Turnbull, Eds.) Academic Press, New York, 249-292, 1960.
- [Douin, 1998]. Joël Douin, Patrick Veyssière and Georges Saada. Comparison between simulated weak-beam images: application to the extinction criterion in elastically anisotropic crystals. *Phil Mag A*, 77(5): 1323-1340, 1998.
- [Downey, 1965] M.E. Downey and B.L. Eyre. Neutron Irradiation Damage in Molybdenum. *Phil Mag.*, 11: 53-70, 1965.
- [Dudarev, 2003] S.L. Dudarev. Coherent motion of interstitial defects in a crystalline material. *Phil Mag* 83: 3577-3597, 2003.
- [Dudarev, 2005] Dudarev and Derlet. A 'magnetic' interatomic potential for molecular dynamics simulations. *J. Phys.: Condens. Matter.*, 17: 7097, 2005.
- [Dudarev, 2008] S.L. Dudarev, R Bullough, P.M. Derlet. Effect of the α - γ Phase Transition on the Stability of Dislocation Loops in bcc Iron. *Phys. Rev. Lett.*, 100: 135503, 2008.
- [Edington, 1975] J.W. Edington. Interpretation of Transmission Electron Micrographs. Macmillan, 1975.
- [Egerton, 1996] R. F. Egerton. Electron Energy Loss Spectroscopy in the Electron Microscope (2nd edition). Plenum, New York, 1996.
- [English, 1980] C A English, B L Eyre and S M Holmes. Electron microscope image contrast from small dislocation loops. IV. Application of theoretical predictions for non-edge loops to defect analysis in irradiated molybdenum. *J. Phys. F: Metal Phys.* 10: 1065, 1980.
- [Eshelby, 1951] J.D. Eshelby and A.N. Stroh. Dislocations in thin plates. *Phil. Mag.* 42: 1401-1405, 1951.
- [Eyre, 1965a] B.L. Eyre and A.F. Bartlett. An electron microscope study of neutron irradiation damage in alpha-iron. *Phil Mag.*, 12: 261-272, 1965.
- [Eyre, 1965b] B.L. Eyre and R. Bullough. On the formation of interstitial loops in b.c.c. metals. *Philos Mag.*, 12(115): 31-39, 1965.
- [Eyre, 1977a], B L Eyre, D M Maher, and R C Perrint. Electron microscope image contrast from small dislocation loops : I. Theoretical predictions for edge dislocation loops in a BCC crystal. *J. Phys. F: Metal Phys.*, 7(8): 1359-1369, 1977.
- [Eyre, 1977b], B L Eyre, D M Maher, and R C Perrint. Electron microscope image contrast from small dislocation loops : II. Application of theoretical predictions to defect analysis in irradiated metals. *J. Phys. F: Metal Phys.*, 7(8): 1371-1382, 1977.
- [Featherston, 1963] Featherston, F. H.; Neighbours, J. R., Elastic Constants of Tantalum, Tungsten, and Molybdenum, *Physical Review*, 130(4), 1324-1333, 1963.
- [Fischer, 1964] E. S. Fisher and C. J. Renken. Single-Crystal Elastic Moduli and the hcp->bcc Transformation in Ti, Zr, and Hf. *Phys. Rev.*, 135: 482-494, 1964.
- [Fitzgerald, 2009], Steven P. Fitzgerald and Zhongwen Yao. Shape of prismatic dislocation loops in anisotropic α -Fe. *Phil. Mag. Letters*, 89(9): 581-588, 2009.
- [Fitzgerald, 2013] S.P. Fitzgerald, S. Xu. Dislocation instabilities and microstructure in anisotropic α -Fe, *Phil. Mag. Letters*, 93(11): 625-630, 2013.
- [Fivel, 1996] M C Fivel, T J Gosling and G R Canova. Implementing image stresses in a 3D dislocation simulation. *Modelling Simul. Mater. Sci. Eng.*, 4: 581-596, 1996.
- [Fredholm, 1990] I. Fredholm. Sur les equations de l'équilibre d'un corps solide elastique. *Act Math.*, 23: 1-42, 1990.
- [Garner, 2000] F.A Garner, M.B Toloczko, B.H Sencer. Comparison of swelling and irradiation creep behavior of fcc-austenitic and bcc-ferritic/martensitic alloys at high neutron exposure. *J. Nucl. Mater.*, 276: 123-142, 2000.

- [Giessen, 2010] Erik Van der Giessen. Discrete Dislocation Plasticity Analysis of Cracks and Fracture, Multiscale Modelling of Plasticity and Fracture by Means of Dislocation Mechanics. CISM International Centre for Mechanical Sciences, 522: 185-212, 2010.
- [Gosling, 1994] T.J. Gosling, J.R. Willis. A line-integral representation for the stresses due to an arbitrary dislocation in an isotropic half-space. *Journal of the Mechanics and Physics of Solids*, 42(8): 1199-1221, 1994.
- [Goodman, 1974] P. Goodman and A. F. Moodie. Numerical evaluations of N-beam wave functions in electron scattering by the multi-slice method. *Acta Crystallographica Section A.*, 30(2): 280-290, 1974.
- [Graef, 2003] Marc de Graef. Introduction to conventional transmission electron microscopy. Cambridge University, 2003.
- [Haeussermann, 1972] F. Haeussermann. Eine elektronenmikroskopische analyse von versetzungsringen in wolfram nach bestrahlung mit 60 keV-goldionen. *Phils Mag.*, 25(3): 561-581, 1972.
- [Haghighat, 2010] Seyed Masood Hafez Haghighat. Multiscale Modelling of Irradiation Induced Effects on the Plasticity of Fe and Fe-Cr. PhD thesis, EPFL, 2010.
- [Hartmaier, 1999] A Hartmaier, M C Fivel, G R Canova and P Gumbsch. Image stresses in a free-standing thin film. *Modelling Simul. Mater. Sci. Eng.*, 7: 781–793, 1999.
- [Hazzledine, 1975] P.M. Hazzledine, H.P. Karnthaler and G. Wintner. Non-parallel dissociation of dislocations in thin foils. *Phil. Mag.*, 32(1): 81-97, 1975.
- [Head, 1953] A K Head. Edge Dislocations in Inhomogeneous Media. *Proc. Phys. Soc. B.*, 66: 793, 1953.
- [Head, 1973] A.K. Head, P.Humble, L.M.Clarebrough, A J. Morton and C.T.Forwood. Computed electron micrographs and defect identification. North Holland Publication, 1973.
- [Hernández, 2008], M. Hernández-Mayoral, Z. Yao, M.L. Jenkins and M.A. Kirk. Heavy-ion irradiations of Fe and Fe–Cr model alloys Part 2: Damage evolution in thin-foils at higher doses. *Phils Mag.*, 88(21): 2881-2897, 2008.
- [Hirth, 2007] P. B. Hirth , Z. Zhou and D. J. H. Cockayne. Determination of the sign of screw dislocations viewed end-on by weak-beam diffraction contrast. *Phil. Mag.*, 87(34): 5421-5434, 2007.
- [Hirth, 1969] P. B. Hirth, A. Howie, M. J. Whelan, D. W. Pashley, and R. B. Nicholson. *Electron Microscopy in Thin Crystals*. Butterworth, London, 1969.
- [Hirth, 1982] Hirth and Lothe. *Theory of dislocations* (2nd edition). Krieger Publishing Company, Malabar, Florida, 1982.
- [Hirth, 2006]. P. Hirth, D. Cockayne, J. Spence and M. Whelan. 50 Years of TEM of dislocations: Past, present and future. *Phil. Mag.*, 86(29-31): 4519-4528, 2006.
- [Horton, 1982] L.L. Horton, J. Bentley, K. Farrell. A TEM study of neutron-irradiated iron. *J. Nucl. Mater.*, 108-109: 222-233, 1982.
- [Howie, 1961] A. Howie and M.J. Whelan. Diffraction Contrast of Electron Microscope Images of Crystal Lattice Defects. II. The Development of a Dynamical Theory. *Proc. Roy. Soc. London Ser. A.*, 263: 217-237, 1961.
- [Howie, 1968] Howie, A and Basinski, Z S. Approximations of the Dynamical Theory of Diffraction Contrast. *Phil. Mag.*, 17: 1039–1063, 1968.
- [Howie, 1970] A. Howie and H. Sworn. Column Approximation Effects in High Resolution Electron Microscopy using Weak Diffracted Beams. *Phil. Mag.*, 21: 861-864, 1970.
- [Hudson, 2004]. Hudson TS, Dudarev SL, Sutton AP. Confinement of interstitial cluster diffusion by oversized solute atoms. *Proceedings of the Royal Society A: Mathematical, Physical and Engineering Sciences*, 460: 2457-2475, 2004.
- [Hwu, 1991] C. Hwu and W.J. Yen. Green's functions of two-dimensional anisotropic plates containing an elliptic hole. *Int. J. Solids Structures*, 27: 1705–1719, 1991.
- [Iakoubovskii, 2008a] Iakoubovskii, K.; Mitsuishi, K.; Nakayama, Y.; Furuya, K. Thickness measurements with electron energy loss spectroscopy. *Microscopy Research and Technique*, 71(8): 626–631, 2008.
- [Iakoubovskii, 2008b] Iakoubovskii, Konstantin; Mitsuishi, Kazutaka; Nakayama, Yoshiko; Furuya, Kazuo. Mean free path of inelastic electron scattering in elemental solids and oxides using

- transmission electron microscopy: Atomic number dependent oscillatory behavior. *Physical Review B*, 77(10): 104102, 2008.
- [Ishizuka, 1998] K. Ishizuka. Multislice Implementation for Inclined Illumination and Convergent-Beam Electron Diffraction. Proc. International Symposium on Hybrid Analyses For Functional Nanostructure, Kyoto, 1998.
- [Jagannadham, 1978] K. Jagannadham and M. J. Marcinkowski. Comparison of the Image and Surface Dislocation Models. *phys. stat. sol. (a)*, 50: 293-302, 1978.
- [Janssens, 1992] Koenraad G. F. Janssens, Jan Vanhellefont, Marc De Graef, and Omer Van der Biest. SIMCON: a versatile software package for the simulation of electron diffraction contrast images of arbitrary displacement fields. *Ultramicroscopy*, 45: 323-335, 1992.
- [Jenkins, 2001] M.L. Jenkins and M.A. Kirk. Characterization of Radiation Damage by Transmission Electron Microscopy. Institute of Physics Series in Microscopy in Materials Science, Series Editors B. Cantor and M.J. Goringe, Institute of Physics, Bristol and London, 2001.
- [Jenkins, 2009] M.L. Jenkins, Z. Yao, M. Hernandez-Mayoral, M.A. Kirk. Damage development in Fe-Cr alloys under heavy-ion irradiation by IVEM. *Journal of Nuclear Materials*, 389: 197-202, 2009.
- [Jouffrey, 1967] B. Jouffrey and D. Taupin. On the validity of the column approximation in electron microscopy. *Phil. Mag.*, 16: 703-715, 1967.
- [Kirk, 2000] M. A. Kirk, M. L. Jenkins, H. Fukushima. "The Search for Interstitial Dislocation Loops Produced in Displacement Cascades at 20 K in Copper". *J. Nuclear Mater.*, 276: 50-58, 2000.
- [Kirkland, 2010] E. J. Kirkland, *Advanced Computing in Electron Microscopy (2nd Edition)*. Springer Science, New York, 2010.
- [Kiritani, 2000] M. Kiritani. Similarity and difference between fcc, bcc and hcp metals from the view point of point defect cluster formation. *Journal of Nuclear Materials*, 276(1-3): 41-49, 2000.
- [Klimenkov, 2011] M. Klimenkov, E. Materna-Morris, A. Möslang. Characterization of radiation induced defects in EUROFER 97 after neutron irradiation. *J. Nucl. Mater.*, 417: 124-126, 2011.
- [Kohyama, 1996] A. Kohyama, A. Hishinuma, D.S. Gelles, R.L. Klueh, W. Dietz, K. Ehrlich. Low-activation ferritic and martensitic steels for fusion application. *Journal of Nuclear Materials*, 233-237: 138-147, 1996.
- [Kuksenko, 2011] Viacheslav Kuksenko. Université de Rouen-UFR des sciences et techniques, Ph.D thesis, 2011.
- [Ledbetter, 1974] H. M. Ledbetter and E. R. Naimon. Elastic Properties of metals and alloys. II. Copper. *J. Phys. Chem. Ref. Data*, 3(4): 898-935, 1974.
- [Lewis, 1979] A.L. Lewis and R.E. Villagrana. Effects of the column approximation on weak-beam calculations. *Acta Crystallogr. A*35: 276-282, 1979.
- [Li, 2008]. Shaofan Li, Gang Wang. *Introduction To Micromechanics And Nanomechanics*. World Scientific Publishing Company, 2008.
- [Little, 1980] E. A. Little, R. Bullough and M. H. Wood. On the Swelling Resistance of Ferritic Steel. *Proc. R. Soc. Lond.*, 372: 565-576, 1980.
- [Liu, 2005] X H Liu and K W Schwarz. Modelling of dislocations intersecting a free surface. *Modelling Simul. Mater. Sci. Eng.*, 13: 1233-1247, 2005.
- [Lothe, 1982] Lothe J, Indenbom VL, Chamrov VA. Elastic Field and Self-Force of Dislocations Emerging at the Free Surfaces of an Anisotropic Half space. *Phys Stat Sol (b)*, 111: 671, 1982.
- [Luppo, 2000] M.I Luppo, C Bailat, R Schäublin, M Victoria. Tensile properties and microstructure of 590 MeV proton-irradiated pure Fe and a Fe-Cr alloy. *J. Nucl. Mater.*, 283-287: 483-487, 2000.
- [Malerba, 2008] Lorenzo Malerba, Alfredo Caro, Janne Wallenius. Multiscale modelling of radiation damage and phase transformations: The challenge of Fe-Cr alloys. *Journal of Nuclear Materials*, 382(2-3), 112-125, 2008.
- [Marian, 2002] Jaime Marian, Brian D. Wirth, and J. Manuel Perlado. Mechanism of Formation and Growth of $\langle 100 \rangle$ Interstitial Loops in Ferritic Materials. *Phys. Rev. Lett.*, 88: 255507-1, 2002.
- [Masters, 1963] B. C. Masters, Dislocation loops in irradiated iron, *Nature*, 200, 254, 1963.
- [Masters, 1965] B.C. Masters. Dislocation loops in irradiated iron. *Phil. Mag.*, 11: 881-893, 1965.
- [Mendis, 2008] B.G. Mendis, K.J. Hemker, Bloch wave analysis of the Eshelby twist contrast around end-on screw dislocations in bcc Mo, *Ultramicroscopy*, 108, 855- 864, 2008.
- [Meakin, 1965] J.D. Meakin and I.G. Greenfield. Interstitial loops in neutron irradiated molybdenum. *Phil. Mag.*, 11: 277-290, 1965.

- [Mesquita, 2013] Amir Zacarias Mesquita. Current Research in Nuclear Reactor Technology in Brazil and Worldwide. InTech, 2013.
- [Mills, 1989] M. J. Mills and P. A. Stadelmann. A study of the structure of lomer and 60 degree dislocations in aluminium using high-resolution transmission electron microscopy. *Phil. Mag.*, 60: 355-384, 1989.
- [Moll, 2013], S. Moll, T. Jourdan, and H. Lefaix-Jeuland. Direct Observation of Interstitial Dislocation Loop Coarsening in-Iron. *PRL*, 111: 015503, 2013.
- [Mura, 1963] Mura, T. Continuous distribution of moving dislocations. *Phil. Mag.*, 8: 843-857, 1963.
- [Mura, 1968] Mura, T. "Continuum Theory of Dislocations and Plasticity," *Mechanics of Generalized Continua*. Springer-Verlag, New York, 269-278, 1968.
- [Mura, 1987] Toshio Mura. *Micromechanics of defects in solids*, Second, revised edition. Martinus Nijhoff publishers, 1987.
- [Muroga, 1996] T. Muroga, Y. Nonaka, N. Yoshida. Dislocation evolution in a model and a candidate ferritic alloy during steady and varying temperature electron irradiations. *J. Nucl. Mater.*, 233-237: 1035-1039, 1996.
- [Murty, 2008] K.L. Murty, I. Charit. Structural materials for Gen-IV nuclear reactors: Challenges and opportunities. *Journal of Nuclear Materials*, 383: 189-195, 2008.
- [Nabarro, 2007] Frank Nabarro, John Hirth. *Dislocation in solid*. volume 13, Elsevier Science, 2007.
- [Narayan, 1976] J. Narayan and S.M. Ohr. The characteristics of 15 MeV and fission neutron damage in niobium. *J. Nucl. Mater.*, 63: 454-459, 1976.
- [Ohr, 1977]. Ohr S M. Proc. 35th Annual Meeting of Electron Microscopy Society of America. 52, 1977.
- [Ohsawa, 2009] K Ohsawa, M Yagi, H Koizumi and E Kuramoto. Stress function for dislocation loops in anisotropic crystals. *IOP Conf. Series: Materials Science and Engineering*, 3: 012027, 2009.
- [Ohsawa, 2011] Kazuhito Ohsawa, Masatoshi Yagi, Hirokazu Koizumi, Eiichi Kuramoto. Interaction energy between dislocation loops in an anisotropic crystal: Application of elasticity theory. *Journal of Nuclear Materials*, 417:1071-1073, 2011.
- [Packan, 1979] N. H. Packan and K. Farrell. Simulation of first wall damage: Effects of the method of gas implantation. *Journal of Nuclear Materials*, 85-86, Part 2(0): 677 - 681, 1979.
- [Pan, 2000b] Ernian Pan, Fulvio Tonon. Three-dimensional Green's functions in anisotropic piezoelectric solids. *International Journal of Solids and Structures*, 37: 943-958, 2000.
- [Peach, 1950] M. Peach and J. S. Kohler. The forces exerted on dislocations and the stress fields produced by them. *Phys. Rev.*, 80: 436-439, 1950.
- [Prokhodtseva, 2013] Anna Prokhodtseva. *Modelling Oriented Investigations of Primary Radiation Damage in Ultra High Purity Fe and Fe-Cr Alloys*. PhD thesis, EPFL, 2013.
- [Rasmussen, 1991] Rasmussen, D R and Carter, C B. A Computer Program for Many-Beam Image Simulation of Amplitude-Contrast Images. *J. Electron Microsc. Techniques*, 18: 429-36, 1991.
- [Reuss, 1929] Reuss A. Berechnung der fließgrenze von mischkristallen auf grund der plastizitätsbedingung für einkristalle. *Z. Angew. Math. Mech.*, 9: 49-58, 1929.
- [Robertson, 1982] I.M. Robertson, M.L. Jenkins, C.A. English. Low-dose neutron-irradiation damage in α -iron. *J. Nucl. Mater.*, 108-109: 209-221, 1982.
- [Ruhle, 1965] Ruhle M, Wilkens M, U Essman. Zur Deutung der elektronenmikroskopischen Kontrasterscheinungen an Fehlstellenagglomeraten in neutronenbestrahltem Kupfer. *Phys. Status Solidi*, 11(2): 819-829, 1965.
- [Saldin, 1979a] D. K. Saldin and M. J. Whelan. Displacement fields of dislocation loops and stacking-fault tetrahedra from angular dislocation segments. *Phil. Trans. Roy. Soc.*, A292: 513, 1979.
- [Saldin, 1979b], D. K. Saldin, A. Y. Stathopoulos, M. J. Whelan. Electron Microscope Image Contrast of Small Dislocation Loops and Stacking-Fault Tetrahedra. *Philosophical Transactions of the Royal Society of London. Series A, Mathematical and Physical Sciences*. 292(1397): 523-537, 1979.
- [Schäublin, 1993], R. Schäublin, P. Stadelmann. A method for simulating electron microscope dislocation images, *Materials Science and Engineering, A*, 164: 373-378, 1993.
- [Schäublin, 2000], R. Schäublin, A. Almazouzi, Y. Dai, Yu.N. Osetsky, M. Victoria. Quantitative analysis of CTEM images of small dislocation loops in Al and stacking fault tetrahedra in Cu generated by molecular dynamics simulation. *Journal of Nuclear Materials*, 276: 251-257, 2000.

- [Schäublin, 2002] R. Schaeublin, D. Gelles, M. Victoria. Microstructure of irradiated ferritic/martensitic steels in relation to mechanical properties. *J. Nucl. Mater.*, 307-311: 197-202, 2002.
- [Schaublin, 2006], R. Schaublin. Nanometric Crystal Defects in Transmission Electron Microscopy. *Microscopy Research and Technique*, 69: 305–316, 2006.
- [Shiraishi, 1974] K. Shiraishi, K. Fukaya, Y. Katano. Radiation and anneal hardening in neutron-irradiated vanadium. *J. Nucl. Mater.*, 54: 275, 1974.
- [Sikka, 1973] V.K. Sikka and J. Moteff. “Rafting” in neutron irradiated tungsten. *J. Nucl. Mater.*, 46: 217, 1973.
- [Stadelmann, 1987] P. A. Stadelmann. EMS - a software package for electron diffraction analysis and HREM image simulation in materials science. *Ultramicroscopy*, 21:131-146, 1987.
- [Stobbs, 1971] W.M. Stobbs, C.H. Sworn. The weak beam technique as applied to the determination of the stacking-fault energy of copper. *Philos. Mag.* 24(192), 1365-1381, 1971.
- [Straumanis, 1969] M. E. Straumanis And L. S. Yu, Lattice Parameters, Densities, Expansion Coefficients and Perfection of Structure of Cu and of Cu-In a Phase, *Acta Cryst.* (1969). A25, 676-682.
- [Stroh, 1958] A.N. Stroh. Dislocations and cracks in anisotropic elasticity. *Phil. Mag.*, 3: 625–646, 1958.
- [Stroh, 1962] A.N. Stroh. Steady state problems in anisotropic elasticity. *J. Math. Phys.*, 41: 77–103, 1962.
- [Suganuma, 1981] K. Suganuma and H. Kayano. Dislocation loops in electron irradiated ferritic stainless steel. *Radiation Effects.*, 54: 81, 1981.
- [Suganuma, 1982] Katsuki Suganuma, Hideo Kayano, Seishi Yajima. Mechanical properties changes of Fe-Cr alloys by fast neutron irradiation. *J. Nucl. Mater.*, 105(1): 23-35, 1982.
- [Takagi, 1962] Takagi, S. Dynamical Theory of Diffraction Applicable to Crystals with Any Kind of Small Distortion. *Acta Cryst.*, 15: 1311–1312, 1962.
- [Takagi, 1969] Satio Takagi. A Dynamical Theory of Diffraction for a Distorted Crystal. *J. Phys. Soc. Jpn.*, 26: 1239-1253, 1969.
- [Tang, 2006] Meijie Tang, Wei Cai, Guanshui Xu and Vasily V Bulatov. A hybrid method for computing forces on curved dislocations intersecting free surfaces in three-dimensional dislocation dynamics. *Modelling Simul. Mater. Sci. Eng.*, 14: 1139–1151, 2006.
- [Khraishi, 2002] Tariq A. Khraishi, Hussein M. Zbib. Free-Surface Effects in 3D Dislocation Dynamics: Formulation and Modeling. *Transactions of the ASME*, 124: 342-351, 2002.
- [Terentyev, 2005] D. Terentyev, L. Malerba, A.V. Barashev. On the correlation between self-interstitial cluster diffusivity and irradiation-induced swelling in Fe–Cr alloys. *Phil. Mag. Letters*, 85: 587, 2005.
- [Terentyev, 2009] D. Terentyev, M. Klimenkov, L. Malerba. Confinement of motion of interstitial clusters and dislocation loops in BCC Fe-Cr alloys. *Journal of Nuclear Materials*, 393: 30-35, 2009.
- [Ting, 1982] T.C.T. Ting. Effects of change of reference coordinates on the stress analyses of anisotropic elastic materials. *Int. J. Solids Structures*, 18: 139–152, 1982.
- [Ting, 1992] T.C.T. Ting. Image singularities of Green’s functions for anisotropic elastic half-spaces and bimetals. *Q.J. Mech. Appl. Math.*, 45: 120–139, 1992.
- [Tunstall, 1964] W.J. Tunstall, P.B. Hirth and J. Steeds. Effects of surface stress relaxation on the electron microscope images of dislocations normal to thin metal foils. *Phil. Mag.*, 9: 99, 1964.
- [Ullmaier, 1980] Ullmaier H, Schilling W. Radiation damage in metallic reactor materials. In: *Physics of Modern Materials*, vol. I. IAEA, Vienna, 1980.
- [Voigt, 1889] W. Voigt. Ueber die Beziehung zwischen den beiden Elasticitätsconstanten isotroper Körper. *Ann. Phys.*, 38: 573, 1889.
- [Volterra, 1907] Volterra, V. Sur l’équilibre des corps élastiques multiplement connexes. *Ann. Ecole Norm. Super.*, 24: 400, 1907.
- [Wang, 1994] C.-Y. Wang. 2D elastostatic Green’s functions for general anisotropic solids and generalization of Stroh’s formalism. *Int. J. Solids Structure*, 31: 2591–2597, 1994.
- [Wang, 1997] C.-Y. WANG. Elastic fields produced by a point source in solids of general anisotropy. *Journal of Engineering Mathematics*, 32: 41–52, 1997.
- [Ward, 1989] A.E. Ward and S.B. Fisher. Dislocation loop growth in pure iron under electron irradiation. *J. Nucl. Mater.*, 166: 227, 1989.

- [Was, 2007] Gary S Was. *Fundamentals of Radiation Materials Science*. Springer, 2007.
- [Weinberger, 2007] Christopher R. Weinberger, Wei Cai. Computing image stress in an elastic cylinder, *Journal of the Mechanics and Physics of Solids*, 55: 2027–2054, 2007.
- [Weinberger, 2009] Christopher R Weinberger, Sylvie Aubry, Seok-Woo Lee, William D Nix and Wei Cai. Modelling dislocations in a free-standing thin film, *Modelling Simul. Mater. Sci. Eng.*, 17: 075007, 2009.
- [Whelan, 1957] M.J.Whelan, P.B. Hirth, R.W.Horne and W.Bollman. Dislocations and stacking faults in Stainless Steel. *Proc. Roy. Soc.*, 240: 524-538, 1957.
- [Wiezorek, 1995] Wiezorek JM, Preston AR, Humphreys CJ. Column approximation effects on partial dislocation weak beam images. *Institute of Physics Conference Series.*, IOP Publishing Ltd., 455–458, 1995.
- [Wilkens, 1972] M. Wilkens and M. Rühle. Black-white contrast figures from small dislocation loops I. analytical first order perturbation solution. *Phys. Stat. Sol.*, (b) 49:749, 1972.
- [Wilkens, 1981], M.Wilkens, H.O.K. Kirchner. Black-white contrast on transmission electron microscope images of small dislocation loops in elastically anisotropic crystals. *Phil. Mag.*, 43(1): 139-156, 1981.
- [Willaime, 2005] F. Willaime, C.C. Fu, M.C. Marinica, J. Dalla Torre. Stability and mobility of self-interstitials and small interstitial clusters in α -iron: ab initio and empirical potential calculations. *Nucl. Instr. Meth. In Phy. Res. B.*, 228: 92-99, 2005.
- [Williams, 2009] David B. Williams, C. Barry Carter. *Transmission Electron Microscopy-A Textbook for Materials Science*. Springer, 2nd edition, 2009.
- [Wu, 2012] Wenwang Wu, Robin Schäublin, Jiachao Chen. General dislocation image stress of anisotropic cubic thin film. *Journal of Applied Physics*, 112: 093522, 2012.
- [Xu, 2013] H. Xu, R. E. Stoller, Yu. N. Osetsky, and D. Terentyev. Solving the puzzle of [100] interstitial loop formation in bcc iron. *Physical Review Letters*, 110: 265503, 2013.
- [Yao, 2005] Zhongwen Yao. The relationship between the irradiation induced damage and the mechanical properties of single crystal Ni, PhD thesis, EPFL, 2005.
- [Yao, 2008] Yao, Z.; Hernandez-Mayoral, M.; Jenkins, M. L.; Kirk, M. A. Heavy-ion irradiations of Fe and Fe–Cr model alloys Part 1: Damage evolution in thin-foils at lower doses. *Phil.Mag.*, 88(21): 2851-2880, 2008.
- [Yin, 2010] Jie Yin, David M. Barnett, and Wei Cai. Efficient Computation of Forces on Dislocation Segments in Anisotropic Elasticity. *Modelling and Simulation in Materials Science and Engineering*, 18(4): 045013, 2010.
- [Yoffe, 1960] Yoffe, E. H. The angular dislocation. *Phil. Mag.*, 5: 161-175, 1960.
- [Yvon, 2009] P. Yvon, F. Carré. Structural materials challenges for advanced reactor systems. *Journal of Nuclear Materials*, 385: 217-222, 2009.
- [Zhou, 2005] Zhongfu Zhou. *Electron Microscopy and Elastic Diffuse Scattering of Nanostructures*. PhD thesis, University of Oxford, 2005.
- [Zhou, 2006]. Z. Zhou, M. L. Jenkins, S. L. Dudarev, A. P. Sutton and M. A. Kirk. Simulations of weak-beam diffraction contrast images of dislocation loops by the many-beam Howie–Basinski equations. *Philosophical Magazine*, 86(29-31): 4851-4881, 2006.
- [Zhou, 2004] Z. Zhou, S. L. Dudarev, M. L. Jenkins and A. P. Sutton. A comparison of the Column Approximation and the Howie-Basinski approach in simulations of TEM images under weak-beam conditions. Source: *Institute of Physics Conference Series*, 179: 203-206, 2004.
- [Zinkle, 2000] S.J. Zinkle, N.M. Ghoniem. Operating temperature windows for fusion reactor structural materials. *Fusion Engineering and Design*, 51–52: 55–71, 2000.
- [Zinkle, 2006] S.J. Zinkle, B.N. Singh. Microstructure of neutron-irradiated iron before and after tensile deformation. *J. Nucl. Mater.*, 351: 269-284, 2006.

Appendix

Appendix A: The invisibility criterion $\mathbf{g}\cdot\mathbf{b}$ for bcc Fe crystal

\mathbf{g}	\mathbf{b}							
	$\frac{1}{2} [111]$	$\frac{1}{2} [\bar{1}11]$	$\frac{1}{2} [1\bar{1}1]$	$\frac{1}{2} [11\bar{1}]$	$\frac{1}{2} [\bar{1}\bar{1}1]$	$\frac{1}{2} [1\bar{1}\bar{1}]$	$\frac{1}{2} [\bar{1}1\bar{1}]$	$\frac{1}{2} [1\bar{1}\bar{1}]$
$[\bar{1}10]$	0	-1	1	0	0	1	-1	0
$[\bar{1}\bar{1}0]$	0	1	-1	0	0	-1	1	0
$[\bar{1}10]$	-1	0	0	-1	1	0	0	1
$[110]$	1	0	0	1	-1	0	0	-1
$[020]$	1	1	-1	1	-1	-1	1	-1
$[0\bar{2}0]$	-1	-1	1	-1	1	1	-1	1
$[200]$	-1	1	-1	-1	1	-1	1	1
$[\bar{2}00]$	1	-1	1	1	-1	1	-1	-1

Table A. 1: The invisibility criterion $\mathbf{g}\cdot\mathbf{b}$ for diffraction vectors in the $[001]$ pattern for the $\frac{1}{2} a_0 \langle 111 \rangle$ dislocation in bcc Fe.

\mathbf{g}	\mathbf{b}							
	$\frac{1}{2} [111]$	$\frac{1}{2} [\bar{1}11]$	$\frac{1}{2} [1\bar{1}1]$	$\frac{1}{2} [11\bar{1}]$	$\frac{1}{2} [\bar{1}\bar{1}1]$	$\frac{1}{2} [1\bar{1}\bar{1}]$	$\frac{1}{2} [\bar{1}1\bar{1}]$	$\frac{1}{2} [1\bar{1}\bar{1}]$
$[01\bar{1}]$	0	0	-1	1	-1	0	1	0
$[0\bar{1}1]$	0	0	1	-1	1	0	-1	0
$[\bar{2}00]$	-1	1	-1	-1	1	-1	1	1
$[200]$	1	-1	1	1	-1	1	-1	-1
$[\bar{2}\bar{1}1]$	1	-1	2	0	0	1	-2	-1
$[\bar{2}1\bar{1}]$	-1	1	-2	0	0	-1	2	1
$[\bar{2}\bar{1}\bar{1}]$	-1	1	0	-2	2	-1	0	1
$[21\bar{1}]$	1	-1	0	2	-2	1	0	-1

Table A. 2: The invisibility criterion $\mathbf{g}\cdot\mathbf{b}$ for diffraction vectors in the $[011]$ pattern for the $\frac{1}{2} a_0 \langle 111 \rangle$ dislocation in bcc Fe.

\mathbf{g}	\mathbf{b}							
	$\frac{1}{2} [111]$	$\frac{1}{2} [\bar{1}11]$	$\frac{1}{2} [1\bar{1}1]$	$\frac{1}{2} [11\bar{1}]$	$\frac{1}{2} [\bar{1}\bar{1}1]$	$\frac{1}{2} [1\bar{1}\bar{1}]$	$\frac{1}{2} [\bar{1}1\bar{1}]$	$\frac{1}{2} [1\bar{1}\bar{1}]$
$[01\bar{1}]$	0	0	-1	1	-1	0	1	0
$[110]$	1	0	0	1	-1	0	0	-1
$[101]$	1	0	1	0	0	0	-1	-1
$[0\bar{1}1]$	0	0	1	-1	1	0	-1	0
$[\bar{1}10]$	-1	0	0	-1	1	0	0	1
$[\bar{1}0\bar{1}]$	-1	0	-1	0	0	0	1	1
$[\bar{2}\bar{1}\bar{1}]$	-2	0	-1	-1	1	0	1	2
$[1\bar{1}2]$	1	0	2	-1	1	0	-2	-1
$[12\bar{1}]$	1	0	-1	2	-2	0	1	-1

Table A. 3: The invisibility criterion $\mathbf{g}\cdot\mathbf{b}$ for diffraction vectors in the $[111]$ pattern for the $\frac{1}{2} a_0 \langle 111 \rangle$ dislocation in bcc Fe.

Appendix B: Anisotropic image stress matrix for half space and film

Appendix B. 1: [001] cubic semi space

 (a) the $(k_x \neq 0, k_y \neq 0)$ mode.

$$\begin{cases} \xi_j = (-k_y^2 C_{11} - k_x^2 C_{44} + q_j^2 C_{44})(q_j^2 C_{11} - k_x^2 C_{44} - k_y^2 C_{44}) + k_y^2 q_j^2 (C_{12} + C_{44})^2; \\ \eta_j = -k_x k_y q_j^2 (C_{12} + C_{44})^2 + k_x k_y (C_{12} + C_{44})(q_j^2 C_{11} - k_x^2 C_{44} - k_y^2 C_{44}); \quad (j = 1, 2, 3) \\ \zeta_j = -ik_x k_y q_j (C_{12} + C_{44})^2 - ik_x q_j (C_{12} + C_{44})(-k_y^2 C_{11} - k_x^2 C_{44} + q_j^2 C_{44}); \end{cases} \quad (\text{A.2-1})$$

$$[N^-] = \begin{pmatrix} N_{11} & N_{12} & N_{13} \\ N_{21} & N_{22} & N_{23} \\ N_{31} & N_{32} & N_{33} \end{pmatrix}; \begin{cases} N_{1j} = \xi_j e^{+q_j z}; \\ N_{2j} = \eta_j e^{+q_j z}; \quad (j = 1, 2, 3) \\ N_{3j} = \zeta_j e^{+q_j z}; \end{cases} \quad (\text{A.2-2})$$

$$[M^-] = \begin{pmatrix} M_{11} & M_{12} & M_{13} \\ M_{21} & M_{22} & M_{23} \\ M_{31} & M_{32} & M_{33} \end{pmatrix}; \begin{cases} M_{1j} = C_{44} (\xi_j q_j + ik_x \zeta_j) e^{+q_j z}; \\ M_{2j} = C_{44} (\eta_j q_j + ik_y \zeta_j) e^{+q_j z}; \quad (j = 1, 2, 3) \\ M_{3j} = (ik_x C_{12} \zeta_j + ik_y C_{12} \eta_j + C_{11} \zeta_j q_j) e^{+q_j z}; \end{cases} \quad (\text{A.2-3})$$

 (b) the $(k_x = 0, k_y \neq 0)$ mode.

$$[N^-] = \begin{pmatrix} N_{11} & 0 & 0 \\ 0 & N_{22} & N_{23} \\ 0 & N_{32} & N_{33} \end{pmatrix}; \begin{cases} N_{11} = e^{+|k_y|z}; \\ N_{2j} = ik_y q_j (C_{12} + C_{44}) e^{+q_j z}; \quad (j = 2, 3) \\ N_{3j} = -(C_{44} q_j^2 - C_{11} k_y^2) e^{+q_j z}; \end{cases} \quad (\text{A.2-4})$$

$$[M^-] = \begin{pmatrix} M_{11} & 0 & 0 \\ 0 & M_{22} & M_{23} \\ 0 & M_{32} & M_{33} \end{pmatrix}; \begin{cases} M_{11} = |k_y| C_{44} e^{+|k_y|z}; \\ M_{2j} = iC_{44} (C_{12} + C_{44}) k_y q_j^2 e^{+q_j z} - ik_y C_{44} (C_{44} q_j^2 - C_{11} k_y^2) e^{+q_j z}; \quad (j = 2, 3) \\ M_{3j} = -C_{12} (C_{12} + C_{44}) (k_y)^2 q_j e^{+q_j z} - q_j C_{11} (C_{44} q_j^2 - C_{11} k_y^2) e^{+q_j z}; \end{cases} \quad (\text{A.2-5})$$

 (c) the $(k_x \neq 0, k_y = 0)$ mode.

$$[N^-] = \begin{pmatrix} 0 & N_{12} & N_{13} \\ N_{21} & 0 & 0 \\ 0 & N_{32} & N_{33} \end{pmatrix}; \begin{cases} N_{1j} = ik_x q_j (C_{12} + C_{44}) e^{+q_j z}; \\ N_{21} = e^{+|k_x|z}; \quad (j = 2, 3) \\ N_{3j} = -(C_{44} q_j^2 - C_{11} k_x^2) e^{+q_j z}; \end{cases} \quad (\text{A.2-6})$$

$$[M^-] = \begin{pmatrix} 0 & M_{12} & M_{13} \\ M_{21} & 0 & 0 \\ 0 & M_{32} & M_{33} \end{pmatrix}; \begin{cases} M_{1j} = iC_{44} (C_{12} + C_{44}) k_x q_j^2 e^{+q_j z} - ik_x C_{44} (C_{44} q_j^2 - C_{11} k_x^2) e^{+q_j z}; \\ M_{21} = |k_x| C_{44} e^{+|k_x|z}; \quad (j = 2, 3) \\ M_{3j} = -C_{12} (C_{12} + C_{44}) k_x^2 q_j e^{+q_j z} - q_j C_{11} (C_{44} q_j^2 - C_{11} k_x^2) e^{+q_j z}; \end{cases} \quad (\text{A.2-7})$$

Appendix B. 2: [0001] HCP semi space

 (a) the $(k_x \neq 0, k_y \neq 0)$ mode.

$$\frac{U_j}{\xi_j} = \frac{V_j}{\eta_j} = \frac{W_j}{\zeta_j} = K_j; \quad (j = 1, 2, 3) \quad (\text{A.2-8})$$

$$\xi_j = \det \begin{pmatrix} D_{22} & D_{23} \\ D_{32} & D_{33} \end{pmatrix}; \eta_j = \det \begin{pmatrix} D_{23} & D_{21} \\ D_{33} & D_{31} \end{pmatrix}; \zeta_j = \det \begin{pmatrix} D_{21} & D_{22} \\ D_{31} & D_{32} \end{pmatrix}.$$

$$\begin{cases} D_{11} = -k_x^2 \cdot C_{11} - k_y^2 \cdot \frac{1}{2}(C_{11} - C_{12}) + q_j^2 \cdot C_{44}; \\ D_{22} = q_j^2 \cdot C_{44} - k_x^2 \cdot \frac{1}{2}(C_{11} - C_{12}) - k_y^2 \cdot C_{11}; \\ D_{33} = q_j^2 \cdot C_{33} - k_y^2 \cdot C_{44} - k_x^2 \cdot C_{44}; \\ D_{23} = D_{32} = (ik_y q_j)(C_{44} + C_{13}); \\ D_{31} = D_{13} = (ik_x q_j)(C_{13} + C_{44}); \\ D_{12} = D_{21} = -k_x k_y \frac{1}{2}(C_{11} + C_{12}); \end{cases} \quad ; (j = 1, 2, 3) \quad (\text{A.2-9})$$

$$[N^-] = \begin{pmatrix} N_{11} & N_{12} & N_{13} \\ N_{21} & N_{22} & N_{23} \\ N_{31} & N_{32} & N_{33} \end{pmatrix}; \begin{cases} N_{1j} = \xi_j \exp(q_j \cdot z); \\ N_{2j} = \eta_j \exp(q_j \cdot z); \\ N_{3j} = \zeta_j \exp(q_j \cdot z); \end{cases} \quad (j = 1, 2, 3) \quad (\text{A.2-10})$$

$$[M^-] = \begin{pmatrix} M_{11} & M_{12} & M_{13} \\ M_{21} & M_{22} & M_{23} \\ M_{31} & M_{32} & M_{33} \end{pmatrix}; \begin{cases} M_{1j} = C_{44}(q_j \cdot \xi_j + ik_x \cdot \zeta_j) \exp(q_j \cdot z); \\ M_{2j} = C_{44}(q_j \cdot \eta_j + ik_y \cdot \zeta_j) \exp(q_j \cdot z); \\ M_{3j} = (C_{13} ik_x \cdot \xi_j + C_{13} ik_y \cdot \eta_j + C_{33} q_j \cdot \zeta_j) \exp(q_j \cdot z); \end{cases} \quad (j = 1, 2, 3) \quad (\text{A.2-11})$$

(b) the $(k_x = 0, k_y \neq 0)$ mode.

$$[N^-] = \begin{pmatrix} N_{11} & 0 & 0 \\ 0 & N_{22} & N_{23} \\ 0 & N_{32} & N_{33} \end{pmatrix}; \begin{cases} N_{11} = \exp\left(|k_y| \cdot \sqrt{\frac{1}{2} \frac{(C_{11} - C_{12})}{C_{44}}} \cdot z\right); \\ N_{2j} = (iq_j k_y)(C_{44} + C_{13}) \exp(+q_j \cdot z); \\ N_{3j} = -(q_j^2 \cdot C_{44} - k_y^2 \cdot C_{11}) \exp(+q_j \cdot z); \end{cases} \quad (j = 2, 3) \quad (\text{A.2-12})$$

$$[M^-] = \begin{pmatrix} M_{11} & 0 & 0 \\ 0 & M_{22} & M_{23} \\ 0 & M_{32} & M_{33} \end{pmatrix}; \begin{cases} M_{11} = \left(|k_y| \cdot \sqrt{\frac{1}{2} \frac{(C_{11} - C_{12})}{C_{44}}}\right) C_{44} \exp\left(|k_y| \cdot \sqrt{\frac{1}{2} \frac{(C_{11} - C_{12})}{C_{44}}} \cdot z\right); \\ M_{2j} = (ik_y) C_{44} (C_{13} q_j^2 + k_y^2 \cdot C_{11}) \cdot \exp(q_j \cdot z); \\ M_{3j} = [-C_{13} k_y^2 q_j (C_{44} + C_{13}) - C_{33} q_j (q_j^2 C_{44} - k_y^2 C_{11})] \cdot \exp(q_j \cdot z); \end{cases} \quad (j = 2, 3) \quad (\text{A.2-13})$$

(c) the $(k_x \neq 0, k_y = 0)$ mode.

$$[N^-] = \begin{pmatrix} 0 & N_{12} & N_{13} \\ N_{21} & 0 & 0 \\ 0 & N_{32} & N_{33} \end{pmatrix}; \begin{cases} N_{1j} = (ik_x q_j)(C_{44} + C_{13}) \exp(+q_j \cdot z); \\ N_{21} = \exp\left(|k_x| \cdot \sqrt{\frac{1}{2} \frac{(C_{11} - C_{12})}{C_{44}}} \cdot z\right); \\ N_{3j} = -(q_j^2 C_{44} - k_x^2 C_{11}) \exp(+q_j \cdot z); \end{cases} \quad (j = 2, 3) \quad (\text{A.2-14})$$

$$[M^-] = \begin{pmatrix} 0 & M_{12} & M_{13} \\ M_{21} & 0 & 0 \\ 0 & M_{32} & M_{33} \end{pmatrix}; \begin{cases} M_{1j} = (ik_x) C_{44} (q_j^2 C_{13} + k_x^2 C_{11}) \exp(+q_j \cdot z); \\ M_{21} = \left(|k_x| \cdot \sqrt{\frac{1}{2} \frac{(C_{11} - C_{12})}{C_{44}}}\right) C_{44} \exp\left(|k_x| \cdot \sqrt{\frac{1}{2} \frac{(C_{11} - C_{12})}{C_{44}}} \cdot z\right); \\ M_{3j} = [-C_{13} k_x^2 q_j (C_{44} + C_{13}) - C_{33} q_j (q_j^2 C_{44} - k_x^2 C_{11})] \exp(+q_j \cdot z); \end{cases} \quad (j = 2, 3) \quad (\text{A.2-15})$$

Appendix B. 3: [001] cubic film

 (a) the $(k_x \neq 0, k_y \neq 0)$ mode.

$$\begin{cases} \xi_j^S = \left[-k_y^2 C_{11} - k_x^2 C_{44} + (q_j^S)^2 C_{44} \right] \left[(q_j^S)^2 C_{11} - k_x^2 C_{44} - k_y^2 C_{44} \right] + k_y^2 (q_j^S)^2 (C_{12} + C_{44})^2; \\ \eta_j^S = -k_x k_y (q_j^S)^2 (C_{12} + C_{44})^2 + k_x k_y (C_{12} + C_{44}) \left[(q_j^S)^2 C_{11} - k_x^2 C_{44} - k_y^2 C_{44} \right]; \\ \zeta_j^S = -ik_x k_y^2 q_j^S (C_{12} + C_{44})^2 - ik_x q_j^S (C_{12} + C_{44}) \left[-k_y^2 C_{11} - k_x^2 C_{44} + (q_j^S)^2 C_{44} \right]; \end{cases} \quad (j=1,2,3) \quad (\text{A.2-16})$$

$$\left[N^S \right] = \begin{pmatrix} N_{11} & N_{12} & N_{13} \\ N_{21} & N_{22} & N_{23} \\ N_{31} & N_{32} & N_{33} \end{pmatrix}; \begin{cases} N_{1j} = \xi_j^S \sinh(+q_j^S z); \\ N_{2j} = \eta_j^S \sinh(+q_j^S z); \\ N_{3j} = \zeta_j^S \cosh(+q_j^S z); \end{cases} \quad (j=1,2,3) \quad (\text{A.2-17})$$

$$\left[M^S \right] = \begin{pmatrix} M_{11} & M_{12} & M_{13} \\ M_{21} & M_{22} & M_{23} \\ M_{31} & M_{32} & M_{33} \end{pmatrix}; \begin{cases} M_{1j} = C_{44} (\xi_j^S q_j^S + ik_x \zeta_j^S) \cosh(+q_j^S z); \\ M_{2j} = C_{44} (\eta_j^S q_j^S + ik_y \zeta_j^S) \cosh(+q_j^S z); \\ M_{3j} = (ik_x \xi_j^S C_{12} + ik_y \eta_j^S C_{12} + q_j^S \zeta_j^S C_{11}) \sinh(+q_j^S z); \end{cases} \quad (j=1,2,3) \quad (\text{A.2-18})$$

$$\begin{cases} \xi_j^A = \left[-k_y^2 C_{11} - k_x^2 C_{44} + (q_j^A)^2 C_{44} \right] \left[(q_j^A)^2 C_{11} - k_x^2 C_{44} - k_y^2 C_{44} \right] + k_y^2 (q_j^A)^2 (C_{12} + C_{44})^2; \\ \eta_j^A = -k_x k_y (q_j^A)^2 (C_{12} + C_{44})^2 + k_x k_y (C_{12} + C_{44}) \left[(q_j^A)^2 C_{11} - k_x^2 C_{44} - k_y^2 C_{44} \right]; \\ \zeta_j^A = -ik_x k_y^2 q_j^A (C_{12} + C_{44})^2 - ik_x q_j^A (C_{12} + C_{44}) \left[-k_y^2 C_{11} - k_x^2 C_{44} + (q_j^A)^2 C_{44} \right]; \end{cases} \quad (i=1,2,3) \quad (\text{A.2-19})$$

$$\left[N^A \right] = \begin{pmatrix} N_{11} & N_{12} & N_{13} \\ N_{21} & N_{22} & N_{23} \\ N_{31} & N_{32} & N_{33} \end{pmatrix}; \begin{cases} N_{1j} = \xi_j^A \cosh(+q_j^A z); \\ N_{2j} = \eta_j^A \cosh(+q_j^A z); \\ N_{3j} = \zeta_j^A \sinh(+q_j^A z); \end{cases} \quad (j=1,2,3) \quad (\text{A.2-20})$$

$$\left[M^A \right] = \begin{pmatrix} M_{11} & M_{12} & M_{13} \\ M_{21} & M_{22} & M_{23} \\ M_{31} & M_{32} & M_{33} \end{pmatrix}; \begin{cases} M_{1j} = C_{44} (\xi_j^A q_j^A + ik_x \zeta_j^A) \sinh(+q_j^A z); \\ M_{2j} = C_{44} (\eta_j^A q_j^A + ik_y \zeta_j^A) \sinh(+q_j^A z); \\ M_{3j} = (ik_x \xi_j^A C_{12} + ik_y \eta_j^A C_{12} + q_j^A \zeta_j^A C_{11}) \cosh(+q_j^A z); \end{cases} \quad (j=1,2,3) \quad (\text{A.2-21})$$

 (b) the $(k_x = 0, k_y \neq 0)$ mode.

$$\left[N^S \right] = \begin{pmatrix} N_{11} & 0 & 0 \\ 0 & N_{22} & N_{23} \\ 0 & N_{32} & N_{33} \end{pmatrix}; \begin{cases} N_{1j} = \sinh(+|k_y|z); \\ N_{2j} = ik_y q_j^S (C_{12} + C_{44}) \sinh(+q_j^S z); \\ N_{3j} = -\left[-k_y^2 C_{11} + (q_j^S)^2 C_{44} \right] \cosh(+q_j^S z); \end{cases} \quad (j=1,2,3) \quad (\text{A.2-22})$$

$$\left[M^S \right] = \begin{pmatrix} M_{11} & 0 & 0 \\ 0 & M_{22} & M_{23} \\ 0 & M_{32} & M_{33} \end{pmatrix}; \begin{cases} M_{11} = C_{44} |k_y| \cosh(+|k_y|z); \\ M_{2j} = iC_{44} k_y (q_j^S)^2 (C_{12} + C_{44}) \cosh(+q_j^S z) - iC_{44} k_y \left[-k_y^2 C_{11} + (q_j^S)^2 C_{44} \right] \cosh(+q_j^S z); \\ M_{3j} = -k_y^2 q_j^S C_{12} (C_{12} + C_{44}) \sinh(+q_j^S z) - C_{11} q_j^S \left[-k_y^2 C_{11} + (q_j^S)^2 C_{44} \right] \sinh(+q_j^S z); \end{cases} \quad (j=1,2,3) \quad (\text{A.2-23})$$

$$[N^A] = \begin{pmatrix} N_{11} & 0 & 0 \\ 0 & N_{22} & N_{23} \\ 0 & N_{32} & N_{33} \end{pmatrix}; \begin{cases} N_{11} = \cosh(+|k_y|z); \\ N_{2j} = ik_y q_j^A (C_{12} + C_{44}) \cosh(+q_j^A z); \quad (j = 2, 3) \\ N_{3j} = -[(q_j^A)^2 C_{44} - k_y^2 C_{11}] \sinh(+q_j^A z); \end{cases} \quad (\text{A.2-24})$$

$$[M^A] = \begin{pmatrix} M_{11} & 0 & 0 \\ 0 & M_{22} & M_{23} \\ 0 & M_{32} & M_{33} \end{pmatrix}; \begin{cases} M_{11} = |k_y| C_{44} \sinh(+|k_y|z); \\ M_{2j} = iC_{44} k_y (q_j^A)^2 (C_{12} + C_{44}) \sinh(+q_j^A z) - iC_{44} k_y [(q_j^A)^2 C_{44} - k_y^2 C_{11}] \sinh(+q_j^A z); \quad (j = 2, 3) \\ M_{3j} = -k_y^2 C_{12} (C_{12} + C_{44}) q_j^A \cosh(+q_j^A z) - C_{11} q_j^A [(q_j^A)^2 C_{44} - k_y^2 C_{11}] \cosh(+q_j^A z); \end{cases} \quad (\text{A.2-25})$$

(c) the $(k_x \neq 0, k_y = 0)$ mode.

$$[N^S] = \begin{pmatrix} 0 & N_{12} & N_{13} \\ N_{21} & 0 & 0 \\ 0 & N_{32} & N_{33} \end{pmatrix}; \begin{cases} N_{1j} = ik_x q_j^S (C_{12} + C_{44}) \sinh(+q_j^S z); \\ N_{21} = \sinh(+|k_x|z); \quad (j = 2, 3) \\ N_{3j} = -[C_{44} (q_j^S)^2 - C_{11} k_x^2] \cosh(+q_j^S z); \end{cases} \quad (\text{A.2-26})$$

$$[M^S] = \begin{pmatrix} 0 & M_{12} & M_{13} \\ M_{21} & 0 & 0 \\ 0 & M_{32} & M_{33} \end{pmatrix}; \begin{cases} M_{1j} = ik_x C_{44} (C_{12} + C_{44}) (q_j^S)^2 \cosh(q_j^S z) - ik_x C_{44} [C_{44} (q_j^S)^2 - C_{11} k_x^2] \cosh(+q_j^S z); \\ M_{21} = |k_x| C_{44} \cosh(+|k_x|z); \quad (j = 2, 3) \\ M_{3j} = -C_{12} (C_{12} + C_{44}) k_x^2 q_j^S \sinh(q_j^S z) - C_{11} q_j^S [C_{44} (q_j^S)^2 - C_{11} k_x^2] \sinh(+q_j^S z); \end{cases} \quad (\text{A.2-27})$$

$$[N^A] = \begin{pmatrix} 0 & N_{12} & N_{13} \\ N_{21} & 0 & 0 \\ 0 & N_{32} & N_{33} \end{pmatrix}; \begin{cases} N_{1j} = ik_x q_j^A (C_{12} + C_{44}) \cosh(+q_j^A z); \\ N_{21} = \cosh(+|k_x|z); \quad (j = 2, 3) \\ N_{3j} = -[(q_j^A)^2 C_{44} - k_x^2 C_{11}] \sinh(+q_j^A z); \end{cases} \quad (\text{A.2-28})$$

$$[M^A] = \begin{pmatrix} 0 & M_{12} & M_{13} \\ M_{21} & 0 & 0 \\ 0 & M_{32} & M_{33} \end{pmatrix}; \begin{cases} M_{1j} = ik_x C_{44} (C_{12} + C_{44}) (q_j^A)^2 \sinh(q_j^A z) - ik_x C_{44} [(q_j^A)^2 C_{44} - k_x^2 C_{11}] \sinh(+q_j^A z); \\ M_{21} = |k_x| C_{44} \sinh(+|k_x|z); \quad (j = 2, 3) \\ M_{3j} = -k_x^2 q_j^A C_{12} (C_{12} + C_{44}) \cosh(q_j^A z) - q_j^A C_{11} [(q_j^A)^2 C_{44} - k_x^2 C_{11}] \cosh(+q_j^A z); \end{cases} \quad (\text{A.2-29})$$

Appendix B. 4: [111] cubic film

(a) the $(k_{x'} = 0, k_{y'} \neq 0)$ and $(k_{x'} \neq 0, k_{y'} = 0)$ mode.

$$\frac{U_j'}{\xi_j'} = \frac{V_j'}{\eta_j'} = \frac{W_j'}{\zeta_j'} = K_j'; \quad (j = 1, 2, 3) \quad (\text{A.2-30})$$

$$\xi_j' = \det \begin{pmatrix} D_{22}' & D_{23}' \\ D_{32}' & D_{33}' \end{pmatrix}; \eta_j' = \det \begin{pmatrix} D_{23}' & D_{21}' \\ D_{33}' & D_{31}' \end{pmatrix}; \zeta_j' = \det \begin{pmatrix} D_{21}' & D_{22}' \\ D_{31}' & D_{32}' \end{pmatrix}.$$

$$\begin{cases}
 D_{11}^j = \left[-C_{11}' k_x'^2 + 2ik_x' q_j' \cdot C_{16}' - C_{55}' k_y'^2 + (q_j')^2 \cdot C_{44}' \right]; \\
 D_{22}^j = \left[C_{44}' (q_j')^2 - 2ik_x' \cdot C_{16}' q_j' - k_x'^2 \cdot C_{55}' - k_y'^2 \cdot C_{11}' \right]; \\
 D_{33}^j = \left[-k_y'^2 \cdot C_{44}' - k_x'^2 \cdot C_{44}' + C_{22}' (q_j')^2 \right]; \\
 D_{23}^j = D_{32}^j = \left[ik_y' \cdot C_{44}' q_j' + 2k_x' k_y' \cdot C_{16}' + ik_x' q_j' \cdot C_{12}' \right]; \\
 D_{13}^j = D_{31}^j = \left[-k_x'^2 \cdot C_{16}' + ik_x' \cdot C_{44}' q_j' + ik_x' q_j' \cdot C_{12}' + k_y'^2 \cdot C_{16}' \right]; \\
 D_{12}^j = D_{21}^j = \left[-ik_y' \cdot C_{16}' q_j' - k_x' k_y' \cdot C_{55}' - k_y' k_x' \cdot C_{13}' - ik_y' q_j' \cdot C_{16}' \right];
 \end{cases} \quad (j=1,2,3) \tag{A.2-31}$$

$$[N^S] = \begin{pmatrix} N_{11}' & N_{12}' & N_{13}' \\ N_{21}' & N_{22}' & N_{23}' \\ N_{31}' & N_{32}' & N_{33}' \end{pmatrix}; \begin{cases} N_{1j} = \xi_j' \sinh(q_j' \cdot z'); \\ N_{2j} = \eta_j' \sinh(q_j' \cdot z'); \\ N_{3j} = \zeta_j' \cosh(q_j' \cdot z'); \end{cases} \quad (j=1,2,3) \tag{A.2-32}$$

$$[M^S] = \begin{pmatrix} M_{11}' & M_{12}' & M_{13}' \\ M_{21}' & M_{22}' & M_{23}' \\ M_{31}' & M_{32}' & M_{33}' \end{pmatrix}; \begin{cases} M_{1j} = [ik_x' \cdot \xi_j C_{16}' + q_j' \cdot \xi_j C_{44}' - ik_y' \cdot \eta_j C_{16}' + ik_x' \cdot \zeta_j C_{44}'] \cdot \cosh(q_j' \cdot z'); \\ M_{2j} = [q_j' \cdot \eta_j C_{44}' + ik_y' \cdot \zeta_j C_{44}' - ik_x' \cdot \eta_j C_{16}' - ik_y' \cdot \xi_j C_{16}'] \cdot \cosh(q_j' \cdot z'); \\ M_{3j} = [ik_x' \cdot \xi_j C_{12}' + ik_y' \cdot \eta_j C_{12}' + q_j' \cdot \zeta_j C_{22}'] \cdot \sinh(q_j' \cdot z'); \end{cases} \quad (j=1,2,3) \tag{A.2-33}$$

$$[N^A] = \begin{pmatrix} N_{11}' & N_{12}' & N_{13}' \\ N_{21}' & N_{22}' & N_{23}' \\ N_{31}' & N_{32}' & N_{33}' \end{pmatrix}; \begin{cases} N_{1j} = \xi_j' \cosh(q_j' \cdot z'); \\ N_{2j} = \eta_j' \cosh(q_j' \cdot z'); \\ N_{3j} = \zeta_j' \sinh(q_j' \cdot z'); \end{cases} \quad (j=1,2,3) \tag{A.2-34}$$

$$[M^A] = \begin{pmatrix} M_{11}' & M_{12}' & M_{13}' \\ M_{21}' & M_{22}' & M_{23}' \\ M_{31}' & M_{32}' & M_{33}' \end{pmatrix}; \begin{cases} M_{1j} = [ik_x' \cdot \xi_j C_{16}' + q_j' \cdot \xi_j C_{44}' - ik_y' \cdot \eta_j C_{16}' + ik_x' \cdot \zeta_j C_{44}'] \cdot \sinh(q_j' \cdot z'); \\ M_{2j} = [q_j' \cdot \eta_j C_{44}' + ik_y' \cdot \zeta_j C_{44}' - ik_x' \cdot \eta_j C_{16}' - ik_y' \cdot \xi_j C_{16}'] \cdot \sinh(q_j' \cdot z'); \\ M_{3j} = [ik_x' \cdot \xi_j C_{12}' + ik_y' \cdot \eta_j C_{12}' + q_j' \cdot \zeta_j C_{22}'] \cdot \cosh(q_j' \cdot z'); \end{cases} \quad (j=1,2,3) \tag{A.2-35}$$

(b) the $(k_x' \neq 0, k_y' = 0)$ mode.

$$[N^S] = \begin{pmatrix} 0 & N_{12}' & N_{13}' \\ N_{21}' & 0 & 0 \\ 0 & N_{32}' & N_{33}' \end{pmatrix}; \begin{cases} N_{1j} = (ik_x' \cdot q_j' C_{44}' + ik_x' \cdot q_j' C_{12}' - k_x'^2 \cdot C_{16}') \sinh(+q_j' \cdot z'); \\ N_{21} = \sinh\left(\frac{ik_x' C_{16}' + |k_x'| \cdot \sqrt{(C_{55}' C_{44}' - C_{16}' C_{16}')}}{C_{44}'} \cdot z'\right); \\ N_{3j} = -\left[C_{44}' (q_j')^2 + 2ik_x' C_{16}' q_j' - k_x'^2 \cdot C_{11}'\right] \cosh(+q_j' \cdot z'); \end{cases} \quad (j=2,3) \tag{A.2-36}$$

$$[M^S] = \begin{pmatrix} 0 & M_{12}' & M_{13}' \\ M_{21}' & 0 & 0 \\ 0 & M_{32}' & M_{33}' \end{pmatrix}; \begin{cases} M_{1j} = [+ik_x' (q_j')^2 C_{44}' C_{12}' + ik_x'^3 \cdot C_{11}' C_{44}' - k_x'^2 q_j' C_{16}' C_{12}' - ik_x'^3 \cdot C_{16}' C_{16}'] \cosh(q_j' \cdot z'); \\ M_{21} = (+|k_x'| \cdot \sqrt{(C_{55}' C_{44}' - C_{16}' C_{16}')}) \cosh\left(+\frac{ik_x' C_{16}' + |k_x'| \cdot \sqrt{(C_{55}' C_{44}' - C_{16}' C_{16}')}}{C_{44}'} z\right); \\ M_{3j} = \begin{bmatrix} -k_x'^2 q_j' \cdot C_{12}' C_{44}' - k_x'^2 q_j' \cdot C_{12}' C_{12}' - ik_x'^3 \cdot C_{12}' C_{16}' \\ -(q_j')^3 C_{22}' C_{44}' - 2ik_x' (q_j')^2 C_{22}' C_{16}' + k_x'^2 q_j' \cdot C_{22}' C_{11}' \end{bmatrix} \sinh(q_j' \cdot z'); \end{cases} \quad (j=2,3) \tag{A.2-37}$$

$$\left[N^A \right] = \begin{pmatrix} 0 & N'_{12} & N'_{13} \\ N'_{21} & 0 & 0 \\ 0 & N'_{32} & N'_{33} \end{pmatrix}; \begin{cases} N'_{1j} = (ik_{x'} \cdot q'_j C'_{44} + ik_{x'} \cdot q'_j C'_{12} - k_{x'}^2 \cdot C'_{16}) \cosh(+q'_j \cdot z'); \\ N'_{21} = \cosh \left(\frac{ik_{x'} C'_{16} + |k_{x'}| \cdot \sqrt{(C'_{55} C'_{44} - C'_{16} C'_{16})}}{C'_{44}} \cdot z' \right); \quad (j=2,3) \\ N'_{3j} = - \left[C'_{44} (q'_j)^2 + 2ik_{x'} C'_{16} q'_j - k_{x'}^2 \cdot C'_{11} \right] \sinh(+q'_j \cdot z'); \end{cases} \quad (\text{A.2-38})$$

$$\left[M^A \right] = \begin{pmatrix} 0 & M'_{12} & M'_{13} \\ M'_{21} & 0 & 0 \\ 0 & M'_{32} & M'_{33} \end{pmatrix}; \begin{cases} M'_{1j} = \left[+ik_{x'} (q'_j)^2 C'_{44} C'_{12} + ik_{x'}^3 \cdot C'_{11} C'_{44} - k_{x'}^2 q'_j C'_{16} C'_{12} - ik_{x'}^3 \cdot C'_{16} C'_{16} \right] \sinh(q'_j \cdot z'); \\ M'_{21} = \left(+|k_{x'}| \cdot \sqrt{(C'_{55} C'_{44} - C'_{16} C'_{16})} \right) \sinh \left(+ \frac{ik_{x'} C'_{16} + |k_{x'}| \cdot \sqrt{(C'_{55} C'_{44} - C'_{16} C'_{16})}}{C'_{44}} z' \right); \quad (j=2,3) \\ M'_{3j} = \left[-k_{x'}^2 q'_j \cdot C'_{12} C'_{44} - k_{x'}^2 q'_j \cdot C'_{12} C'_{12} - ik_{x'}^3 \cdot C'_{12} C'_{16} \right. \\ \left. - (q'_j)^3 C'_{22} C'_{44} - 2ik_{x'} (q'_j)^2 C'_{22} C'_{16} + k_{x'}^2 q'_j \cdot C'_{22} C'_{11} \right] \cosh(q'_j \cdot z'); \end{cases} \quad (\text{A.2-39})$$

Appendix C: CUFOUR subroutines algorithm for TEM image simulation

Algorithm. 4.1:

The details for implementing inclined isotropic Devincere-Weinberger image gradient model into CUFOUR are described as following:

-
- 1 Input: Parameters declaration ($\mathbf{r}, \mathbf{r}', \mathbf{C}_{ijkl}, \mathbf{SN}, \mathbf{T}_{\text{dislocation}}, \mathbf{T}_{\text{foil}}, \mathbf{T}_{\text{beam}}, \mathbf{n}, \mathbf{b}$).
 - 2 Output: ($\mathbf{du}/\mathbf{dz}, \mathbf{dv}/\mathbf{dz}, \mathbf{dw}/\mathbf{dz}$)
 - 3 **Step.1: Building up the simulation physical condition.**
 - 4 Define simulated TEM image sizes, and receive the calculated position vector \mathbf{r} from TEM image simulation code CUFOUR.
 - 5 Define geometrical and physical parameters of TEM foil, diffraction beam, dislocation loop, such as: modulus \mathbf{C}_{ijkl} , core radius \mathbf{CR} , inclined dislocation segmentation number \mathbf{SN} , and initialize the transformation matrix between crystal coordinate, beam coordinate, TEM foil coordinate and inclined dislocation coordinate: $\mathbf{T}_{\text{dislocation}}, \mathbf{T}_{\text{foil}}, \mathbf{T}_{\text{beam}}$ respectively.
 - 6 Define inclined dislocation direction vector and Burger vector \mathbf{LV}, \mathbf{b} respectively.
 - 7 Calculate Voigt isotropic equivalent modulus $\boldsymbol{\mu}$, poisson ratio \mathbf{v} , and Lamé $\boldsymbol{\lambda}$.
 - 8 Initialize the Kronecker-Delta operator $\boldsymbol{\delta}_{ij}$, Levi-Civita permutation operator $\boldsymbol{\epsilon}_{ijk}$.
 - 9 Segmentation of inclined dislocation, and the position of dislocation segment is described by \mathbf{r}' .
 - 10 **Step.2: Calculate the image stress field at free surfaces of thin TEM foil.**
 - 11 Meshing the free surface of thin foil with given periodic length and meshing step (\mathbf{PL}, \mathbf{MS}).
 - 12 **for** $-\mathbf{PL}/2 < \mathbf{x} < \mathbf{PL}/2, -\mathbf{PL}/2 < \mathbf{y} < \mathbf{PL}/2$ **do**
 - 13 **If** \mathbf{r} is within the dislocation core region of inclined dislocation of TEM thin foil, then
 - 14 Calculate dislocation core stress tensor $\boldsymbol{\sigma}_{ij}^{\text{core}}$, according to eigengenstress in basic crystal coordinate, and the user can decide including core stress or not into the following simulation.
 - 15 **else**
 - 16 Calculate the inclined dislocation induced bulk stress value via isotropic Devincere dislocation segment integration at given position \mathbf{r} , according to formula (4-1) to (4-5) in crystal coordinate.
 - 17 Perform integration along dislocation line, and harvest the bulk stress and image stress at free surfaces of thin TEM foil, according to free traction BC.
 - 18 **end if**
 - 19 **end for**
 - 20 Transform the image stress field from crystal coordinate to beam coordinate.
 - 21 **Step.3: Perform isotropic Weinberger image gradient calculation in Fourier space.**
 - 22 Perform 2D discrete Fourier transformation of the harvested image stress field through isotropic Devincere dislocation segment integration, and comparison will be made between isotropic Devincere dislocation segment integration model and isotropic Weinberger image stress models in Fourier space, thus satisfying free traction BC for each $(\mathbf{k}_x, \mathbf{k}_y)$ Fourier mode. Then, the 2D discrete Fourier coefficients for the symmetrical and asymmetrical image displacement field of isotropic Weinberger image stress model can be calculated out respectively.
 - 23 Finally, the 2D discrete Fourier coefficients are employed for image gradient value ($\mathbf{du}/\mathbf{dz}, \mathbf{dv}/\mathbf{dz}, \mathbf{dw}/\mathbf{dz}$) calculation in electron beam coordinate via reverse FFT transformation process at given position \mathbf{r} within thin TEM foil, and returned back into CUFOUR for Runge-Kutta integration along electron propagation direction.
-

Algorithm. 4.2:

The details for implementing inclined isotropic Mura-Weinberger image gradient model into CUFOUR are described as following:

-
- 1 Input: Parameters declaration ($\mathbf{r}, \mathbf{r}', \mathbf{C}_{ijkl}, \mathbf{SN}, \mathbf{T}_{\text{dislocation}}, \mathbf{T}_{\text{foil}}, \mathbf{T}_{\text{beam}}, \mathbf{n}, \mathbf{b}$).
 - 2 Output: ($\mathbf{du}/\mathbf{dz}, \mathbf{dv}/\mathbf{dz}, \mathbf{dw}/\mathbf{dz}$)
 - 3 **Step.1: Building up the simulation physical condition.**
 - 4 Define simulated TEM image sizes, and receive the calculated position vector \mathbf{r} from TEM image simulation code CUFOUR.
 - 5 Define geometrical and physical parameters of TEM foil, diffraction beam, dislocation loop, such as: modulus \mathbf{C}_{ijkl} , core radius \mathbf{CR} , inclined dislocation segmentation number \mathbf{SN} , and initialize the

transformation matrix between crystal coordinate, beam coordinate, TEM foil coordinate and inclined dislocation coordinate: $\mathbf{T}_{\text{dislocation}}$, \mathbf{T}_{foil} , \mathbf{T}_{beam} respectively.

6 Define inclined dislocation direction vector , and Burger vector \mathbf{LV} , \mathbf{b} respectively.

7 Calculate Voigt isotropic equivalent modulus $\boldsymbol{\mu}$, poisson ratio \mathbf{v} , and Lamé $\boldsymbol{\lambda}$.

8 Initialize the Kronecker-Delta operator $\boldsymbol{\delta}_{ij}$, Levi-Civita permutation operator $\boldsymbol{\epsilon}_{ijk}$.

9 Segmentation of inclined dislocation, and the position of dislocation segment is described by \mathbf{r}' .

10 **Step.2: Calculate the image stress field at free surfaces of thin TEM foil.**

11 Meshing the free surface of thin foil with given periodic length and meshing step (\mathbf{PL} , \mathbf{MS}).

12 **for** $-\mathbf{PL}/2 < \mathbf{x} < \mathbf{PL}/2$, $-\mathbf{PL}/2 < \mathbf{y} < \mathbf{PL}/2$ **do**

13 **If** \mathbf{r} is within the dislocation core region of inclined dislocation of TEM thin foil, then

14 Calculate dislocation core stress tensor $\boldsymbol{\sigma}_{ij}^{\text{core}}$, according to eigenstress in basic crystal coordinate, and the user can decide including core stress or not into the following simulation.

15 **else**

16 Calculate the inclined dislocation induced bulk stress value via isotropic Mura dislocation segment integration at given position \mathbf{r} , according to formula (4-6) to (4-9) in crystal coordinate.

17 Perform integration along dislocation line, and harvest the bulk stress and image stress at free surfaces of thin TEM foil, according to free traction BC.

18 **end if**

19 **end for**

20 Transform the image stress field from crystal coordinate to beam coordinate.

21 **Step.3: Perform isotropic Weinberger image gradient calculation in Fourier space.**

22 Perform 2D discrete Fourier transformation of the harvested image stress field through isotropic Mura dislocation segment integration, and comparison will be made between isotropic Mura dislocation segment integration model and isotropic Weinberger image stress models in Fourier space, thus satisfying free traction BC for each $(\mathbf{k}_x, \mathbf{k}_y)$ Fourier mode. Then, the 2D discrete Fourier coefficients for the symmetrical and asymmetrical image displacement field of isotropic Weinberger image stress model can be calculated out respectively.

23 Finally, the 2D discrete Fourier coefficients are employed for image gradient value $(\mathbf{du}/\mathbf{dz}, \mathbf{dv}/\mathbf{dz}, \mathbf{dw}/\mathbf{dz})$ calculation in electron beam coordinate via reverse FFT transformation process at given position \mathbf{r} within thin TEM foil, and returned back into CUFOUR for Runge-Kutta integration along electron propagation direction.

Algorithm. 4.3:

The details for implementing inclined anisotropic WSL-Wu image gradient model into CUFOUR are described as following:

1 Input: Parameters declaration $(\mathbf{r}, \mathbf{r}', \mathbf{C}_{ijkl}, \mathbf{SN}, \mathbf{T}_{\text{dislocation}}, \mathbf{T}_{\text{foil}}, \mathbf{T}_{\text{beam}}, \mathbf{n}, \mathbf{b})$.

2 Output: $(\mathbf{du}/\mathbf{dz}, \mathbf{dv}/\mathbf{dz}, \mathbf{dw}/\mathbf{dz})$

3 Step.1: **Building up the simulation physical condition.**

4 Define simulated TEM image sizes, and receive the calculated position vector \mathbf{r} from TEM image simulation code CUFOUR.

5 Define geometrical and physical parameters of TEM foil, diffraction beam, dislocation loop, such as: modulus \mathbf{C}_{ijkl} , core radius \mathbf{CR} , inclined dislocation segmentation number \mathbf{SN} , and initialize the transformation matrix between crystal coordinate, beam coordinate, TEM foil coordinate and inclined dislocation coordinate: $\mathbf{T}_{\text{dislocation}}$, \mathbf{T}_{foil} , \mathbf{T}_{beam} respectively.

6 Define inclined dislocation direction vector , and Burger vector \mathbf{LV} , \mathbf{b} respectively.

7 Calculate Voigt isotropic equivalent modulus $\boldsymbol{\mu}$, poisson ratio \mathbf{v} , and Lamé $\boldsymbol{\lambda}$.

8 Initialize the Kronecker-Delta operator $\boldsymbol{\delta}_{ij}$, Levi-Civita permutation operator $\boldsymbol{\epsilon}_{ijk}$.

9 Segmentation of inclined dislocation, and the position of dislocation segment is described by \mathbf{r}' .

10 **Step.2: Calculate the image stress field at free surfaces of thin TEM foil.**

11 Meshing the free surface of thin foil with given periodic length and meshing step (\mathbf{PL} , \mathbf{MS}).

12 **for** $-\mathbf{PL}/2 < \mathbf{x} < \mathbf{PL}/2$, $-\mathbf{PL}/2 < \mathbf{y} < \mathbf{PL}/2$ **do**

13 **If** \mathbf{r} is within the dislocation core region of inclined dislocation of TEM thin foil, then

14 Calculate dislocation core stress tensor $\boldsymbol{\sigma}_{ij}^{\text{core}}$, according to eigenstress in basic crystal coordinate, and the user can decide including core stress or not into the following simulation.

15 **else**

-
- 16 Calculate the inclined dislocation induced bulk stress value via anisotropic WSL dislocation segment integration at given position \mathbf{r} , according to formula (4-10) to (4-18) in crystal coordinate.
 - 17 Perform integration along dislocation line, and harvest the bulk stress and image stress at free surfaces of thin TEM foil, according to free traction BC.
 - 18 **end if**
 - 19 **end for**
 - 20 Transform the image stress field from crystal coordinate to beam coordinate.
 - 21 **Step.3: Perform anisotropic Wu image gradient calculation in Fourier space.**
 - 22 Perform 2D discrete Fourier transformation of the harvested image stress field through anisotropic WSL dislocation segment integration, and comparison will be made between anisotropic WSL dislocation segment integration model and anisotropic Wu image stress models in Fourier space, thus satisfying free traction BC for each $(\mathbf{k}_x, \mathbf{k}_y)$ Fourier mode. Then, the 2D discrete Fourier coefficients for the symmetrical and asymmetrical image displacement field of anisotropic Wu image stress model can be calculated out respectively.
 - 23 Finally, the 2D discrete Fourier coefficients are employed for image gradient value $(\mathbf{du}/\mathbf{dz}, \mathbf{dv}/\mathbf{dz}, \mathbf{dw}/\mathbf{dz})$ calculation in electron beam coordinate via reverse FFT transformation process at given position \mathbf{r} within thin TEM foil, and returned back into CUFOUR for Runge-Kutta integration along electron propagation direction.
-

Algorithm. 4.4:

The details for implementing inclined isotropic Mura finite gradient model into CUFOUR are described as following:

- 1 Input: Parameters declaration $(\mathbf{r}, \mathbf{r}', \mathbf{C}_{ijkl}, \mathbf{SN}, \mathbf{T}_{\text{dislocation}}, \mathbf{T}_{\text{foil}}, \mathbf{T}_{\text{beam}}, \mathbf{n}, \mathbf{b})$.
 - 2 Output: $(\mathbf{du}/\mathbf{dz}, \mathbf{dv}/\mathbf{dz}, \mathbf{dw}/\mathbf{dz})$
 - 3 Step.1: **Building up the simulation physical condition.**
 - 4 Define simulated TEM image sizes, and receive the calculated position vector \mathbf{r} from TEM image simulation code CUFOUR.
 - 5 Define geometrical and physical parameters of TEM foil, diffraction beam, dislocation loop, such as: modulus \mathbf{C}_{ijkl} , core radius \mathbf{CR} , inclined dislocation segmentation number \mathbf{SN} , and initialize the transformation matrix between crystal coordinate, beam coordinate, TEM foil coordinate and inclined dislocation coordinate: $\mathbf{T}_{\text{dislocation}}, \mathbf{T}_{\text{foil}}, \mathbf{T}_{\text{beam}}$ respectively.
 - 6 Define inclined dislocation direction vector, and Burger vector \mathbf{LV}, \mathbf{b} respectively.
 - 7 Calculate Voigt isotropic equivalent modulus $\boldsymbol{\mu}$, poisson ratio \mathbf{v} , and Lamé $\boldsymbol{\lambda}$.
 - 8 Initialize the Kronecker-Delta operator $\boldsymbol{\delta}_{ij}$, Levi-Civita permutation operator $\boldsymbol{\epsilon}_{ijk}$.
 - 9 Segmentation of inclined dislocation, and the position of dislocation segment is described by \mathbf{r}' .
 - 10 **Step.2: Calculate the Mura isotropic finite gradient value within thin TEM foil.**
 - 11 **If** \mathbf{r} is within the dislocation core region of inclined dislocation of TEM thin foil, then
 - 12 Calculate dislocation core gradient $\mathbf{u}_{ij}^{\text{core}}$, according to eigengenstrain (or averaging gradient around dislocation segments) in crystal coordinate.
 - 13 **else**
 - 14 Calculate the inclined dislocation induced finite gradient value via Mura isotropic dislocation segment integration at given position \mathbf{r} , according to formula (4-6) and (4-7) in crystal coordinate.
 - 15 Perform integration along dislocation line, and harvest the finite gradient at the calculated position vector \mathbf{r} .
 - 16 **end if**
 - 17 Transform the finite gradient value from crystal coordinate to beam coordinate.
 - 18 Finally, harvest the finite gradient value $(\mathbf{du}/\mathbf{dz}, \mathbf{dv}/\mathbf{dz}, \mathbf{dw}/\mathbf{dz})$ in electron beam coordinate at given position \mathbf{r} within thin TEM foil, and returned back into CUFOUR for Runge-Kutta integration along electron propagation direction.
-

Algorithm. 4.5:

The details for implementing inclined anisotropic WSL finite gradient model model into CUFOUR are described as following:

-
- 1 Input: Parameters declaration ($\mathbf{r}, \mathbf{r}', \mathbf{C}_{ijkl}, \mathbf{SN}, \mathbf{T}_{\text{dislocation}}, \mathbf{T}_{\text{foil}}, \mathbf{T}_{\text{beam}}, \mathbf{n}, \mathbf{b}$).
 - 2 Output: ($\mathbf{du}/\mathbf{dz}, \mathbf{dv}/\mathbf{dz}, \mathbf{dw}/\mathbf{dz}$)
 - 3 Step.1: *Building up the simulation physical condition.*
 - 4 Define simulated TEM image sizes, and receive the calculated position vector \mathbf{r} from TEM image simulation code CUFOUR.
 - 5 Define geometrical and physical parameters of TEM foil, diffraction beam, dislocation loop, such as: modulus \mathbf{C}_{ijkl} , core radius \mathbf{CR} , inclined dislocation segmentation number \mathbf{SN} , and initialize the transformation matrix between crystal coordinate, beam coordinate, TEM foil coordinate and inclined dislocation coordinate: $\mathbf{T}_{\text{dislocation}}, \mathbf{T}_{\text{foil}}, \mathbf{T}_{\text{beam}}$ respectively.
 - 6 Define inclined dislocation direction vector, and Burger vector \mathbf{LV}, \mathbf{b} respectively.
 - 7 Initialize the Kronecker-Delta operator δ_{ij} , Levi-Civita permutation operator ϵ_{ijk} .
 - 8 Segmentation of inclined dislocation, and the position of dislocation segment is described by \mathbf{r}' .
 - 9 *Step.2: Calculate the WSL anisotropic finite gradient value within thin TEM foil.*
 - 10 **If** \mathbf{r} is within the dislocation core region of inclined dislocation of TEM thin foil, then
 - 11 Calculation dislocation core gradient $\mathbf{u}_{ij}^{\text{core}}$, according to eigengenstrain (or averaging gradient around dislocation segments) in crystal coordinate.
 - 12 **else**
 - 13 Calculate the inclined dislocation induced finite gradient value via WSL anisotropic dislocation segment integration at given position \mathbf{r} , according to formula (4-10) and (4-16) in crystal coordinate.
 - 14 Perform integration along dislocation line, and harvest the finite gradient at the calculated position vector \mathbf{r} .
 - 15 **end if**
 - 16 Transform the finite gradient value from crystal coordinate to beam coordinate.
 - 17 Finally, harvest the finite gradient value ($\mathbf{du}/\mathbf{dz}, \mathbf{dv}/\mathbf{dz}, \mathbf{dw}/\mathbf{dz}$) in electron beam coordinate at given position \mathbf{r} within thin TEM foil, and returned back into CUFOUR for Runge-Kutta integration along electron propagation direction.
-

Algorithm. 4.6:

The details for implementing inclined isotropic Devincre-Weinberger-Mura total gradient model into CUFOUR are described as following:

- 1 Input: Parameters declaration ($\mathbf{r}, \mathbf{r}', \mathbf{C}_{ijkl}, \mathbf{SN}, \mathbf{T}_{\text{dislocation}}, \mathbf{T}_{\text{foil}}, \mathbf{T}_{\text{beam}}, \mathbf{n}, \mathbf{b}$).
- 2 Output: ($\mathbf{du}/\mathbf{dz}, \mathbf{dv}/\mathbf{dz}, \mathbf{dw}/\mathbf{dz}$)
- 3 Step.1: *Building up the simulation physical condition.*
- 4 Define simulated TEM image sizes, and receive the calculated position vector \mathbf{r} from TEM image simulation code CUFOUR.
- 5 Define geometrical and physical parameters of TEM foil, diffraction beam, dislocation loop, such as: modulus \mathbf{C}_{ijkl} , core radius \mathbf{CR} , inclined dislocation segmentation number \mathbf{SN} , and initialize the transformation matrix between crystal coordinate, beam coordinate, TEM foil coordinate and inclined dislocation coordinate: $\mathbf{T}_{\text{dislocation}}, \mathbf{T}_{\text{foil}}, \mathbf{T}_{\text{beam}}$ respectively.
- 6 Define inclined dislocation direction vector and Burger vector \mathbf{LV}, \mathbf{b} respectively.
- 7 Calculate Voigt isotropic equivalent modulus μ , poisson ratio ν , and Lamé λ .
- 8 Initialize the Kronecker-Delta operator δ_{ij} , Levi-Civita permutation operator ϵ_{ijk} .
- 9 Segmentation of inclined dislocation, and the position of dislocation segment is described by \mathbf{r}' .
- 10 *Step.2: Calculate the image stress field at free surfaces of thin TEM foil.*
- 11 Meshing the free surface of thin foil with given periodic length and meshing step (\mathbf{PL}, \mathbf{MS}).
- 12 for $-\mathbf{PL}/2 < \mathbf{x} < \mathbf{PL}/2, -\mathbf{PL}/2 < \mathbf{y} < \mathbf{PL}/2$ do
- 13 **If** \mathbf{r} is within the dislocation core region of inclined dislocation of TEM thin foil, then
- 14 Calculate dislocation core stress tensor $\sigma_{ij}^{\text{core}}$, according to eigenstress in basic crystal coordinate, and the user can decide including core stress or not into the following simulation.
- 15 **else**
- 16 Calculate the inclined dislocation induced bulk stress value via isotropic Devincre dislocation segment integration at given position \mathbf{r} , according to formula (4-1) to (4-5) in crystal coordinate.
- 17 Perform integration along dislocation line, and harvest the bulk stress and image stress at free surfaces of thin TEM foil, according to free traction BC.
- 18 **end if**
- 19 **end for**

-
- 20 Transform the image stress field from crystal coordinate to beam coordinate.
- 21 **Step.3: Perform isotropic Weinberger image gradient calculation in Fourier space.**
- 22 Perform 2D discrete Fourier transformation of the harvested image stress field through isotropic Devincire dislocation segment integration, and comparison will be made between isotropic Devincire dislocation segment integration model and isotropic Weinberger image stress models in Fourier space, thus satisfying free traction BC for each $(\mathbf{k}_x, \mathbf{k}_y)$ Fourier mode. Then, the 2D discrete Fourier coefficients for the symmetrical and asymmetrical image displacement field of isotropic Weinberger image stress model can be calculated out respectively.
- 23 Finally, the 2D discrete Fourier coefficients are employed for image gradient value $(\mathbf{du}/\mathbf{dz}, \mathbf{dv}/\mathbf{dz}, \mathbf{dw}/\mathbf{dz})$ calculation in electron beam coordinate via reverse FFT transformation process at given position \mathbf{r} within thin TEM foil.
- 24 **Step.4: Calculate the Mura isotropic finite gradient value within thin TEM foil.**
- 25 **If** \mathbf{r} is within the dislocation core region of inclined dislocation of TEM thin foil, then
- 26 Calculate dislocation core gradient $\mathbf{u}_{ij}^{\text{core}}$, according to eigengenstrain (or averaging gradient around dislocation segments) in crystal coordinate.
- 27 **else**
- 28 Calculate the inclined dislocation induced finite gradient value via Mura isotropic dislocation segment integration at given position \mathbf{r} , according to formula (4-6) and (4-7) in crystal coordinate.
- 29 Perform integration along dislocation line, and harvest the finite gradient at the calculated position vector \mathbf{r} .
- 30 **end if**
- 31 Transform the finite gradient value from crystal coordinate to beam coordinate.
- 32 Add the image gradient value via isotropic Devincire-Weinberger image gradient model and finite gradient value via Mura isotropic dislocation segment integration together as the final total gradient value $(\mathbf{du}/\mathbf{dz}, \mathbf{dv}/\mathbf{dz}, \mathbf{dw}/\mathbf{dz})$ in electron beam coordinate at given position \mathbf{r} within thin TEM foil, and returned back into CUFOUR for Runge-Kutta integration along electron propagation direction.
-

Algorithm. 4.7:

The details for implementing inclined isotropic Mura-Weinberger-Mura total gradient model into CUFOUR are as following:

- 1 Input: Parameters declaration $(\mathbf{r}, \mathbf{r}', \mathbf{C}_{ijkl}, \mathbf{SN}, \mathbf{T}_{\text{dislocation}}, \mathbf{T}_{\text{foil}}, \mathbf{T}_{\text{beam}}, \mathbf{n}, \mathbf{b})$.
- 2 Output: $(\mathbf{du}/\mathbf{dz}, \mathbf{dv}/\mathbf{dz}, \mathbf{dw}/\mathbf{dz})$
- 3 **Step.1: Building up the simulation physical condition.**
- 4 Define simulated TEM image sizes, and receive the calculated position vector \mathbf{r} from TEM image simulation code CUFOUR.
- 5 Define geometrical and physical parameters of TEM foil, diffraction beam, dislocation loop, such as: modulus \mathbf{C}_{ijkl} , core radius \mathbf{CR} , inclined dislocation segmentation number \mathbf{SN} , and initialize the transformation matrix between crystal coordinate, beam coordinate, TEM foil coordinate and inclined dislocation coordinate: $\mathbf{T}_{\text{dislocation}}, \mathbf{T}_{\text{foil}}, \mathbf{T}_{\text{beam}}$ respectively.
- 6 Define inclined dislocation direction vector and Burger vector \mathbf{LV}, \mathbf{b} respectively.
- 7 Calculate Voigt isotropic equivalent modulus $\boldsymbol{\mu}$, poisson ratio \mathbf{v} , and Lamé $\boldsymbol{\lambda}$.
- 8 Initialize the Kronecker-Delta operator $\boldsymbol{\delta}_{ij}$, Levi-Civita permutation operator $\boldsymbol{\epsilon}_{ijk}$.
- 9 Segmentation of inclined dislocation, and the position of dislocation segment is described by \mathbf{r}' .
- 10 **Step.2: Calculate the image stress field at free surfaces of thin TEM foil.**
- 11 Meshing the free surface of thin foil with given periodic length and meshing step $(\mathbf{PL}, \mathbf{MS})$.
- 12 for $-\mathbf{PL}/2 < \mathbf{x} < \mathbf{PL}/2, -\mathbf{PL}/2 < \mathbf{y} < \mathbf{PL}/2$ do
- 13 **If** \mathbf{r} is within the dislocation core region of inclined dislocation of TEM thin foil, then
- 14 Calculate dislocation core stress tensor $\boldsymbol{\sigma}_{ij}^{\text{core}}$, according to eigenstress in basic crystal coordinate, and the user can decide including core stress or not into the following simulation.
- 15 **else**
- 16 Calculate the inclined dislocation induced bulk stress value via isotropic Mura dislocation segment integration at given position \mathbf{r} , according to formula (4-6) to (4-9) in crystal coordinate.
- 17 Perform integration along dislocation line, and harvest the bulk stress and image stress at free surfaces of thin TEM foil, according to free traction BC.
- 18 **end if**
- 19 **end for**

-
- 20 Transform the image stress field from crystal coordinate to beam coordinate.
- 21 **Step.3: Perform isotropic Weinberger image gradient calculation in Fourier space.**
- 22 Perform 2D discrete Fourier transformation of the harvested image stress field through isotropic Mura dislocation segment integration, and comparison will be made between isotropic Mura dislocation segment integration model and isotropic Weinberger image stress models in Fourier space, thus satisfying free traction BC for each $(\mathbf{k}_x, \mathbf{k}_y)$ Fourier mode. Then, the 2D discrete Fourier coefficients for the symmetrical and asymmetrical image displacement field of isotropic Weinberger image stress model can be calculated out respectively.
- 23 Finally, the 2D discrete Fourier coefficients are employed for image gradient value $(\mathbf{du}/\mathbf{dz}, \mathbf{dv}/\mathbf{dz}, \mathbf{dw}/\mathbf{dz})$ calculation in electron beam coordinate via reverse FFT transformation process at given position \mathbf{r} within thin TEM foil.
- 24 **Step.4: Calculate the Mura isotropic finite gradient value within thin TEM foil.**
- 25 **If** \mathbf{r} is within the dislocation core region of inclined dislocation of TEM thin foil, then
- 26 Calculate dislocation core gradient $\mathbf{u}_{ij}^{\text{core}}$, according to eigengenstrain (or averaging gradient around dislocation segments) in crystal coordinate.
- 27 **else**
- 28 Calculate the inclined dislocation induced finite gradient value via Mura isotropic dislocation segment integration at given position \mathbf{r} , according to formula (4-6) and (4-7) in crystal coordinate.
- 29 Perform integration along dislocation line, and harvest the finite gradient at the calculated position vector \mathbf{r} .
- 30 **end if**
- 31 Transform the finite gradient value from crystal coordinate to beam coordinate.
- 32 Add the image gradient value via isotropic Mura-Weinberger image gradient model and finite gradient value via Mura isotropic dislocation segment integration together as the final total gradient value $(\mathbf{du}/\mathbf{dz}, \mathbf{dv}/\mathbf{dz}, \mathbf{dw}/\mathbf{dz})$ in electron beam coordinate at given position \mathbf{r} within thin TEM foil, and returned back into CUFOUR for Runge-Kutta integration along electron propagation direction.
-

Algorithm. 4.8:

The details for implementing inclined anisotropic WSL-Wu-WSL total gradient model into CUFOUR are as following:

- 1 Input: Parameters declaration $(\mathbf{r}, \mathbf{r}', \mathbf{C}_{ijkl}, \mathbf{SN}, \mathbf{T}_{\text{dislocation}}, \mathbf{T}_{\text{foil}}, \mathbf{T}_{\text{beam}}, \mathbf{n}, \mathbf{b})$.
- 2 Output: $(\mathbf{du}/\mathbf{dz}, \mathbf{dv}/\mathbf{dz}, \mathbf{dw}/\mathbf{dz})$
- 3 **Step.1: Building up the simulation physical condition.**
- 4 Define simulated TEM image sizes, and receive the calculated position vector \mathbf{r} from TEM image simulation code CUFOUR.
- 5 Define geometrical and physical parameters of TEM foil, diffraction beam, dislocation loop, such as: modulus \mathbf{C}_{ijkl} , core radius \mathbf{CR} , inclined dislocation segmentation number \mathbf{SN} , and initialize the transformation matrix between crystal coordinate, beam coordinate, TEM foil coordinate and inclined dislocation coordinate: $\mathbf{T}_{\text{dislocation}}, \mathbf{T}_{\text{foil}}, \mathbf{T}_{\text{beam}}$ respectively.
- 6 Define inclined dislocation direction vector, and Burger vector \mathbf{LV}, \mathbf{b} respectively.
- 7 Initialize the Kronecker-Delta operator δ_{ij} , Levi-Civita permutation operator ϵ_{ijk} .
- 8 Segmentation of inclined dislocation, and the position of dislocation segment is described by \mathbf{r}' .
- 9 **Step.2: Calculate the image stress field at free surfaces of thin TEM foil.**
- 10 Meshing the free surface of thin foil with given periodic length and meshing step $(\mathbf{PL}, \mathbf{MS})$.
- 11 **for** $-\mathbf{PL}/2 < \mathbf{x} < \mathbf{PL}/2, -\mathbf{PL}/2 < \mathbf{y} < \mathbf{PL}/2$ **do**
- 12 **If** \mathbf{r} is within the dislocation core region of inclined dislocation of TEM thin foil, then
- 13 Calculate dislocation core stress tensor $\sigma_{ij}^{\text{core}}$, according to eigenstress in crystal coordinate, and the user can decide including core stress or not into the following simulation.
- 14 **else**
- 15 Calculate the inclined dislocation induced bulk stress value via anisotropic WSL dislocation segment integration at given position \mathbf{r} , according to formula (4-10) to (4-18) in crystal coordinate.
- 16 Perform integration along dislocation line, and harvest the bulk stress and image stress at free surfaces of thin TEM foil, according to free traction BC.
- 17 **end if**
- 18 **end for**
- 19 Transform the image stress field from crystal coordinate to beam coordinate.

-
- 20 **Step.3: Perform anisotropic Wu image gradient calculation in Fourier space.**
- 21 Perform 2D discrete Fourier transformation of the harvested image stress field through anisotropic WSL dislocation segment integration, and comparison will be made between anisotropic WSL dislocation segment integration model and anisotropic Wu image stress models in Fourier space, thus satisfying free traction BC for each $(\mathbf{k}_x, \mathbf{k}_y)$ Fourier mode. Then, the 2D discrete Fourier coefficients for the symmetrical and asymmetrical image displacement field of anisotropic Wu image stress model can be calculated out respectively.
- 22 Finally, the 2D discrete Fourier coefficients are employed for image gradient value $(\mathbf{du}/\mathbf{dz}, \mathbf{dv}/\mathbf{dz}, \mathbf{dw}/\mathbf{dz})$ calculation in electron beam coordinate via reverse FFT transformation process at given position \mathbf{r} within thin TEM foil.
- 23 **Step.4: Calculate the WSL anisotropic finite gradient value within thin TEM foil.**
- 24 **If** \mathbf{r} is within the dislocation core region of inclined dislocation of TEM thin foil, then
- 25 Calculate dislocation core gradient $\mathbf{u}_{ij}^{\text{core}}$, according to eigengenstrain (or averaging gradient around dislocation segments) in crystal coordinate.
- 26 **else**
- 27 Calculate the inclined dislocation induced finite gradient value via WSL anisotropic dislocation segment integration at given position \mathbf{r} , according to formula (4-10) and (4-16) in crystal coordinate.
- 28 Perform integration along dislocation line, and harvest the finite gradient at the calculated position vector \mathbf{r} .
- 29 **end if**
- 30 Transform the finite gradient value from crystal coordinate to beam coordinate.
- 31 Finally, harvest the finite gradient value $(\mathbf{du}/\mathbf{dz}, \mathbf{dv}/\mathbf{dz}, \mathbf{dw}/\mathbf{dz})$ in electron beam coordinate at given position \mathbf{r} within thin TEM foil.
- 32 Transform the finite gradient value from crystal coordinate to beam coordinate.
- 33 Add the image gradient value via anisotropic WSL-Weinberger image gradient model and finite gradient value via anisotropic WSL dislocation segment integration together as the final total gradient value $(\mathbf{du}/\mathbf{dz}, \mathbf{dv}/\mathbf{dz}, \mathbf{dw}/\mathbf{dz})$ in electron beam coordinate at given position \mathbf{r} within thin TEM foil, and returned back into CUFOUR for Runge-Kutta integration along electron propagation direction.
-

Algorithm. 4.9:

The details for implementing inclined isotropic Hirth-Lothe infinite gradient model into CUFOUR are described as following:

- 1 Input: Parameters declaration $(\mathbf{r}, \mathbf{r}', \mathbf{C}_{ijkl}, \mathbf{SN}, \mathbf{T}_{\text{dislocation}}, \mathbf{T}_{\text{foil}}, \mathbf{T}_{\text{beam}}, \mathbf{n}, \mathbf{b})$.
- 2 Output: $(\mathbf{du}/\mathbf{dz}, \mathbf{dv}/\mathbf{dz}, \mathbf{dw}/\mathbf{dz})$
- 3 Step.1: **Building up the simulation physical condition.**
- 4 Define simulated TEM image sizes, and receive the calculated position vector \mathbf{r} from TEM image simulation code CUFOUR.
- 5 Define geometrical and physical parameters of TEM foil, diffraction beam, dislocation loop, such as: modulus \mathbf{C}_{ijkl} , core radius \mathbf{CR} , inclined dislocation segmentation number \mathbf{SN} , and initialize the transformation matrix between crystal coordinate, beam coordinate, TEM foil coordinate and inclined dislocation coordinate: $\mathbf{T}_{\text{dislocation}}, \mathbf{T}_{\text{foil}}, \mathbf{T}_{\text{beam}}$ respectively.
- 6 Define inclined dislocation direction vector, and Burger vector \mathbf{LV}, \mathbf{b} respectively.
- 7 Calculate Voigt isotropic equivalent modulus μ , poisson ratio ν , and Lamé λ .
- 8 Initialize the Kronecker-Delta operator δ_{ij} , Levi-Civita permutation operator ϵ_{ijk} .
- 9 Segmentation of inclined dislocation, and the position of dislocation segment is described by \mathbf{r}' .
- 10 **Step.2: Calculate the isotropic Hirth-Lothe infinite gradient value within thin TEM foil.**
- 11 **If** \mathbf{r} is within the dislocation core region of inclined dislocation of TEM thin foil, then
- 12 Calculate dislocation core gradient $\mathbf{u}_{ij}^{\text{core}}$, according to eigengenstrain in crystal coordinate.
- 13 **else**
- 14 Calculate the inclined dislocation induced infinite gradient value via inclined isotropic infinite Hirth-Lothe model at given position \mathbf{r} , according to formula (4-19) and (4-23) in crystal coordinate.
- 15 Perform integration along dislocation line, and harvest the infinite gradient at the calculated position vector \mathbf{r} .
- 16 **end if**
- 17 Transform the infinite gradient value from crystal coordinate to beam coordinate.

-
- 18 Finally, harvest the infinite gradient value (\mathbf{du}/\mathbf{dz} , \mathbf{dv}/\mathbf{dz} , \mathbf{dw}/\mathbf{dz}) in electron beam coordinate at given position \mathbf{r} within thin TEM foil, and returned back into CUFOUR for Runge-Kutta integration along electron propagation direction.
-

Algorithm. 4.10:

The details for implementing inclined anisotropic infinite Stroh model into CUFOUR are described as following:

- 1 Input: Parameters declaration (\mathbf{r} , \mathbf{r}' , \mathbf{C}_{ijkl} , \mathbf{SN} , $\mathbf{T}_{\text{dislocation}}$, \mathbf{T}_{foil} , \mathbf{T}_{beam} , \mathbf{n} , \mathbf{b}).
 - 2 Output: (\mathbf{du}/\mathbf{dz} , \mathbf{dv}/\mathbf{dz} , \mathbf{dw}/\mathbf{dz})
 - 3 *Step.1: Building up the simulation physical condition.*
 - 4 Define simulated TEM image sizes, and receive the calculated position vector \mathbf{r} from TEM image simulation code CUFOUR.
 - 5 Define geometrical and physical parameters of TEM foil, diffraction beam, dislocation loop, such as: modulus \mathbf{C}_{ijkl} , core radius \mathbf{CR} , inclined dislocation segmentation number \mathbf{SN} , and initialize the transformation matrix between crystal coordinate, beam coordinate, TEM foil coordinate and inclined dislocation coordinate: $\mathbf{T}_{\text{dislocation}}$, \mathbf{T}_{foil} , \mathbf{T}_{beam} respectively.
 - 6 Define inclined dislocation direction vector and Burger vector \mathbf{LV} , \mathbf{b} respectively.
 - 7 Initialize the Kronecker-Delta operator δ_{ij} , Levi-Civita permutation operator ϵ_{ijk} .
 - 8 Segmentation of inclined dislocation, and the position of dislocation segment is described by \mathbf{r}' .
 - 9 *Step.2: Calculate the anisotropic Stroh infinite gradient value within thin TEM foil.*
 - 10 **If** \mathbf{r} is within the dislocation core region of inclined dislocation of TEM thin foil, then
 - 11 Calculate dislocation core gradient $\mathbf{u}_{i,j}^{\text{core}}$, according to eigenstrain in crystal coordinate.
 - 12 **else**
 - 13 Calculate the inclined dislocation induced infinite gradient value via inclined anisotropic Stroh infinite gradient model at given position \mathbf{r} , according to formula (4-24) and (4-30) in crystal coordinate.
 - 14 Perform integration along dislocation line, and harvest the infinite gradient at the calculated position vector \mathbf{r} .
 - 15 **end if**
 - 16 Transform the infinite gradient value from crystal coordinate to beam coordinate.
 - 17 Finally, harvest the infinite gradient value (\mathbf{du}/\mathbf{dz} , \mathbf{dv}/\mathbf{dz} , \mathbf{dw}/\mathbf{dz}) in electron beam coordinate at given position \mathbf{r} within thin TEM foil, and returned back into CUFOUR for Runge-Kutta integration along electron propagation direction.
-

Algorithm. 4.11:

The details for implementing dislocation loop isotropic Devincere-Weinberger image gradient model into CUFOUR are described as following:

- 1 Input: Parameters declaration (\mathbf{r} , \mathbf{r}' , \mathbf{C}_{ijkl} , \mathbf{SN} , \mathbf{T}_{loop} , \mathbf{T}_{foil} , \mathbf{T}_{beam} , \mathbf{n} , \mathbf{R} , \mathbf{d} , \mathbf{b}).
- 2 Output: (\mathbf{du}/\mathbf{dz} , \mathbf{dv}/\mathbf{dz} , \mathbf{dw}/\mathbf{dz})
- 3 *Step.1: Building up the simulation physical condition.*
- 4 Define simulated TEM image sizes, and receive the calculated position vector \mathbf{r} from TEM image simulation code CUFOUR.
- 5 Define geometrical and physical parameters of TEM foil, diffraction beam, dislocation loop, such as: modulus \mathbf{C}_{ijkl} , core radius \mathbf{CR} , loop radius \mathbf{R} , dislocation loop center depth within thin TEM foil from bottom \mathbf{d} , and initialize the transformation matrix between crystal coordinate, beam coordinate, TEM foil coordinate and dislocation loop coordinate: \mathbf{T}_{loop} , \mathbf{T}_{foil} , \mathbf{T}_{beam} respectively.
- 6 Define dislocation loop habit plane normal vector and Burger vector \mathbf{HN} , \mathbf{b} respectively.
- 7 Calculate Voigt isotropic equivalent modulus μ , poisson ratio ν , and Lamé λ .
- 8 Initialize the Kronecker-Delta operator δ_{ij} , Levi-Civita permutation operator ϵ_{ijk} .
- 9 Segmentation of dislocation loop perimeter, and the position of dislocation segment is described by \mathbf{r}' .
- 10 *Step.2: Calculate the image stress field at free surfaces of thin TEM foil.*
- 11 Meshing the free surface of thin foil with given periodic length and meshing step (\mathbf{PL} , \mathbf{MS}).
- 12 **for** $-\mathbf{PL}/2 < \mathbf{x} < \mathbf{PL}/2$, $-\mathbf{PL}/2 < \mathbf{y} < \mathbf{PL}/2$ **do**
- 13 Calculate the dislocation loop induced bulk stress value via isotropic Devincere dislocation segment integration at given position \mathbf{r} , according to formula (4-1) to (4-5) in crystal coordinate.

-
- 14 Perform integration along dislocation loop perimeter, and harvest the bulk stress and image stress at free surfaces of thin TEM foil, according to free traction BC.
 - 15 **end for**
 - 16 Transform the image stress field from crystal coordinate to beam coordinate.
 - 17 **Step.3: Perform isotropic Weinberger image gradient calculation in Fourier space.**
 - 18 Perform 2D discrete Fourier transformation of the harvested image stress field through isotropic Devincere dislocation segment integration, and comparison will be made between isotropic Devincere dislocation segment integration model and isotropic Weinberger image stress model in Fourier space, thus satisfying free traction BC for each $(\mathbf{k}_x, \mathbf{k}_y)$ Fourier mode. Then, the 2D discrete Fourier coefficients for the symmetrical and asymmetrical image displacement field of dislocation loop isotropic Weinberger image gradient model can be calculated out respectively.
 - 19 Finally, the 2D discrete Fourier coefficients are employed for image gradient value $(\mathbf{du}/\mathbf{dz}, \mathbf{dv}/\mathbf{dz}, \mathbf{dw}/\mathbf{dz})$ calculation in electron beam coordinate via reverse FFT transformation process at given position \mathbf{r} within thin TEM foil, and returned back into CUFOUR for Runge-Kutta integration along electron propagation direction.
-

Algorithm. 4.12:

The details for details for implementing dislocation loop isotropic Mura-Weinberger image gradient model into CUFOUR are described as following:

- 1 Input: Parameters declaration $(\mathbf{r}, \mathbf{r}', \mathbf{C}_{ijkl}, \mathbf{SN}, \mathbf{T}_{loop}, \mathbf{T}_{foil}, \mathbf{T}_{beam}, \mathbf{n}, \mathbf{R}, \mathbf{d}, \mathbf{b})$.
 - 2 Output: $(\mathbf{du}/\mathbf{dz}, \mathbf{dv}/\mathbf{dz}, \mathbf{dw}/\mathbf{dz})$
 - 3 **Step.1: Building up the simulation physical condition.**
 - 4 Define simulated TEM image sizes, and receive the calculated position vector \mathbf{r} from TEM image simulation code CUFOUR.
 - 5 Define geometrical and physical parameters of TEM foil, diffraction beam, dislocation loop, such as: modulus \mathbf{C}_{ijkl} , core radius \mathbf{CR} , loop radius \mathbf{R} , dislocation loop center depth within thin TEM foil from bottom \mathbf{d} , and initialize the transformation matrix between crystal coordinate, beam coordinate, TEM foil coordinate and dislocation loop coordinate: $\mathbf{T}_{loop}, \mathbf{T}_{foil}, \mathbf{T}_{beam}$ respectively.
 - 6 Define dislocation loop habit plane normal vector and Burger vector \mathbf{HN}, \mathbf{b} respectively.
 - 7 Calculate Voigt isotropic equivalent modulus $\boldsymbol{\mu}$, poisson ratio \mathbf{v} , and Lamé $\boldsymbol{\lambda}$.
 - 8 Initialize the Kronecker-Delta operator $\boldsymbol{\delta}_{ij}$, Levi-Civita permutation operator $\boldsymbol{\epsilon}_{ijk}$.
 - 9 Segmentation of dislocation loop perimeter, and the position of dislocation segment is described by \mathbf{r}' .
 - 10 **Step.2: Calculate the image stress field at free surfaces of thin TEM foil.**
 - 11 Meshing the free surface of thin foil with given periodic length and meshing step $(\mathbf{PL}, \mathbf{MS})$.
 - 12 **for** $-\mathbf{PL}/2 < \mathbf{x} < \mathbf{PL}/2, -\mathbf{PL}/2 < \mathbf{y} < \mathbf{PL}/2$ **do**
 - 13 Calculate the dislocation loop induced bulk stress value via isotropic Mura dislocation segment integration at given position \mathbf{r} , according to formula (4-6) to (4-9) in crystal coordinate.
 - 14 Perform integration along dislocation loop perimeter, and harvest the bulk stress and image stress at free surfaces of thin TEM foil, according to free traction BC.
 - 15 **end for**
 - 16 Transform the image stress field from crystal coordinate to beam coordinate.
 - 17 **Step.3: Perform isotropic Weinberger image gradient calculation in Fourier space.**
 - 18 Perform 2D discrete Fourier transformation of the harvested image stress field through isotropic Mura dislocation segment integration, and comparison will be made between isotropic Mura dislocation segment integration model and isotropic Weinberger image stress model in Fourier space, thus satisfying free traction BC for each $(\mathbf{k}_x, \mathbf{k}_y)$ Fourier mode. Then, the 2D discrete Fourier coefficients for the symmetrical and asymmetrical image displacement field of dislocation loop isotropic Weinberger image gradient model can be calculated out respectively.
 - 19 Finally, the 2D discrete Fourier coefficients are employed for image gradient value $(\mathbf{du}/\mathbf{dz}, \mathbf{dv}/\mathbf{dz}, \mathbf{dw}/\mathbf{dz})$ calculation in electron beam coordinate via reverse FFT transformation process at given position \mathbf{r} within thin TEM foil, and returned back into CUFOUR for Runge-Kutta integration along electron propagation direction.
-

Algorithm. 4.13:

The details for implementing dislocation loop anisotropic WSL-Wu-WSL total gradient model into CUFOUR are described as following:

-
- 1 Input: Parameters declaration ($\mathbf{r}, \mathbf{r}', \mathbf{C}_{ijkl}, \mathbf{SN}, \mathbf{T}_{loop}, \mathbf{T}_{foil}, \mathbf{T}_{beam}, \mathbf{n}, \mathbf{R}, \mathbf{d}, \mathbf{b}$).
 - 2 Output: ($\mathbf{du}/\mathbf{dz}, \mathbf{dv}/\mathbf{dz}, \mathbf{dw}/\mathbf{dz}$)
 - 3 **Step.1: Building up the simulation physical condition.**
 - 4 Define simulated TEM image sizes, and receive the calculated position vector \mathbf{r} from TEM image simulation code CUFOUR.
 - 5 Define geometrical and physical parameters of TEM foil, diffraction beam, dislocation loop, such as: modulus \mathbf{C}_{ijkl} , core radius \mathbf{CR} , loop radius \mathbf{R} , dislocation loop center depth within thin TEM foil from bottom \mathbf{d} , and initialize the transformation matrix between crystal coordinate, beam coordinate, TEM foil coordinate and dislocation loop coordinate: $\mathbf{T}_{loop}, \mathbf{T}_{foil}, \mathbf{T}_{beam}$ respectively.
 - 6 Define dislocation loop habit plane normal vector and Burger vector \mathbf{HN}, \mathbf{b} respectively.
 - 7 Initialize the Kronecker-Delta operator δ_{ij} , Levi-Civita permutation operator ϵ_{ijk} .
 - 8 Segmentation of dislocation loop perimeter, and the position of dislocation segment is described by \mathbf{r}' .
 - 9 **Step.2: Calculate the image stress field at free surfaces of thin TEM foil.**
 - 10 Meshing the free surface of thin foil with given periodic length and meshing step (\mathbf{PL}, \mathbf{MS}).
 - 11 **for** $-\mathbf{PL}/2 < \mathbf{x} < \mathbf{PL}/2, -\mathbf{PL}/2 < \mathbf{y} < \mathbf{PL}/2$ **do**
 - 12 Calculate the dislocation loop induced bulk stress value via anisotropic WSL dislocation segment integration at given position \mathbf{r} , according to formula (4-10) to (4-18) in crystal coordinate.
 - 13 Perform integration along dislocation loop perimeter, and harvest the bulk stress and image stress at free surfaces of thin TEM foil, according to free traction BC.
 - 14 **end for**
 - 15 Transform the image stress field from crystal coordinate to beam coordinate.
 - 16 **Step.3: Perform anisotropic Wu image gradient calculation in Fourier space.**
 - 17 Perform 2D discrete Fourier transformation of the harvested image stress field through anisotropic WSL dislocation segment integration, and comparison will be made between anisotropic WSL dislocation segment integration model and anisotropic WSL image stress model in Fourier space, thus satisfying free traction BC for each $(\mathbf{k}_x, \mathbf{k}_y)$ Fourier mode. Then, the 2D discrete Fourier coefficients for the symmetrical and asymmetrical image displacement field of dislocation loop anisotropic Wu image stress model can be calculated out respectively.
 - 18 Finally, the 2D discrete Fourier coefficients are employed for image gradient value ($\mathbf{du}/\mathbf{dz}, \mathbf{dv}/\mathbf{dz}, \mathbf{dw}/\mathbf{dz}$) calculation in electron beam coordinate via reverse FFT transformation process at given position \mathbf{r} within thin TEM foil, and returned back into CUFOUR for Runge-Kutta integration along electron propagation direction.
-

Algorithm. 4.14:

The details for implementing dislocation loop anisotropic Mura-Wu-WSL total gradient model into CUFOUR are described as following:

-
- 1 Input: Parameters declaration ($\mathbf{r}, \mathbf{r}', \mathbf{C}_{ijkl}, \mathbf{SN}, \mathbf{T}_{loop}, \mathbf{T}_{foil}, \mathbf{T}_{beam}, \mathbf{n}, \mathbf{R}, \mathbf{d}, \mathbf{b}$).
 - 2 Output: ($\mathbf{du}/\mathbf{dz}, \mathbf{dv}/\mathbf{dz}, \mathbf{dw}/\mathbf{dz}$)
 - 3 **Step.1: Building up the simulation physical condition.**
 - 4 Define simulated TEM image sizes, and receive the calculated position vector \mathbf{r} from TEM image simulation code CUFOUR.
 - 5 Define geometrical and physical parameters of TEM foil, diffraction beam, dislocation loop, such as: modulus \mathbf{C}_{ijkl} , core radius \mathbf{CR} , loop radius \mathbf{R} , dislocation loop center depth within thin TEM foil from bottom \mathbf{d} , and initialize the transformation matrix between crystal coordinate, beam coordinate, TEM foil coordinate and dislocation loop coordinate: $\mathbf{T}_{loop}, \mathbf{T}_{foil}, \mathbf{T}_{beam}$ respectively.
 - 6 Define dislocation loop habit plane normal vector and Burger vector \mathbf{HN}, \mathbf{b} respectively.
 - 7 Initialize the Kronecker-Delta operator δ_{ij} , Levi-Civita permutation operator ϵ_{ijk} .
 - 8 Segmentation of dislocation loop perimeter, and the position of dislocation segment is described by \mathbf{r}' .
 - 9 **Step.2: Calculate the image stress field at free surfaces of thin TEM foil.**
 - 10 Meshing the free surface of thin foil with given periodic length and meshing step (\mathbf{PL}, \mathbf{MS}).
 - 11 **for** $-\mathbf{PL}/2 < \mathbf{x} < \mathbf{PL}/2, -\mathbf{PL}/2 < \mathbf{y} < \mathbf{PL}/2$ **do**
 - 12 Calculate the dislocation loop induced bulk stress value via dislocation loop anisotropic Mura dislocation segment integration at given position \mathbf{r} , according to formula (4-31) to (4-37) in crystal coordinate.
-

-
- 13 Perform integration along dislocation loop perimeter, and harvest the bulk stress and image stress at free surfaces of thin TEM foil, according to free traction BC.
 - 14 **end for**
 - 15 Transform the image stress field from crystal coordinate to beam coordinate.
 - 16 **Step.3: Perform anisotropic Wu image gradient calculation in Fourier space.**
 - 17 Perform 2D discrete Fourier transformation of the harvested image stress field through anisotropic Mura dislocation segment integration, and comparison will be made between anisotropic Mura dislocation segment integration model and anisotropic WSL image stress model in Fourier space, thus satisfying free traction BC for each $(\mathbf{k}_x, \mathbf{k}_y)$ Fourier mode. Then, the 2D discrete Fourier coefficients for the symmetrical and asymmetrical image displacement field of dislocation loop anisotropic Wu image stress model can be calculated out respectively.
 - 18 Finally, the 2D discrete Fourier coefficients are employed for image gradient value $(\mathbf{du}/\mathbf{dz}, \mathbf{dv}/\mathbf{dz}, \mathbf{dw}/\mathbf{dz})$ calculation in electron beam coordinate via reverse FFT transformation process at given position \mathbf{r} within thin TEM foil, and returned back into CUFOUR for Runge-Kutta integration along electron propagation direction.
-

Algorithm. 4.15:

The details for implementing dislocation loop isotropic Mura bulk gradient model into CUFOUR are described as following:

- 1 Input: Parameters declaration $(\mathbf{r}, \mathbf{r}', \mathbf{C}_{ijkl}, \mathbf{SN}, \mathbf{T}_{loop}, \mathbf{T}_{foil}, \mathbf{T}_{beam}, \mathbf{n}, \mathbf{R}, \mathbf{d}, \mathbf{b})$.
 - 2 Output: $(\mathbf{du}/\mathbf{dz}, \mathbf{dv}/\mathbf{dz}, \mathbf{dw}/\mathbf{dz})$
 - 3 **Step.1: Building up the simulation physical condition.**
 - 4 Define simulated TEM image sizes, and receive the calculated position vector \mathbf{r} from TEM image simulation code CUFOUR.
 - 5 Define geometrical and physical parameters of TEM foil, diffraction beam, dislocation loop, such as: modulus \mathbf{C}_{ijkl} , core radius \mathbf{CR} , loop radius \mathbf{R} , dislocation loop center depth within thin TEM foil from bottom \mathbf{d} , and initialize the transformation matrix between crystal coordinate, beam coordinate, TEM foil coordinate and dislocation loop coordinate: $\mathbf{T}_{loop}, \mathbf{T}_{foil}, \mathbf{T}_{beam}$ respectively.
 - 6 Define dislocation loop habit plane normal vector and Burger vector \mathbf{HN}, \mathbf{b} respectively.
 - 7 Calculate Voigt isotropic equivalent modulus μ , poisson ratio ν , and Lamé λ .
 - 8 Initialize the Kronecker-Delta operator δ_{ij} , Levi-Civita permutation operator ϵ_{ijk} .
 - 9 Segmentation of dislocation loop perimeter, and the position of dislocation segment is described by \mathbf{r}' .
 - 10 **Step.2: Calculate the Mura isotropic finite gradient value within thin TEM foil.**
 - 11 **If** \mathbf{r} is within the dislocation core region of dislocation loop within TEM thin foil, then
 - 12 Calculate dislocation loop core gradient \mathbf{u}_{ij}^{core} , according to eigengenstrain in crystal coordinate.
 - 13 **else**
 - 14 Calculate the dislocation loop induced finite gradient value via Mura isotropic dislocation segment integration at given position \mathbf{r} , according to formula (4-6) and (4-7) in crystal coordinate.
 - 15 **endif**
 - 16 Perform integration along dislocation loop perimeter, and harvest the finite gradient at the calculated position vector \mathbf{r} .
 - 17 Transform the finite gradient value from crystal coordinate to beam coordinate.
 - 18 Finally, harvest the finite gradient value $(\mathbf{du}/\mathbf{dz}, \mathbf{dv}/\mathbf{dz}, \mathbf{dw}/\mathbf{dz})$ in electron beam coordinate at given position \mathbf{r} within thin TEM foil, and returned back into CUFOUR for Runge-Kutta integration along electron propagation direction.
-

Algorithm. 4.16:

The details for implementing dislocation loop isotropic Mura bulk gradient model into CUFOUR are described as following:

- 1 Input: Parameters declaration $(\mathbf{r}, \mathbf{r}', \mathbf{C}_{ijkl}, \mathbf{SN}, \mathbf{T}_{loop}, \mathbf{T}_{foil}, \mathbf{T}_{beam}, \mathbf{n}, \mathbf{R}, \mathbf{d}, \mathbf{b})$.
- 2 Output: $(\mathbf{du}/\mathbf{dz}, \mathbf{dv}/\mathbf{dz}, \mathbf{dw}/\mathbf{dz})$
- 3 **Step.1: Building up the simulation physical condition.**

-
- 4 Define simulated TEM image sizes, and receive the calculated position vector \mathbf{r} from TEM image simulation code CUFOUR.
 - 5 Define geometrical and physical parameters of TEM foil, diffraction beam, dislocation loop, such as: modulus \mathbf{C}_{ijkl} , core radius \mathbf{CR} , loop radius \mathbf{R} , dislocation loop center depth within thin TEM foil from bottom \mathbf{d} , and initialize the transformation matrix between crystal coordinate, beam coordinate, TEM foil coordinate and dislocation loop coordinate: \mathbf{T}_{loop} , \mathbf{T}_{foil} , \mathbf{T}_{beam} respectively.
 - 6 Define dislocation loop habit plane normal vector and Burger vector \mathbf{HN} , \mathbf{b} respectively.
 - 7 Initialize the Kronecker-Delta operator δ_{ij} , Levi-Civita permutation operator ϵ_{ijk} .
 - 8 Segmentation of dislocation loop perimeter, and the position of dislocation segment is described by \mathbf{r}' .
 - 9 **Step.1: Calculate the WSL anisotropic finite gradient value within thin TEM foil.**
 - 10 **If** \mathbf{r} is within the dislocation core region of dislocation loop within TEM thin foil, then
 - 11 Calculate dislocation loop core gradient \mathbf{u}_{ij}^{core} , according to eigengenstrain in crystal coordinate.
 - 12 **else**
 - 13 Calculate the dislocation loop induced finite gradient value via WSL anisotropic dislocation segment integration at given position \mathbf{r} , according to formula (4-10) to (4-16) in crystal coordinate.
 - 14 **endif**
 - 15 Perform integration along dislocation loop perimeter, and harvest the finite gradient at the calculated position vector \mathbf{r} .
 - 16 Transform the finite gradient value from crystal coordinate to beam coordinate.
 - 17 Finally, harvest the finite gradient value (\mathbf{du}/\mathbf{dz} , \mathbf{dv}/\mathbf{dz} , \mathbf{dw}/\mathbf{dz}) in electron beam coordinate at given position \mathbf{r} within thin TEM foil, and returned back into CUFOUR for Runge-Kutta integration along electron propagation direction.
-

Algorithm. 4.17:

The details for implementing dislocation loop isotropic Devincere-Weinberger-Mura total gradient model into CUFOUR are described as following:

- 1 Input: Parameters declaration (\mathbf{r} , \mathbf{r}' , \mathbf{C}_{ijkl} , \mathbf{SN} , \mathbf{T}_{loop} , \mathbf{T}_{foil} , \mathbf{T}_{beam} , \mathbf{n} , \mathbf{R} , \mathbf{d} , \mathbf{b}).
- 2 Output: (\mathbf{du}/\mathbf{dz} , \mathbf{dv}/\mathbf{dz} , \mathbf{dw}/\mathbf{dz})
- 3 **Step.1: Building up the simulation physical condition.**
- 4 Define simulated TEM image sizes, and receive the calculated position vector \mathbf{r} from TEM image simulation code CUFOUR.
- 5 Define geometrical and physical parameters of TEM foil, diffraction beam, dislocation loop, such as: modulus \mathbf{C}_{ijkl} , core radius \mathbf{CR} , loop radius \mathbf{R} , dislocation loop center depth within thin TEM foil from bottom \mathbf{d} , and initialize the transformation matrix between crystal coordinate, beam coordinate, TEM foil coordinate and dislocation loop coordinate: \mathbf{T}_{loop} , \mathbf{T}_{foil} , \mathbf{T}_{beam} respectively.
- 6 Define dislocation loop habit plane normal vector and Burger vector \mathbf{HN} , \mathbf{b} respectively.
- 7 Calculate Voigt isotropic equivalent modulus $\boldsymbol{\mu}$, poisson ratio \mathbf{v} , and Lamé $\boldsymbol{\lambda}$.
- 8 Initialize the Kronecker-Delta operator δ_{ij} , Levi-Civita permutation operator ϵ_{ijk} .
- 9 Segmentation of dislocation loop perimeter, and the position of dislocation segment is described by \mathbf{r}' .
- 10 **Step.2: Calculate the image stress field at free surfaces of thin TEM foil.**
- 11 Meshing the free surface of thin foil with given periodic length and meshing step (\mathbf{PL} , \mathbf{MS}).
- 12 **for** $-\mathbf{PL}/2 < \mathbf{x} < \mathbf{PL}/2$, $-\mathbf{PL}/2 < \mathbf{y} < \mathbf{PL}/2$ **do**
- 13 Calculate the dislocation loop induced bulk stress value via isotropic Devincere dislocation segment integration at given position \mathbf{r} , according to formula (4-1) to (4-5) in crystal coordinate.
- 14 Perform integration along dislocation loop perimeter, and harvest the bulk stress and image stress at free surfaces of thin TEM foil, according to free traction BC.
- 15 **end for**
- 16 Transform the image stress field from crystal coordinate to beam coordinate.
- 17 **Step.3: Perform isotropic Weinberger image gradient calculation in Fourier space.**
- 18 Perform 2D discrete Fourier transformation of the harvested image stress field through isotropic Devincere dislocation segment integration, and comparison will be made between isotropic Devincere dislocation segment integration model and isotropic Weinberger image stress model in Fourier space, thus satisfying free traction BC for each $(\mathbf{k}_x, \mathbf{k}_y)$ Fourier mode. Then, the 2D discrete Fourier coefficients for the symmetrical and asymmetrical image displacement field of dislocation loop isotropic Weinberger image gradient model can be calculated out respectively.

-
- 19 Finally, the 2D discrete Fourier coefficients are employed for image gradient value (\mathbf{du}/\mathbf{dz} , \mathbf{dv}/\mathbf{dz} , \mathbf{dw}/\mathbf{dz}) calculation in electron beam coordinate via reverse FFT transformation process at given position \mathbf{r} within thin TEM foil.
- 18 **Step.4: Calculate the Mura isotropic finite gradient value within thin TEM foil.**
- 19 **If** \mathbf{r} is within the dislocation core region of dislocation loop within TEM thin foil, then
- 20 Calculate dislocation loop core gradient $\mathbf{u}_{ij}^{\text{core}}$, according to eigengenstrain in crystal coordinate.
- 21 **else**
- 22 Calculate the dislocation loop induced finite gradient value via Mura isotropic dislocation segment integration at given position \mathbf{r} , according to formula (4-6) and (4-7) in crystal coordinate.
- 23 **endif**
- 24 Perform integration along dislocation loop perimeter, and harvest the finite gradient at the calculated position vector \mathbf{r} .
- 25 Transform the finite gradient value from crystal coordinate to beam coordinate.
- 26 Add the image gradient value via isotropic Devincere-Weinberger image gradient model and finite gradient value via isotropic Mura dislocation segment integration together as the final total gradient value (\mathbf{du}/\mathbf{dz} , \mathbf{dv}/\mathbf{dz} , \mathbf{dw}/\mathbf{dz}) in electron beam coordinate at given position \mathbf{r} within thin TEM foil, and returned back into CUFOUR for Runge-Kutta integration along electron propagation direction.
-

Algorithm. 4.18:

The details for implementing dislocation loop isotropic Mura-Weinberger-Mura total gradient model into CUFOUR are described as following:

- 1 Input: Parameters declaration (\mathbf{r} , \mathbf{r}' , \mathbf{C}_{ijkl} , \mathbf{SN} , \mathbf{T}_{loop} , \mathbf{T}_{foil} , \mathbf{T}_{beam} , \mathbf{n} , \mathbf{R} , \mathbf{d} , \mathbf{b}).
- 2 Output: (\mathbf{du}/\mathbf{dz} , \mathbf{dv}/\mathbf{dz} , \mathbf{dw}/\mathbf{dz})
- 3 **Step.1: Building up the simulation physical condition.**
- 4 Define simulated TEM image sizes, and receive the calculated position vector \mathbf{r} from TEM image simulation code CUFOUR.
- 5 Define geometrical and physical parameters of TEM foil, diffraction beam, dislocation loop, such as: modulus \mathbf{C}_{ijkl} , core radius \mathbf{CR} , loop radius \mathbf{R} , dislocation loop center depth within thin TEM foil from bottom \mathbf{d} , and initialize the transformation matrix between crystal coordinate, beam coordinate, TEM foil coordinate and dislocation loop coordinate: \mathbf{T}_{loop} , \mathbf{T}_{foil} , \mathbf{T}_{beam} respectively.
- 6 Define dislocation loop habit plane normal vector and Burger vector \mathbf{HN} , \mathbf{b} respectively.
- 7 Calculate Voigt isotropic equivalent modulus μ , poisson ratio ν , and Lamé λ .
- 8 Initialize the Kronecker-Delta operator δ_{ij} , Levi-Civita permutation operator ϵ_{ijk} .
- 9 Segmentation of dislocation loop perimeter, and the position of dislocation segment is described by \mathbf{r}' .
- 10 **Step.2: Calculate the image stress field at free surfaces of thin TEM foil.**
- 11 Meshing the free surface of thin foil with given periodic length and meshing step (\mathbf{PL} , \mathbf{MS}).
- 12 **for** $-\mathbf{PL}/2 < \mathbf{x} < \mathbf{PL}/2$, $-\mathbf{PL}/2 < \mathbf{y} < \mathbf{PL}/2$ **do**
- 13 Calculate the dislocation loop induced bulk stress value via isotropic Mura dislocation segment integration at given position \mathbf{r} , according to formula (4-6) to (4-9) in crystal coordinate.
- 14 Perform integration along dislocation loop perimeter, and harvest the bulk stress and image stress at free surfaces of thin TEM foil, according to free traction BC.
- 15 **end for**
- 16 Transform the image stress field from crystal coordinate to beam coordinate.
- 17 **Step.3: Perform isotropic Weinberger image gradient calculation in Fourier space.**
- 18 Perform 2D discrete Fourier transformation of the harvested image stress field through isotropic Mura dislocation segment integration, and comparison will be made between isotropic Mura dislocation segment integration model and isotropic Weinberger image stress model in Fourier space, thus satisfying free traction BC for each $(\mathbf{k}_x, \mathbf{k}_y)$ Fourier mode. Then, the 2D discrete Fourier coefficients for the symmetrical and asymmetrical image displacement field of dislocation loop isotropic Weinberger image gradient model can be calculated out respectively.
- 19 Finally, the 2D discrete Fourier coefficients are employed for image gradient value (\mathbf{du}/\mathbf{dz} , \mathbf{dv}/\mathbf{dz} , \mathbf{dw}/\mathbf{dz}) calculation in electron beam coordinate via reverse FFT transformation process at given position \mathbf{r} within thin TEM foil.
- 20 **Step.4: Calculate the Mura isotropic finite gradient value within thin TEM foil.**
- 21 **If** \mathbf{r} is within the dislocation core region of dislocation loop within TEM thin foil, then
- 22 Calculate dislocation loop core gradient $\mathbf{u}_{ij}^{\text{core}}$, according to eigengenstrain in crystal coordinate.

-
- 23 **else**
- 24 Calculate the dislocation loop induced finite gradient value via Mura isotropic dislocation segment integration at given position \mathbf{r} , according to formula (4-6) and (4-7) in crystal coordinate.
- 25 **endif**
- 26 Perform integration along dislocation loop perimeter, and harvest the finite gradient at the calculated position vector \mathbf{r} .
- 27 Transform the finite gradient value from crystal coordinate to beam coordinate.
- 28 Add the image gradient value via isotropic Mura-Weinberger image gradient model and finite gradient value via isotropic Mura dislocation segment integration together as the final total gradient value (\mathbf{du}/\mathbf{dz} , \mathbf{dv}/\mathbf{dz} , \mathbf{dw}/\mathbf{dz}) in electron beam coordinate at given position \mathbf{r} within thin TEM foil, and returned back into CUFOUR for Runge-Kutta integration along electron propagation direction.
-

Algorithm. 4.19:

The details for implementing dislocation loop anisotropic WSL-Wu-WSL total gradient model into CUFOUR are described as following:

- 1 Input: Parameters declaration (\mathbf{r} , \mathbf{r}' , \mathbf{C}_{ijkl} , \mathbf{SN} , \mathbf{T}_{loop} , \mathbf{T}_{foil} , \mathbf{T}_{beam} , \mathbf{n} , \mathbf{R} , \mathbf{d} , \mathbf{b}).
- 2 Output: (\mathbf{du}/\mathbf{dz} , \mathbf{dv}/\mathbf{dz} , \mathbf{dw}/\mathbf{dz})
- 3 **Step.1: Building up the simulation physical condition.**
- 4 Define simulated TEM image sizes, and receive the calculated position vector \mathbf{r} from TEM image simulation code CUFOUR.
- 5 Define geometrical and physical parameters of TEM foil, diffraction beam, dislocation loop, such as: modulus \mathbf{C}_{ijkl} , core radius \mathbf{CR} , loop radius \mathbf{R} , dislocation loop center depth within thin TEM foil from bottom \mathbf{d} , and initialize the transformation matrix between crystal coordinate, beam coordinate, TEM foil coordinate and dislocation loop coordinate: \mathbf{T}_{loop} , \mathbf{T}_{foil} , \mathbf{T}_{beam} respectively.
- 6 Define dislocation loop habit plane normal vector and Burger vector \mathbf{HN} , \mathbf{b} respectively.
- 7 Initialize the Kronecker-Delta operator δ_{ij} , Levi-Civita permutation operator ϵ_{ijk} .
- 8 Segmentation of dislocation loop perimeter, and the position of dislocation segment is described by \mathbf{r}' .
- 9 **Step.2: Calculate the image stress field at free surfaces of thin TEM foil.**
- 10 Meshing the free surface of thin foil with given periodic length and meshing step (\mathbf{PL} , \mathbf{MS}).
- 11 **for** $-\mathbf{PL}/2 < \mathbf{x} < \mathbf{PL}/2$, $-\mathbf{PL}/2 < \mathbf{y} < \mathbf{PL}/2$ **do**
- 12 Calculate the dislocation loop induced bulk stress value via anisotropic WSL dislocation segment integration at given position \mathbf{r} , according to formula (4-10) to (4-18) in crystal coordinate.
- 13 Perform integration along dislocation loop perimeter, and harvest the bulk stress and image stress at free surfaces of thin TEM foil, according to free traction BC.
- 14 **end for**
- 15 Transform the image stress field from crystal coordinate to beam coordinate.
- 16 **Step.3: Perform anisotropic Wu image gradient calculation in Fourier space.**
- 17 Perform 2D discrete Fourier transformation of the harvested image stress field through anisotropic WSL dislocation segment integration, and comparison will be made between anisotropic WSL dislocation segment integration model and anisotropic Wu image stress model in Fourier space, thus satisfying free traction BC for each $(\mathbf{k}_x, \mathbf{k}_y)$ Fourier mode. Then, the 2D discrete Fourier coefficients for the symmetrical and asymmetrical image displacement field of dislocation loop anisotropic Wu image stress model can be calculated out respectively.
- 18 Finally, the 2D discrete Fourier coefficients are employed for image gradient value (\mathbf{du}/\mathbf{dz} , \mathbf{dv}/\mathbf{dz} , \mathbf{dw}/\mathbf{dz}) calculation in electron beam coordinate via reverse FFT transformation process at given position \mathbf{r} within thin TEM foil.
- 19 **Step.4: Calculate the WSL anisotropic finite gradient value within thin TEM foil.**
- 20 **If** \mathbf{r} is within the dislocation core region of dislocation loop within TEM thin foil, then
- 21 Calculate dislocation loop core gradient \mathbf{u}_{ij}^{core} , according to eigengenstrain in crystal coordinate.
- 22 **else**
- 23 Calculate the dislocation loop induced finite gradient value via WSL anisotropic dislocation segment integration at given position \mathbf{r} , according to formula (4-10) to (4-16) in crystal coordinate.
- 24 **endif**
- 25 Perform integration along dislocation loop perimeter, and harvest the finite gradient at the calculated position vector \mathbf{r} .
- 26 Transform the finite gradient value from crystal coordinate to beam coordinate.

-
- 27 Add the image gradient value via anisotropic WSL-Wu image gradient model and finite gradient value via anisotropic WSL dislocation segment integration together as the final total gradient value (\mathbf{du}/\mathbf{dz} , \mathbf{dv}/\mathbf{dz} , \mathbf{dw}/\mathbf{dz}) in electron beam coordinate at given position \mathbf{r} within thin TEM foil, and returned back into CUFOUR for Runge-Kutta integration along electron propagation direction.
-

Algorithm. 4.20:

The details for implementing dislocation loop anisotropic Mura-Wu-WSL total gradient model into CUFOUR are described as following:

- 1 Input: Parameters declaration (\mathbf{r} , \mathbf{r}' , \mathbf{C}_{ijkl} , \mathbf{SN} , \mathbf{T}_{loop} , \mathbf{T}_{foil} , \mathbf{T}_{beam} , \mathbf{n} , \mathbf{R} , \mathbf{d} , \mathbf{b}).
 - 2 Output: (\mathbf{du}/\mathbf{dz} , \mathbf{dv}/\mathbf{dz} , \mathbf{dw}/\mathbf{dz})
 - 3 **Step.1: Building up the simulation physical condition.**
 - 4 Define simulated TEM image sizes, and receive the calculated position vector \mathbf{r} from TEM image simulation code CUFOUR.
 - 5 Define geometrical and physical parameters of TEM foil, diffraction beam, dislocation loop, such as: modulus \mathbf{C}_{ijkl} , core radius \mathbf{CR} , loop radius \mathbf{R} , dislocation loop center depth within thin TEM foil from bottom \mathbf{d} , and initialize the transformation matrix between crystal coordinate, beam coordinate, TEM foil coordinate and dislocation loop coordinate: \mathbf{T}_{loop} , \mathbf{T}_{foil} , \mathbf{T}_{beam} respectively.
 - 6 Define dislocation loop habit plane normal vector and Burger vector \mathbf{HN} , \mathbf{b} respectively.
 - 7 Initialize the Kronecker-Delta operator δ_{ij} , Levi-Civita permutation operator ϵ_{ijk} .
 - 8 Segmentation of dislocation loop perimeter, and the position of dislocation segment is described by \mathbf{r}' .
 - 9 **Step.2: Calculate the image stress field at free surfaces of thin TEM foil.**
 - 10 Meshing the free surface of thin foil with given periodic length and meshing step (\mathbf{PL} , \mathbf{MS}).
 - 11 **for** $-\mathbf{PL}/2 < \mathbf{x} < \mathbf{PL}/2$, $-\mathbf{PL}/2 < \mathbf{y} < \mathbf{PL}/2$ **do**
 - 12 Calculate the dislocation loop induced bulk stress value via dislocation loop anisotropic Mura dislocation segment integration at given position \mathbf{r} , according to formula (4-31) to (4-37) in crystal coordinate.
 - 13 Perform integration along dislocation loop perimeter, and harvest the bulk stress and image stress at free surfaces of thin TEM foil, according to free traction BC.
 - 14 **end for**
 - 15 Transform the image stress field from crystal coordinate to beam coordinate.
 - 16 **Step.3: Perform anisotropic Wu image gradient calculation in Fourier space.**
 - 17 Perform 2D discrete Fourier transformation of the harvested image stress field through anisotropic Mura dislocation segment integration, and comparison will be made between anisotropic Mura dislocation segment integration model and anisotropic Wu image stress model in Fourier space, thus satisfying free traction BC for each $(\mathbf{k}_x, \mathbf{k}_y)$ Fourier mode. Then, the 2D discrete Fourier coefficients for the symmetrical and asymmetrical image displacement field of dislocation loop anisotropic Wu image stress model can be calculated out respectively.
 - 18 Finally, the 2D discrete Fourier coefficients are employed for image gradient value (\mathbf{du}/\mathbf{dz} , \mathbf{dv}/\mathbf{dz} , \mathbf{dw}/\mathbf{dz}) calculation in electron beam coordinate via reverse FFT transformation process at given position \mathbf{r} within thin TEM foil.
 - 19 **Step.4: Calculate the WSL anisotropic finite gradient value within thin TEM foil.**
 - 20 **If** \mathbf{r} is within the dislocation core region of dislocation loop within TEM thin foil, then
 - 21 Calculate dislocation loop core gradient \mathbf{u}_{ij}^{core} , according to eigengenstrain in crystal coordinate.
 - 22 **else**
 - 23 Calculate the dislocation loop induced finite gradient value via WSL anisotropic dislocation segment integration at given position \mathbf{r} , according to formula (4-10) to (4-16) in crystal coordinate.
 - 24 **endif**
 - 25 Perform integration along dislocation loop perimeter, and harvest the finite gradient at the calculated position vector \mathbf{r} .
 - 26 Transform the finite gradient value from crystal coordinate to beam coordinate.
 - 27 Add the image gradient value via anisotropic Green-Wu image gradient model and finite gradient value via anisotropic WSL dislocation segment integration together as the final total gradient value (\mathbf{du}/\mathbf{dz} , \mathbf{dv}/\mathbf{dz} , \mathbf{dw}/\mathbf{dz}) in electron beam coordinate at given position \mathbf{r} within thin TEM foil, and returned back into CUFOUR for Runge-Kutta integration along electron propagation direction.
-

Appendix D: Numerical implementation scheme for CUFOUR

Originally, CUFOUR is employing displacement field $g \cdot R(r)$ implementation scheme. The displacement field of defects is calculated out through dislocation theory or MD firstly; then, the derivative operation $\frac{d}{dz}(g \cdot R(r))$ and Runge-Kutta integration along beam direction will be performed. In order to display simulated TEM image of inclined dislocation, a transformation Cartesian coordinate is defined, which is the mathematical operation of beam direction vector \mathbf{B} and dislocation direction vector \mathbf{U} ,

$$\begin{cases} x = -(B \times U) \\ y = -B \\ z = (B \times U) \times B \end{cases} \quad (\text{A 4-1})$$

The diffraction vector g and displacement field $R(r)$ of dislocation is calculated in the above-mentioned Cartesian coordinate, whose z direction is not along the electron beam propagation direction. The purpose of such coordinate transformation operation is making the simulated dislocation along x direction, independent of beam diffraction condition.

In the current thesis, alternative displacement gradient field $\frac{d}{dz}(g \cdot R(r))$ implementation scheme is employed in CUFOUR, and the displacement gradient of defects is calculated out through dislocation theory directly, then integration along beam direction will be performed for $\frac{d}{dz}R(r)$.

The details of the current implementation scheme are described as following:

When performing TEM diffraction imaging experiments with certain diffraction direction g , only the lattice distortion of certain plane set (normal to the selected diffraction vector) will contribute to the final TEM image black-white contrast, and a Cartesian coordinate whose z is along election beam transmisson direction is employed for explanation of the emplementation scheme.

The diffraction beam can be written as:

$$g = [g_x \ 0 \ 0] + [0 \ g_y \ 0] \quad (\text{A. 4-2})$$

Thus, there is no g_z component in electron beam coordinate.

The displacement gradient vector can be decomposed as:

$$\frac{\partial R}{\partial z} = \left[\frac{\partial u}{\partial z}, 0, 0 \right] + \left[0, \frac{\partial v}{\partial z}, 0 \right] + \left[0, 0, \frac{\partial w}{\partial z} \right] \quad (\text{A. 4-3})$$

Then,

$$g \cdot \frac{\partial R}{\partial z} = g \cdot \left[\frac{\partial u}{\partial z}, 0, 0 \right] + g \cdot \left[0, \frac{\partial v}{\partial z}, 0 \right] + g \cdot \left[0, 0, \frac{\partial w}{\partial z} \right] \quad (\text{A. 4-4})$$

Finally,

$$g \cdot \frac{\partial R}{\partial z} = g_x \frac{\partial u}{\partial z} + g_y \frac{\partial v}{\partial z} \quad (\text{A. 4-5})$$

Thus, $\frac{\partial w}{\partial z}$ will not have any contribution to the final TEM diffraction image contrast.

Acknowledgements

I would like to express my sincere gratitude to all people who have been involved and have made practical contribution to the PhD thesis accomplishment.

I am grateful to my thesis directors Prof Cecile Hebert and Dr. Robin Schäublin for their research guide and supervision on doing research and rational scientific discussion.

Especially, I would like to thank Dr. Robin Schäublin, who incubate and guide the PhD thesis topic on TEM diffraction image simulation of defects. I will always be grateful to him for his generous contribution and encouragement on developing new ideas, not giving up and always take responsible, positive and proactive attitude at things.

I would like to thank Mrs. Eugenia Minikus, Drs. Elisabeth Mueller and Drs. Sousan Abolhassani for their kind help with TEM operation and theoretical explanation with enthusiasm and patience.

I would like to thank my colleagues Mr Kun Wang, Dr. Tielong Shen, Mrs. Vieh Christiane, Dr. Cozzo Cedric, Drs. Maria Cabanes, Drs. Anna Prokhodtseva, Dr. Andi Idhil Ismail, Dr. Yong Dai, Dr. Manuel Pouchon and other people with whom I worked with at PSI, especially the colleagues from ANM (Advanced Nuclear Material) group of NES (Nuclear Energy and Safety) department of PSI.

Wenwang Wu,
2014-03-18,
Villigen, Switzerland.

Curriculum Vitae

Personal

Name	Wenwang Wu
Date of birth	10th December, 1984
Place of birth	Funan, Anhui, China
Citizenship	China

Education

2010-2014	PhD student, Department of material science and engineering, Ecole Polytechnique Fédérale de Lausanne (EPFL), Switzerland. The work was performed at the Advanced Nuclear Material group of NES, Paul Scherrer Institute, Villigen, Switzerland.
2005-2008	Master degree in Science, School of Aerospace, Tsinghua University, Beijing, China.
2000-2004	Bachelor in theoretical and applied mechanics, Department of Modern Mechanics, University of Science and Technology of China , Hefei, China.

Journal publication:

Wenwang Wu, Robin Schäublin, Jiachao Chen. General dislocation image stress of anisotropic cubic thin film. *J. Appl. Phys.* 112, 093522, 2012.

Presentations:

Wenwang Wu, et al. Image stress effect on TEM image simulation of dislocations in thin film. Seminar on Nuclear Materials (EPFL, MSE-625), March 28, Flumsberg, Switzerland, 2012.

Wenwang Wu, et al. Possible image stress effect on TEM image simulation of dislocations. NES PHD Day, June 13, PSI Villigen, Switzerland, 2012.

Wenwang Wu, et al. Simulation of dislocation loops in irradiated FeCr. NES PHD Day, May 23, PSI Villigen, Switzerland, 2013.

Posters:

Wenwang Wu, et al. Image stress effects of dislocation loops in anisotropic thin film. Numat 2012 conference, October 22-25, Osaka, Japan, 2012.

Wenwang Wu, et al. Many weak beam TEM image simulation of inclined dislocation. The 6th EDMX Research Day, September 6, EPFL Lausanne, Switzerland, 2013.

Wenwang Wu, et al. Many weak beam TEM image simulation of dislocation and dislocation loops. ICMRF16, October 20-26, Beijing, China, 2013.

